

## Polarization handling in photonic integrated circuits

**Citation for published version (APA):**

Augustin, L. M. (2008). *Polarization handling in photonic integrated circuits*. [Phd Thesis 1 (Research TU/e / Graduation TU/e), Electrical Engineering]. Technische Universiteit Eindhoven. <https://doi.org/10.6100/IR634815>

**DOI:**

[10.6100/IR634815](https://doi.org/10.6100/IR634815)

**Document status and date:**

Published: 01/01/2008

**Document Version:**

Publisher's PDF, also known as Version of Record (includes final page, issue and volume numbers)

**Please check the document version of this publication:**

- A submitted manuscript is the version of the article upon submission and before peer-review. There can be important differences between the submitted version and the official published version of record. People interested in the research are advised to contact the author for the final version of the publication, or visit the DOI to the publisher's website.
- The final author version and the galley proof are versions of the publication after peer review.
- The final published version features the final layout of the paper including the volume, issue and page numbers.

[Link to publication](#)

**General rights**

Copyright and moral rights for the publications made accessible in the public portal are retained by the authors and/or other copyright owners and it is a condition of accessing publications that users recognise and abide by the legal requirements associated with these rights.

- Users may download and print one copy of any publication from the public portal for the purpose of private study or research.
- You may not further distribute the material or use it for any profit-making activity or commercial gain
- You may freely distribute the URL identifying the publication in the public portal.

If the publication is distributed under the terms of Article 25fa of the Dutch Copyright Act, indicated by the "Taverne" license above, please follow below link for the End User Agreement:

[www.tue.nl/taverne](http://www.tue.nl/taverne)

**Take down policy**

If you believe that this document breaches copyright please contact us at:

[openaccess@tue.nl](mailto:openaccess@tue.nl)

providing details and we will investigate your claim.

# Polarization Handling in Photonic Integrated Circuits



# Polarization Handling in Photonic Integrated Circuits

PROEFSCHRIFT

ter verkrijging van de graad van doctor  
aan de Technische Universiteit Eindhoven,  
op gezag van de Rector Magnificus, prof.dr.ir. C.J. van Duijn,  
voor een commissie aangewezen door het College voor Promoties  
in het openbaar te verdedigen op  
maandag 2 juni 2008 om 16.00 uur

door

Ludovicus Marie Augustin

geboren te Maastricht

Dit proefschrift is goedgekeurd door de promotoren:

prof.dr.ir. M.K. Smit  
en  
prof.dr.ir. R. Baets

Copromotor:  
dr. J.J.G.M. van der Tol

This work was supported by the Dutch Ministry of Economic Affairs (NRC Photonics) and the European Community (IST-MUFINS, IST-STOLAS).

Copyright ©2008 Ludovicus Marie Augustin

Typeset using L<sup>A</sup>T<sub>E</sub>X, printed in The Netherlands.

CIP-DATA LIBRARY TECHNISCHE UNIVERSITEIT EINDHOVEN

Augustin, Ludovicus Marie

Polarization handling in photonic integrated circuits / by Ludovicus Marie Augustin. -  
Eindhoven : Technische Universiteit Eindhoven, 2008.

Proefschrift. - ISBN 978-90-386-1854-8

NUR 959

Trefw.: opto-elektronica / geïntegreerde optica / optische polarisatie / 3-5 verbindingen.

Subject headings: optoelectronic devices / integrated optoelectronics / light polarisation /  
III-V semiconductors.

aon pap en mam



---

# Contents

---

<b>1</b>	<b>Introduction</b>	<b>1</b>
1.1	Generic integration technology with polarization handling capability .....	2
1.1.1	POLARIS wavelength converter .....	4
1.1.2	Polarization independent SOA .....	5
1.1.3	Polarization MZI .....	6
1.2	Structure of this thesis .....	6
<b>2</b>	<b>Integrated components and their polarization properties</b>	<b>9</b>
2.1	Active-passive integration .....	10
2.2	Waveguides .....	11
2.3	MMI couplers .....	15
2.3.1	Design .....	15
2.3.2	Reflections .....	18
2.4	Spot size converters .....	22
2.4.1	Horizontal tapers .....	22
2.4.2	2D tapers .....	23
2.5	SOAs .....	28
2.5.1	Design .....	31
2.5.2	Measurements on the QW SOA .....	32
2.6	Conclusions .....	34
<b>3</b>	<b>Integration technology</b>	<b>37</b>
3.1	Introduction .....	37
3.2	Active-passive integration .....	37
3.2.1	Active-Passive butt-joint .....	38
3.2.2	PIC processing .....	39



3.3	High resolution lithography.....	42
3.3.1	Waferstepper.....	42
3.3.2	Electron beam lithography.....	43
3.3.3	Technology.....	44
3.4	Technology for packaging.....	45
3.4.1	Alignment on the submount.....	45
3.4.2	Vertical taper.....	47
3.5	Sloped sidewalls.....	50
3.5.1	Wet etch.....	50
3.5.2	Masking.....	51
3.6	Conclusions.....	52
<b>4</b>	<b>Polarization converters</b>	<b>55</b>
4.1	Introduction.....	55
4.2	Principle.....	56
4.3	First generation.....	60
4.3.1	Design.....	60
4.3.2	Fabrication.....	63
4.3.3	Characterization.....	65
4.3.4	Integration.....	66
4.4	Second generation.....	68
4.4.1	Design.....	69
4.4.2	Fabrication.....	69
4.4.3	Characterization.....	73
4.5	Conclusion.....	74
<b>5</b>	<b>Polarization splitters</b>	<b>75</b>
5.1	Introduction.....	75
5.2	Directional coupler polarization splitter.....	77
5.2.1	Principle.....	77
5.2.2	Simulations.....	81
5.2.3	Design.....	84
5.2.4	Fabrication.....	84
5.2.5	Characterization.....	85
5.3	MZI Polarization splitter.....	87
5.3.1	Principle.....	88
5.3.2	Simulation.....	89
5.3.3	Design.....	93
5.3.4	Fabrication I.....	94
5.3.5	Characterization I.....	95
5.3.6	Design and fabrication II.....	96
5.3.7	Characterization II.....	97
5.4	Conclusions.....	98

---

<b>6</b>	<b>Wavelength converters</b>	<b>99</b>
6.1	Introduction .....	99
6.2	Principle .....	100
6.3	First generation .....	102
6.3.1	Design and fabrication.....	102
6.3.2	Static characterization .....	102
6.3.3	Dynamic characterization .....	105
6.4	Second generation.....	109
6.4.1	Design and fabrication.....	109
6.4.2	Packaging .....	111
6.4.3	Static characterization .....	111
6.4.4	Electrical switching.....	113
6.4.5	Dynamic characterization .....	114
6.5	Conclusions .....	114
<b>7</b>	<b>POLARIS</b>	<b>117</b>
7.1	Introduction .....	117
7.2	Principle of the POLARIS wavelength converter.....	118
7.3	Simulation study and POLARIS concepts .....	119
7.4	Fiber based POLARIS.....	124
7.4.1	Experiments.....	125
7.5	Integrated POLARIS.....	128
7.5.1	Design.....	128
7.5.2	Generic integration technology with polarization handling capability ....	130
7.5.3	Finished chip.....	131
7.6	Conclusions .....	134
<b>8</b>	<b>Conclusions and Outlook</b>	<b>137</b>
8.1	Conclusions .....	137
8.2	Recommendations .....	138
8.3	Outlook .....	139
8.3.1	Polarization control.....	139
8.3.2	Polarization switchable laser .....	141
<b>A</b>	<b>Polarization description and visualization tools</b>	<b>143</b>
A.1	Polarization.....	143
A.2	Jones vector .....	144
A.3	Stokes parameters.....	146
	<b>References</b>	<b>149</b>
	<b>List of abbreviations</b>	<b>157</b>

---

<b>Summary</b>	<b>159</b>
<b>Samenvatting</b>	<b>161</b>
<b>Dankwoord</b>	<b>163</b>
<b>Curriculum Vitae</b>	<b>167</b>
<b>List of publications</b>	<b>169</b>
Journal articles .....	169
Conference contributions .....	169

---

# Chapter 1

## Introduction

---

Optical communications has been part of human life since ancient history. The first optical communication was based on visible transmission of messages: evolving from simple smoke-signalling to the optical telegraph in 1792: semaphores with relay stations invented by Claude Chappe. Only in the last half of the twentieth century fiber-optic communication became reality, by invention of the laser in 1960 [1], but mainly by the development of the semiconductor laser [2] and the low-loss fiber [3] in 1970. It took until approximately 1990 for the first long distance links to be commercially employed. This became possible by the invention of the Erbium Doped Amplifier (EDFA) in 1987.

Optical fiber communication is the core of the internet. In the last decade the internet has grown enormously. This growth still continues and therefore the amount of data traffic is increasing dramatically. To deal with this increasing demand, the optical networks need to be improved even further. The bandwidth of the fibers is very large. With Wavelength Division Multiplexing (WDM), this bandwidth can be employed to increase the capacity of the network further. In this technique, multiple wavelengths are used in parallel in a single fiber for carrying multiple independent signals.

In the nodes of the network, optical and electrical components are present to manipulate the light: to amplify, to regenerate, to convert to another wavelength, or to switch the light to the desired destination. These functions can be performed in two ways: by converting the light to an electrical signal, analyse and process it, and convert it back to the desired optical signal again; or by doing it all-optically. All-optical signal processing will enable the highest switching speeds, because the limited speed of electronics is still a bottleneck.

Photonic Integrated Circuits (PICs) are promising devices for all-optical processing. By inte-

grating optical functions in a single chip in a PIC the reliability and stability can be improved, the size and costs can be reduced with respect to using separate bulk components, and the scalability improved.

A disadvantage of the small size of a PIC is the coupling to an optical fiber. The coupling tolerances are tight and the losses high. A solution is to integrate spot size converters into the PIC to ease the coupling and to decrease the losses.

Another problem is that the planar geometry of a PIC causes different behavior for the two orthogonally polarized modes. TE polarized modes: where the electric field vector is parallel to the PIC surface, and TM polarized modes: where the electric field vector is perpendicular to the surface, have different boundary conditions which lead to different propagation constants and confinement factors. Given the fact that the fibers in the network do not preserve the state of polarization of the light, this leads to a varying performance of the PIC as the polarization of the incoming light changes.

To overcome this problem, different approaches can be applied. One approach is to remove polarization dependence by changing the properties of the material [4, 5] or the geometry of the waveguides [6, 7]. This can be difficult or even impossible, and furthermore will always be compromising with respect to optimal performance for one of the polarization states.

An alternative is polarization diversity: create subcircuits for each of the two polarization states. In this way, components optimized for one well-defined state of polarization can be used and the polarization can be matched to the optimal performance.

Polarization is not only a problem, it can be very useful. A consequence of the waveguide structure and its birefringence is that the two polarizations are very stable inside the waveguides in a PIC. Conversion between them is only obtained in very short bends or specially designed devices. Because of this, the polarization can be used for new functions [8, 9], some of which will be discussed in this thesis.

On-chip manipulation of the polarization can help to achieve polarization diversity and to add extra functionality based on polarization. This requires a generic technology for polarization components that can be integrated with standard active and passive components on a PIC. The next section will present an overview of this generic technology.

## 1.1 Generic integration technology with polarization handling capability

In this thesis a generic technology for PICs with integrated polarization manipulation functions is developed. This is achieved by extending the existing technology. The standard COBRA active-passive technology consists of the following building blocks.

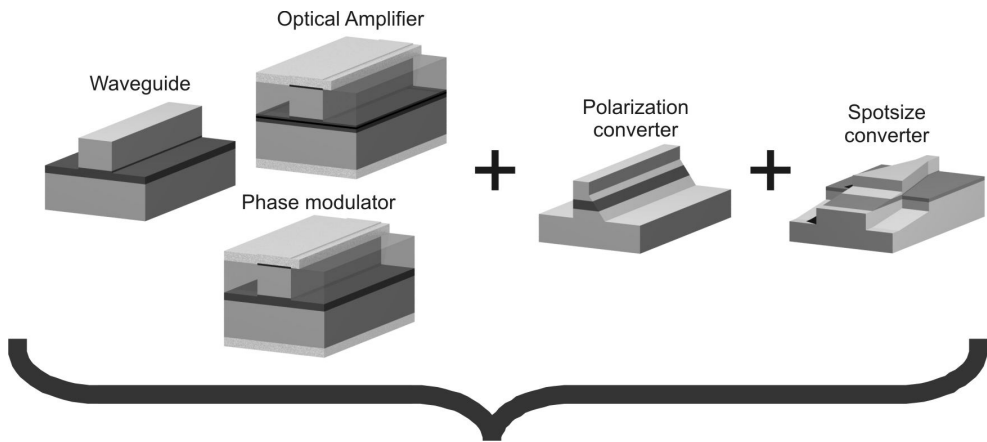
- Passive devices, such as waveguides and splitters, which are transparent for the operation wavelengths and can be used for functions like guiding, splitting and filtering of the light on the chip.
- Electro-optic phase modulators that are used to control the phase of the light.

- Semiconductor Optical Amplifiers (SOAs), which are used to amplify light and can be used as a non-linear element, with a power-dependent transfer for both amplitude and phase of the light.

In this thesis, the extension of the standard technology with an improved integrated spot size converter is described. This eases the coupling of a PIC to a standard single mode fiber and reduces the coupling losses, enabling the possibility of packaging the PIC.

In the standard components the performance is polarization dependent. These properties can be used to manipulate the phase and amplitude difference between the two polarizations. However, for full polarization handling two additional components are required: polarization converters and polarization splitters. Polarization converters are needed to convert one polarization state into the other. Polarization splitters are necessary to separate the different polarizations and route them into different optical paths.

The main effort of the work described in this thesis focuses on extending the standard technology with a new type of polarization converter and its application in a novel polarization independent wavelength converter. Furthermore a novel type of polarization splitter has been developed that consists of a passive Mach Zehnder Interferometer and polarization converters. Thus by only adding a polarization converter, the generic platform with polarization handling, including a polarization splitter is obtained. Secondly by the addition of a spot size converter, packaging of the PICs becomes feasible. Fig. 1.1 shows the full set of devices that is contained in this generic platform.



**Figure 1.1:** Generic integration technology with polarization handling capability.

The next section will show some examples of improvements and new functions that will be possible by using the new generic integration platform with on-chip polarization handling.

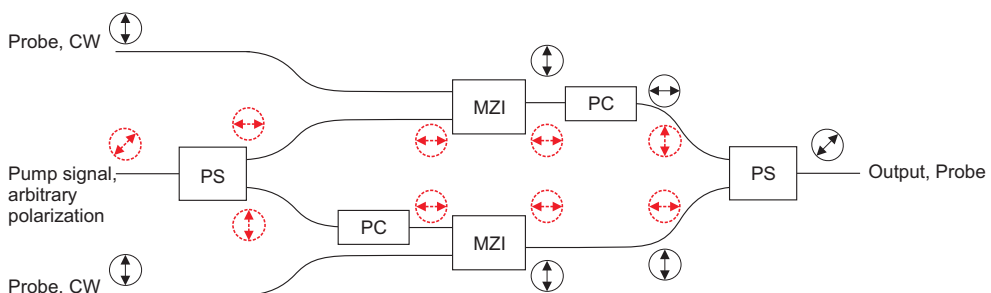
### 1.1.1 POLARIS wavelength converter

The performance of a wavelength converter can be optimized by using the polarization. Wavelength converters are key components in wavelength routed optical networks. The most promising wavelength converters are based on Mach Zehnder Interferometers (MZI) with Semiconductor Optical Amplifiers (SOA) in the arms [10]. In these devices the signal from the network (pump) changes the phase in one of the arms and the data from the pump is transferred to a locally generated signal (probe). These devices operate best if they are used in co-directional operation [11], but this results in the two signals being present in the output of the device. The pump has to be filtered out. For this purpose tuneable wavelength filters are required. These are expensive and difficult to integrate, furthermore it poses a problem if conversion to the same wavelength (for regeneration) is required.

A solution, which allows conversion to the same wavelength and still uses a co-propagation scheme, is the Dual Order Mode (DOMO) wavelength converter [12, 13]. In this scheme, the pump is injected as the first-order mode, while the probe is in the fundamental mode. By using an MMI as a modefilter, the two signals can be separated. Here mode coupling will degrade the performance severely. Furthermore, polarization dependence problems still occur.

To overcome these problems, a new scheme for wavelength conversion is presented. This scheme uses the polarization to facilitate the desired co-directional propagation.

The improved wavelength converter is obtained with the POLARIS concept (POLarization Labeling for Rejection and Isolation of Signals). POLARIS is a polarization diversity scheme in which polarization is used for signal labeling. A schematic drawing is shown in Fig. 1.2. The signal from the network (pump signal), which carries the data, arrives in an arbitrary polarization. This signal is split into two orthogonal polarizations. In one branch, the polarization is rotated to have the pump signal in both branches in the same polarization state (e.g. TE). These signals are injected into the MZIs together with the locally generated CW light (probe signal) in the orthogonal polarization (e.g. TM). After interacting in the MZI the data information is transferred to the CW wavelength and both signals have to be separated. This is achieved by rotating the polarization of the upper branch and then using a polarization splitter/combiner to combine both branches. As only TE in the upper and TM in the lower input of the combiner will couple to the output, filtering of the unwanted signal occurs.



**Figure 1.2:** POLARIS wavelength converter

POLARIS allows polarization independent (with polarization sensitive SOAs), co-propagating wavelength conversion, without the need to use wavelength filters. It even allows data transfer to the same wavelength, for regeneration and full flexibility.

The POLARIS concept can also be employed in a number of other applications where interaction between different optical signals is needed, like in all-optical switches.

Apart from the POLARIS concept, the integration of the polarization components in the generic technology offers many more possibilities. Some examples are given next.

### 1.1.2 Polarization independent SOA

In SOAs the polarization dependent behavior can be problematic, leading to different propagation, amplification and non-linear phase shifts for the two orthogonal polarizations.

In a PESSOA (Polarization Effect Suppression in Semiconductor Optical Amplifiers) device, on-chip polarization manipulation is employed to avoid polarization dependence. Two solutions are depicted in Fig. 1.3. In the first a polarization converter is placed halfway in an SOA, causing any arbitrarily polarized signal at the input to experience TE-amplification and TE-phase shift in one half of the device, but TM-amplification and TM-phase shift in the other half. The net effect is in principle polarization independent, both for amplification and phase shift.

The second solution uses polarization diversity: an incoming optical signal is split into a TE- and a TM-part with a polarization splitter. The TM-part is first converted to TE with a polarization converter and then both signals are fed trough an SOA. In this way both parts experience TE-amplification and TE-phase shift. At the output, a polarization converter is placed in the other branch to balance the losses. In this branch the original TE-part is converted into TM, so both parts can be combined with a polarization splitter.

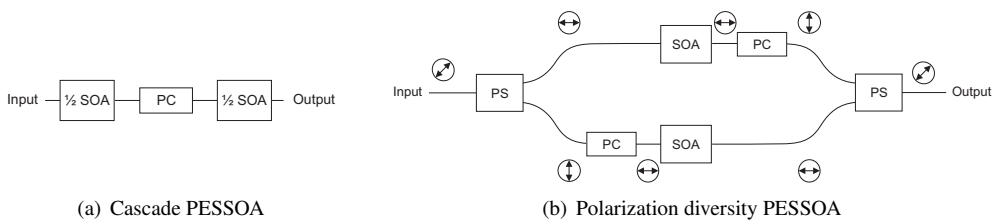


Figure 1.3: Two types of PESSOA (Polarization Effect Suppression in Semiconductor Optical Amplifiers).

This example can be extended to other devices as well. Therefore, with a technology for on-chip polarization handling, new solutions to polarization problems in standard components become possible.

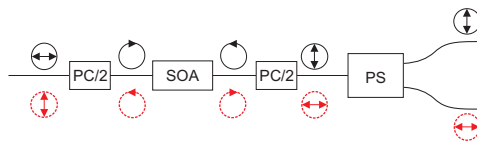


### 1.1.3 Polarization MZI

The polarization can be used to provide light with two independent virtual paths in the same physical waveguide. This can be applied to form an MZI. In a traditional MZI, two different physical paths are used; the phase difference between the two paths results in an interference at the output coupler.

The polarization switch (Fig. 1.4) is basically an MZI in which the two arms are separated by using different polarizations. Nonlinear polarization rotation in an SOA can be used for switching and wavelength conversion [14, 15]. An integrated version of this component is possible with the proposed polarization technology. The advantage is a smaller footprint and lower losses, because of the avoidance of bends.

At the input of the switch, the pump and the probe are converted to orthogonally circular polarized signals in the input half PC. Both signals are injected into the SOA which functions as a nonlinear phase shifter. At the output of the SOA, the TE and TM polarized parts of the signals have experienced a power-dependent phase shift. The signals are combined again into the output half PC. Depending on this relative phase shift, the probe couples to TE or TM. By putting a polarization splitter at the output, switching can be obtained.



**Figure 1.4:** Integrated polarization MZI switch.

These examples show that a generic integration technology of active and passive components with polarization converters enables a broad variety of functions and improvements in PICs. By also integrating a spot size converter the devices can be packaged and be versatilely used. In this way a very strong technology platform is obtained.

## 1.2 Structure of this thesis

The aim of this thesis is to develop a generic technology for on-chip polarization handling. To this end, the development of separate polarization components (converters and splitters) is investigated together with their integration in a single PIC.

The design and polarization properties of the integrated components that are available in the standard technology (waveguides, MMIs and SOAs), are discussed in chapter 2. In this chapter also an improved spot size converter is introduced, that can be integrated with active components.

The required integration technology for PICs is treated in chapter 3. The standard technology

is explained, as well as additional processing steps for advanced features, such as high resolution lithography, spot size converters, precision cleave etches and polarization converters.

The next chapters deal with the polarization components. In chapter 4 two generations of polarization converters are described. The design, fabrication and results are shown. A new PC is developed that is fully integrateable in a PIC. In chapter 5 polarization splitters are discussed. A novel splitter is introduced based on an MZI with polarization converters in its arms. Using this device, the generic platform for polarization manipulation can be obtained by adding only one component, the polarization converter.

A important building block of the POLARIS concept is a Mach Zehnder Interferometer. In chapter 6 we describe two wavelength converters based on MZIs as a first step towards the realization of a POLARIS wavelength converter. One of these SOA-MZIs is integrated with spot size converters and has been packaged. With this device conversion at 40 Gb/s has been demonstrated.

With these building blocks, a POLARIS wavelength converter can be constructed. The concept is explored in more detail in chapter 7. Simulations are shown and the concept is experimentally demonstrated by using the integrated MZI from chapter 6 with the polarization manipulation done outside the chip with fiber based polarization components. Furthermore, the design and fabrication of an integrated version of POLARIS are discussed.

Finally in chapter 8 conclusions are drawn and an outlook is presented.



---

# Chapter 2

## Integrated components and their polarization properties

---

Photonic Integrated Circuits (PIC) contain different components. First of all they contain passive components: waveguides, required to guide the light on the chip, splitters, and couplers. Furthermore, to actively control the light, active components, such as SOAs, and electro-optic devices like phase modulators are needed.

This chapter treats the designs and polarization properties of the passive components and the SOAs that will be used in the PICs of chapters 6 and 7. The polarization manipulating components are discussed separately in chapters 4 and 5.

All components have to be integrated in a layerstack compatible with the active-passive integration scheme. This layerstack will be described first.

In the subsequent sections the passive components are considered. First shallow and deep waveguides, then Multi Mode Interference (MMI) couplers, used as splitters and combiners, are discussed. Their properties and the measures taken to reduce reflections are presented and experimentally confirmed. Furthermore fiber-chip coupling is examined. First simple lateral tapers to improve this are described. Next a full spot size converter is introduced to couple PICs efficiently to single mode fibers.

In the last section, the design and characterization of the SOAs are discussed, including the measures that are developed to prevent lasing because of reflections.

## 2.1 Active-passive integration

The material system of choice for PICs is InP/InGaAsP. These materials are direct bandgap semiconductors and hence light can be generated and amplified inside them. By changing its composition, the bandgap of InGaAsP can be adjusted, while keeping it lattice matched to InP, which is needed to allow epitaxial growth on InP. The bandgap can be tuned over a wide wavelength range, ranging from 1 $\mu\text{m}$  to beyond 1.6  $\mu\text{m}$ . This makes the material system specially suited for operation at the telecom wavelengths around 1.55  $\mu\text{m}$ . The bandgap can be tuned for passive components to be transparent for 1.55  $\mu\text{m}$ , and for active functions to be absorbing and, when current is injected, amplifying.

The layerstacks for integration of both active and passive functions are discussed here.

### Passive layerstack

The passive layerstack is designed to transport light with low loss. The waveguide layer consist of a Quaternary (InGaAsP) layer with a bandgap of 1.25  $\mu\text{m}$ . This value is a trade-off between high index contrast with respect to InP for good waveguiding, high electro-optical phase modulation, low absorption loss for a wavelength of 1.55  $\mu\text{m}$ , and good absolute refractive index control [16]. A thickness of 500 nm is chosen to be as thick as possible for low loss, while maintaining the mono-mode condition in the vertical direction. This Q(1.25) layer is sandwiched between InP layers. The first 300 nm of the upper cladding are non intentionally doped, to avoid doping induced losses. All thicknesses and doping levels are optimized according to [17]. The total passive layerstack is shown in table 2.1, the tints are used throughout this thesis.

### Active layerstack

The active layerstack contains an active region centered in a Q(1.25) waveguide layer. In the first experiments, the active region consists of a 120 nm thick bulk Q(1.55) active region as was used in [17, 16]<sup>1</sup>. In later experiments the active region consists of 8 pairs of unstrained InGaAs Quantum Wells (QW)<sup>2</sup> with strained InGaAs barriers, having a total thickness of 89 nm. The choices made for the number and nature of the QWs is explained in section 2.5. The total thickness of the active waveguide layer is 500 nm to match the passive waveguide layer.









The first 300 nm of the upper cladding are lowly P-doped in this case, with a doping concentration high enough to reduce the series resistance for the SOA and low enough to avoid additional losses. Because of Zn diffusion some doping will be present in the upper part of the Q1.25 layer. This will result in a PN junction close to the active region. The total active layerstack is shown in table 2.2.

---

<sup>1</sup>The bulk active material was grown at JDS Uniphase, Eindhoven

<sup>2</sup>The QW active material was grown at the Centre for Integrated Photonics, Ipswich, UK

**Table 2.1:** Passive layerstack

Thickness [nm]	Material	Doping level [ $\text{cm}^{-3}$ ]	Legend
100	P-InGaAs	$> 1 \cdot 10^{19}$	
1000	P-InP	$1 \cdot 10^{18}$	
200	P-InP	$5 \cdot 10^{17}$	
20	P-Q(1.25)	$3 \cdot 10^{17}$	
300	i-InP	n.i.d.	
500	i-Q(1.25)	n.i.d.	
500	N-InP	$3.5 \cdot 10^{17}$	
substrate	N-InP	$2 \cdot 10^{18}$	

## 2.2 Waveguides

Transparent waveguides are used to guide the light on a PIC. For the purpose of this thesis, the main properties of waveguides are the birefringence and the propagation losses. The loss in a waveguide should be as small as possible. The birefringence can be either enhanced, to be able to use it, or made as small as possible, to be able to neglect it.











The main design parameters are the width and the etch depth. Two types of waveguides are distinguished: shallowly and deeply etched waveguides. Shallow waveguides are etched 100 nm into the film layer; deep waveguides are etched completely through.

The birefringence, the difference in refractive index for the two orthogonal polarizations, is causing polarization dependent behavior. In a waveguide, the modal birefringence, the difference in effective index ( $\Delta N_{eff} = N_{eff, TM} - N_{eff, TE}$ ) that the propagating polarization modes experience, is caused by a different confinement of the light for the two polarizations, by different electromagnetic boundary conditions, and by the possible presence of material birefringence. These different causes of birefringence are now investigated further.

### Modal birefringence

Given a certain material refractive index (and birefringence, the difference in the refractive indices  $\Delta n$ ), the modal birefringence can be designed. The birefringence depends on the geometry of the waveguide, especially on the width and the thickness of the topcladding.

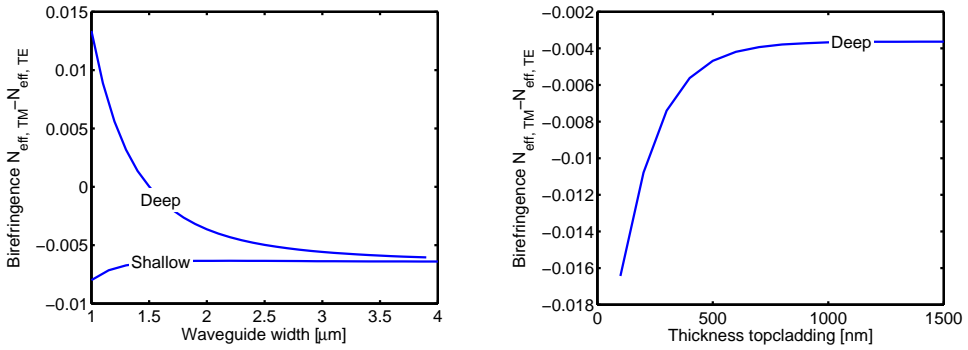
Table 2.2: Active layerstack

Thickness [nm]	Material	Doping level [ $\text{cm}^{-3}$ ]	Legend
100	P-InGaAs	$> 1 \cdot 10^{19}$	
1000	P-InP	$1 \cdot 10^{18}$	
200	P-InP	$5 \cdot 10^{17}$	
20	P-Q(1.25)	$3 \cdot 10^{17}$	
300	P-InP	$3 \cdot 10^{17}$	
190 / 205	i-Q(1.25)	n.i.d.	
120 / 89.5	i-Q(1.55) / 8 41Å InGaAs Quantum Wells, 9 63Å In-GaAs Barriers	n.i.d.	
190 / 205	i-Q(1.25)	n.i.d.	
500	N-InP	$3.5 \cdot 10^{17}$	
substrate	N-InP	$2 \cdot 10^{18}$	

The birefringence in the waveguide is calculated using the Film Mode Matching method [18]. The birefringence as a function of width for a wavelength of 1555 nm is plotted in Fig. 2.1(a) for both deep and shallow waveguides. For deep waveguides, the birefringence is 0 for a width of 1.5  $\mu\text{m}$  (Fig. 2.1(a)). A polarization independent waveguide can be obtained for this width, but the slope of the tangent at this point is steep, so the tolerance in width is very small. In contrast to a deep waveguide, the birefringence in a shallow waveguide is small and cannot be influenced much by changing the width and no polarization independent waveguide can be obtained in this case.

In Fig. 2.1(b) the birefringence as a function of the topcladding thickness is shown for a 2  $\mu\text{m}$  wide deep waveguide. The birefringence is largest for a thin cladding, as the air-semiconductor boundary is close to the field in that case. For a thickness above 600 nm the birefringence remains constant.

If high birefringence is needed, a thin topcladding is preferred. Narrowing the waveguides will increase the birefringence, but will also decrease the width tolerances.

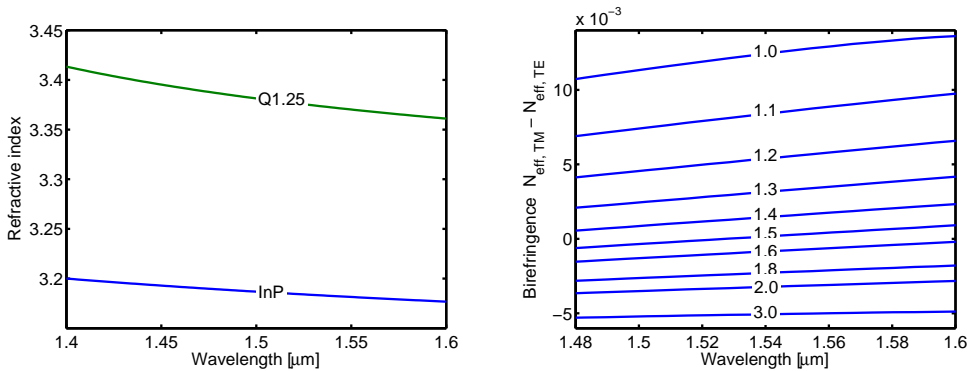


(a) Modal birefringence as a function of width, for a 1500 nm topcladding. (b) Modal birefringence as a function of topcladding thickness, for a 2  $\mu m$  wide waveguide.

**Figure 2.1:** Modal birefringence as a function of width (left) and topcladding (right).

The birefringence has a dispersive nature, which has to be taken into account when operation over a wide wavelength range is required.

The material dispersion and refractive indices [19] as well as the dispersion of the modal birefringence are plotted in Fig. 2.2.



**Figure 2.2:** Material dispersion (left) and calculated effective index difference between TE and TM (right) as a function of wavelength for different waveguide widths.

The dispersion of the birefringence is largest for narrow waveguides and approaches 0 for waveguides wider than 3  $\mu m$ . It has to be noted that for waveguides with widths around 1.5  $\mu m$ , the birefringence changes sign around 1540 nm. So for shorter wavelengths  $N_{eff, TM} > N_{eff, TE}$ , while for longer wavelengths  $N_{eff, TE}$  is larger. It is important to take this into account if the phase difference is used for the function of a device, e.g. in the polarization splitter demonstrated in chapter 5.



## Material birefringence

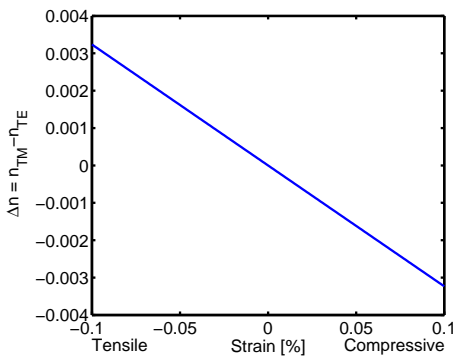
The modal birefringence can also be influenced by material birefringence. Material birefringence is caused by a different material refractive index for different orientations of the polarization. In InP/InGaAsP this phenomenon is in principle absent, but it can occur due to e.g. photo-elastic and electro-optic effects. In a passive waveguide, only the photo-elastic effect can cause material birefringence.

The material birefringence is influenced by strain, introduced in the growth. The birefringence for quaternary material grown on (100) InP substrate is linearly dependent on the strain. The difference between refractive indices parallel ( $n_{\parallel}$ , for TE polarized light) and perpendicular ( $n_{\perp}$ , for TM polarized light) to the interface of the layers can be calculated from [20]:

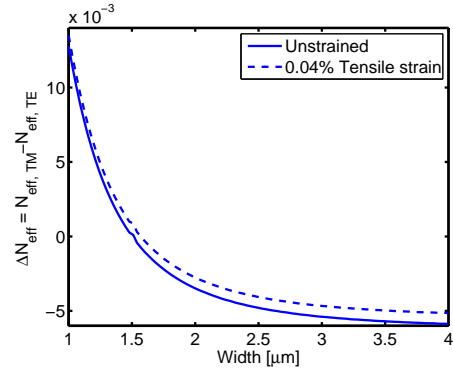
$$n_{\parallel}^2 - n_{\perp}^2 = \frac{\alpha_{pe}}{S_{11} + S_{12}} \left( -\frac{a_e - a_s}{a_e} \right) \quad (2.1)$$

where  $\frac{a_e - a_s}{a_e}$  is the strain in the material, with  $a_s$ ,  $a_e$ , the lattice constants of the substrate and the epitaxial layer respectively,  $S_{11}$  and  $S_{12}$  [21, 22] are the components of the elastic compliance tensor, and  $\alpha_{pe}$  is the linear photo-elastic coefficient, calculated for lattice matched Q(1.25) with the model in [23].

The resulting material birefringence as a function of the strain is plotted in Fig. 2.3. The birefringence is positive ( $n_{TM} > n_{TE}$ ) for tensile and negative for compressive strain. These



**Figure 2.3:** Material birefringence of strained Q(1.25) on InP as a function of strain.



**Figure 2.4:** Modal birefringence of 0.04% tensile strained compared to unstrained Q(1.25)

results are used to calculate the influence of strain on the modal birefringence. For a typical value of 0.04% tensile strain, the modal birefringence is calculated as a function of width for deep waveguides. This is plotted in Fig. 2.4. For narrow widths, the additional material birefringence has only a small influence on the modal birefringence; the confinement because of the geometry of the waveguide plays a larger role. For wider waveguides the material birefringence is more important.

Narrow waveguides are preferred for a device tolerant to strain in the material, but wide wave-

guides show a more width-tolerant birefringence. This is a trade-off that has to be made depending on the requirements for a device.

In a shallow waveguide the light is less confined as compared to a deep waveguide. Because of the lower confinement, the influence of sidewall roughness is smaller. A shallow waveguide therefore has the advantage of lower losses compared to a deep one.  $3\ \mu\text{m}$  wide waveguides are used in most situations to guide light on the PIC. A disadvantage is the large bending radius, because of the low confinement. Bends should have radii above  $450\ \mu\text{m}$  to avoid radiation losses. If the chip area allows this, large shallow bends are used.

For shorter bends, deep waveguides are required. Deep waveguides can have bending radii well below  $100\ \mu\text{m}$ , but unwanted polarization conversion can occur. In this thesis, the minimum bending radius taken for a  $2\ \mu\text{m}$  wide deep waveguide is  $150\ \mu\text{m}$  to minimize polarization conversion [24].

A low-loss ( $< 0.1\ \text{dB}$ ) connection between shallow and deep waveguides is made by tapering with a  $100\ \mu\text{m}$  long parabolic taper from the deep waveguide to a width of  $3.4\ \mu\text{m}$  to obtain a mode size equal to that of the  $3\ \mu\text{m}$  wide shallow waveguide [25].

The  $3\ \mu\text{m}$  shallow as well as the  $2\ \mu\text{m}$  deep waveguides are multimode. Excitation of the higher-order modes can occur, but by using modefilters, the second-order modes can be stripped. Modefilters are  $1 \times 1$  Multi Mode Interference (MMI) couplers, which are explained in the next section.

## 2.3 MMI couplers

Couplers are needed on a PIC to split and combine signals. A Multi Mode Interference (MMI) coupler is the component of choice for this, because of its large operation bandwidth, fabrication tolerance, and polarization independence [26]. These devices are based on self imaging: the input field profile of a multimode waveguide is reproduced in single or multiple images at a certain (periodically repeating) distance. By injecting light from a narrow waveguide into a wide waveguide, higher-order modes are excited in that wide waveguide. The resulting interference of these modes images the input at well defined positions along the length of the waveguide. By placing output waveguides at these positions, the multiple images can be used to obtain splitting.

### 2.3.1 Design

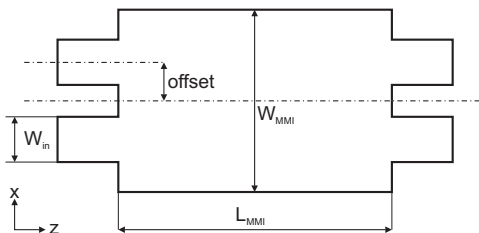
In our case,  $1 \times 2$  and  $2 \times 2$  3-dB couplers, and  $1 \times 1$  mode filters are needed. Both shallow and deep etched couplers are designed. In this section the design of a shallow  $2 \times 2$  MMI is discussed as a representative example. The other couplers are designed in a similar way. Their properties are given at the end of this section.

Paired interference couplers [26, 27] are designed. Paired interference is obtained by restricting the number of excited modes inside the multimode waveguide. This results in shorter and more tolerant couplers. The 2 outputs are imaged at a distance  $L_\pi/2$ , where the beatlength is:

$$L_\pi = \frac{\pi}{\beta_0 - \beta_1} \quad (2.2)$$

$\beta_0, \beta_1$  are the propagation constants for the fundamental and first-order mode in the wide waveguide.

A schematic of the MMI coupler is shown in Fig. 2.5. A completely shallow device is designed, having a width  $W_{MMI}$  of 12  $\mu\text{m}$ . For this width, an MMI length  $L_{MMI} = L_\pi/2$  of 230  $\mu\text{m}$  is required. The width of the input waveguides  $W_{in}$  is 3  $\mu\text{m}$  and the offset is 2.2  $\mu\text{m}$ . This device is simulated using the scattering matrix method developed by Leijtens et al. [28].



**Figure 2.5:** Schematic drawing of the MMI coupler.

The simulated field intensity profile is plotted in Fig. 2.6(left). The excitation of the higher-order modes inside the wide waveguide is clearly visible. The simulated imbalance and loss versus the wavelength is plotted in the right figure of Fig. 2.6. The device has an expected maximum imbalance of 0.15 dB and loss below 0.5 dB over the entire wavelength range of 100 nm.

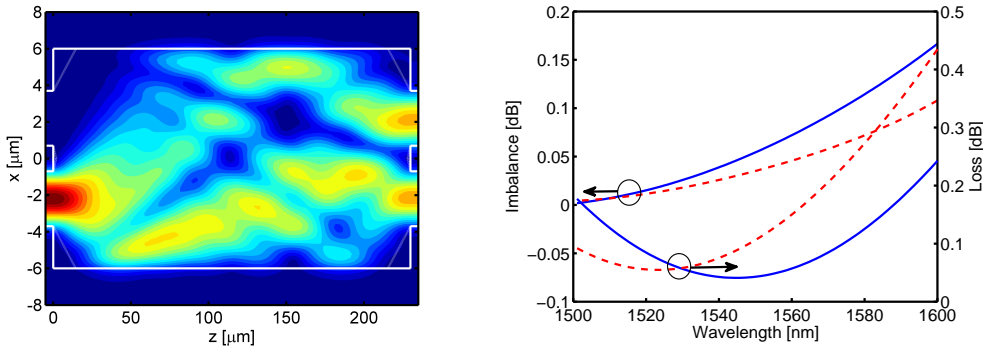
The simulated imbalance and loss as a function of the deviation in the width are given in Fig. 2.7. It shows that the imbalance is below 0.1 dB and that the loss is below 0.5 dB for a width deviation of  $\pm 200$  nm.

### Polarization dependence

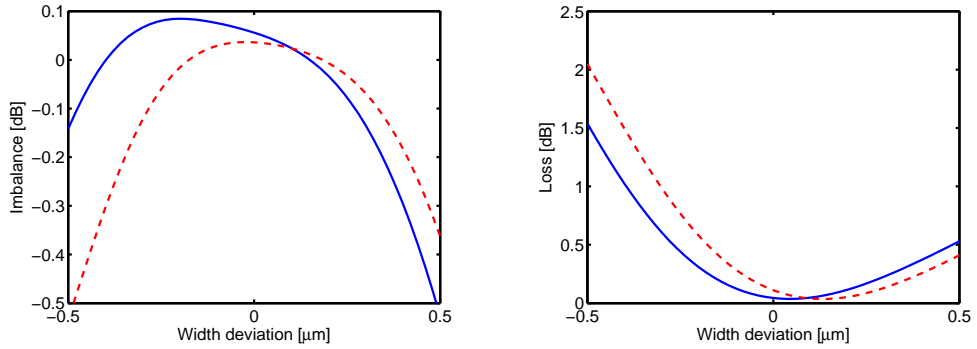
The propagation constants are polarization dependent, but as the multimode waveguide in the MMI is wide, this difference is small. The device itself is therefore only weakly polarization dependent. The simulated imbalance and loss of the designed MMI (shown in Fig. 2.6 and Fig. 2.7) for both polarizations, shows this.

### Other MMIs

Apart from the shallow  $2 \times 2$  MMI, 4 other types of MMIs are needed. A special MMI is the  $1 \times 1$  MMI, which functions as a modefilter. The fundamental mode in the input waveguide is



**Figure 2.6:** Intensity profile in the designed MMI coupler (left) and the imbalance and loss of the coupler as a function of wavelength for TE (solid) and TM (dashed).



**Figure 2.7:** Imbalance (left) and loss (right) in a shallow MMI as a function of the width deviation for TE (solid) and TM (dashed).

imaged onto the output, but the first-order mode is not, and is thus effectively filtered out. The dimensions of the 4 other MMIs are summarized in table 2.3. Their tolerances in width are specified in the table. The width tolerance ( $\Delta W$ ) is the width range in which the MMI has an imbalance smaller than 0.2 dB and a loss smaller than 0.5 dB for both polarizations. The maximum polarization dependence within this width range is indicated by the maximum difference in imbalance ( $\Delta$ Imbalance) and loss ( $\Delta$ Loss) between the two polarizations.

The deep devices are to be used in the polarization splitters and are smaller and therefore less tolerant to width deviations. The polarization dependent imbalance is negligible and the polarization dependent loss acceptable.

Table 2.3: Properties of the different MMIs

Description							
	$L_{MMI}$ [ $\mu\text{m}$ ]	$W_{MMI}$ [ $\mu\text{m}$ ]	$W_{in}$ [ $\mu\text{m}$ ]	Offset [ $\mu\text{m}$ ]	$\Delta W$ [ $\mu\text{m}$ ]	$\Delta\text{Imbalance}$ [dB]	$\Delta\text{Loss}$ [dB]
Shallow $1 \times 2$ 3-dB coupler	115	10	3	2.69	-0.61 – 0.33	x	0.22
Shallow $1 \times 1$ Modefilter	97	6	3	0	-0.29 – 0.59	x	0.23
Deep $1 \times 2$ 3-dB coupler	49	6.8	2	1.7	-0.10 – 0.16	x	0.24
Deep $2 \times 2$ 3-dB coupler	142	10	3	1.7	-0.16 – 0.10	0.12	0.4

### 2.3.2 Reflections

The coupler can suffer from reflections that disturb the operation of the PIC. The reflections can result in formation of an optical cavity, which can lead to unwanted lasing operation for an integrated SOA (see section 2.5).

In literature the reflection properties of the MMI coupler are studied both theoretically [29] and experimentally [30].

The reflections in the MMI are caused by small deviations from the design. Because of these, the image of the input waveguide is not exactly positioned on the output waveguides, but partly next to it. The image will reflect on the straight wall and form a new image on the input waveguide. This results in a reflected signal into the input.

In order to reduce the reflections a design with a lossy waveguide is proposed in [31]. This solution however complicates the device and is not generally applicable.

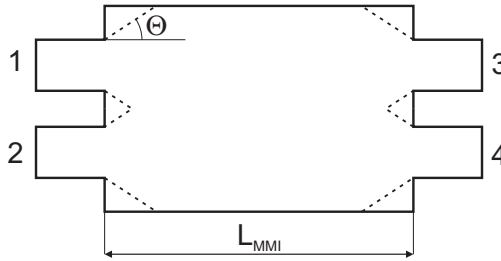
A more general solution to reduce the reflections from the MMI is achieved by cutting the corners of the walls on which the reflections occur, as shown in Fig. 2.8. The light incident next to the waveguide is now reflected out of the MMI and does no longer reach the input waveguide.

The proposed design is applied for both shallow and deep etched devices for the  $1 \times 2$  and  $2 \times 2$  MMI couplers and for the shallow  $1 \times 1$  modefilter. Here the design and results for the shallow  $2 \times 2$  3-dB coupler are presented.

### Design

In the optical field pattern inside the MMI coupler (Fig. 2.6), the field is absent from the areas next to the access waveguides. As explained before, those areas are a potential source of reflections. In the new design, these areas are removed, as is depicted in Fig. 2.8. The dashed line indicates the tilted front and back walls, the original design as presented before is shown with solid lines. The shape of the MMI coupler is obtained by cutting the corners near the

access waveguides by an angle  $\Theta$ . This angle is chosen to be larger than the divergence angle of the light, which is inversely proportional to the effective width of the mode entering the MMI section. This divergence angle is estimated to be around  $7.5^\circ$  for the waveguides used. Because of this, the light entering the wide waveguide will not interact immediately with the cut sidewalls of the MMI coupler. Therefore the multi-modal interference properties, and thus the self imaging are not affected. The total length of the MMI with the cut corners remains the same as with the original one.



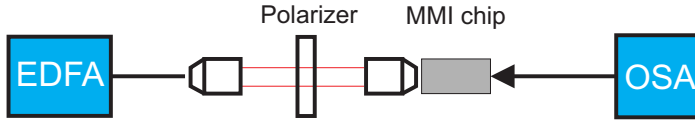
**Figure 2.8:** Schematic of the MMI, the original (solid) and the optimized (dashed) design.

A shallowly etched (100nm into the film layer) MMI is designed. The MMI length ( $230\mu\text{m}$ ), the width ( $12\mu\text{m}$ ) and the offset of the in- and outputs ( $2.2\mu\text{m}$ ) are the same as before, the tilt angle  $\Theta$  is  $20^\circ$ , well above the divergence angle. On one chip both the normal and the reduced reflection MMIs are present, as well as shallowly etched straight reference waveguides. The fabrication of the MMIs is done using the standard technology as described in chapter 3. The chip is cleaved in such a way that the MMI couplers are not exactly centered between the two facets of the chip. This allows distinguishing between the different reflections involving the facets of the chip and the MMI coupler.

## Measurements

The splitting ratio of the reduced reflection MMI and the original design are measured to be equal and around 0.46 ( $-0.37$  dB imbalance). This indicates deviations from the design, which may cause reflections. It also indicates that the splitting ratio of the reduced reflection MMI is not affected by the adjustment. The method for reflection determination is based on analyzing the transmitted spectrum by using a Fast Fourier Transformation [32]. Because of the limited sensitivity of the high resolution optical spectrum analyzer (HR-OSA), a high input power (5 dBm in the fiber) is required in order to monitor the possible reflections inside the chip. The optical setup used is presented in Fig. 2.9.

An erbium-doped fiber amplifier (EDFA) is used as a source. TE polarized light is selected using a polarizer. The light is launched in one of the inputs of the MMI coupler by means of a microscope objective. At the straight through (bar) output port of the MMI coupler a tapered fiber is used to collect the light. This is fed to the input of the HR-OSA, which records the



**Figure 2.9:** Measurement setup used for the characterization of the MMI couplers.

transmitted spectrum. The high resolution (0.8 pm) will easily monitor large cavity lengths, up to tens of centimeters, much larger than typical chip sizes of 10 mm.

A cavity of length  $L$  will result in a period  $\Delta\lambda$  in the spectrum according to:

$$\Delta\lambda = \frac{\lambda^2}{2N_{eff}L} \quad (2.3)$$

in which  $\lambda$  is the central wavelength, and  $N_{eff}$  is the effective group index.

The periods present in the spectrum can be obtained by applying a Fast Fourier Transformation (FFT) to the recorded spectrum. Every component  $k$  of the FFT of a spectrum of  $2N$  datapoints, corresponds to periodicity  $\Delta\lambda$  of  $\frac{N_{res}}{k}$ , in which  $res$  is the resolution at which the spectrum is recorded. The corresponding cavity length  $L$  for every  $k$  can be obtained from eq. (2.3):

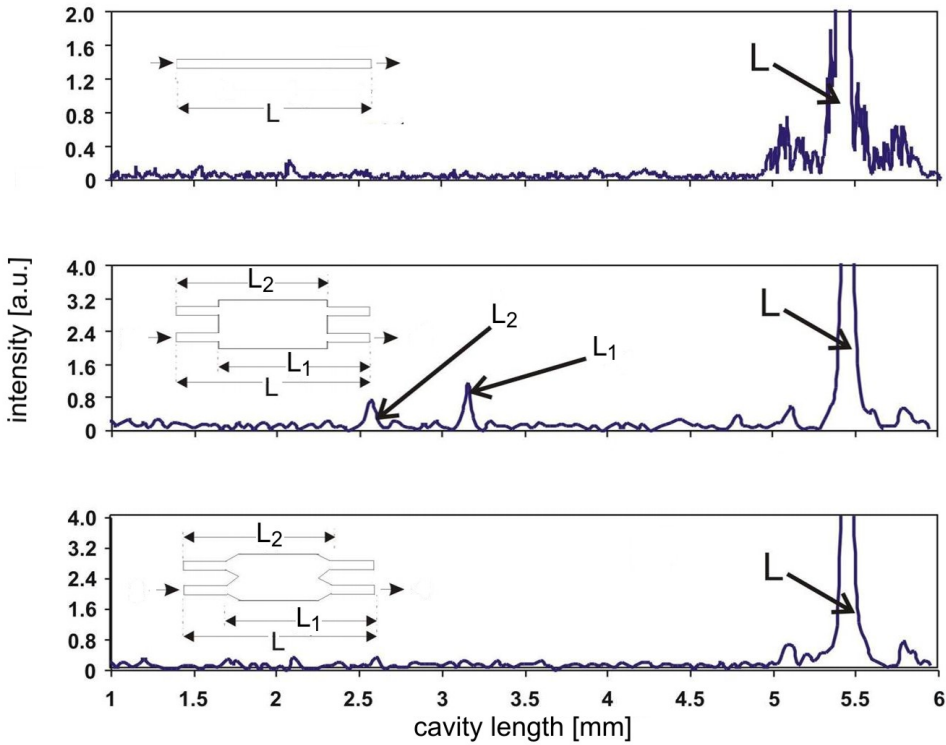
$$L(k) = \frac{k}{N_{res}} \frac{\lambda^2}{2N_{eff}} \quad (2.4)$$

The results of the measurements are shown in Fig. 2.10. First, a single straight waveguide is measured to monitor possible reflections originating from the setup itself. The analyzed data is presented in the upper graph. The only peak present is from the cavity formed by reflection of light on both facets of the chip. This chip-peak occurs around 5.4 mm, which matches the chip length. No disturbing reflections are present in the setup itself. Small satellites are present next to the chip-peak. Their origin is not identified: they possibly result from some residual reflection in the setup. They do not pose a problem in this analysis, because the associated cavity has a different length as those resulting from the MMI reflections.

The middle and lower graphs in Fig. 2.10 present the results for the original and the reduced reflection MMI respectively. For these, the data is plotted for one set of in- and output ports (port 2-4, see Fig. 2.8). The other combinations of input and output ports show a similar behavior.

For the standard MMI coupler, in addition to the chip-peak, two extra peaks can be seen around lengths  $L_1 = 3.16$  mm and  $L_2 = 2.55$  mm. The length  $L_1$  corresponds to the cavity resulting from the reflections between the right-hand facet of the chip and the left-hand side of the MMI.  $L_2$  corresponds to the cavity between the right-hand side of the MMI and the left-hand facet of the chip. As expected these are the walls on which the reflections occur.

In the case of the reduced reflection MMI coupler (lower graph) these two peaks are absent and the graph looks similar to the one obtained for the straight waveguide. This indicates that the reflections corresponding to the cavity length  $L_1$  and  $L_2$  are effectively suppressed.



**Figure 2.10:** Fast Fourier Transformation of the recorded spectra for a straight waveguide (top), a standard MMI (middle) and an reduced reflection MMI (bottom).

It is difficult to give an exact value of the magnitude of the reflection on the walls of the MMI coupler, because of its multiple ports. However, the relative reduction in the reflection can be estimated by using the measured results. The magnitude of the reflection on the MMI walls in the case of the non-optimized MMI coupler is calculated by using the values of the strength of the peak originating from the facets, one of the peaks around  $L_1$  or  $L_2$ , and -4.9 dB (32%) as a value of the reflection on the waveguide facet. By assuming that every peak is originating from a simple FabryPérot cavity, the intensity of the peak  $I_{peak}$  is proportional to

$$\sqrt{R_{chip-facet} R_{MMI}} \tag{2.5}$$

where  $R_{chip-facet}$ ,  $R_{MMI}$  are the reflectivities of the facets of the chip and the MMI wall respectively. The value obtained from this consideration for the reflection from the MMI is approximately -30 dB. For the reduced reflection MMI with cut corners, the reflection value is much lower and cannot be distinguished from the trace in Fig. 2.10. This implies that the reflection is more than 10 dB suppressed with respect to the original MMIs. The rather high



reflection value obtained for the original MMI coupler is most probably due to deviation from design parameters. Values better than -40 dB are reported in [30]. The etch depth of the fabricated MMI was 150 nm deeper than the design and the guiding layer was 50 nm thinner. These two effects lead to increased reflections. The new design still shows the reflection suppression, which indicates that this solution is very tolerant to fabrication errors.

## 2.4 Spot size converters

PICs in the InP/InGaAsP system use high-contrast narrow waveguides in a planar geometry. This yields small and elliptical spot sizes at the output waveguides that do not match the spot size of a fiber. Connecting a fiber to a PIC will therefore result in large overlap losses and strict tolerances. The losses can be reduced by using tapered fibers. The reduced circular spot size of such a fiber can be made to match the spot size of waveguide in one dimension only. The coupling losses will decrease, but strict tolerances apply.

By enlarging the spot size of the output waveguides to match that of a standard single-mode fiber, the coupling is simplified and the losses are substantially reduced. This enables packaging of the PIC. This becomes even more necessary if multiple in- and outputs are used, that need to be coupled to an array of fibers. This will be the case in the wavelength converter of chapter 6.

### 2.4.1 Horizontal tapers

The simplest approach for improving the fiber-chip coupling is to horizontally taper the output waveguide. In this way a matching of the waveguide mode and the fiber mode is obtained in one dimension. As the spot size of the waveguide is very small, tapered fibers have to be used with this taper. In Fig. 2.11 the coupling losses based on the overlap of the field from the tapered fiber, with a circular spot with a Mode Field Diameter (MFD)<sup>3</sup> of 3  $\mu\text{m}$ , and a shallow waveguide are calculated as a function of the width and the horizontal offset between the fiber and the waveguide.

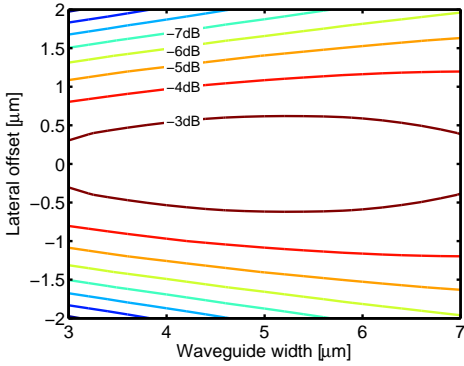
From this it can be concluded that the optimal width is 5  $\mu\text{m}$ . For this width the minimal losses are 2.5 dB, a loss penalty smaller than 0.5 dB (3 dB total loss) is maintained with the largest alignment tolerances. The standard 3  $\mu\text{m}$  shallow waveguides on the PIC are therefore tapered using 150  $\mu\text{m}$  long tapers to 5  $\mu\text{m}$  wide waveguides at the outputs.

### Reflections

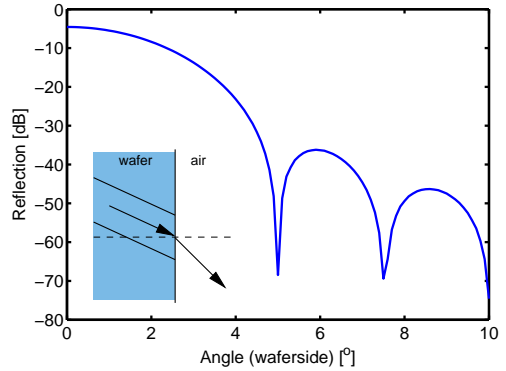
The facet reflections have to be very low, especially for active devices, where lasing might occur. By placing the waveguide at a sufficiently large angle to the facet, the reflected light will not be coupled back into the waveguide. For a waveguide width of 5  $\mu\text{m}$ , the facet-reflection back into the waveguide is calculated as a function of the angle of the waveguide on the chip. The results are shown in Fig. 2.12.

---

<sup>3</sup>The Mode Field Diameter (MFD) or the spot size is  $1/e^2$  of the intensity ( $1/e$  of the field)



**Figure 2.11:** Overlap loss of the tapered fiber with the waveguide as a function of the waveguide width and the offset between fiber and waveguide.



**Figure 2.12:** Reflection of the 5 $\mu\text{m}$  wide output waveguide as a function of the angle.

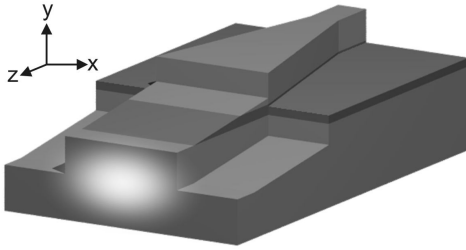
An angle of 7° is suited for a reflection well below -40 dB. This taper has been used in a number of circuits, but has eventually been replaced with the 2D Spot Size Converter (SSC) reported in the next section, because of the expected improved performance of that device.

### 2.4.2 2D tapers

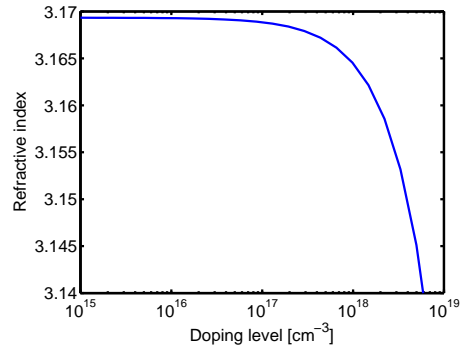
The fiber-chip coupling can be improved further. First of all, in the previous section, a tapered fiber has to be used to reduce the mode size to be comparable to that of the waveguide. This fiber introduces additional problems. It has to be specially made to match the waveguide, and the coupling tolerances are rather tight because of the small mode sizes involved. It is much easier to couple to a simple cleaved single mode fiber (SMF). For matching the spot size of such a fiber, to decrease the coupling losses further, the integration of a spot size converter is needed.

#### Principle

The SSC is based on a previous design for passive PICs [33, 34]. In this thesis an optimized design is needed, suitable for integration with active components. The device, shown in Fig. 2.13, is made by tapering the standard waveguide both horizontally and vertically down to a secondary waveguide layer. This waveguide layer has to accommodate a larger spot size, matched to a single mode fiber, and is therefore referred to as the Fiber Matched Waveguide (FMW) layer. This FMW layer is obtained by using a decreased n-doping in this layer with respect to the substrate doping. This decrease yields a larger refractive index [35, 36] for this layer (Fig. 2.14).



**Figure 2.13:** A schematic of the implemented SSC.



**Figure 2.14:** Refractive index of InP as a function of the doping level.

## Design

The design of the spot size converter consists of two elements. First a waveguide has to be designed in which a mode exists that matches the spot size of a single mode fiber. Furthermore a taper is required to couple the light from the narrow well-confined mode in the standard waveguide to the large mode in the fiber matched waveguide.

**Fiber Matched Waveguide** The refractive index as a function of doping [37] is plotted in Fig. 2.14. From the figure it is clear that the refractive index changes significantly at a doping level above  $1 \cdot 10^{18} \text{ cm}^{-3}$ . To obtain sufficient index contrast, the substrate doping has to be above this level. The FMW layer has to be moderately doped, because the active devices on the PIC use the backside as the N-contact. For the FMW layer a doping of  $3.5 \cdot 10^{17} \text{ cm}^{-3}$  is used. This results in a refractive index of 3.1676. A substrate with a doping level of  $2 \cdot 10^{18} \text{ cm}^{-3}$  is used, which has a refractive index of 3.1596 at 1550 nm.

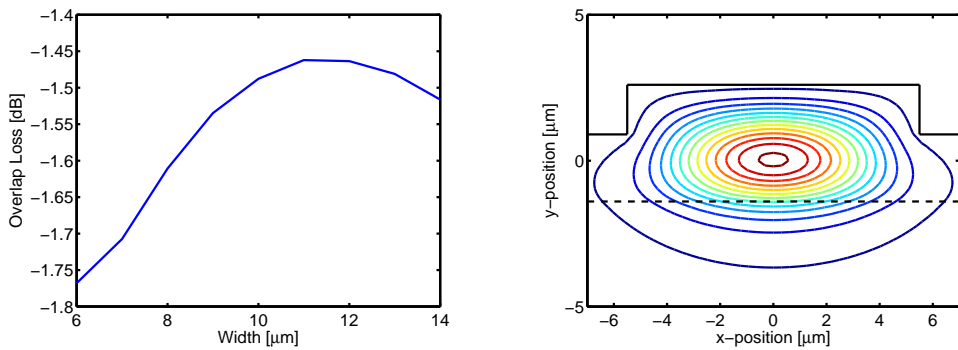
The SSC has to be optimized for efficient coupling to a standard SMF having a circular spot with a MFD of  $10.4 \mu\text{m}$ . The spot size of the FMW has to match this in both the vertical and the horizontal direction.

The vertical spot size is determined by the thickness of the layer and its index contrast. A thick layer is required to match the spot size of the fiber, but above a thickness of  $4.5 \mu\text{m}$ , the FMW becomes multimode. Furthermore the growth of thick layers is difficult and expensive. In the growth an error of  $\pm 10\%$  can occur, so to avoid a multimode waveguide in the vertical direction, a thickness of  $4 \mu\text{m}$  is chosen. The guide can still be multimode if the index contrast is increased due to differences from the designed doping. The doping of the substrates has been specified to  $2 \pm 0.5 \cdot 10^{18} \text{ cm}^{-3}$ . A substrate doping of  $2.5 \cdot 10^{18} \text{ cm}^{-3}$  will still result in a single mode waveguide at  $4.4 \mu\text{m}$  thickness. Even if the FMW is multimode, the propagation constant of higher-order mode will not match the propagation constant in the normal waveguide and no coupling will occur.

Apart from possible multi-modal behavior, an increase in the substrate doping will decrease the

spot size. From simulations, additional 0.15 dB loss is expected for a doping of  $2.5 \cdot 10^{18} \text{ cm}^{-3}$ . This is an acceptable penalty.

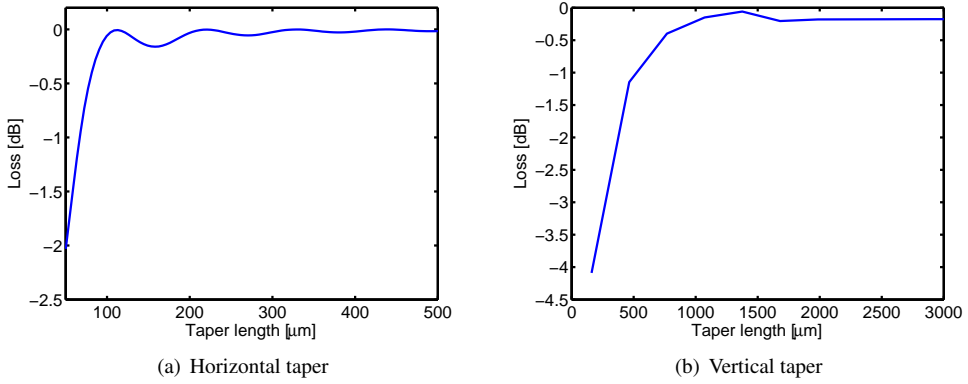
The horizontal spot size is determined by the width of the waveguide and the etch depth into the FMW layer. The overlap with the MFD of an SMF is calculated as a function of the width of the FMW for an etch depth of  $1.7 \text{ }\mu\text{m}$  (Fig. 2.15). This depth is chosen such that it can be etched together with a standard shallow waveguide, as will be explained in chapter 3. The optimum width is  $11 \text{ }\mu\text{m}$ . For this width the mode field is plotted as well. The profile is not completely elliptical, because the mode is extending below the etched region. This decreases the overlap by approximately 0.1 dB with respect to a completely elliptical shape.



**Figure 2.15:** Calculated overlap loss with an SMF (left) and intensity profile of the FMW (right).

**Horizontal and vertical taper** The mode of the standard, narrow waveguide has to be converted to the large mode inside the FMW. For this a taper is needed that tapers in both the horizontal and the vertical direction. The design is split into two parts; the horizontal taper is designed first. This is a parabolic adiabatic taper from  $3 \text{ }\mu\text{m}$  to the wide  $11 \text{ }\mu\text{m}$  waveguide. A 2D Beam Propagation Method (BPM) [38] is used to calculate the minimum length of the taper. The problem is reduced to 2D by using the Effective Index Method (EIM). The results are given in Fig. 2.16(a). A length of  $350 \text{ }\mu\text{m}$  is chosen which has less than 0.01 dB loss penalty.

The vertical taper is also simulated using a 2D BPM. Here the vertical cross section in the propagation direction is used, with the real material refractive indices. The 3rd dimension can be neglected in this case. The resulting loss as function of length is plotted in Fig. 2.16(b). A length of  $2 \text{ mm}$  is chosen for a reasonable loss penalty of 0.2 dB. These simulations are performed for TE polarization, but since the tapers are adiabatic devices, the results are also representative for TM.



**Figure 2.16:** Calculated losses in the tapers as function of width (TE polarization).

## Measurements

A chip on which the SSCs are present is fabricated with the process as described in the next chapter.

The SSC is analyzed using a CCD camera to view the output field. This is plotted in Fig. 2.17. The measured mode profile agrees very well with the simulations. From these traces the Mode Field Diameter is obtained to be  $10.4 \mu\text{m}$  in the horizontal and  $4.7 \mu\text{m}$  in the vertical direction. The overlap losses are estimated using a Gaussian approximation of the field at the Fiber Matched Waveguide and the fiber:

$$Loss = 4 \frac{MFD_{FMW,x} \cdot MFD_{FMW,y} \cdot MFD_{SMF}^2}{(MFD_{FMW,x}^2 + MFD_{SMF}^2) (MFD_{FMW,y}^2 + MFD_{SMF}^2)} \quad (2.6)$$

Here,  $MFD_{FMW,x}$  and  $MFD_{FMW,y}$  are the MFDs of the FMW in the horizontal and vertical direction respectively.  $MFD_{SMF}$  is the spot size of the SMF. For the observed values, an overlap loss of 1.3 dB is expected.

The coupling tolerance to an SMF as a function of the offset is investigated. The measured and simulated overlap losses are plotted in Fig. 2.18. The measured tolerance agrees well to the simulations. This results in a horizontal and a vertical alignment tolerance of  $\pm 1.5 \mu\text{m}$  for 1 dB excess loss, as can be seen in Fig. 2.19.

## Reflections

As with the horizontal taper of the previous section, for this spot size converter, the waveguides should be at an angle to reduce reflections. Also for the FMW an angle of  $7^\circ$  is sufficient to suppress the reflection below -40 dB, as can be seen in Fig. 2.20.

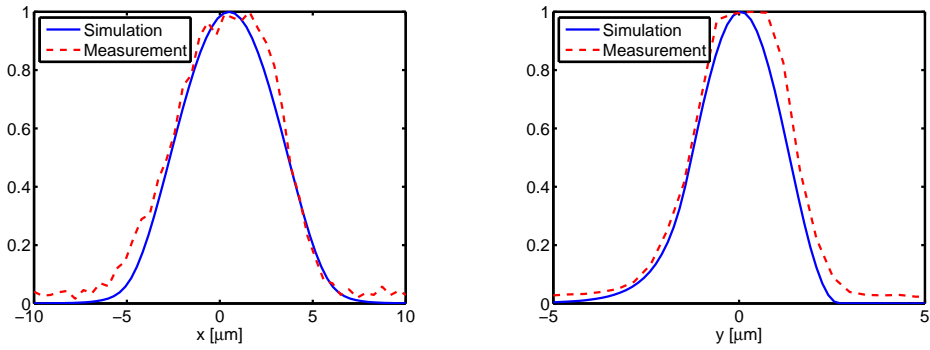


Figure 2.17: CCD trace of the output field of the SSC (dashed) compared to simulations (solid) for the horizontal (left) and vertical (right) direction.

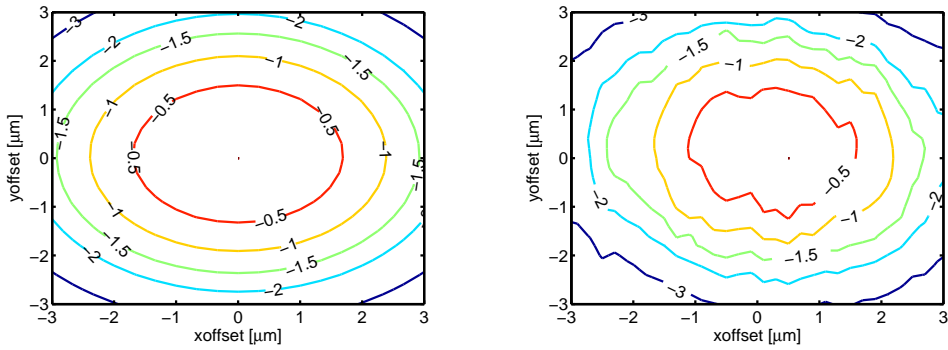


Figure 2.18: Coupling tolerance of the SSC to a SMF, simulated (left) and measured (right).

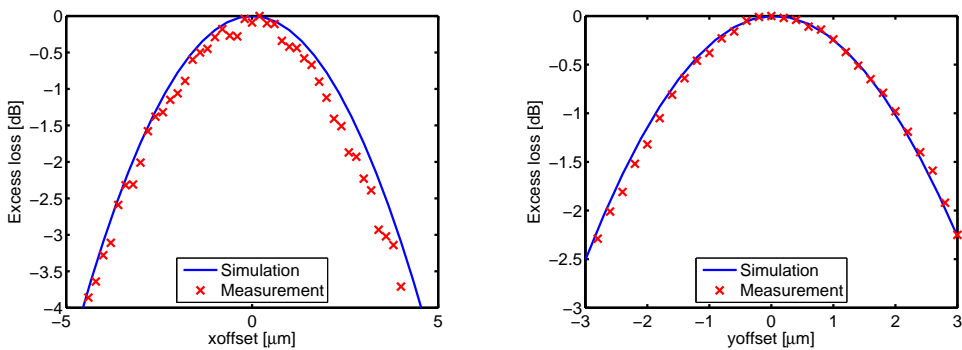
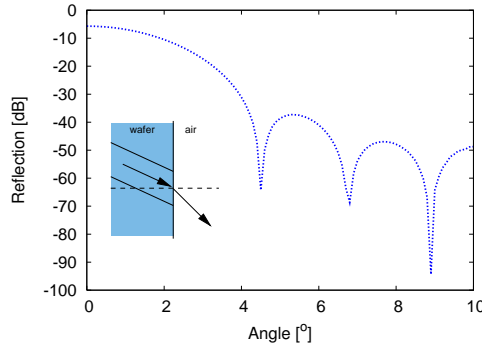


Figure 2.19: Coupling tolerance of the SSC to a SMF in the horizontal (left) and vertical (right) direction, simulated (solid line) and measured (X).



**Figure 2.20:** Reflection of the FMW output waveguide as a function of the angle.

## 2.5 SOAs

Semiconductor Optical Amplifiers are used in the PIC, either for amplification, or because of their non-linear properties that are employed e.g. in a wavelength converter or in an all-optical switch.

An SOA consists of a waveguide with an active layer inside the waveguide layer. Because of the planar geometry, the propagation constants, amplification and non-linear phase shifts differ for the two polarizations.

In the active layer of the SOA, with a material gain  $g_m$ , the incoming light is amplified if current is injected. Only a part of the light propagates through the active layer. This fraction is expressed by the confinement factor  $\Gamma$ . Apart from the gain, the device has internal losses,  $\alpha_{\text{int}}$ . A simple model for the net modal gain coefficient in an SOA is:

$$g_{\text{net}} = \Gamma g_m - \alpha_{\text{int}} \quad (2.7)$$

For an SOA of length  $L$  this leads to a linear gain  $G$  for the SOA:

$$G = e^{(\Gamma g_m - \alpha_{\text{int}})L} \quad (2.8)$$

### Confinement factor

The confinement factor  $\Gamma$  usually is polarization dependent; it can be twice as large for TE as for TM [39, 40]. This causes a polarization dependent gain, even if the material gain is isotropic as is the case in unstrained bulk material.

For the case of an SOA with a 120 nm bulk Q(1.55) active region centered in a 500 nm thick Q(1.25) waveguide layer, the confinement factor and propagation constants are calculated using the Film Mode Matching method [18] for an equivalent passive waveguide as specified in Fig. 2.21. The complex part of the refractive index is not taken into account as its influence on the propagation constants and the mode fields is negligible.

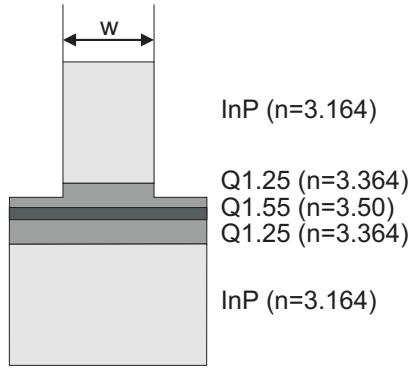


Figure 2.21: Equivalent passive waveguide of the SOA used in calculations.

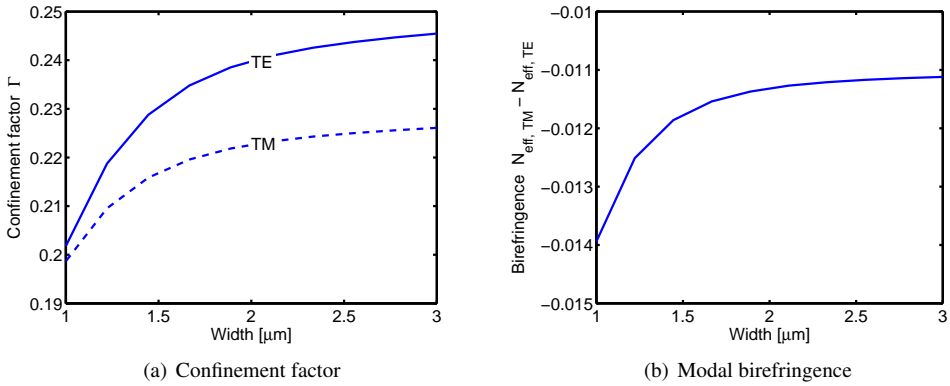


Figure 2.22: Confinement factor and modal birefringence of a shallow SOA as a function of width.



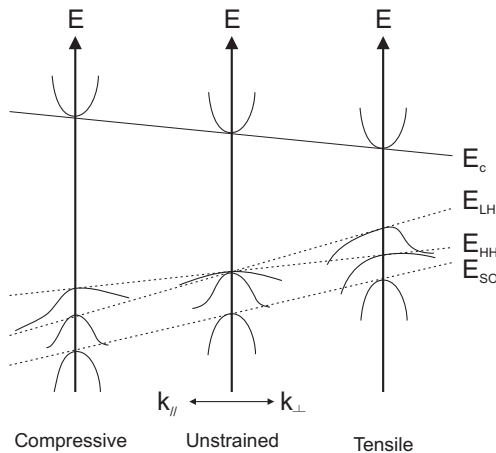
Fig. 2.22(a) shows the confinement as a function of the waveguide width. The confinement factor is very polarization dependent, resulting in a different net gain for TE and TM. Only for very narrow waveguides this polarization difference disappears, at the cost of a reduced confinement.

The modal birefringence is calculated and plotted in 2.22(b). This confirms the presence of modal birefringence in the SOA and a phase difference between the two polarizations occurs while they propagate through the device. Note that, similar to passive shallow waveguides, no polarization independent propagation can be obtained by adjustment of the width. Furthermore the birefringence is larger than in a passive waveguide because of the presence of extra interfaces between the active and passive layers.

### Material gain

Apart from the geometrical properties influencing the confinement factor, and thus the net gain, the material gain  $g_m$  itself can be polarization dependent as well [14, 41]. Strain applied in the growth is the main parameter that determines the gain for the two polarizations.

Strain introduced in the material will influence the shape of the valence band. It results in the heavy hole subband lying above the light hole subband for compressive strain, or below it for tensile strain as shown for a quantum well in Fig. 2.23. TM gain is caused by light-hole transitions, while TE gain is caused by light hole (for approximately 25%) and heavy hole (for 75%) transitions [14]. By applying tensile strain, the TM gain is enhanced; compressive strain will enhance TE gain.



**Figure 2.23:** Influence of strain on the valence band structure of quantum wells [42].

By employing strain, the gain can be equalized for TE and TM to compensate for differences in losses and confinement factors.

The gain is dependent on the optical input power  $P_{in}$ . As the input power increases, the gain will saturate because of carrier depletion. The saturation of the material gain can be described

as [43]:

$$g_{m,TE,TM} = \frac{g_{0,TE,TM}}{1 + P_{in}/P_{sat,TE,TM}} \quad (2.9)$$

Here  $g_{0,TE,TM}$  is the unsaturated material gain for the respective polarization,  $P_{sat}$  is the saturation power. This is the power for which the gain drops by 3 dB.

### Non-linear phase shift

Apart from the linear phase shift (caused by birefringence, see Fig. 2.22(b)), a non-linear phase change, caused by a change in refractive index as a function of carrier density (and thus gain) is present in the SOA. In the saturation regime, the index modulation is largest. The non-linear phase change in the SOA can be described as [43]:

$$\Delta\phi = \frac{1}{2}\Delta g_{net,TE,TM}\alpha_{TE,TM}L \quad (2.10)$$

where  $\alpha_{TE,TM}$  is the  $\alpha$ -factor or line width enhancement factor, describing the carrier induced index change:

$$\alpha_{TE,TM} = -\frac{4\pi}{\lambda} \frac{dn}{dN} \bigg/ \frac{dg_{net,TE,TM}}{dN}, \quad (2.11)$$

where  $n$  is the effective refractive index,  $N$  is the carrier density.

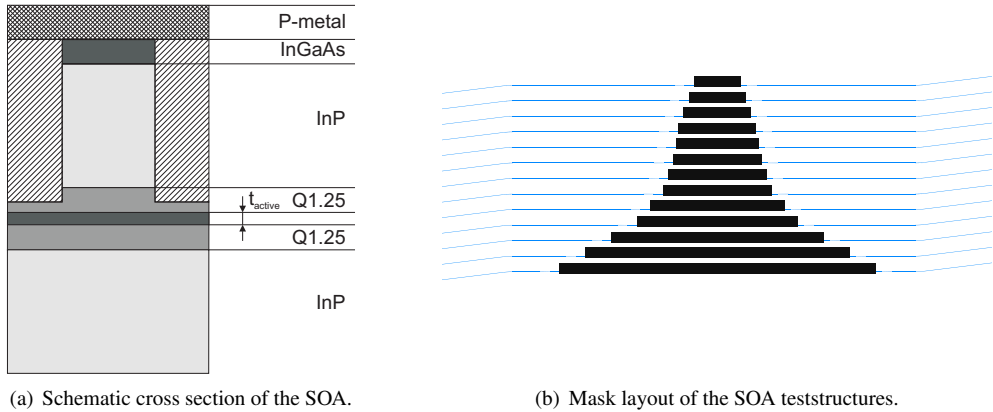
The  $\alpha$ -factor can depend on the polarization. In an SOA both the gain and the phase responses are polarization dependent. This property can be used to actively manipulate the polarization, for example in a polarization MZI as described in chapter 1.

### 2.5.1 Design

The SOA design suited for all-optical switching is based on the trade-offs and designs in [16]. A schematic cross section of the SOA is depicted in Fig. 2.24(a). A 2  $\mu\text{m}$  wide shallow active waveguide is used, the waveguide is connected using 100  $\mu\text{m}$  long tapers to 3  $\mu\text{m}$  wide shallow waveguides. The active layerstack used in the first realization (chapter 6, section 6.3) consists of a bulk Q(1.55) active layer similar to [16], with a thickness  $t_{active}$  of 120 nm.

In a next generation the active layer is replaced by a multiple Quantum Well (QW) layer. The layer consists of 41Å unstrained InGaAs Quantum Wells, and 63Å strained InGaAs barriers. The strain applied to the barriers is used to obtain the required well potential. The active layer thickness is initially kept to 120 nm (equal to 11 QWs) to have the same optical confinement as in the bulk case.

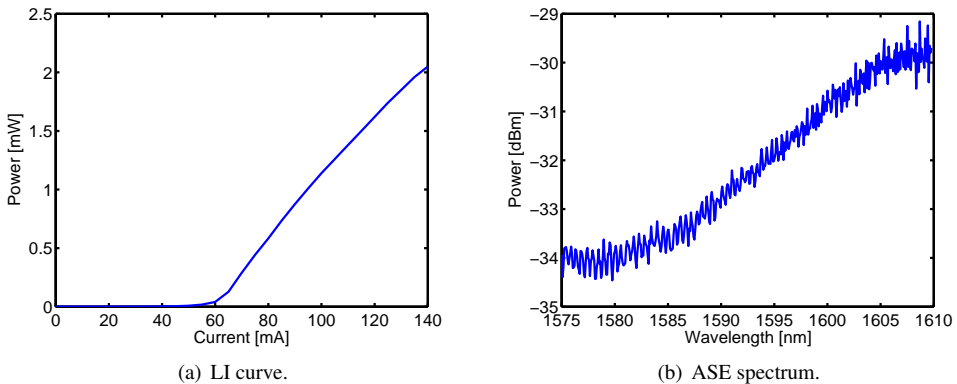
SOAs with different length are processed according to the standard processing in chapter 3. The mask layout is shown in Fig. 2.24(b). The SOAs have angled output waveguides to prevent reflections from the facets, as explained earlier.



**Figure 2.24:** SOA cross section and layout.

## 2.5.2 Measurements on the QW SOA

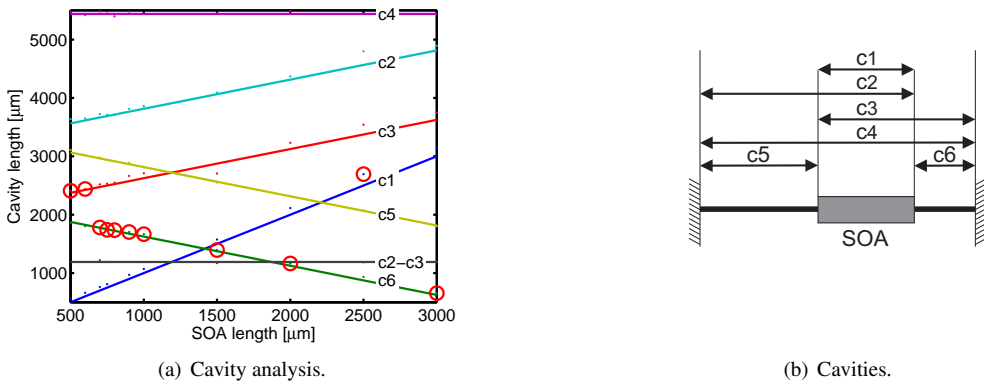
The QW SOAs are investigated further. The devices are biased with a current source and their output is monitored with a power meter and an Optical Spectrum Analyzer (OSA). The recorded LI-curve and spectrum for a 900  $\mu\text{m}$  long SOA is plotted in Fig. 2.25. Large ripples are visible in the spectrum and above a threshold of 60 mA, the device starts to lase. The reflections in the device form a cavity and cause lasing. This indicates also that the QW-material has a very high gain, higher than the previously used bulk material. An analysis of the cavities is performed to identify the origin of the reflections.



**Figure 2.25:** LI curve and ASE spectrum of a 900  $\mu\text{m}$  long SOA.

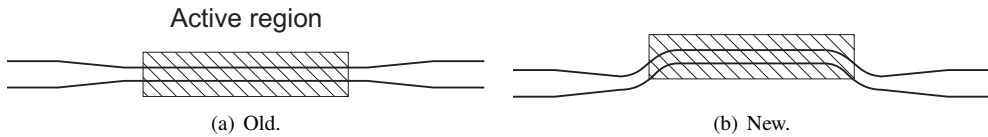
**Reflections**

The spectrum is analyzed using an FFT, similar to the method used for the MMIs. The spectra for a number of SOAs with increasing length are analyzed. The possible cavities vary with the length of the SOA as can be seen in Fig. 2.24(b) and 2.26(b). This eases the identification of the cavities. The identified cavities are shown in Fig. 2.26(b) and drawn as straight lines in the plot in Fig. 2.26(a). The cavities obtained from the spectrum are plotted in the same graph. The dominant cavities are indicated with circles. The dominant cavity is in most cases cavity *c*6. This cavity does not contain the SOA. It nevertheless shows up in the spectrum because it corresponds to the beating of resonances from other cavities (*c*3-*c*1, *c*4-*c*2). The devices are clearly lasing on at least one of the butt joints and one of the facets, which indicates that the reflections from the butt joints as well as from the facets are significant.



**Figure 2.26:** ASE spectrum and cavity analysis of the SOA.

The reflections at the butt joints are probably caused by a non-optimal connection between the passive and the active regions. The waveguides are crossing the butt joints straight (shown in Fig. 2.27(a)), which causes the reflections to couple back into the waveguides. By entering the active region at an angle of 10° (shown in Fig. 2.27(b)) the reflections at the butt joint are directed out of the waveguides [44]. This design is used in the second realization MZI (chapter 6).



**Figure 2.27:** Topview of the SOA.

The reflections from the facets can be reduced further by applying an Anti Reflection (AR)

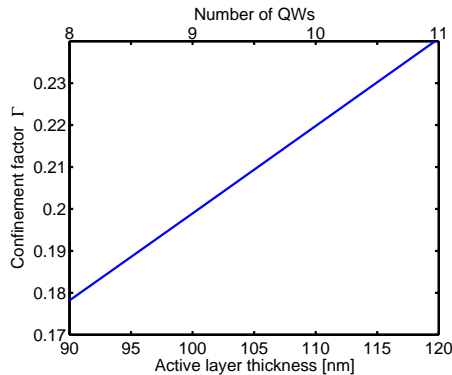
coating in addition to the  $7^\circ$  output waveguide angle.

## Gain

Apart from the reflections, another problem is present in the SOA. The ASE-spectrum (in Fig. 2.25(b)) shows that the gain peak is close to 1620 nm. This is particularly problematic for non-linear operation; the largest  $\alpha$ -factor, and hence the largest index modulation is expected at the red-side of the gain peak [45, 46].

The material is designed to employ bandfilling to obtain a blueshift, so high injection currents are required. As the devices start lasing at moderate injection levels ( $3.3 \text{ kA/cm}^2$ ), gain-clamping is obtained. Hence the required high-current densities (in the order of  $12 \text{ kA/cm}^2$ ) cannot be achieved.

The problem can be solved by reducing the number of QWs. In that case, the active layer thickness decreases and thus the confinement factor. The simulated confinement factor as a function of active layer thickness is plotted in Fig. 2.28. A thickness of 89.3 nm, corresponding to 8 QWs, will result in a confinement factor of 0.18, which is close to buried hetero SOAs fabricated in similar material [47]. This will yield a reduced net gain, which will prevent the device from lasing, together with the reflection reduction measures from the previous section. It will still provide sufficient gain for the required operation. Furthermore, because of the reduced number of QWs, the total required carrier density to employ bandfilling is reduced, so lower injection currents are needed. This layer stack is used in the second generation WLC (section 6.4).



**Figure 2.28:** Confinement factor as a function of active layer thickness.

## 2.6 Conclusions

In this chapter passive and active devices required in a PIC are discussed. Shallow waveguides can be used for low-loss connections on the chip with a minimum bending radius of  $450 \mu\text{m}$ .

Deep waveguides are used if sharp bends are required. Furthermore if birefringent waveguides are needed, deep waveguides are preferred. The birefringence can be enhanced by partly removing the topcladding.

The designed MMI couplers show a good splitting ratio and function almost independently of the polarization. A design is presented to overcome the reflections that can occur from this device. By cutting the corners from the multimode region a suppression of the reflection of at least 10 dB can be obtained.

The fiber-chip coupling can be made more tolerant and less lossy by tapering the output waveguide laterally to 5  $\mu\text{m}$ . The overall losses to a tapered fiber are still rather large: around 3 dB. Coupling efficiency to a cleaved single mode fiber can be improved by using 2D spot size converters. A taper is designed to taper a standard waveguide to a large fiber matched waveguide with a spot size close to that of a fiber. Experimentally determined overlap with a standard fiber indicate coupling losses around 1.5 dB.

According to simulations, the reflections at the facets are reduced to below -40 dB in both cases by tilting the waveguides to an angle of  $7^\circ$ .

SOAs are polarization dependent and can be used to manipulate the amplitude and phase difference of the two polarizations.

Devices for non-linear switching are designed based on previous designs, but problems arise in the reflections from the butt joints in combination with very large gain. This causes lasing and prevents bandfilling to obtain the correct operation wavelength. The reflections are reduced by entering the SOA under an angle. The gain is reduced by reducing the number of Quantum Wells. This will also increase the effect of the injection current on the bandfilling.

The devices presented in this chapter will be used to construct the integrated circuits of chapter 6. Together with the polarization devices from chapters 4 and 5, the circuits in chapter 7 can be constructed.



---

# Chapter 3

## Integration technology

---

### 3.1 Introduction

Within COBRA an integration technology is used, consisting of a limited variety of components that can be integrated in a PIC. These are the standard active and passive components from the previous chapter. The aim of this thesis is to extend this technology to a generic technology capable of on-chip polarization handling and with the possibility for mounting and packaging.

This chapter will introduce the standard technology first. The butt joint integration of active and passive material is shown and the processing of the standard components introduced in the previous chapter is demonstrated.

After that processes for high resolution lithography are described, required for the definition of polarization converters. Additional technology steps for mounting the chips in a submount for packaging are discussed. Finally a process for etching sloped sidewalls in the polarization converters (PC) is demonstrated.

### 3.2 Active-passive integration

The butt-joint integration of the active and passive layerstacks, introduced in chapter 2 will be described in this section. Furthermore a processing scheme in which both active and passive components can be integrated is considered.



### 3.2.1 Active-Passive butt-joint

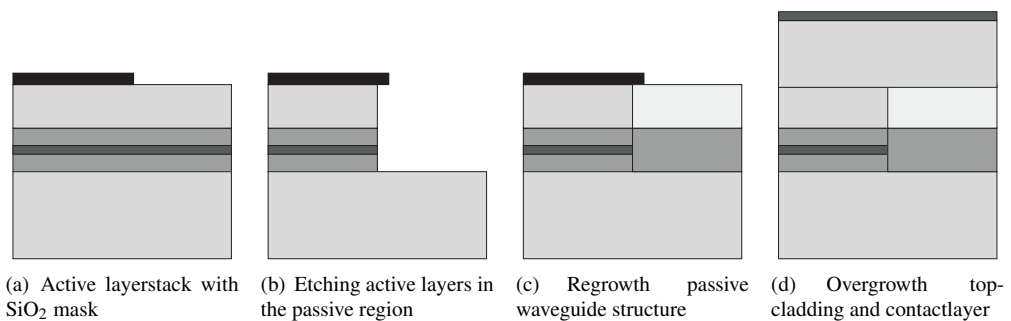
The monolithic integration of active and passive components can be done in a number of ways: by Quantum Well intermixing [48], by Selective Area Growth based on growth enhancement near masked areas [49], by offset Quantum Wells that interact with the evanescent field [50] and are etched in the transparent regions, by an active vertical coupler [51], by using the polarization [52], or by using selective area growth of the passive material butt-joint to the active regions [53]. All PICs discussed in this thesis are made by butt-joint coupling of the active and passive structures. This technique has the advantage over the other mentioned methods that the active and the passive layerstack can be optimized separately, as long as the substrate and the top cladding are the same for the active and passive regions. However this technique puts strict conditions on the processing.

The integration is based on selective area Low Pressure Metal Organic Vapor Phase Epitaxy (LP-MOVPE). The first step is to grow the active layer structure (Fig. 3.1(a)). A Silicon Oxide ( $\text{SiO}_2$ ) mask layer is deposited on top of the grown structure. The active regions are lithographically defined on this mask layer. The mask is etched and the active layers are etched away in the passive regions. A well defined underetch is required to obtain a sufficiently planar regrowth (Fig. 3.1(b)).

The structure is then regrown with the passive structure (Fig. 3.1(c)). The growth will only occur on the semiconductor. On top of the  $\text{SiO}_2$  layer no deposition will take place. The butt-joint has to be well connected; voids in the connection can lead to unwanted reflections and losses. The doping of the passive cladding is lower than the active cladding (indicated by the lighter shade) and can be freely chosen.

After this the  $\text{SiO}_2$  mask is removed and the top cladding will be overgrown in a final growth step (Fig. 3.1(d)).

The wafer obtained in this way is used for further processing of the PICs.



**Figure 3.1:** Active-passive butt-joint process (the materials are defined in tables 2.1 and 2.2)

### 3.2.2 PIC processing

The standard technology for realizing PICs consists of the integration of shallow and deep waveguides with SOAs. The processing has a modular approach; it can be divided in 3 major parts:

- the definition and etching of the (waveguide) components on the PIC,
- the passivation of the PN-junction in the opto-electronic components,
- the metallization.

The standard process is depicted in Fig. 3.2. The alphabetic listing of the steps in the description below corresponds to the figure.

The first part, the definition and etching of the waveguides, consists of the following steps:

- a. First the wafer is covered with 50 nm Silicon Nitride ( $\text{SiN}_x$ ) by Plasma Enhanced Chemical Vapour Deposition (PECVD). Positive photoresist is spun and baked. The waveguides are defined in the resist using optical contact lithography. After development of the photoresist the  $\text{SiN}_x$  is etched using  $\text{CHF}_3/\text{O}_2$  Reactive Ion Etching (RIE).
- b. The sample is covered with thick positive resist, and the regions for the deep waveguides are opened. It is important to have the resist thick enough as the resist is attacked in the RIE of the semiconductor. This can cause two problems: firstly the top layer becomes hard and crusted and will be hard to remove. The second problem can occur if the resist is attacked so much, that the underlying semiconductor is etched as well. This results in partly etched pits in the surface.  
By using a resist thickness of more than 2  $\mu\text{m}$ , sufficient resist is present below the crusted layer and this layer can be lift-off by dissolving the un-attacked resist in acetone.
- c. The open areas are etched using a  $\text{CH}_4/\text{H}_2$  RIE. In this step, the difference between deep and shallow waveguides has to be etched. The etch depth has to be deep enough so that after the etch steps to follow, the waveguides will be etched more than 100 nm below the waveguide layer. This depth is tolerant as long as it is deep enough. So an overetching of approximately 100 nm is taken into account.
- d. After the removal of the resist, all waveguides are etched simultaneously using the  $\text{SiN}_x$  as a mask. In this step it is important that the shallow waveguides are etched to a depth which is shallow enough to ensure complete removal of the InGaAs contact layer in the final etch step (f). By etching approximately 100 nm too shallow, in the next etch step (f), the contactlayer is certainly removed. A small part of the InP top cladding ( $< 100$  nm) is etched as well, but this does not have a large influence on the waveguide properties.
- e. The SOAs are covered with resist and the  $\text{SiN}_x$  mask is removed from the passives. The contact on the SOA remains protected by the nitride mask, while the contactlayer on the passive waveguides is left open.

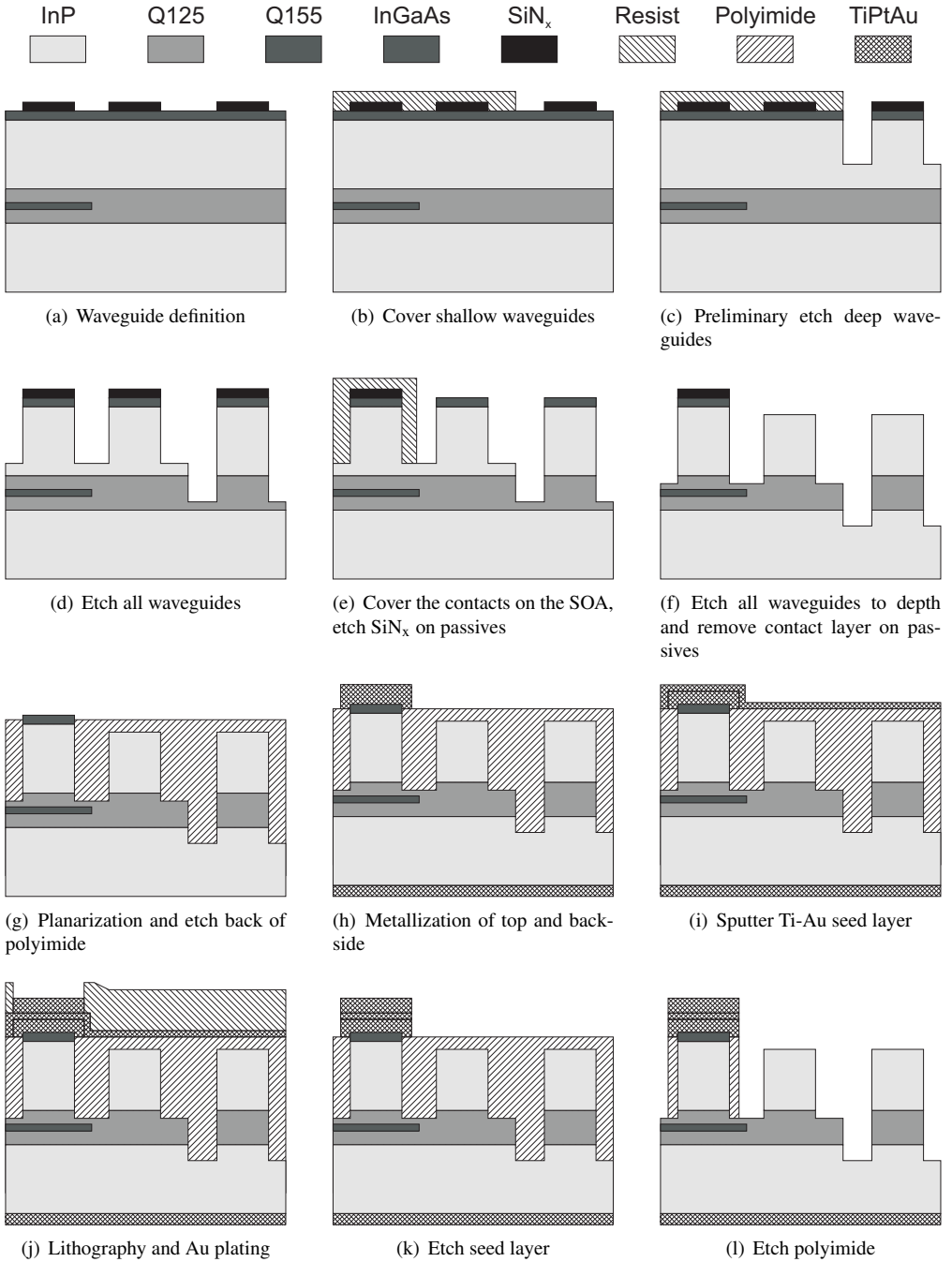


Figure 3.2: Standard process

- f. The contact layer on the passives is removed by etching the top together with the lower parts. This is a critical step, the etch depth has to be  $100 \text{ nm} \pm 50 \text{ nm}$  into the waveguide-layer for the shallow waveguides and the SOAs. As stated before, the remaining top cladding depends on the etch depth in step (d).

After etching of the waveguides, the next step is passivation and planarization of the structure.

- g. Polyimide (PI) is used for both passivation and planarization of the SOAs. The sidewalls of the waveguides are cleaned first by oxidation in an  $\text{O}_2$  plasma and oxide-removal in  $\text{H}_3\text{PO}_4:\text{H}_2\text{O}$ .

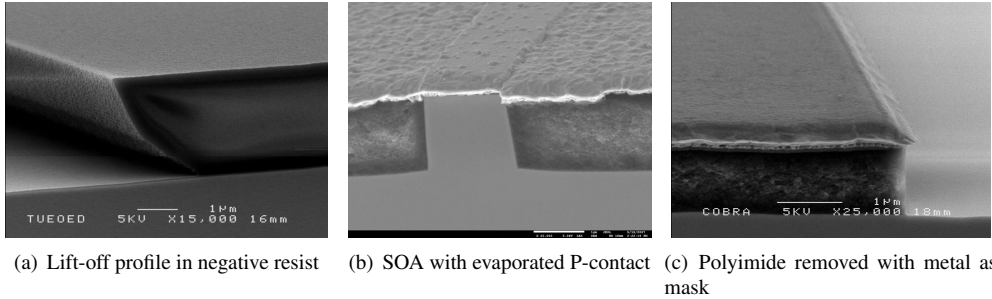
The planarization has to be carefully done to ensure good adhesion of the PI. For this, multiple layers of polyimide are spun. After every spin step the polyimide layer is baked at slowly rising temperature starting from roomtemperature. Every layer of PI is completely cured before spinning another layer.

After a number of steps, the sample is planar to within 100 nm height difference. The polyimide is etched back in an isotropic  $\text{O}_2/\text{CF}_4$  plasma until the level of the contact-layer.

The final steps consist of the metallization of the opto-electronic components (i.e. SOAs in this case and possibly phasemodulators).

- h. The sample is covered by negative resist and exposed using the metallization mask. A good lift-off profile is obtained after development (Fig. 3.3(a)). Titanium, platinum, and gold (Ti, Pt, Au) are evaporated twice on the sample, once on the P-contact on top, and once on the backside of the sample for the N-contact. After lift-off in acetone, on the top, only the P-contacts remain, while the backside stays completely covered to form the N-contact. A SEM photograph of an SOA with a top P-contact is shown in Fig. 3.3(b).
- i. An important parameter is the resistance of the metal contact along the SOA to achieve uniform current-injection. A thick and wide contact is required for this. A thick contact is obtained with Au-plating. A TiAu seed layer is sputtered over the whole sample.
- j. On the seed-layer a lithography step is done to open the P-contacts. To protect the backside, it is covered with resist. Gold is plated in an electro-chemical process and in the openings in the resist on top of the P-contact, a thick,  $\approx 2\mu\text{m}$ , gold layer is obtained.
- k. The seed layer has to be removed from the sample. First all resist is removed from the sample. After that, the seed layer is etched in two steps, by wet chemically etching first the Au-layer and after that the Ti layer. As this is done without any masking, the contact itself is attacked as well. The seed layer is thin compared to the thickness of the contact, so if the etch is timed carefully, at least  $1.5\mu\text{m}$  gold remains on the contacts.
- l. The final step is to remove the polyimide everywhere from the sample, except where the contacts are. This is done in an  $\text{CHF}_3/\text{O}_2$  RIE. The contacts are used as a mask. They are not attacked if the power is sufficiently low (50 W). From Fig. 3.3(c) it can be seen

that the PI is removed without underetch and that the contacts are not attacked in this step.



**Figure 3.3**

It is possible to add other functional and technological blocks to the ones described here, without major changes to the processing steps. This becomes clear in the next sections, where the technology for higher resolution lithography for the waveguides; the integration of alignment features for packaging, spotsizer converters, and sloped sidewall etching for polarization converters will be discussed.

### 3.3 High resolution lithography

The technology discussed in the previous section has a limitation in the resolution. The width of features cannot go below approximately  $1\ \mu\text{m}$ , since the reproducibility of smaller widths is a problem with contact lithography. Furthermore sub-micron alignment is very difficult using a standard mask-aligner.

This section will discuss two options to improve both the resolution and the alignment accuracy: high resolution optical lithography with a waferstepper and Electron Beam Lithography. These lithographical steps can replace the standard waveguide lithography, or be used in connection with it. High resolution lithography will be used for the realization of Polarization Converters (PC), which require high accuracy and submicron size.

#### 3.3.1 Waferstepper

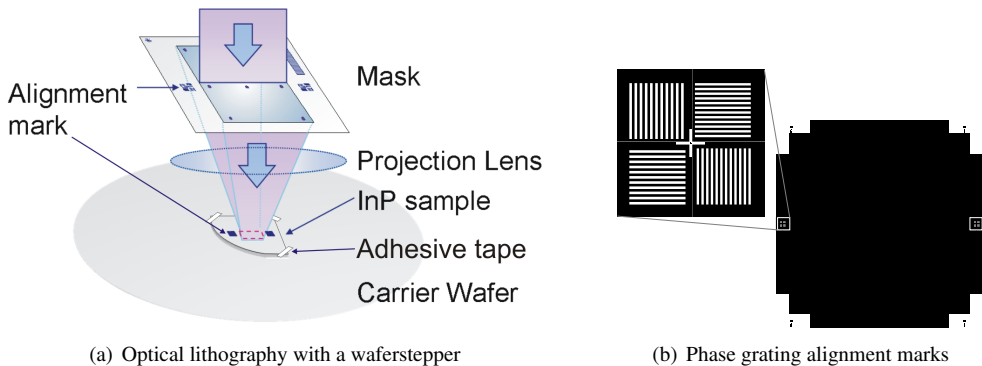
The first method investigated is optical lithography using an ASML PAS5500/250  $5\times$  reduction wafer stepper. This is an i-line tool, with an exposure wavelength of 365 nm. This allows an accurate width control, better than 20 nm on an 800 nm line. The alignment accuracy is approximately  $\pm 60$  nm. This optical lithography is advantageous as compared to Electron Beam Lithography (EBL), because it has a large writing field ( $22 \times 22\ \text{mm}^2$ ), better uniformity and is suited for mass-production.

The machine is equipped for exposures on wafers from 4 to 8 inch. In our process quarter pieces of a 2 inch wafer are used. To align and expose these quarter pieces, they are centered on a 6 inch wafer and fixed using adhesive tape [54]. A schematic of the machine is presented in Fig. 3.4(a).

### Alignment marks

For the alignment, phase grating alignment marks designed by ASML are fabricated on the quarter pieces of InP. A mask with these alignment marks (Fig. 3.4(b)) is transferred using standard optical contact lithography. The gratings are RIE etched, 120 nm into the InP. The same alignment marks are reused in multiple process steps. Care has to be taken not to remove or alter the marks in processing. The alignment procedure uses red light at a wavelength of 633 nm. The photoresist is insensitive to this wavelength and the marks are not exposed during alignment.

The thickness of the  $\text{SiN}_x$  mask that is deposited on the wafer has to be such that a minimum in the reflection is avoided. For the thicknesses used in our process this is not a problem.



**Figure 3.4:** High resolution optical lithography

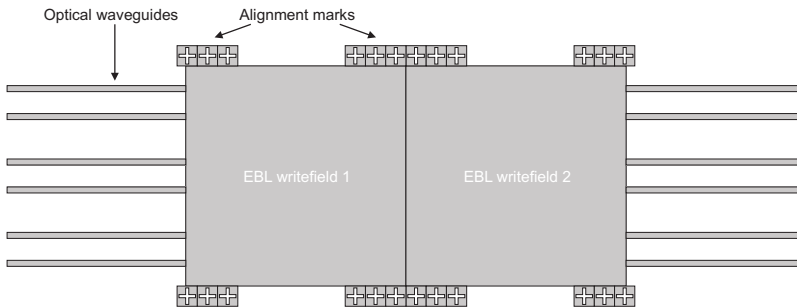
### 3.3.2 Electron beam lithography

A second option to achieve high resolution is electron beam lithography (EBL). This technique has the advantage that it is a direct-write technique, so no masks need to be fabricated. A Raith-150 E-beam machine is available within COBRA, which allows a higher resolution with respect to the high resolution optical lithography (theoretically features as small as 30 nm can be achieved). Disadvantages are a worse reproducibility in the line width definition and a limited write field size. The write field is the area that can be exposed without moving the stage on which the sample is mounted. In our case this is limited to  $200 \times 200 \mu\text{m}^2$ . Furthermore every feature has to be written separately which takes a lot of time, typically 10 min. per write

field for the structures in this thesis.

### Alignment marks

Because of the limited write field size and the long time needed for EBL exposures, only the critical structures are exposed using EBL. Therefore the EBL write fields have to be aligned to optically defined waveguides using alignment marks defined in the same mask as the waveguides. Multiple write fields can be cascaded in the same way, by defining alignment marks for each write field. A schematic overview of the mask is shown in Fig. 3.5.



**Figure 3.5:** Optical mask showing waveguides, EBL writefields and EBL alignment marks

The figure shows the optical waveguides, and two adjacent writefields. In this design, every write field has 3 sets of 4 marks. This is needed because multiple EBL exposures are to be done on the same sample and the marks are exposed when aligning. This is made clear by explaining the alignment procedure. Fig. 3.6 shows the mask design with the scan regions identified by dark gray color. The machine scans with the electron beam along these regions and determines the middle of the cross shaped alignment mark, as shown in Fig. 3.7.

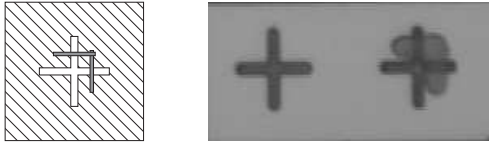
While scanning, the scan region is exposed. After development, it will be opened as can be seen in the rightmost photograph in Fig. 3.6. This makes the mask unreliable and even unusable for subsequent alignments.

By using a separate mark for each step, this problem is avoided.

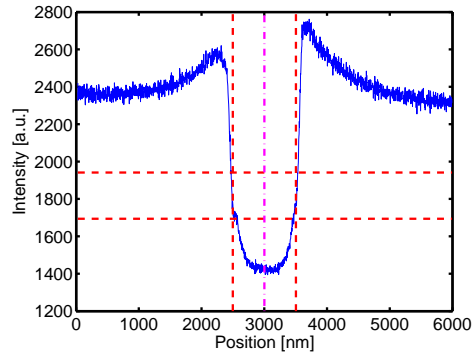
### 3.3.3 Technology

For both types of high resolution lithography described in this section only positive resist is available. This means that the exposed parts will be opened after development. This process can be used in steps where most of the sample has to be covered and only a small area needs to be opened.

A problem is that for the waferstepper only positive masks (i.e. a transparent pattern on a chromium mask plate) are available, and in the EBL only a limited area can be written. This requires a reversal process to define narrow lines. So for the definition of waveguides, a lift-off



**Figure 3.6:** EBL alignment marks: Mask design and optical photograph of an unexposed and an exposed mark



**Figure 3.7:** Linescan to determine middle of mark; the dashed lines indicate the detected edges, the dash-dotted line indicates the resulting middle point.

process is used. The resist is exposed with the waveguide mask and developed. The waveguide pattern is transferred to the resist and after this, Ti is evaporated and after dissolving the resist, the pattern is transferred to the Ti.

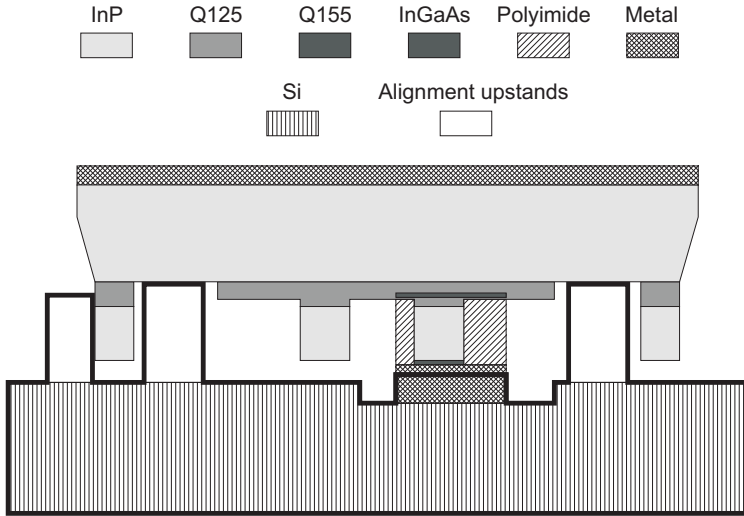
### 3.4 Technology for packaging

Chips need to be packaged to be able to use them in systems. This requires coupling of optical and electrical signals from and to the chip. The waveguides used in PICs are small, typically around 3 μm. This makes the coupling to the outside world (e.g. optical fiber) difficult, because of the submicron precision needed. Some of the chips, described in chapter 6, are packaged. For the packaging, the PICs will be flip-chip mounted on a Si submount as shown in Fig. 3.8. This submount will be mounted on a motherboard in which fiber-assemblies are coupled to the in- and outputs. This is similar to hybrid integration [55] of active and passive structures. To allow this type of packaging, additional features have to be present. The techniques to fabricate these are explained next. To allow a relaxed fiber-chip coupling, spotsizer converters are needed. The technology to fabricate them is described afterwards.

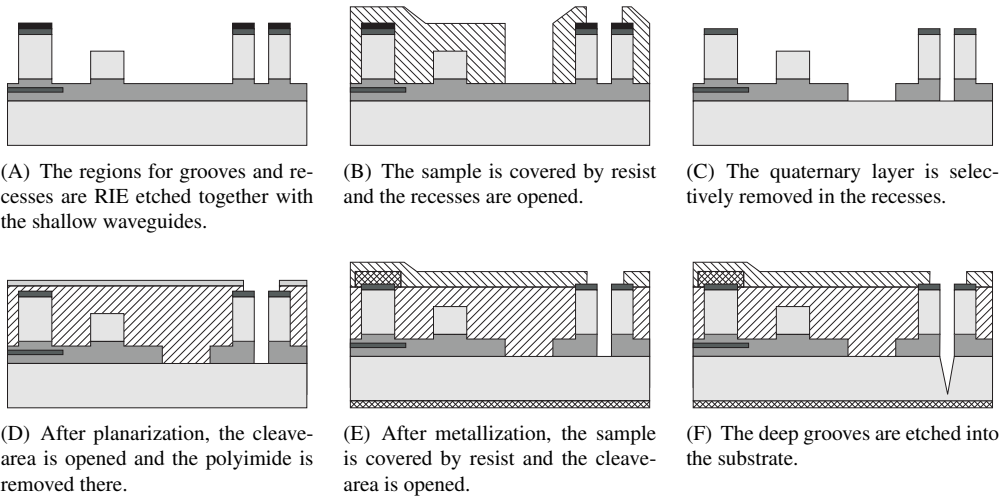
#### 3.4.1 Alignment on the submount

The chips have to be vertically and horizontally aligned with respect to the submount to allow coupling to fibers and to connect the metal contacts of the PIC to the predefined metal pads on the submount. For this recesses need to be etched and the chips have to be cleaved with submicron precision. The technology needed is depicted in Fig. 3.9.





**Figure 3.8:** InP PIC flip-chip bonded onto a Si submount, the submount is indicated with the thick lines.



**Figure 3.9:** Technology steps for the alignment features, the definition of the material corresponds to Fig. 3.8.

## Technology

The sample is vertically aligned by Silicon Oxide pillars on the submount. A well-defined height is needed on the InP PIC to align to these pillars. The substrate level, just below the quaternary waveguide layer, is used for this.

The horizontal alignment is achieved by pushing the chip against stops on the submount. For this, exact, i.e. sub-micron accurate, dimensions of the PIC are required. This is achieved by wet etching deep grooves at which the chip can be cleaved. The position of these precision-cleaves has to be accurate within less than a micron with respect to the position of the in- and output waveguides. It is thus important to define these in the same step as the waveguides.

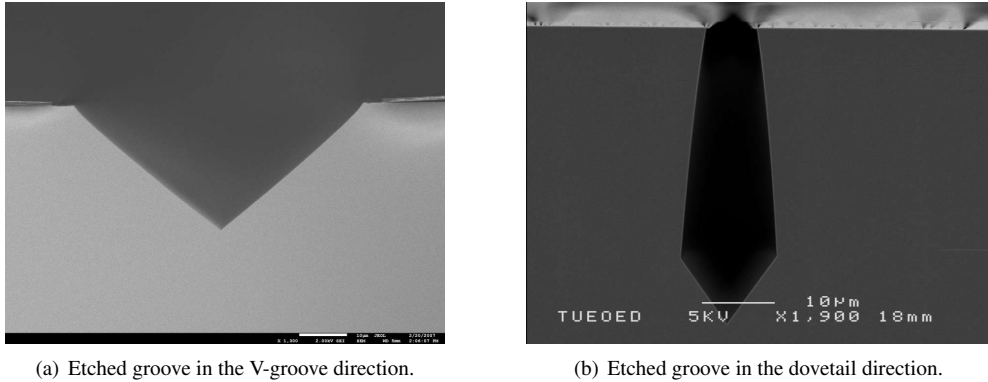
In the standard process of the PIC, some additional steps are required. They are listed here, the alphabetical listing corresponds to the figures in Fig. 3.9.

- A. Two walls defining each precision-cleave groove are etched together with the shallow waveguides. The difference is that the  $\text{SiN}_x$  is left on top of the groove-walls in step (e) (in Fig. 3.2(e)). In step (f) of the standard process, when the shallow waveguides are etched into the quaternary waveguide layer, the recesses are etched.
- B. In an additional step after the waveguide etching, the sample is covered with resist and the region of the recesses and the grooves, is opened.
- C. The quaternary layer is selectively removed using  $\text{H}_2\text{SO}_4:\text{H}_2\text{O}_2:\text{H}_2\text{O}$ . This etchant etches the quaternary material fast, but does not attack the underlying InP. With this process, the required well-defined level is achieved.
- D. After planarization of the sample, a Ti lift-off process is used to cover the sample. Only the area where the grooves are is opened. With this Ti mask, the polyimide is etched in a  $\text{O}_2/\text{CHF}_3$  RIE to completely open the grooves.
- E. After metallization, (step (h) in the standard process), the sample is covered by resist and the cleave-area is opened. The backside is protected with resist as well.
- F. Now  $\text{HCl}:\text{H}_2\text{O}$  is used to selectively etch the InP using the quaternary layer as a mask. For the two orthogonal cleave directions the etch behaves differently. In the  $[0\bar{1}1]$  direction, the etch stops at the (112) plane, resulting in a V-groove as can be seen in Fig. 3.10(a). The depth of the groove is determined by the width of the opening, as the etch stops completely on the crystal plane at an angle of  $35.3^\circ$  with respect to the surface [56]. In the  $[011]$  direction the etch results in a 'tie'-shape. The depth of this etch is determined by the time of etching.

With minor changes to the standard process and adding some additional steps, the alignment features can be integrated in a PIC in this way.

### 3.4.2 Vertical taper

For efficient and tolerant coupling of the PIC to a fiber, spotsizer converters are required. The design and results of the spotsizer converters we developed was discussed in chapter 2. Here the



**Figure 3.10:** SEM photographs of the precision cleave grooves.

technology for realizing them is presented. The device consists of a horizontal and a vertical taper. The fabrication of the most difficult part, the vertical taper, is based on the process described in [57]. This uses a tapered resist profile, which is obtained with a sliding raster mask, similar to a sliding window method [58]. The vertically tapered profile in the resist is transferred to the semiconductor by a non-selective etch.

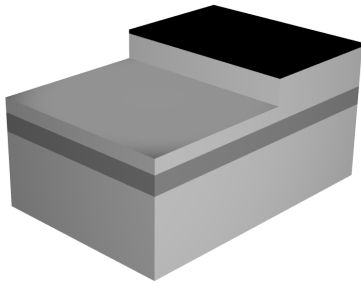
The technology needed to fabricate this taper is depicted in Fig. 3.11. It is designed to be integrated with the standard process. All these steps should precede the standard process steps of Fig. 3.2.

- A. The first step is to define the region where the taper is to be made. The taper has to extend vertically to stop at the substrate. The slope of the taper is fixed and the quaternary layer has to be fully removed at the end of the taper. In order to limit the length of the taper, it will start at a level 300 nm above the quaternary waveguide layer. (Fig. 3.12) For this the semiconductor has to be etched in the regions where the taper is to be made.

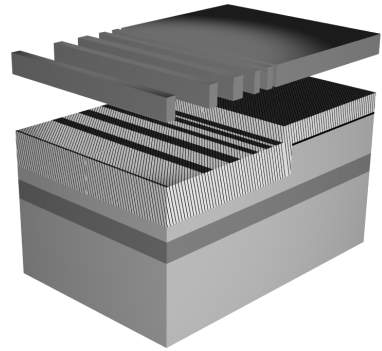
In this step  $\text{SiN}_x$  is deposited on top of the wafer. Photoresist is spun and the taper region is lithographically opened. The silicon nitride is etched using a  $\text{CHF}_3/\text{O}_2$  RIE. After the etching, the resist is removed and the semiconductor is etched in a  $\text{CH}_4/\text{H}_2$  RIE to the desired depth.

- B. Resist is spun on the sample. A discrete transition is obtained in the previous step, but this is not a problem as the resist used is thick enough to cover the step. The resist is first soft-baked at  $100^\circ\text{C}$  to get rid of the solvents. After this, another soft-bake step at  $115^\circ\text{C}$  is done to decrease the photosensitivity of the resist and obtain slow development. This makes the development less critical.

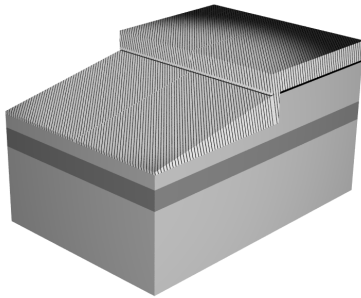
The taper is defined by a sliding raster mask. The openings are put on the mask with a  $3\ \mu\text{m}$  period. They increase linearly in size. The exposure of the resist is determined by the size of the opening. By sliding the mask over approximately  $170\ \mu\text{m}$  the exposure dose varies linearly with position over the taper region and the discrete raster openings



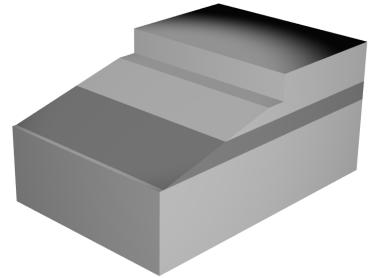
(A) Etch of the taper region



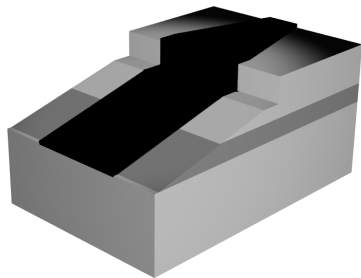
(B) Lithography with sliding raster mask



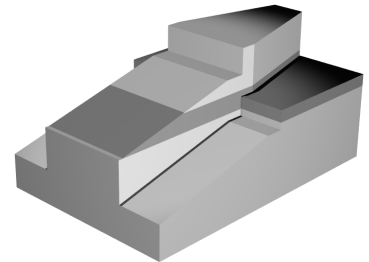
(C) Vertical taper in resist



(D) Etch of the vertical taper using ICP

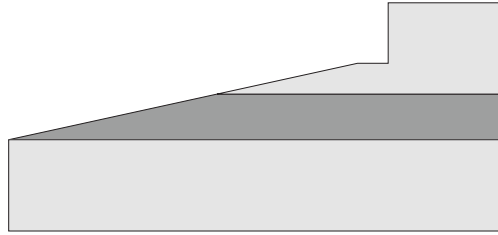


(E) Silicon Nitride mask of the waveguide



(F) Waveguide etch

**Figure 3.11:** Process for the vertical taper



**Figure 3.12:** Cross section of the vertical taper.

are averaged out. After illumination the resist is baked again to smoothen standing wave patterns in the resist.

- C. The sample is developed and a taper is obtained in the photoresist.
- D. The sample is etched using an Inductively Coupled Plasma (ICP) etch. The etch conditions are tuned to have a non-selective etch for the semiconductor and the resist. The best obtained ratio of the etch rates of resist and InP/InGaAsP is approximately 0.6. In this way the taper transferred into the semiconductor is slightly steeper than the taper in the resist.
- E. This taper is the starting point for the standard processing. In this step  $\text{SiN}_x$  is deposited and the waveguide mask is transferred to the  $\text{SiN}_x$  in the same way as in Fig. 3.2(a).
- F. The next step is the waveguide etch, exactly the same as for the normal waveguides. In the waveguide mask a horizontal taper is defined. After the etching, a vertical as well as a horizontal taper is present in the structure.

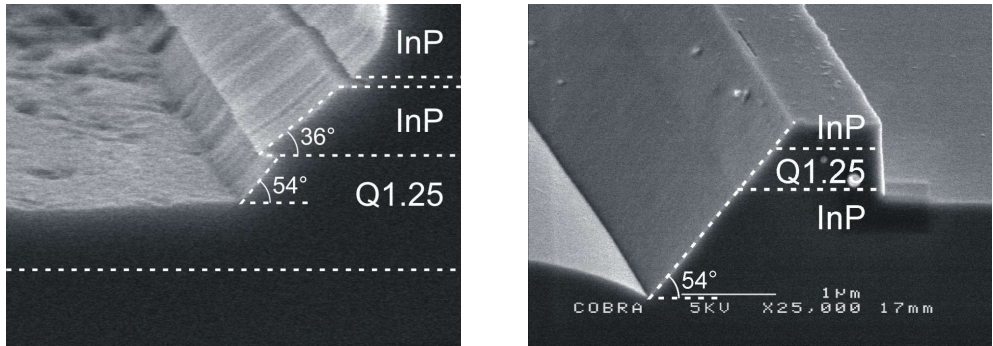
After these steps, the standard process can continue.

## 3.5 Sloped sidewalls

The polarization converter (PC) consists of a waveguide with a straight and a sloped sidewall [59]. The design is explained in detail in chapter 4. The processing of polarization converters requires additional process steps that will be discussed next.

### 3.5.1 Wet etch

A sloped sidewall is obtained by wet etching. Several solutions can be employed for this. Most etchants however are selective for InP and InGaAsP, so two etchants need to be used. Another disadvantage is that the slopes have a different orientation for the different materials. For stripes in the [011] direction, InP etched using  $\text{HCl}:\text{H}_3\text{PO}_4$  stops on the (112) plane which has a slope of  $35.3^\circ$  [56]. InGaAsP has to be etched with  $\text{H}_2\text{SO}_4:\text{H}_2\text{O}_2:\text{H}_2\text{O}$ , the etch stops



(a) Underetch of quaternary below InP with  $\text{H}_2\text{SO}_4:\text{H}_2\text{O}_2:\text{H}_2\text{O}$ .

(b) Smooth etch of quaternary and InP with  $\text{Br}_2:\text{CH}_3\text{OH}$ .

**Figure 3.13:** Different etchants for InGaAsP and InP.

at the (111) plane which has an angle of  $54.7^\circ$  with respect to the surface[60]. Furthermore there is a large underetch below the InP as is visible in Fig. 3.13(a). Such an underetch next to the quaternary layer will result in high propagation loss. This makes these etchants less suitable to use for producing polarization converters. Another possible etchant is bromine ( $\text{Br}_2$ ) dissolved in methanol [56, 61] a very diluted solution (1:1500). This  $\text{Br}_2:\text{CH}_3\text{OH}$  etches both InP and InGaAsP and stops at the (111) planes for both. This results in a very smooth etch (Fig. 3.13(b)). Therefore this is the etchant of choice for the polarization converters.

### 3.5.2 Masking

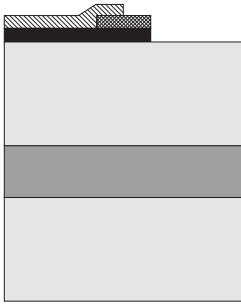
An important parameter in the realization of PCs is the masking material. As stated before, the polarization converter consists of one straight and one slanted sidewall. To obtain these different slopes, the sides have to be opened separately, while keeping the dimensions. For this, 2 mask materials are required that can be selectively removed with respect to one another. Silicon Nitride and Titanium are chosen for this purpose.

The top of the PC, which has critical dimensions, is defined in Ti on top of the  $\text{SiN}_x$  by using high resolution lithography. By using resist and the Ti pattern as a mask, one side can be opened. This is depicted in Fig. 3.14(a). With this mask, the straight side can be etched using RIE.

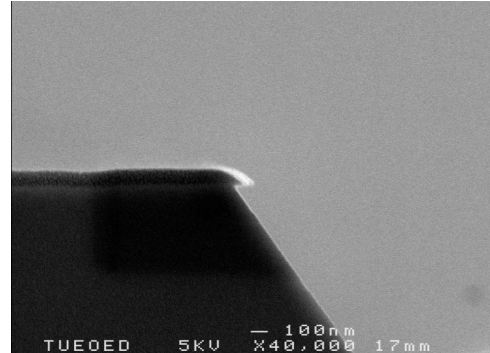
Photoresist is dissolved in methanol, so this cannot be used as a mask in the  $\text{Br}_2:\text{CH}_3\text{OH}$  etch. Therefore, when the sloped side is etched, all the rest has to be covered by  $\text{SiN}_x$ . The  $\text{SiN}_x$  is deposited using a PECVD, with this technique both the top and the sides are covered. If the initial mask is covered by another layer of  $\text{SiN}_x$ , the stress in the nitride can cause a loading effect on the material. This can lead to a "lifting" of the mask, and thus to an underetch as is shown in Fig. 3.14(b). The underetch is reproducible and can be corrected for in the design.

Although the nitride at the sides is slightly thinner than at the top, it can function as a mask

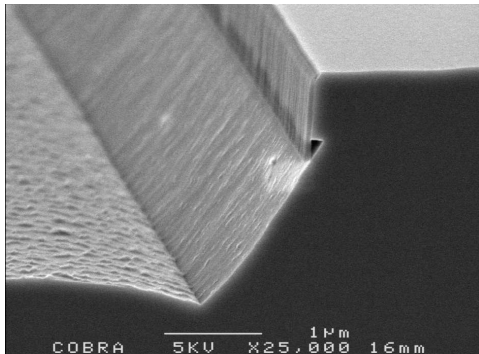
on the sides as well. Stress in the material can also cause an underetch in this case as is clear from Fig. 3.14(c). In this case, it has to be taken into account that the slope starts at the semiconductor side of the mask. The underetch is not present if the force of the stress in the  $\text{SiN}_x$  can be compensated by the adhesion to the semiconductor, or if the stress is neutralized by having a symmetric loading. This is shown in Fig. 3.14(d).



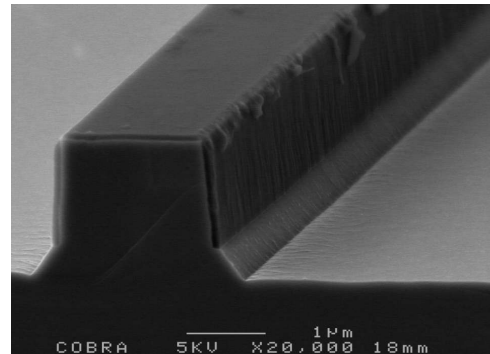
(a) Define critical dimensions in Ti, etch  $\text{SiN}_x$  using Ti and resist as mask.



(b) Underetch below  $\text{SiN}_x$ .



(c) Underetch below  $\text{SiN}_x$  at the sidewalls.



(d) No underetch below  $\text{SiN}_x$  if no loading is present.

**Figure 3.14:** Mask definition and properties for the polarization converter

The integration of this device in the standard processing and its design is investigated further in chapters 4 and 7

### 3.6 Conclusions

The standard process for components on a PIC is presented in this chapter. The modular nature of the process is explained. This allows the introduction of additional steps that can be

integrated with the standard process.

For critical width definitions high resolution optical lithography or electron beam lithography are introduced. They can replace the contact lithography where necessary. To allow accurate alignment, some additional processing is needed to obtain alignment marks.

Precision cleaves and vertical alignment features, both required for packaging, can be introduced in the standard process without influencing the rest of the processing.

The technology for producing spotsize converters is presented. A sloped resist profile can be obtained with a sliding raster mask and this can be used to ICP etch vertical tapers.

Polarization converters can be defined with the high resolution lithography and Ti and SiN<sub>x</sub> are a good combination to be used as mask for this. Br<sub>2</sub>:CH<sub>3</sub>OH gives good quality sloped sidewalls required for the PC. The underetch obtained in this etch has to be considered in the design.

The modular nature of the technology platform allows introduction of additional steps without major changes to the existing steps. This opens the possibility for creating a generic active-passive technology platform suited for on-chip polarization handling and with the capability for packaging.





---

# Chapter 4

## Polarization converters

---

### 4.1 Introduction

Polarization conversion is an important function if on-chip polarization manipulation is required. As shown before, polarization converters (PC) that can be integrated with other functions on a chip are needed.

A well-known principle for polarization conversion is the application of electro optic effects. This is mainly used in  $\text{LiNbO}_3$ , and has been reported for InP [62]. In InP the electro optic effect is small, which results in very large devices. Furthermore electro-optic polarization conversion requires phasematching between the two polarizations, which is hard to achieve and wavelength dependent.

For our application, passive polarization conversion is preferred, because of the easier fabrication and because there is no need for tuning. A number of passive PCs have been reported in literature. Polarization conversion can be obtained by cascading sections of waveguides with partially tilted modes. At the junctions between the sections partial conversion occurs. The section can consist of slanted waveguides [59], periodically loaded waveguides [63, 64], or integrated bends [24]. These devices have the advantage of an easy fabrication, but are long (close to or larger than 1 mm), and are wavelength dependent. The bandwidth is limited due to the phase-matching that has to be obtained between the different sections.

Recently progress is made towards single section devices, full conversion occurs at the junction with a straight waveguide and only a single section is required.

Another class of short devices are converters that make use of mode-evolution [65, 66] to adiabatically couple from one polarization to the other. These devices have waveguides with a

changing waveguide cross-section and do not fit in our layer stack and integration scheme. The single sections devices that make use of tilted birefringent modes are the most promising for integration. The most important ones are shown in Table 4.1.

The tilting of the modes is obtained by different techniques: in device *A*, the modes are tilted by etching a narrow waveguide with tilted sidewalls on both sides by using Chemically Assisted Ion Beam Etching (CAIBE), the same etching is used in device *B*, in which tilted slits are etched to cause the modes to be tilted. Although both these devices show promising results, their processing is not compatible with the active passive integration shown in chapter 3 and these will not be considered.

In device *C* slits with varying depth effectively make a slanted side and tilt the modes inside the device. The lag effect in the RIE is employed to achieve different etch depths for different slit widths for this design, both the width and the depth have to be controlled extremely accurate, which makes this devices very intolerant to fabricate. Device *D* uses a RIE etched straight sidewall in combination with a wet etched sloped sidewall. This device is the most promising to integrate with active and passive waveguides. A wet etch introduces more process steps as compared to e.g. device *C*, but is advantageous over the dry etch, because of the tolerances. A wet etch will stop on a crystal plane, so the slope is always well-defined. This chapter describes the principle of the polarization converter based on a wet etched slope. Furthermore the design, fabrication and results of two generations of such polarization converters are discussed.

## 4.2 Principle

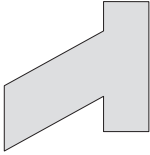
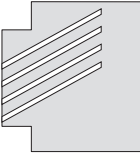
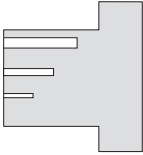
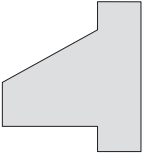
The polarization converter using tilted birefringent modes is the integrated optical analogue of the half wave plate in bulk optics. A half-wave plate has a slow and a fast axis: two orthogonal modes can exist with differing propagation constants. When the plate is tilted with respect to the input polarization, both modes are excited and after propagating over a certain distance through the device, the two modes are out of phase and recombine to a different polarization state.

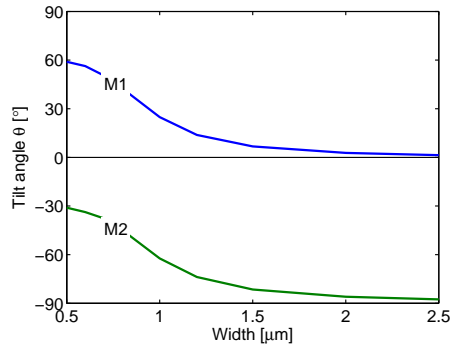
The equivalent integrated device consists of a ridge waveguide with a straight and a slanted sidewall (Fig. 4.2(a)). The waveguide is narrow, typically below 1  $\mu\text{m}$ . This brings the slanted sidewall close to the field of the mode. Because of the ‘tilted’ boundary conditions, the hybrid nature of the modes is enlarged. Ideally this causes the modes to tilt for  $+45^\circ$  and  $-45^\circ$  respectively. Furthermore, the geometry of the waveguide causes a different propagation constant for the two modes. The angle of the sloped sidewall does not have to be  $45^\circ$  (in our case it is  $54^\circ$  with respect to the surface). The tilt angle of the modes for a certain slope angle is determined by the width. In Fig. 4.1 the tilt angle

$$\theta = \arctan \frac{E_y}{E_x} \quad (4.1)$$

is plotted as a function of the width of the polarization converter waveguide for the modes inside the converter.

**Table 4.1:** Different single section polarization converters

Reference	Principle	Schematic	Fabrication	Performance
A [67]	Waveguide with tilted sidewalls.		Chemically Assisted Ion Beam Etching (CAIBE) for both sides in one step.	<ul style="list-style-type: none"> <li>• L = 48 <math>\mu\text{m}</math></li> <li>• c = 97%</li> <li>• Loss 1 dB</li> </ul>
B [68]	Ridge waveguide with tilted slits.		2 times CAIBE for slits and ridge separately.	<ul style="list-style-type: none"> <li>• L = 1.6 <math>\mu\text{m}</math></li> <li>• c = 96%</li> <li>• Loss 3 dB</li> </ul>
C [69]	Ridge waveguide with straight slits with varying depth.		RIE for slits and ridge in one step. The lag-effect is used to obtain different depth for different slit-width.	<ul style="list-style-type: none"> <li>• L = 280 <math>\mu\text{m}</math></li> <li>• c = 96%</li> <li>• Loss 2.5 dB</li> </ul>
D [70, 71, 72]	Asymmetric waveguide with a straight and a slanted wall.		Reactive Ion Etching (RIE) for straight wall, wet etch for slope.	<ul style="list-style-type: none"> <li>• L = 125 <math>\mu\text{m}</math></li> <li>• c = 95%</li> <li>• Loss &lt; 1 dB</li> </ul>

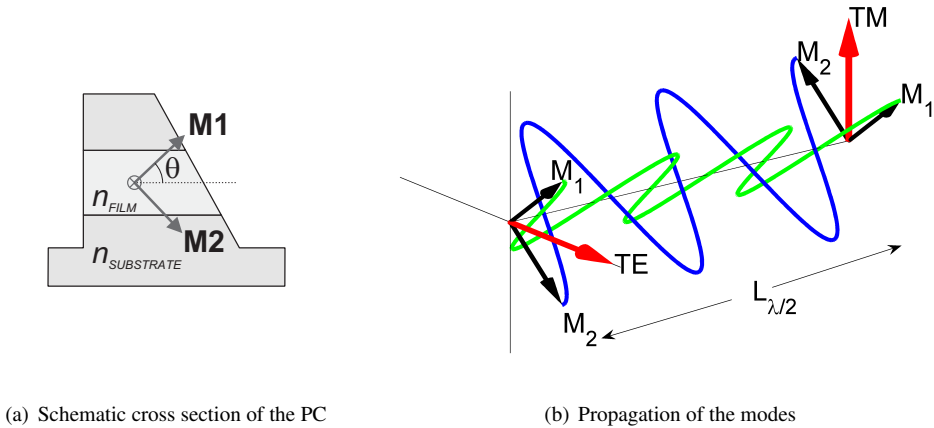


**Figure 4.1:** Tilt angle of the modes inside the PC as a function of waveguide width.

If light in a straight waveguide is coupled to the PC waveguide, both tilted modes are excited. After a half beatlength,

$$L_{\lambda/2} = \frac{\pi}{\beta_1 - \beta_2}, \quad (4.2)$$

where  $\beta_n$  is the propagation constant of mode  $n$ , the modes are completely out of phase and recombine into the orthogonal polarization in a straight output waveguide as shown in Fig. 4.2. This is clarified in Fig. 4.2(b), where the propagation of modes  $M_1$  and  $M_2$  is shown over a length  $L_{\lambda/2}$ , corresponding to a phase difference  $\phi = \pi$  rad.



(a) Schematic cross section of the PC

(b) Propagation of the modes

**Figure 4.2:** Principle of the integrated polarization converter

The properties of the conversion of the PC can be explained using Jones matrices (see Appendix A). The PC with length  $L_{\lambda/2}$  creates a phase difference  $\phi$  between the two orthogonal

modes. In the coordinate system of the tilted modes, the transfer matrix  $\mathbf{T}_{PCI}$  of the PC itself is:

$$\mathbf{T}_{PCI} = \begin{bmatrix} 1 & 0 \\ 0 & e^{-j\phi} \end{bmatrix} \tag{4.3}$$

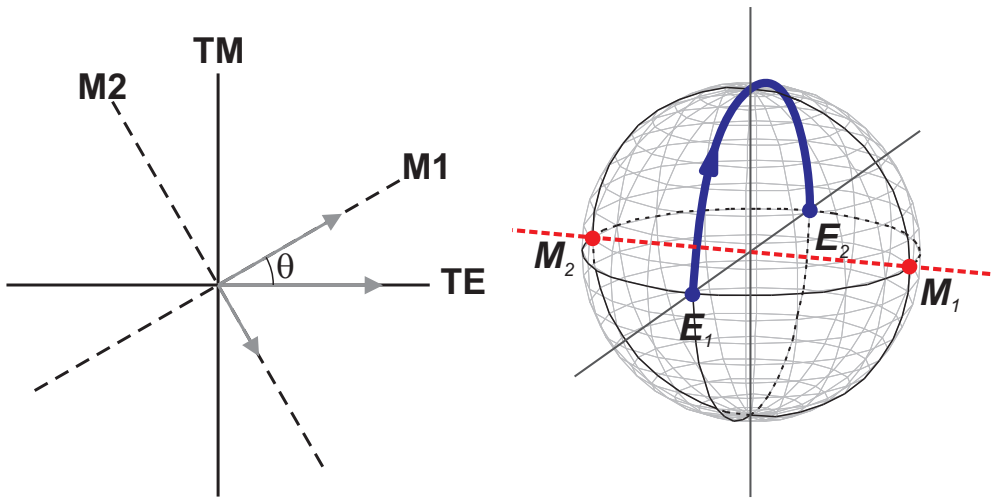
The two modes inside the PC are in the regular coordinate system (normal along the y-axis):

$$\mathbf{M}_1 = \begin{bmatrix} \sin(\theta) \\ \cos(\theta) \end{bmatrix} \quad \mathbf{M}_2 = \begin{bmatrix} \cos(\theta) \\ -\sin(\theta) \end{bmatrix} \tag{4.4}$$

The modes inside the PC are tilted over an angle  $\theta$  with respect to the modes in the straight waveguide. The total transfer of the PC is obtained by a coordinate transformation. The tilted modes form the new base for the calculations of the PC. The transfer with respect to the TE-TM bases are obtained by multiplication with a rotation matrix  $\mathbf{R}(\theta)$ :

$$\mathbf{R}(\theta) = \begin{bmatrix} \cos(\theta) & \sin(\theta) \\ -\sin(\theta) & \cos(\theta) \end{bmatrix} \tag{4.5}$$

Fig. 4.3(a) shows the transformation to the new bases.



(a) Coordinate transformation to new bases for PC

(b) Conversion of the PC plotted on the Poincaré sphere

**Figure 4.3:** Visualization of the conversion.

The transfer of the PC is:

$$\mathbf{T}_{PC} = \mathbf{R}^{-1}(\theta)\mathbf{T}_{PCI}\mathbf{R}(\theta) \tag{4.6}$$

which is equal to

$$\begin{bmatrix} \cos(\theta)^2 + \sin(\theta)^2 e^{-j\phi} & \cos(\theta) \sin(\theta) - \cos(\theta) \sin(\theta) e^{-j\phi} \\ \cos(\theta) \sin(\theta) - \cos(\theta) \sin(\theta) e^{-j\phi} & \sin(\theta)^2 + \cos(\theta)^2 e^{-j\phi} \end{bmatrix} \tag{4.7}$$

For TE input, this yields an output  $\mathbf{E}_2$ :

$$\mathbf{E}_2 = \begin{bmatrix} \cos(\theta)^2 + \sin(\theta)^2 e^{-j\phi} \\ \cos(\theta) \sin(\theta) - \cos(\theta) \sin(\theta) e^{-j\phi} \end{bmatrix} \quad (4.8)$$

This yields a conversion:

$$c = \frac{P_{converted}}{P_{total}} = 2 \{\cos(\theta) \sin(\theta)\}^2 \{1 - \cos(\phi)\} \quad (4.9)$$

The conversion process can be visualized by plotting the State of Polarization (SOP) on a Poincaré sphere. The two stable modes are  $\mathbf{M}_1$  and  $\mathbf{M}_2$ . Propagation through the PC results in a rotation around the axis between these two points. In Fig. 4.3(b) the conversion from TE ( $\mathbf{E}_1$ ) to TM ( $\mathbf{E}_2$ ) in an ideal PC ( $\theta = \pi/4$  and  $\phi = \pi$ ) is shown.

From eq. (4.8) it is clear that the amplitudes of the two components of  $\mathbf{E}_2$  depend on both the tilting angle  $\theta$  and the phase difference  $\phi$ . Incomplete conversion can have two different causes.

- The PC has the correct width and therefore a required tilt  $\theta$  of  $45^\circ$ , but the length is incorrect. At the output the modes are not exactly out of phase. This leads to an elliptical vertical polarization in the output as shown in Fig. 4.4.
- The PC does not have the correct width; the tilt  $\theta$  is not exactly  $45^\circ$ . After propagation over the beatlength, the two orthogonal modes are completely out of phase and result in a linear polarization. However they do not recombine to a polarization orthogonal to the input. This can be seen on the Poincaré sphere in Fig. 4.5. The two stable modes in the structure in this case are not exactly on the  $\pm 45^\circ$  points, but are on different points on the equator of the sphere, as indicated in Fig. 4.5(a).

The conversion of the PC is the ratio between the converted and the total power, in both examples the ratio is the same, but the output SOP is different. Thus the origin of the incomplete conversion cannot be discovered by regarding the output powers for one device. The  $\theta$ , and thus the maximum possible conversion, can be obtained by a scan in length (i.e. a scan in  $\phi$ ).

## 4.3 First generation

A first design for an integrateable polarization converter is made, based on the design in [72], but now aimed at integration with other passive and active components. The design, fabrication and characterization will be discussed in this section.

### 4.3.1 Design

The polarization converter is designed for active passive integration, the layerstack for this is shown in Fig. 4.6, this is equal to stack in table 2.1. It consists of an InP substrate, a 500 nm InGaAsP [Q(1.25 $\mu$ m)] waveguide layer and a 1500 nm InP topcladding. The topcladding

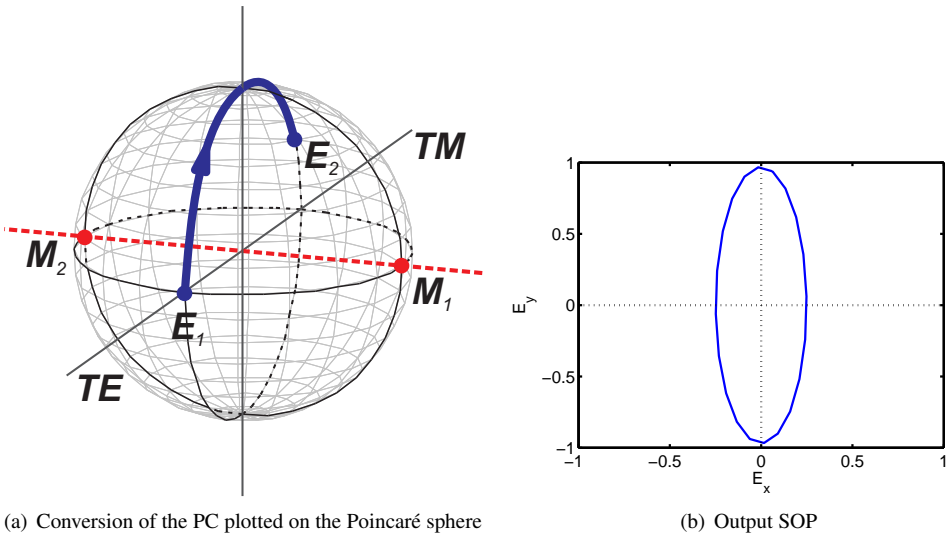


Figure 4.4: Incomplete conversion due to incorrect length

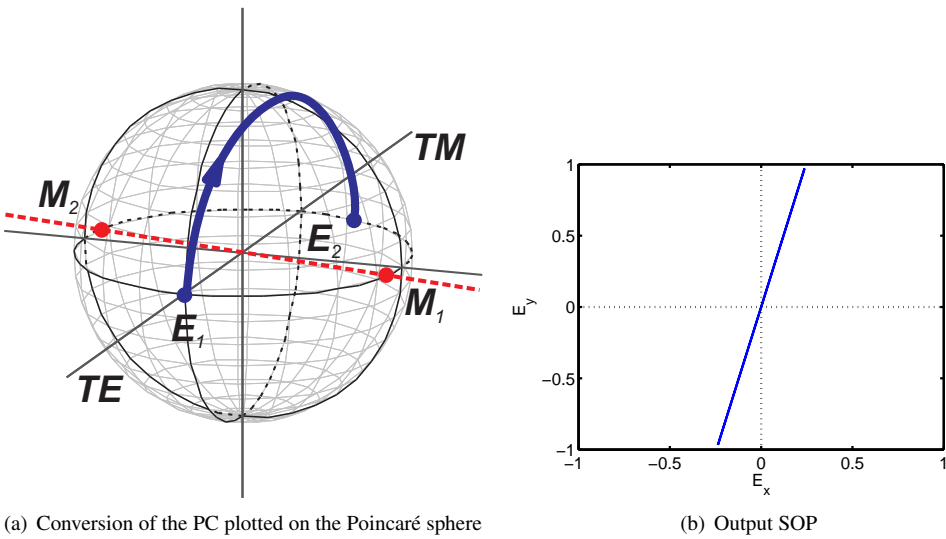


Figure 4.5: Incomplete conversion due to incorrect width

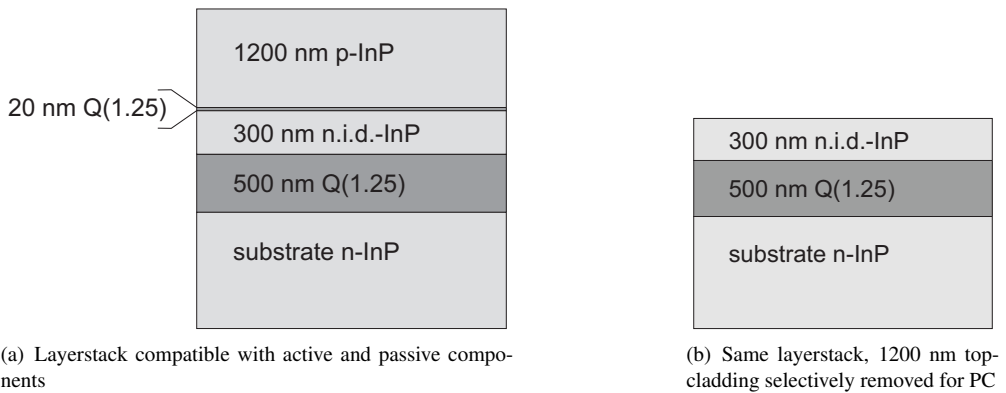


consists of a 300 nm n.i.d. InP layer, on top of which a 20 nm thick Q(1.25) etch-stop layer and a 1200 nm p-InP layer are grown.

For the polarization converters a thin topcladding is used because first of all an accurate control of the width of the converter at the waveguide layer is needed, thus a critical width definition close to the waveguide layer is required. Secondly a large birefringence is desirable, from Fig. 2.1(b) it is clear that to this end a thin topcladding is also needed.

The thin topcladding is obtained by selectively etching back the top InP cladding till the etch-stop layer, and by selectively removing the etch stop layer as well. An accurately defined topcladding of 300 nm is obtained as shown in Fig. 4.6(b). This precisely defined top is used for the PC.

The sloped sidewall will be wet-etched and will stop on the (111) crystal plane, having an angle of  $54^\circ$  with respect to the surface.

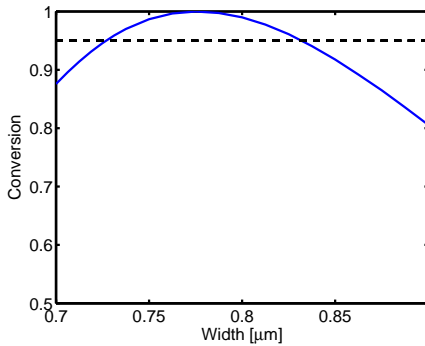


**Figure 4.6:** Layerstack for the integrated PC.

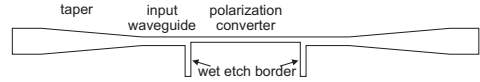
For the simulations the sloped side of the PC is discretized in 60 steps. A full vectorial mode solver (Film Mode Matching [18]) is used to calculate the tilt angle (see Fig. 4.1) and propagation constants for the optimal width and a slope of  $54^\circ$  for a PC in this layerstack. For a width of  $0.78 \mu\text{m}$  the modes are at  $\pm 45^\circ$ . For this width a half beatlength of  $102 \mu\text{m}$  is obtained. The simulation predicts an optimal conversion of TE to TM and vice versa larger than 99%. A conversion above 95% is expected for a width deviation of  $\pm 50 \text{ nm}$  as is shown in Fig. 4.7. 95% conversion is sufficient for the demonstration of the concepts shown in chapter 1 as will become clear in chapter 7.

With this design a 3D simulation is done to optimize the coupling to straight waveguides and to confirm the conversion.

Waveguides used on the rest of the PIC are shallowly etched waveguides, as they have the lowest loss. The PC itself is deeply etched, so the shallow waveguides are connected to deep waveguides using a lowloss shallow-deep transition. The deep waveguides are tapered using  $50 \mu\text{m}$  long parabolic tapers to a width of approximately  $1.3 \mu\text{m}$  to make the connection to the PC as shown in Fig. 4.8. At the interface of the PC and the waveguide a small,  $1 \mu\text{m}$  wide,



**Figure 4.7:** Simulated conversion as a function of width for a fixed length



**Figure 4.8:** Topview of the polarization converter

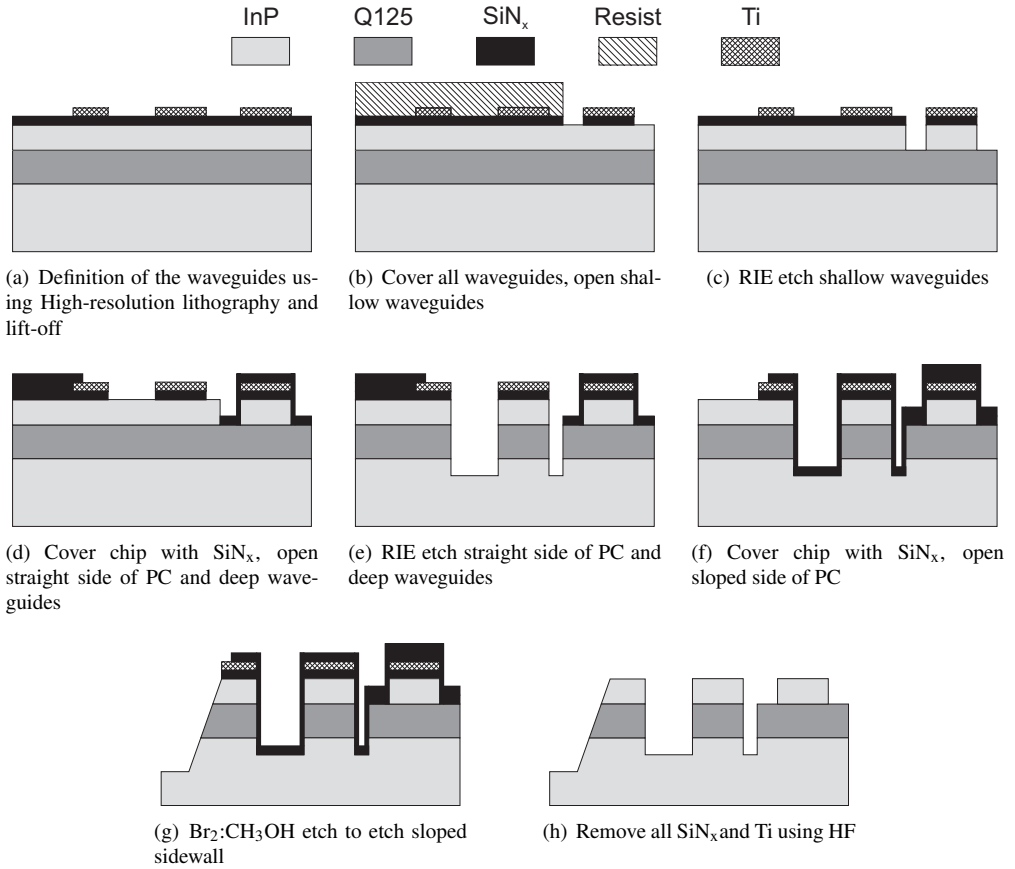
wall is present to confine the wet etch for the sloped side in this area and to prevent etching of the input waveguides. According to simulations this should introduce less than 0.1 dB loss.

### 4.3.2 Fabrication

The fabrication is done as much as possible with the standard technology described in chapter 3. However some changes are necessary, as the width of the device has to be defined accurately, the critical lithography steps are carried out with a  $5\times$  reduction wafer stepper as also explained in chapter 3.

The processing of the polarization converter is shown in Fig. 4.9. The following steps are distinguished.

- a. First the wafer is etched back using an  $\text{HCl}/\text{H}_3\text{PO}_4$  etch to selectively remove the top 1200 nm InP cladding. Next a  $\text{H}_2\text{O}/\text{H}_2\text{SO}_4/\text{H}_2\text{O}_2$  etch is used to remove the Q-etch stop layer. Using standard contact lithography, the phase grating alignment marks are defined and etched with RIE (not shown). They are needed for the alignment in the wafer stepper. After this, a Silicon Nitride ( $\text{SiN}_x$ ) mask layer is deposited using PECVD. The polarization converters and waveguides are defined in Ti on top of the  $\text{SiN}_x$  using the ASML wafer stepper for the lithography in combination with a lift-off process.
- b. The PC and deep waveguides are covered and the shallow waveguides are opened using a standard contact lithography process. The  $\text{SiN}_x$  is etched in a  $\text{CHF}_3$  RIE.
- c. Next the shallow waveguides are etched using a  $\text{CH}_4/\text{H}_2$  RIE. Because the etch depth for these has to be controlled accurately, this is done separately from the other structures.
- d. The wafer is covered with  $\text{SiN}_x$ . The nitride at the straight side of the PC and at the deep waveguides is opened. This is a critical step as the alignment has to be done on a stripe of approximately 800 nm wide. For this step again the wafer stepper is used.



**Figure 4.9:** Processing of the integrated polarization converter (see text).

- e. The deep waveguides and the straight side of the PC are etched using RIE.
- f. Everything is covered again with  $\text{SiN}_x$  and the nitride at the sloped side of the PC is opened, this step is again critical, due to the alignment tolerance which is smaller than 400 nm on the 800 nm wide stripe for the PC. For this step again the wafer stepper is used.
- g.  $\text{Br}_2$ -Methanol is used to etch the slope. This etchant etches both InP and InGaAsP with an angle of  $54.7^\circ$  with respect to the surface (see section 3.5).
- h. Finally all the  $\text{SiN}_x$  and Ti are removed using an HF solution.

A photograph of the fabricated device is shown in 4.10.

The slanted side is etched deeper than the vertical wall, but that has no influence on the modes since both etches are completely through the guiding layer. During the wet etch an underetch of 120 nm occurred. The width of the realized converters is reduced by this amount. This has to be taken into account in the design width.

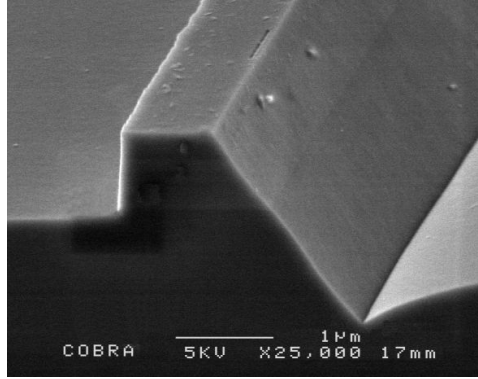


Figure 4.10: SEM photograph of a realized polarization converter.

### 4.3.3 Characterization

The polarization converters are measured using the setup shown in Fig. 4.11. The device is excited using an EDFA as a broad spectral light source with a bandpass filter set to 1555 nm. The filter has a 2 nm bandwidth, which is large enough to average out Fabry-Pérot resonances resulting from the uncoated facets of the chip. A polarizer at the input of the chip is used to select the input polarization. At the output another polarizer selects the polarization that is measured using the photodiode and the lock-in amplifier.

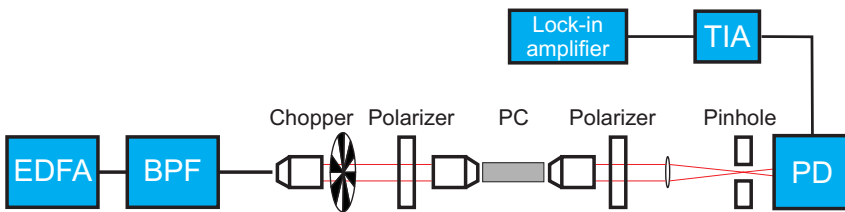


Figure 4.11: Setup used for characterization of the polarization converter. BPF: Bandpass filter, PD: Photodiode, TIA: Trans impedance amplifier

The power in both polarizations at the output is measured for both TE and TM polarized light at the input. The conversion is defined as the fraction of the converted polarization in the output power. The conversion  $C$  for the two polarizations ( $i, j = \text{TE, TM}$ ) is determined from

the following equations:

$$P_{ij} = \alpha_i \alpha_j C P_j; \quad i \neq j \quad (4.10)$$

$$P_{ij} = \alpha_i \alpha_j (1 - C) P_j; \quad i = j \quad (4.11)$$

where  $P_j$  is the input power with polarization  $j$ ;  $P_{ij}$  is the output power in polarization  $i$  when the input polarization is  $j$ ;  $\alpha_{i,j}$  are the losses for the two polarizations in the input and output waveguides.

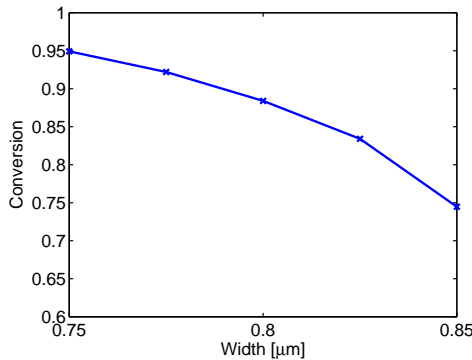
By solving these equations, the propagation losses in the input and the output waveguides for the two polarizations are eliminated and the conversion  $C$  is obtained:

$$C = \frac{\sqrt{x}}{1 + \sqrt{x}} \quad (4.12)$$

where

$$x = \frac{P_j P_{ji}}{P_i P_{jj}}; \quad i \neq j \quad (4.13)$$

The measured conversion is plotted as a function of width in Fig. 4.12.

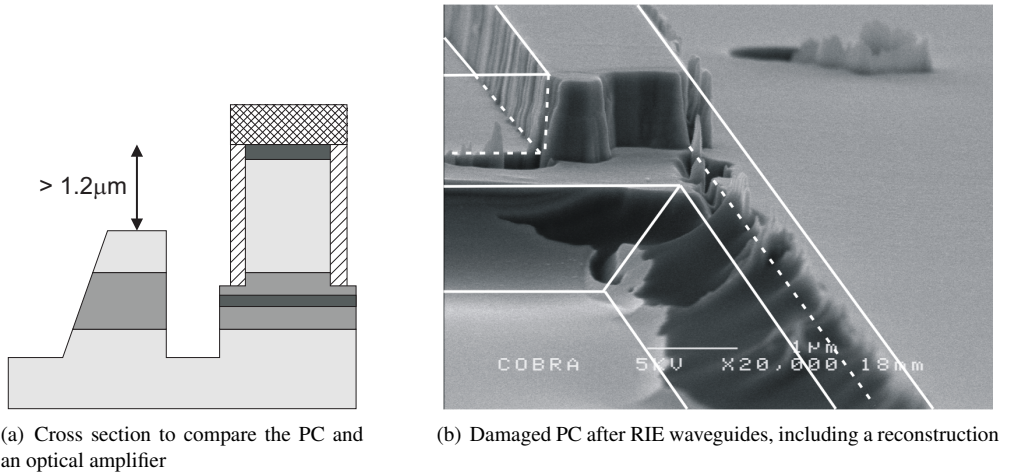


**Figure 4.12:** Measured conversion as a function of width of polarization converter

A conversion of 95% can be achieved for a width of 0.75  $\mu\text{m}$ . For the actually designed width of 0.78  $\mu\text{m}$  a conversion of 89% is obtained. The actual widths deviate from the simulations. This is mainly due to the under etch, which is not exactly 150 nm.

### 4.3.4 Integration

The next step is the integration of the PC with passive and active components. The process for the integration of the PCs with active and passive components is subdivided into two parts, one part for the polarization components and one in which the other components are made.



**Figure 4.13:** Problems in integration of the PC

- The polarization components require a thin topcladding of only 300 nm, the waveguides and the SOAs need a thick topcladding of 1.5  $\mu\text{m}$ . First the area in which the polarization converters are placed is etched down to this level. On this topography the first lithography step is done, which is common for all the waveguides, for the standard components as well as for the polarization converters. This has to be a high resolution step for the PC as described in the process scheme in this chapter. The standard components are covered with an  $\text{SiN}_x$  mask. The complete process as shown in Fig. 4.9 for the PC is performed.
- After this, the polarization converters are covered with  $\text{SiN}_x$  and the standard process as shown in Fig. 3.2 is performed.

The height differences, as shown in Fig. 4.13(a), between the PCs and other components on the chip are larger than 1.2  $\mu\text{m}$ . This proved to cause problems in the lithography: for critical definition, thin resist is needed. With resist thickness below 1  $\mu\text{m}$ , the large step cannot be covered. So thicker resist is required. This limits the resolution, but tests show that this is still useable for the definition of the PC.

Furthermore the limited depth-of-focus will pose problems in a good definition at the lowest level, on which the width of the PC has to be defined.

Another problem occurred when the etching of the standard waveguides was performed, as shown in Fig. 4.13(b). This SEM photograph shows a PC integrated with active and passive components. The drawn lines show the designed structure.

There clearly was a problem in the masking of the sloped side of the PC during the RIE etching of the waveguides. The  $\text{SiN}_x$  mask is eroded on the sloped side and the PC is etched away. The in- and output waveguides of the PC are still present, so the lithographical definition as well as the RIE etching of the straight waveguides has been done right. (It has to be noted that the

critical dimensions are not met.)

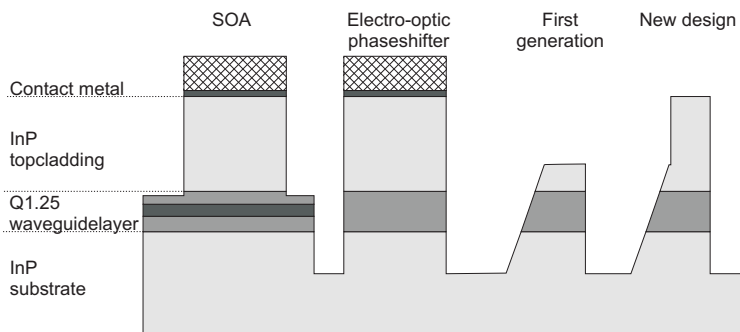
An improved process has to be developed to avoid these problems. First of all the critical width definitions have to be on the same height level, allowing thinner resist and no problems with limited focussing depth. The etching of the PCs and the waveguides are done consecutively, in a next realization the etching for both the PCs and the standard components can be more integrated. The etching of the slope has to be done as a last step to avoid damage afterwards.

## 4.4 Second generation

The problem with the previous design is the difficulty to integrate the PC with passive and specifically with active components. The polarization converters and active components (such as semiconductor optical amplifiers (SOAs) and phaseshifters [73]) can be made in the same layerstack, but the optimal thickness of the top-cladding differs by more than  $1\ \mu\text{m}$ . For polarization converters a large birefringence, and more importantly, a critical width definition close to the waveguide layer is needed: hence a thin topcladding is preferred; for SOAs and electro-optic phaseshifters, a thick topcladding (typically  $1.5\ \mu\text{m}$ ) is needed below the contact to avoid optical losses due to the contactlayer.

This is clarified in Fig. 4.14: an SOA, phaseshifter and a conventional polarization converter are shown. Critical lithographical definition is not possible with these height differences as the photoresist thickness varies over the different heights and the depth of focus is limited for critical definitions. This complicates processing and integration of these devices.

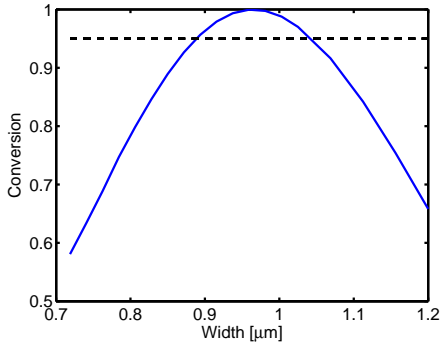
The new design [74] is shown in the rightmost picture in Fig. 4.14. It uses the same thickness of the topcladding as an active device (without the thin contactlayer) and can be integrated with the other components. The birefringence with the thicker cladding is only slightly reduced with respect to the thinner cladding. Hence the increase in length for this design is less than  $40\ \mu\text{m}$ . The critical width definition of the PC is kept during the etching as is explained in the next sections.



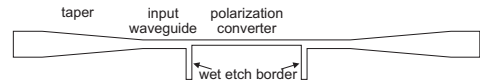
**Figure 4.14:** Cross section of active devices (SOA), phaseshifter, the first generation PC and the new design.

### 4.4.1 Design

The layer stack is the same as used for the standard components (see Fig. 4.6(a)). Film Mode Matching simulations [18] predict an optimal conversion of TE to TM and vice versa larger than 99% for a width of  $0.94\ \mu\text{m}$  and a length of  $141\ \mu\text{m}$ . A conversion above 95% is expected for a width range of  $100\ \text{nm}$  as is shown in Fig. 4.15.



**Figure 4.15:** Simulated conversion as a function of width for a fixed length.



**Figure 4.16:** Topview of the polarization converter

Deviations from the calculated width and length can be expected, because the refractive indices used in the simulations are not accurately known for these materials.

The total device is similar to the first generation PC, it contains an asymmetric waveguide as the converter section,  $1.2\ \mu\text{m}$  wide deep input and output waveguides, coupled to  $3\ \mu\text{m}$  wide shallow waveguides via  $75\ \mu\text{m}$  long tapers (Fig. 4.16).

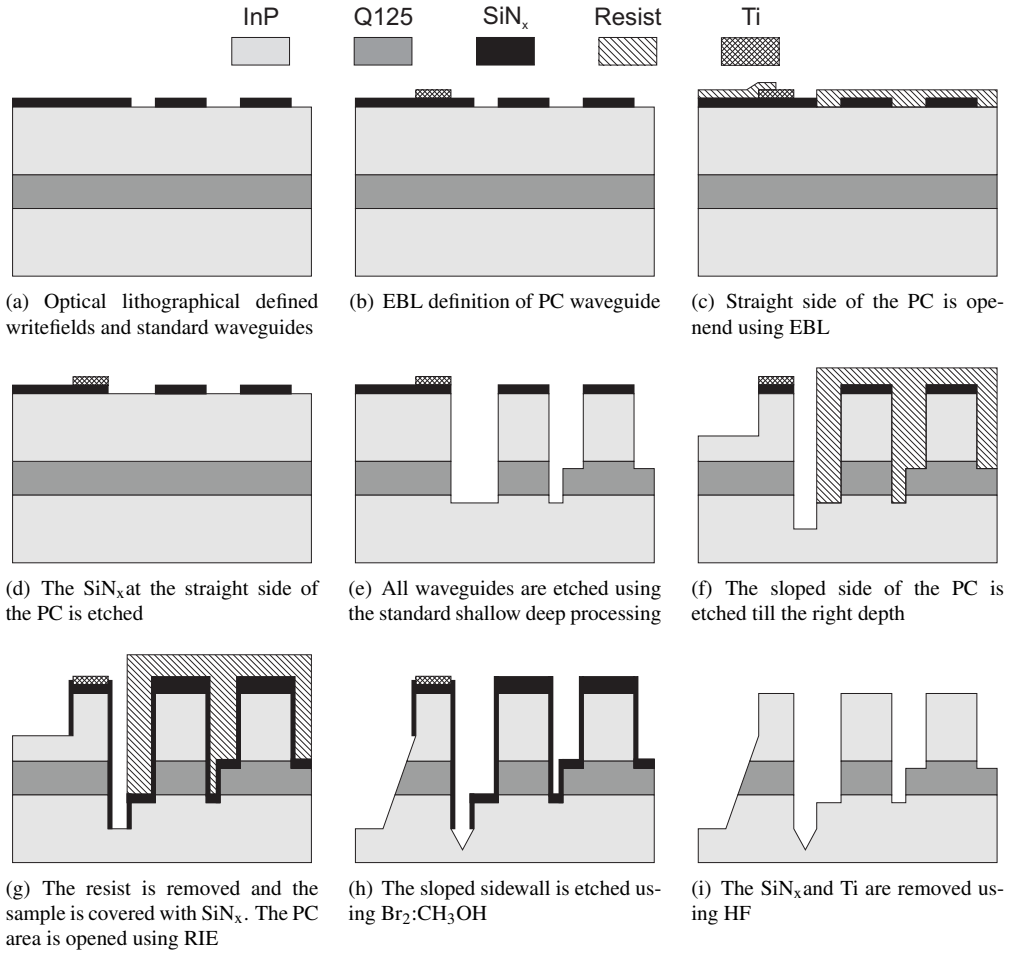
At the interface of the input waveguides and the polarization converter section a small ridge is present, perpendicular to the waveguide. This is needed to prevent etching of the input waveguide in the wet etch for the slanted sidewall. However according to simulations, this does not influence the propagation of the waveguide modes.

### 4.4.2 Fabrication

The polarization converters have strict tolerances in width, so high resolution lithography is required. In this realization, the converter sections have been defined using Electron Beam Lithography (EBL). EBL is not suited for writing large circuits, therefore all other waveguides have been defined using standard optical lithography. The EBL written parts have to be aligned to the optical waveguides as explained in chapter 3.

The processing of the polarization converter is shown in Fig. 4.17 and consists of the following steps:

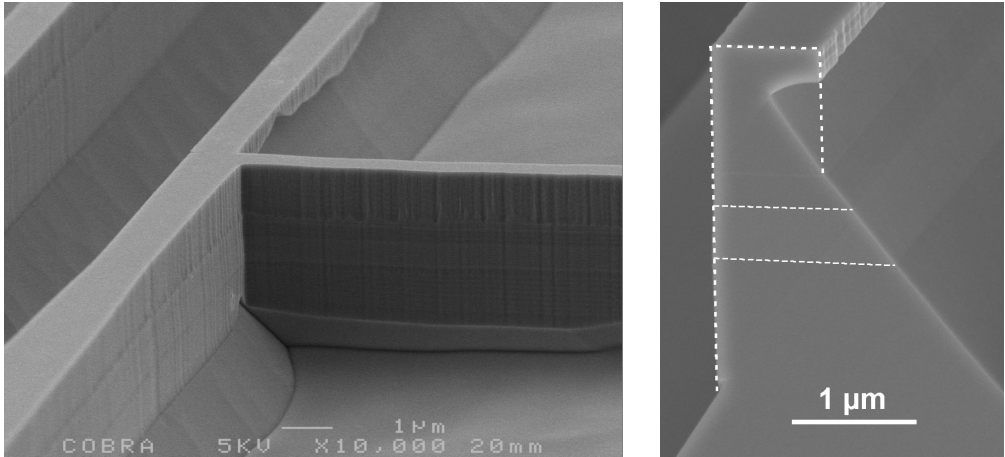




**Figure 4.17:** Processing of the integrated polarization converter (see text).

- a. First the waveguides and writefields for the EBL, including the alignment marks, are defined optically in a Silicon Nitride ( $\text{SiN}_x$ ) mask layer.
- b. The polarization converters are defined in Ti on top of the  $\text{SiN}_x$  using EBL and a lift-off process.
- c. Before etching any waveguide, a second EBL step is done to open the straight side of the PC.
- d. Next the nitride at the straight side of the PC is opened using the EBL-resist and the titanium as a mask.
- e. The shallow and deep waveguides, and the straight side of the PC are etched with  $\text{CH}_4/\text{H}_2$  Reactive Ion Etching (RIE) in a double etch process [75]. This is the same as the standard processing explained in chapter 3.
- f. All shallow waveguides are covered with resist, and the PC area is opened with a non-critical optical lithography step. The  $\text{SiN}_x$  at the sloped side of the PC is opened and the InP topcladding is RIE etched until 300 nm above the waveguide layer. In this step the critical dimensions are kept, because the Ti mask does not erode during the etch and thus the sidewalls are vertical. While etching this side, the straight side of the PC (which is already etched in step e.) is etched even deeper, well below the waveguide layer.
- g. Silicon Nitride is deposited on the whole sample and the shallow waveguides are again covered with resist. The PC area is opened using a non-critical lithography. The  $\text{SiN}_x$  on the PC area is etched back using  $\text{CHF}_3$  RIE. Because of the directional etching, the etched sidewalls stay covered with  $\text{SiN}_x$ , which serves as a mask for the wet etching.
- h.  $\text{Br}_2$ -Methanol is used to etch the slope. This etchant etches both InP and InGaAsP with an angle of  $54.7^\circ$  with respect to the surface (see section 3.5). In this step, the straight side of the PC is etched as well. As this side is already etched well below the waveguide layer, the etching will not influence the performance of the converter. The advantage of this process with respect to the first generation is that here only 2 critical steps are needed (the definition of the PC waveguide (b) and the coverage of the sloped side (c)). A separate step to cover the deep side (step (f) in the first generation) and open the slope side is not necessary.
- i. Finally all the nitride and the Ti is removed using an HF solution.

The fabricated converters are shown in Fig. 4.18. From these figures it is clear that there is an underetch at the shallow side (the sloped side). There is however no underetch at the deep side. This indicates that the underetch can be caused by stress in the masking material during the wet-etching.

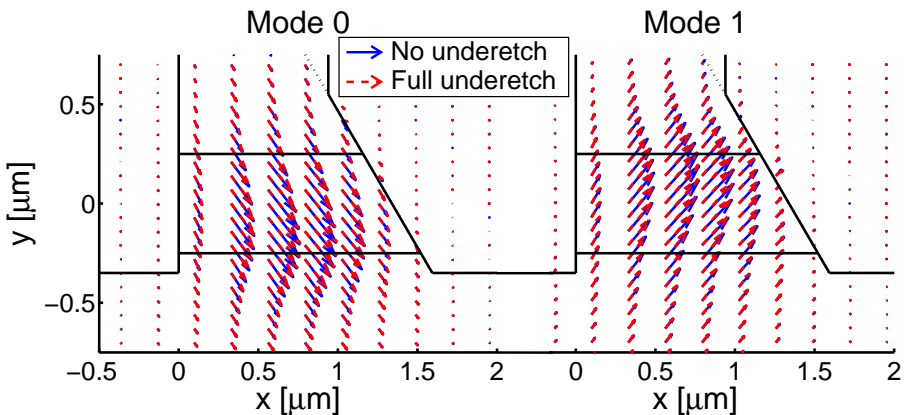


**Figure 4.18:** SEM photographs of the integrated Polarization converter. Left: transition of a straight waveguide to the polarization converter. Right: cross section through the converter.

The influence of this additional underetch on the conversion performance of the device will be small. The width definition at the InGaAsP layer is not affected by this underetch: the slope starts at the desired point, fixed by the Silicon Nitride, and stops on the crystal plane. Fig. 4.19 shows the tilted modes for both cases (with and without underetch). The resulting difference in the tilt angle of the modes is smaller than  $1^\circ$ . Using eq. (4.9), the maximum conversion (for  $\phi = \pi$ ) can be obtained from:

$$c = 4(\cos(\theta)\sin(\theta))^2 \quad (4.14)$$

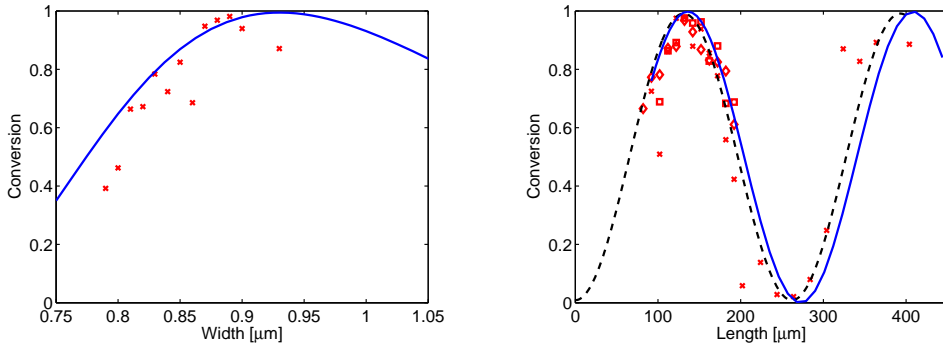
So for a deviation in the tilt angle  $\theta$  of  $\pm 1^\circ$ , the maximum conversion is expected to be beyond 99.9%.



**Figure 4.19:** E-Field of the tilted modes in the polarization converter.

### 4.4.3 Characterization

The polarization converters are measured using the setup as shown before in Fig. 4.11 and analyzed according to the method explained in section 4.3.3. The power in both polarizations at the output is measured for both TE and TM polarized light at the input. The measured conversion is plotted as a function of width and length in Fig. 4.20.



**Figure 4.20:** Simulated conversion (solid), measured values ( $\times$ ,  $\diamond$ ,  $\square$ ), and fit (dashed) as a function of width(left) and length(right). The symbols indicate multiple realizations.

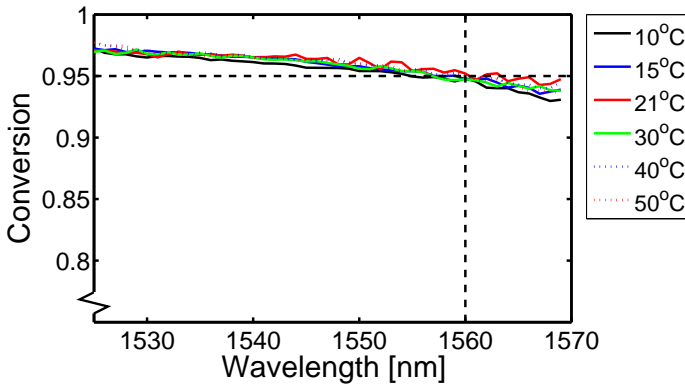
The maximum measured conversion from TE to TM and vice versa occurs at 131  $\mu\text{m}$  length, corresponding to the half beat length between the modes of the converter section. The conversion is back to zero at the full beat length (262  $\mu\text{m}$ ). The maximum conversion for this device is 97%.

The scattered values for the measured conversion are caused by non uniformities in the width along the device, caused in part by deviations in the etch depth, the underetch and the layer thicknesses. A width variation of  $\pm 30$  nm can explain the observed behavior. Previous research has indicated that the width-reproducibility of our EBL is around these values [76, 72].

The right figure shows measurements for multiple realizations of the PC on different wafers, indicated by the different symbols. This shows the reproducibility of the process of the PC. A conversion larger than 95% is obtained in all realizations for the same device dimensions.

Fig. 4.21 shows both the wavelength and the temperature dependence of the PC. A conversion larger than 95% is obtained over a wavelength range larger than 35 nm (limited by the available equipment). The device is insensitive to temperature in the range from 10 to 50°C. This is an important issue as in a PIC with active components heat is generated and the temperatures can rise locally.

The total excess losses of the polarization converter, including input and output tapers, are measured to be  $2.4 \pm 0.3$  dB for TE and  $2.6 \pm 0.3$  dB for TM with respect to a shallow waveguide. The losses can be separated in scattering loss, caused by sidewall roughness of the waveguides, which has a big influence on the narrow deeply etched waveguides, and overlap losses at the junctions (simulated to be approximately 0.25 dB). Most probably extra coupling losses are caused by the non-optimal coupling of the waveguide and the converter because of



**Figure 4.21:** Measured conversion as a function of temperature and wavelength.

the underetch of the access waveguides in the propagation direction. This can be avoided by using a better controlled wet etch and a better masking.

## 4.5 Conclusion

Polarization converters are required for on-chip polarization manipulation. Two generations of polarization converters are demonstrated. The first device shows promising results, but has problems in integrating with active and passive components. These problems are mainly caused by the height difference between the PC and the other components. The PC has a top-cladding that is more than 1  $\mu\text{m}$  thinner than that for the other components on the chip.

A second generation PC is developed that is specifically targeted to be integrated. Here a design is made that has a similar cladding thickness. Thus all the critical definitions can be done at the same level.

Fabricated devices show the feasibility of integration with standard shallow and deep etched waveguides. The device has a maximum conversion of 97%. A conversion larger than 95% is needed for the demonstration of the concepts shown in chapter 1. The conversion is larger than 95% over a large operation window: a wavelength range 35 nm and a temperature range  $>40^\circ\text{C}$ . It is shown that the process is reproducible and a conversion of more than 95% is obtained in all investigated process runs.

These properties demonstrate the capability of a generic integration technology with polarization conversion.

---

# Chapter 5

## Polarization splitters

---

### 5.1 Introduction

In addition to polarization converters, discussed in the previous chapter, polarization splitters (PS) are important devices for on-chip polarization manipulation. Polarization splitters that can be integrated with other functions on a chip are crucial in an integration technology with polarization handling capability.

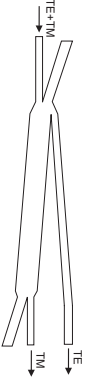
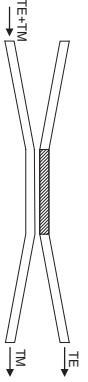
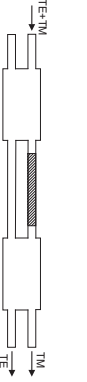

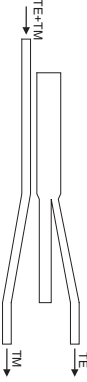
As the name implies, polarization splitters separate the TE and TM modes at the input and route them to different outputs. As these are usually reciprocal devices, they can also be used as polarization combiners. In principle TE and TM signals can be combined from 2 different inputs into one output without any losses. A special case of combiners, which are needed in certain applications (see chapter 7), is the  $2 \times 2$  polarization splitter/coupler. This device works as 100%  $2 \times 2$  coupler for one polarization, but as a 0%  $2 \times 2$  coupler for the other one.

Passive polarization splitting is preferred over active splitting to minimize power consumption and to avoid the need for tuning. For passive splitting, birefringence is required to obtain a difference in propagation for TE and TM polarized light.

The birefringence needed for splitting can be obtained in a number of ways. It can be by loading a waveguide with metal [77, 78]; by using the modal birefringence of the fundamental mode (demonstrated in InP [79, 80] and Si [81, 82]) or of higher-order modes of TE and TM [83, 84]; or by using waveguides with a different geometry for the different polarizations [85, 86]. The most promising devices suited for integration in InP are shown in table 5.1; for all devices the possibility of  $2 \times 2$  splitters is indicated.

As can be seen from the table, the splitting can be obtained by using different principles: split-

Table 5.1: Different passive polarization splitters

Ref.	Principle	Schematic	Fabrication	Performance
A [83]	Mode evolution. Modal birefringence of the first-order mode (only $1 \times 2$ ).		Single shallow RIE etch.	<ul style="list-style-type: none"> <li>• <math>L = 6000 \mu\text{m}</math></li> <li>• <math>\text{SR}_{\text{TE}} = 12.0 \text{ dB}</math></li> <li>• <math>\text{SR}_{\text{TM}} = 13.1 \text{ dB}</math></li> <li>• Loss <math>&lt; 1 \text{ dB}</math></li> </ul>
B [77]	Interference: directional coupler employing birefringence obtained by strip-loading one waveguide with metal ( $2 \times 2$ ).		Au sputtered metal patch, RIE etched shallow waveguides.	<ul style="list-style-type: none"> <li>• <math>L = 1600 \mu\text{m}</math></li> <li>• <math>\text{SR}_{\text{TE}} = 12.2 \text{ dB}</math></li> <li>• <math>\text{SR}_{\text{TM}} = 30 \text{ dB}</math></li> <li>• Loss <math>0.3 \text{ dB}</math></li> </ul>
C [78]	Interference: Mach Zehnder Interferometer employing birefringence obtained by strip-loading one waveguide with metal ( $2 \times 2$ ).		Au sputtered metal patch, RIE etched shallow waveguides.	<ul style="list-style-type: none"> <li>• <math>L = 3300 \mu\text{m}</math></li> <li>• <math>\text{SR}_{\text{TE}} = 16 \text{ dB}</math></li> <li>• <math>\text{SR}_{\text{TM}} = 13 \text{ dB}</math></li> <li>• Loss <math>1.5 \text{ dB}</math></li> </ul>
D [80]	Interference: directional coupler employing modal birefringence of the fundamental system modes ( $1 \times 2$ demonstrated, $2 \times 2$ is possible).		2 step selective wet etch.	<ul style="list-style-type: none"> <li>• <math>L = 3900 \mu\text{m}</math></li> <li>• <math>\text{SR}_{\text{TE}} = 16 \text{ dB}</math></li> <li>• <math>\text{SR}_{\text{TM}} = 17 \text{ dB}</math></li> <li>• Loss <math>&lt; 1.5 \text{ dB}</math></li> </ul>
E [84]	Interference: directional coupler employing modal birefringence of first-order modes ( $1 \times 2$ ).		Single shallow RIE etch.	<ul style="list-style-type: none"> <li>• <math>L = 1100 \mu\text{m}</math></li> <li>• <math>\text{SR}_{\text{TE}} = 13 \text{ dB}</math></li> <li>• <math>\text{SR}_{\text{TM}} = 20 \text{ dB}</math></li> <li>• Loss <math>&lt; 1 \text{ dB}</math></li> </ul>

ting based on mode-evolution in an adiabatic coupler (splitter *A*) [83], which results in tolerant, but very long devices; or splitting based on interference. The splitters based on the latter principle (*B–E*) can be divided in two categories: devices that use metal loading of the waveguides to achieve birefringence (*B, C*) and devices that employ modal birefringence and consist solely of waveguides (*D, E*) that can be etched in a single step. The latter are advantageous over the ones with metal on top, because of the relaxed processing. They have the advantage to be short, have a low loss and a high splitting ratio. A drawback are the very stringent fabrication tolerances.

The device employing the birefringence of the fundamental mode (*D*) has to meet even more strict conditions, as in this case, for both TE and TM, a coupling condition has to be met. TE has to couple through and TM has to have the exact double coupling length to couple through and back again. In the device that uses the modal birefringence of the higher-order modes *E* [84], only one condition has to be met: TE has to couple. This makes the latter device more tolerant and shorter.

Even shorter splitters based on photonic crystal waveguides [87] are reported, but these have the disadvantage of higher losses and more complex processing, making them difficult to integrate.

This makes splitters based on interference the most suitable for the integration with active and passive components.

In this chapter two types of polarization splitters based on interference are described. The principle, design, fabrication and results are discussed.

First a new tolerant  $1 \times 2$  directional coupler based PS is reported. This device has a high splitting ratio, but is very long and hard to integrate. Next a  $1 \times 2$  and a  $2 \times 2$  splitter/coupler based on an Mach Zehnder Interferometer with polarization converters is presented. This device is short and is fully integrateable in the standard active-passive integration scheme.

## 5.2 Directional coupler polarization splitter

As stated before, splitters based on modal birefringence have very stringent fabrication tolerances. Tapering both the waveguides and the coupling region increases the tolerances in directional couplers at the cost of a somewhat increased length [88]. This section will demonstrate a polarization splitter based on modal birefringence with tapered waveguides in combination with a tapered coupling region that has an increased tolerance in fabrication.

### 5.2.1 Principle

In this section the principle of the directional coupler will be explained first, and secondly the implementation of the polarization splitter is explained.



### Directional coupler

A directional coupler consists of two adjacent identical waveguides as depicted in Fig. 5.1. If they are closely spaced, the evanescent field of light injected in one waveguide will excite a mode in the other one and power exchange can take place while propagating [89].

The coupling between the two resonant waveguides can be regarded as an interference of the system modes [90] as shown in the figure. A symmetric (with propagation constant  $\beta_0$ ) and an asymmetric (with propagation constant  $\beta_1$ ) system mode are present in the coupler, they are excited with equal amplitude by the mode in the input waveguide. At the input of the coupler, the modes are in phase, so there is constructive interference in the input waveguide. After propagation over a distance  $L_c$ , the modes will have a phase difference of  $\pi$  and all the power will be transferred to the cross (upper) output waveguide ( $P_x$ ). This distance is the coupling length:

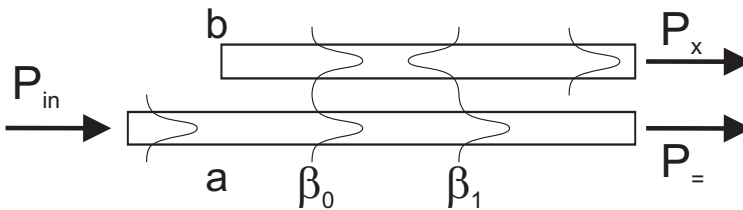
$$L_c = \frac{\pi}{\beta_0 - \beta_1} = \frac{\pi}{2c} \quad (5.1)$$

in which  $c$  is the coupling constant

$$c = \frac{1}{2}(\beta_0 - \beta_1) \quad (5.2)$$

The coupling constant depends exponentially on the gap between the waveguides. With the coupling constant, the power in both waveguides as a function of propagation in the  $z$  direction can be expressed as:

$$\begin{aligned} P_{=} &= \cos^2(cz) \\ P_x &= \sin^2(cz) \end{aligned} \quad (5.3)$$



**Figure 5.1:** Schematic of the directional coupler with the system modes visualized

The modes propagating in the two waveguides in the  $z$ -direction can be expressed as:

$$\begin{aligned} E_{=}(z) &= e_{=}(z)e^{-j\beta_{=}z}, \\ E_x(z) &= e_x(z)e^{-j\beta_x z} \end{aligned} \quad (5.4)$$

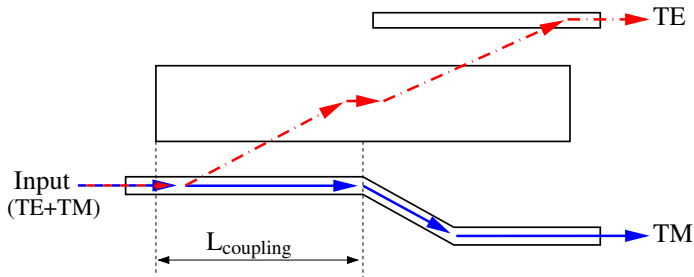
If the waveguides are identical,  $\beta_{=} = \beta_x$  are the propagation constants of the modes in the respective waveguides.  $e_{=,x}$  are the amplitudes of the fields in the corresponding waveguides:

$$\begin{aligned} e_{=}(z) &= \cos(cz), \\ e_x(z) &= j \sin(cz) \end{aligned} \quad (5.5)$$

In this case synchronous coupling is possible and full power exchange between the two waveguides can take place. In the case where  $\beta_{\parallel} \neq \beta_{\perp}$ , asynchronous coupling will occur as the velocity of the modes in the waveguides do not match. This will result in incomplete coupling and only a fraction of the power is transferred to the opposite waveguide [91, 92]. The distance over which coupling takes place is shorter than in the synchronous case.

### Splitter

To use the directional coupler as a polarization splitter, a polarization-dependent coupling is required. The splitting is based on modal birefringence: the propagation constants of the higher-order modes differ significantly for different polarizations. The splitter consists of an asymmetric directional coupler with a narrow and a wide waveguide (Fig. 5.2). The widths are chosen such that the propagation constant of the fundamental mode in the narrow waveguide equals the propagation constant of a higher-order mode in the wide waveguide for one polarization only. Fig. 5.3 shows the calculated mode intensity profiles. It is seen that for TE the fundamental and third-order waveguide modes are resonant, but for TM this is not the case. Only the resonant polarization can couple. Over a distance equal to the coupling length, the light in this polarization is fully transferred from the narrow to the wide waveguide. The same principle is repeated to couple from the wide waveguide to the narrow output waveguide. In this way the third-order mode is converted back to the fundamental mode and a double filtering is achieved. The TM output has to bend away from the wide waveguide to prevent coupling.

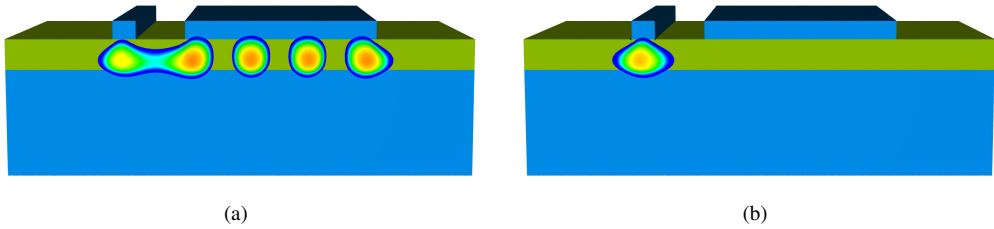


**Figure 5.2:** Principle of the polarization splitter

The resonant modes are determined by calculating the propagation constant as a function of the width at a wavelength of 1555 nm using the effective index method (Fig. 5.5) for a waveguide cross section as shown in Fig. 5.4. This cross section is fully compatible with the layerstack and processing for the first generation polarization converter as treated in section 4.3.

The propagation constants match for  $TE_{00}$  and  $TE_{03}$  for widths of 0.8  $\mu\text{m}$  and 6.9  $\mu\text{m}$  respectively. Furthermore, for a width of 6.9  $\mu\text{m}$  no TM mode is resonant with the fundamental mode for the narrow waveguide.

In fabrication, the width of the waveguides can deviate from the designed width, which causes a change in the propagation constants and thereby destroys the resonance of the modes. This



**Figure 5.3:** Resonant mode for TE (a) and non-resonant mode for TM (b)

leads to a decreased coupling for one polarization and a possibly increased coupling for the other, which will deteriorate the splitting ratio of the device.

To compensate for these errors in fabrication, the wide waveguide is tapered as is shown in Fig. 5.6 [93]. The tapering is possible because from Fig. 5.5 it can be seen that the propagation constant for a higher-order TM mode does not match the propagation constant in the narrow waveguide in a width range more than 750 nm. This large range yields a window for tapering, while preserving the mismatch for TM.

In the tapered device, the coupling region (the position at which the width is such that resonance for TE occurs) shifts along the taper when a width deviation  $\Delta w$  is present. This shift of the coupling region  $\Delta L$  can be calculated in the following way:

$$\left(\frac{d\beta}{dw}\right)_{w_2} \frac{dw}{dz} \Delta L + \left(\frac{d\beta}{dw}\right)_{w_2} \Delta w = \left(\frac{d\beta}{dw}\right)_{w_1} \Delta w \quad (5.6)$$

In this equation  $w_1$  refers to the narrow waveguide,  $w_2$  refers to the wide one. The left part of the equation is the change in the propagation constant in the wide waveguide: the leftmost term is the change in propagation constant  $\beta$  as the coupling region shifts  $\Delta L$  along the taper with taper angle  $\frac{dw}{dz}$ . The second term is the change of the propagation constant as the width changes with  $\Delta w$ . To allow coupling, the propagation constants in both waveguides should remain equal: the right side is the change in propagation constant in the narrow waveguide for a width deviation  $\Delta w$ .

To achieve a constant coupling for a changing width, the coupling constant has to be fixed in the coupling region. Both the position of the coupling region and the coupling constant depend on  $\Delta w$ . The coupling constant depends exponentially on the gap  $g$  between the 2 waveguides, so  $g$  should also be tapered along the length of the device, in such a way that at the coupling region position a fixed gap  $g_0$ , and thus a defined coupling constant, is obtained. The dependence of  $g$  on  $\Delta w$  is:

$$g = g_0 - \Delta w + \frac{dg}{dz} \Delta L \quad (5.7)$$

with the second term on the right-hand side indicating the direct change because of the width deviation and the third term the effect of the tapered gap between the waveguides. These terms

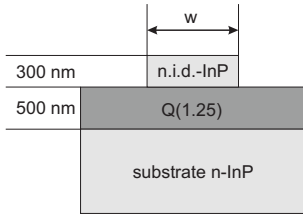


Figure 5.4: Cross section

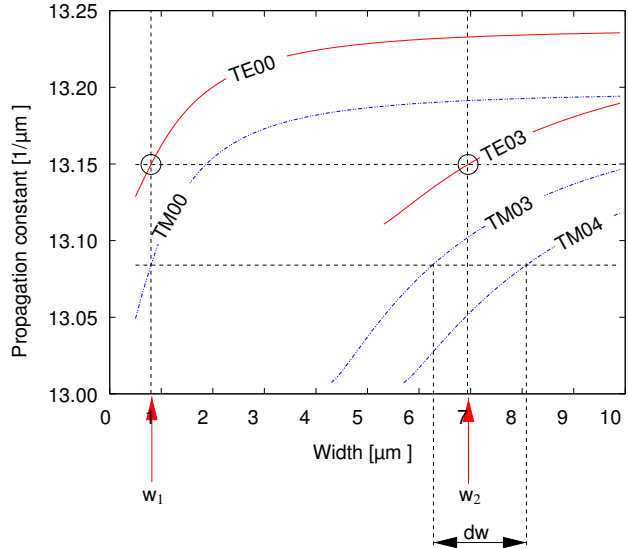


Figure 5.5: Propagation constants as a function of width for the relevant modes.  $w_1$  ( $w_2$ ) is the width of the narrow (wide) waveguide. The horizontal lines indicate matching propagation constants for TE<sub>00</sub> and TE<sub>03</sub>, but not for TM<sub>00</sub> and any other mode.  $dw$  is the range over which there is no matching for TM<sub>00</sub>.

have to cancel out, so  $\frac{dg}{dz} = \frac{\Delta w}{\Delta L}$ . Combining (5.6) and (5.7) results in the relation between the taper angle of the wide waveguide  $\alpha_T = \arctan\left(\frac{dw}{dz}\right)$  and the taper angle of the coupling region  $\alpha_c = \arctan\left(\frac{dg}{dz}\right)$ :

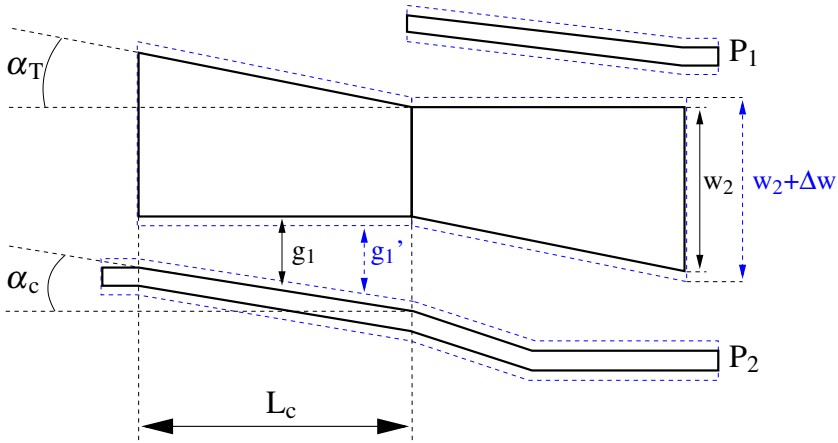
$$\arctan\left(\frac{dg}{dz}\right) = \arctan\left(\frac{dw}{dz}\right) \frac{\left(\frac{d\beta}{dw}\right)_{w_2}}{\left(\frac{d\beta}{dw}\right)_{w_1} - \left(\frac{d\beta}{dw}\right)_{w_2}} \tag{5.8}$$

The derivatives of the propagation constant with respect to the width  $\left(\frac{d\beta}{dw}\right)$  are obtained from the tangent to the corresponding curves in Fig. 5.5.

The total device consists of a cascade of two of these couplers to couple the third-order TE mode to the fundamental mode at the output waveguide. This supplies additional filtering for the unwanted polarization (Fig. 5.6).

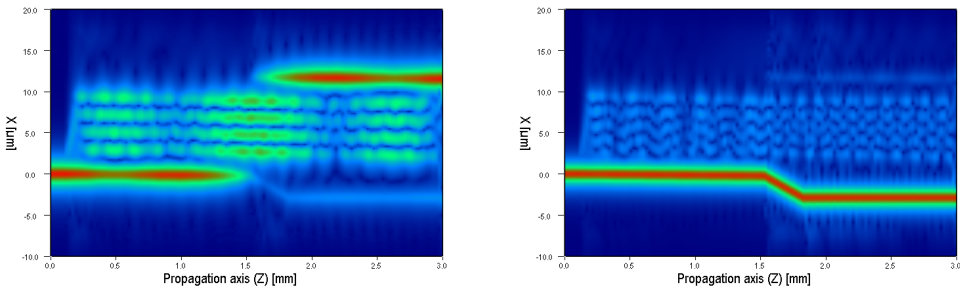
### 5.2.2 Simulations

The polarization splitter is simulated using a 2D Beam Propagation Method (BPM) [38]. The effective index method is used to reduce the problem to 2 dimensions. These simulations are



**Figure 5.6:** Schematic of the polarization splitter, note that the vertical dimensions are enlarged for clarity, the dashed lines visualize the broadening of the waveguides that can be introduced in fabrication.

used to determine the length and to investigate the fabrication tolerances. The propagated field in the splitter for both polarizations for a wavelength of 1555 nm is plotted in Fig. 5.7. It is clearly visible that TE polarized light couples to the central (wide) waveguide and then couples to the upper output waveguide. TM does not couple to the wide waveguide and stays in the lower narrow waveguide.



**Figure 5.7:** Top view of the propagated field in the polarization splitter for TE (left) and TM (right)

In chapter 7 we show that a splitting of more than 95% is needed for a practical polarization diversity scheme [8]. The splitting ratio (SR) of the TE polarization is defined as:

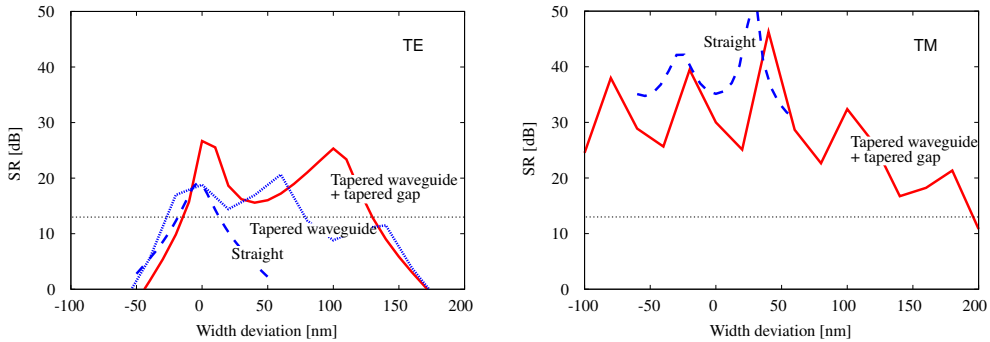
$$SR(TE) = 10 \log \left( \frac{P_1(TE)}{P_2(TE)} \right); \tag{5.9}$$

where  $P_1(TE)$  is the power in the TE-output (output 1) for TE polarized light and  $P_2(TE)$  is the

power in the TM-output (output 2) for TE polarized light. For TM a similar definition is used:

$$SR(TM) = 10 \log \left( \frac{P_2(TM)}{P_1(TM)} \right). \tag{5.10}$$

The SR is calculated as a function of the width deviation<sup>1</sup>. The results are plotted in Fig. 5.8 for both polarizations. The SR for this splitter is compared to a splitter without tapers, and to a splitter without a tapered coupling region, but with a tapered wide waveguide. The dotted



**Figure 5.8:** Simulated polarization splitting ratio as a function of width deviation for TE (left) and TM (right). The dotted line indicates 13 dB splitting ratio

line in Fig. 5.8 indicates an SR of 13 dB (a splitting of 95%). From the graph it is clear that the devices perform well for TM. Because for TM no resonance is present, even for a width range as large as 300 nm no light will couple to the wide waveguide. The possible width range is not as large as expected from the dispersion curves (Fig. 5.5), because also for modes that are not completely resonant, some light can couple. The performance of the device is limited by its behavior for TE. For TE, the straight device is only performing well for a width range of 35 nm. By tapering the wide waveguide the tolerance is improved to 95 nm. By also applying a tapered coupling region according to eq. (5.8), a tolerance range of 145 nm can be reached. The 2 maxima for TE in Fig. 5.8 are present because the device is not only a synchronous directional coupler [94]. In the region of the taper where the propagation constants do not match exactly, only a small deviation from the synchronous waveguide widths is present, because the waveguides are not far apart, the device acts as an asynchronous coupler with changing coupling constant along the taper. The asynchronous coupling plays a role in the performance of the device. As this effect is not taken into account in eq. (5.6), this equation does not fully describe the coupling.

For TM the device is an asynchronous coupler. The large mismatch in propagation constants for the narrow and the wide waveguide results in a short coupling length with a very low coupling constant. This explains the periodic behavior and the large SR for TM.

<sup>1</sup>The width deviation is applied to both the narrow and the wide waveguides, the position of the waveguides is constant, so with increasing the width, the gap is decreased.

**Table 5.2:** Dimensions of the polarization splitter

Parameter	Symbol	Value
Taper length	$L_c$	1325 $\mu\text{m}$
Width input waveguide	$w_1$	0.85 $\mu\text{m}$
Width at the start of the taper	$w_{2s}$	7.27 $\mu\text{m}$
Width at the end of the taper	$w_{2e}$	6.64 $\mu\text{m}$
Gap at the start of the taper	$g_{1s}$	1.81 $\mu\text{m}$
Gap at the end of the taper	$g_{1e}$	2.02 $\mu\text{m}$

### 5.2.3 Design

The 2D BPM simulations in combination with the effective index method can give inaccurate results, especially for the exact coupling length. An optimization of the design is performed by calculating the modal propagation constants of the cross section of the device with a Film Mode Matching (FMM) mode solver [18]. The structure for the FMM simulation is chosen to have the same index difference between the narrow and wide waveguide, and the same coupling strength as used for the BPM calculations, both at the start and endpoint of the taper. With these results, a full-vectorial 3D propagation simulation is done. From this the optimal dimensions are obtained and used for the realization of the component. The optimal dimensions are shown in table 5.2.

### 5.2.4 Fabrication

The devices are fabricated on an InP/InGaAsP layerstack. The layerstack consists of an InP substrate, a 500 nm InGaAsP film layer with a bandgap at a wavelength of 1.25  $\mu\text{m}$  and a 300 nm InP top cladding. This layerstack is fully compatible with the active-passive integration scheme and allows the component to be monolithically integrated with other passive and active devices [73].

A mask is designed on which splitters with a width variation of -100 nm to +100 nm in steps of 20 nm are implemented. The center width of this range is 30 nm wider than in Fig. 5.8, in order to investigate the full tolerance window. All splitters are connected with 100  $\mu\text{m}$  long tapers to 3  $\mu\text{m}$  wide input and output waveguides. The lithographical definition of the waveguides is done in the  $5\times$  reduction wafer stepper as introduced in chapter 3 and used for the first generation polarization converters. It allows a very accurate width control, better than 20 nm on a 800 nm line. This is better than the tolerance needed for the waveguides and the taper, so the tolerances can be investigated.

The etching of the waveguides is done with  $\text{CH}_4/\text{H}_2$  Reactive Ion Etching (RIE). The devices have to be shallowly etched, exactly until the film layer. To ensure the right etch depth, the RIE etch is stopped slightly above the InGaAsP film layer, after which a selective wet etch dip is applied to etch the remaining InP.

An SEM photograph of the cross section is shown in Fig. 5.9. Both the narrow and the wide waveguides are shown. The sidewall roughness which is visible is due to non-optimal process conditions. Reducing the roughness will be important to improve the performance.

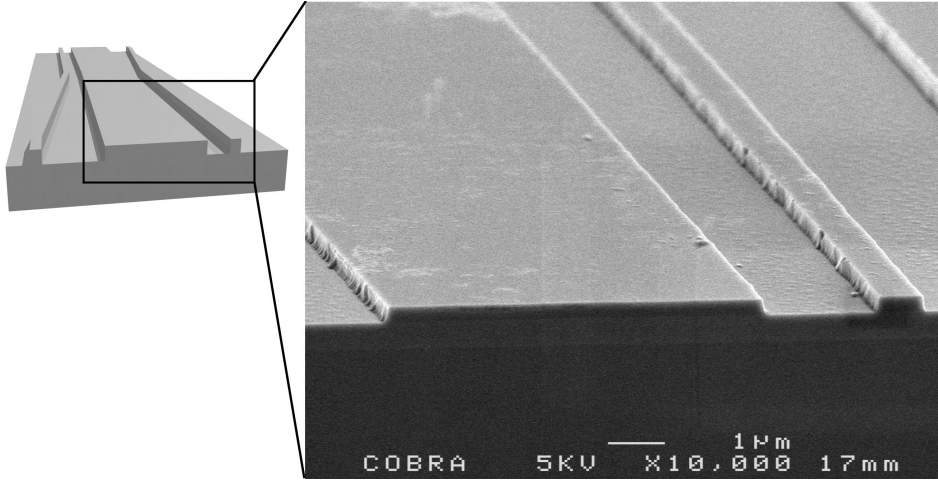


Figure 5.9: SEM photograph of the processed polarization splitter

### 5.2.5 Characterization

Measurements are performed using the setup shown in Fig. 5.10. The device is excited using an EDFA as a source, filtered with a 2.5 nm wide bandpass filter. This averages out the Fabry-Pérot resonances caused by reflections from the facets of the chip, and thus increases the stability. The polarization is selected by a free-space polarizer. The output is imaged onto an InGaAs CCD camera. The obtained image (Fig. 5.11) is analyzed to obtain the power in both outputs simultaneously. The intensity in both ports is obtained, by integrating the intensity values in the lineprofile over a fixed width. From this, the splitting ratio (SR) is determined as defined in eq. (5.9) and (5.10). With this method we can measure a maximum SR of 22 dB, limited by the dynamic range and the noise level of the camera.

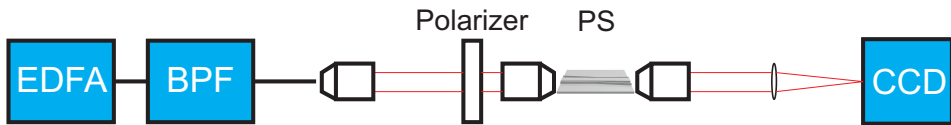
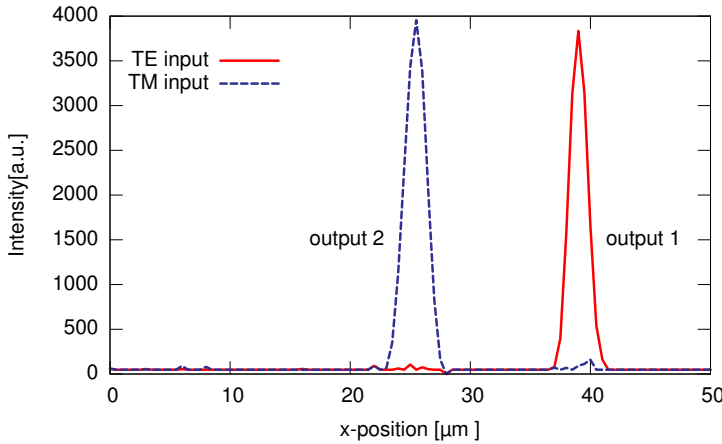


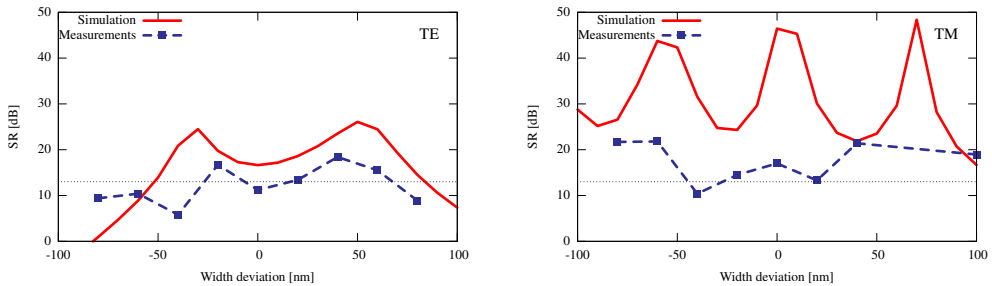
Figure 5.10: Measurement setup used to characterize the polarization splitters.





**Figure 5.11:** Measurement of the power in both outputs using a CCD camera for TE (solid) and TM (dashed) at the input.

The resulting splitting ratio as a function of the width deviation is shown in Fig. 5.12. The measured splitting ratio is compared to the simulated results.



**Figure 5.12:** Splitting ratio measurements at 1560 nm, compared to BPM simulations for TE (left) and TM (right) polarization, the dotted line indicates 13 dB splitting ratio

From the figure it is clear that the measured devices show an SR larger than 13 dB for a large width range. For TM polarized light, the splitter is good for a range of at least 150 nm.

For TE the range is limited to approximately 100 nm. Two maxima are present in the TE results, as is also seen from simulations.

The best splitter (40 nm wider) has an SR of 18 dB for TE and 20 dB for TM, better than any of the devices in table 5.1.

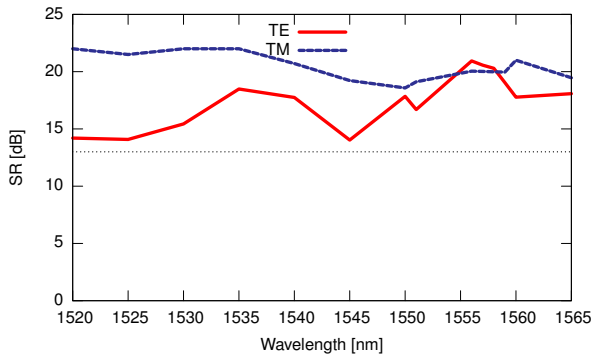
The overall performance as shown in Fig. 5.12 is less than predicted by simulations, most probably caused by scattering from the rough waveguide walls, which can lead to unwanted coupling as will be confirmed by the loss measurements. Because of this, the local minimum

for TE at 0 nm deviation is slightly lower than 13 dB.

The losses are measured using a Fabry-Pérot measurement and are compared to straight waveguides. The 1.5 mm access waveguides to the device have a loss below 0.5 dB for both TE and TM. The excess loss of the device, including input and output tapers, is 3.4–3.6 dB for TE polarized light and 6.5–7.0 dB for TM. In principle, the device should have very low losses, these losses are mainly caused by sidewall roughness as is also visible in Fig. 5.9.

The high losses for TM can be explained because for TM the light will always propagate in the very narrow waveguide, which results in a higher loss. For TE the light will be mostly situated in the wide waveguide with a lower loss. By reducing the roughness, a very wide width range with good polarization splitting can be obtained.

The wavelength dependence of the device having a width of 890 nm (40 nm wider) is measured. The splitting as a function of wavelength is plotted in Fig. 5.13. The device shows polarization



**Figure 5.13:** Splitting ratio as a function of wavelength (width deviation + 40 nm)

splitting better than 14 dB over the entire EDFA wavelength range from 1520 nm to 1565 nm for both polarizations.

The splitter described here cannot be used as a  $2 \times 2$  splitter, the design can be changed to allow such splitting/combining.

A drawback of this design are the large height differences with respect to active and passive components. This leads to similar lithographic difficulties as experienced with the polarization converter in chapter 4.

## 5.3 MZI Polarization splitter

The polarization splitters described in the previous section have the advantage of low loss and high splitting ratios. A drawback is their length (1 to 3 mm) which is large compared to other components on the chip. Furthermore, the devices have to be critically defined at a lower level

than the most active and passive devices, which poses another problem.

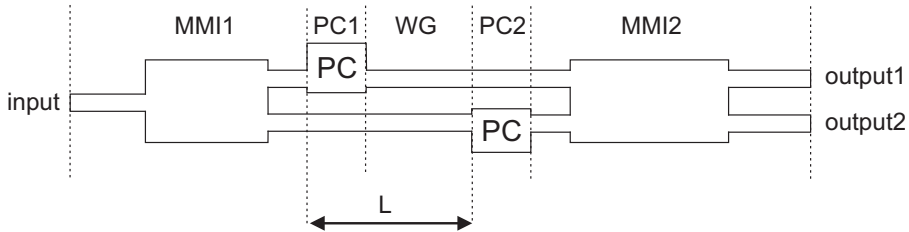
A new design is investigated that solves these problems. This is a compact, 600  $\mu\text{m}$  long, integrated splitter based on polarization converters. It consists solely of passive waveguides and PCs and is thus the device of choice for a generic integration platform in which a polarization converter can be integrated as demonstrated in chapter 4.

Both a  $1 \times 2$  splitter and a  $2 \times 2$  splitter/coupler are studied.

The principle of the device is explained in the next section. It is experimentally demonstrated using the first generation PCs from the previous chapter. By using the second generation PCs, this device is really suitable for active-passive integration. The  $2 \times 2$  splitter is demonstrated using the second generation PCs.

### 5.3.1 Principle

The device consists of a Mach Zehnder Interferometer with polarization converters in both arms, as is depicted in Fig. 5.14. Light coupled into the input waveguide of the first Multi



**Figure 5.14:** Schematic of the MZI polarization splitter/converter

Mode Interference coupler (MMI) is split into the two branches with equal power and phase. In the upper branch a polarization converter is placed that rotates the polarization over  $90^\circ$ , so after this, the orthogonal polarization propagates through this branch.

In the lower branch the light in the original polarization propagates over a distance  $L$  before being rotated in a polarization converter. The birefringence in the waveguides causes a phase shift between light in the arms. This phase shift however is equal in magnitude but opposite in sign for TE and TM. When both signals are combined in the output MMI, the phase difference causes one polarization to appear in one output while the opposite polarization goes to the other output. To achieve the desired splitting, the phase difference between the branches needs to be  $\frac{\pi}{2}$  radians. This is obtained when:

$$L = \frac{\pi}{2(\beta_{\text{TE}} - \beta_{\text{TM}})}, \quad (5.11)$$

where  $\beta_{\text{TE, TM}}$  are the propagation constants for both polarizations.

Apart from  $1 \times 2$  devices, a  $2 \times 2$  polarization splitter/combiner is possible, based on the same concept. The device is depicted in Fig. 5.15. Light coupled into the input waveguide of the first  $2 \times 2$  MMI is split into the two branches with equal power. In this case, the signals in both

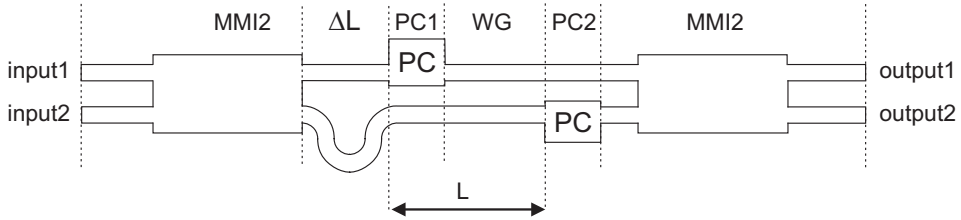


Figure 5.15: Schematic of the MZI polarization splitter/converter

arms have a phase difference of  $\frac{\pi}{2}$ . This phase difference results in destructive interference in one output and constructive in the other. This is depicted in Fig. 5.16. The two polarizations

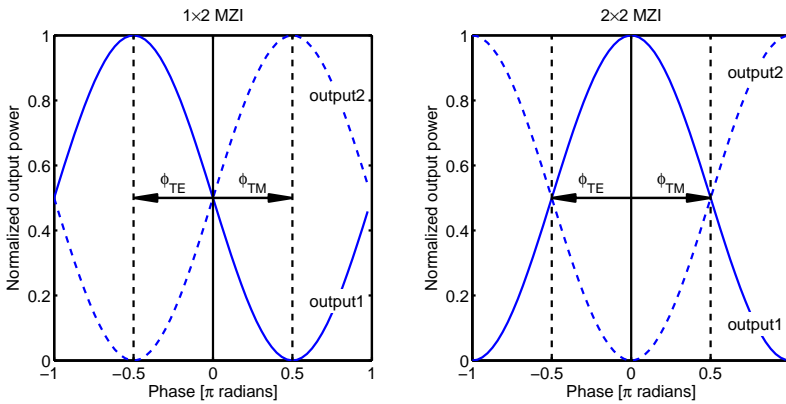


Figure 5.16: Principle of the  $1 \times 2$  and  $2 \times 2$  MZI splitter

always have a phaseshift that is equal in amplitude, but opposite in sign. The arrows in the figure indicate this phaseshift. For the  $2 \times 2$  MZI, no polarization dependent splitting can be obtained. To achieve polarization splitting, an additional polarization independent phaseshift of  $\frac{\pi}{2}$  is required, to obtain the same situation as in the  $1 \times 2$  MZI. In the polarization splitter, in one arm a path length difference  $\Delta L$  is present to achieve this polarization independent phaseshift.

### 5.3.2 Simulation

The polarization splitter circuit is simulated by concatenating the transfer matrices of each of the relevant sections in the device (Fig. 5.14 and 5.15): the input coupler (MMI1/MMI2); a phase compensation section for the  $2 \times 2$  device ( $\Delta L$ ); a Polarization Converter in the upper arm (PC1); straight waveguides of length  $L$  in both branches (WG); a Polarization Converter in the lower arm (PC2) and the output coupler (MMI2). Four different signals can propagate

through the device, which are represented by a 4 element vector:

$$\mathbf{S}_{\text{in}} = \begin{bmatrix} \text{TE}_{\text{upper branch}} \\ \text{TE}_{\text{lower branch}} \\ \text{TM}_{\text{upper branch}} \\ \text{TM}_{\text{lower branch}} \end{bmatrix} \quad (5.12)$$

For the  $1 \times 2$  device, only 2 input signals (TE and TM) are possible. Therefore in that case the "lower branch" input signals are zero.

The transfer matrices of the separate sections indicated in Figs. 5.14 and 5.15 are described next.

The two polarization splitters differ only in the input section. From eq. (5.16) on, the splitters are the same. The input section is described first for the  $1 \times 2$  splitter. Here an input  $1 \times 2$  MMI (MMI1) is present, the transfer of this section is:

$$\mathbf{T}_{\text{MMI}_1} = \begin{bmatrix} \sqrt{k_{1\text{TE}}} & 0 & 0 & 0 \\ \sqrt{k_{1\text{TE}}} & 0 & 0 & 0 \\ 0 & 0 & \sqrt{k_{1\text{TM}}} & 0 \\ 0 & 0 & \sqrt{k_{1\text{TM}}} & 0 \end{bmatrix} \quad (5.13)$$

Here  $k_{1\text{TE}}, k_{1\text{TM}}$  are the coupling constants of the MMI coupler for the respective polarization. The coupling constant is defined as the fraction of the power in the crossed output of the MMI. For a  $1 \times 2$  MMI both outputs are equal as it is a fully symmetric device.

In the case of the  $2 \times 2$  PS, the input section consists of an input  $2 \times 2$  coupler (MMI2) and the phase compensation ( $\Delta L$ ). The transfer matrix of the input coupler is:

$$\mathbf{T}_{\text{MMI}_2} = \begin{bmatrix} \sqrt{k_{2\text{TE}}} & j\sqrt{1-k_{2\text{TE}}} & 0 & 0 \\ j\sqrt{1-k_{2\text{TE}}} & \sqrt{k_{2\text{TE}}} & 0 & 0 \\ 0 & 0 & \sqrt{k_{2\text{TM}}} & j\sqrt{1-k_{2\text{TM}}} \\ 0 & 0 & j\sqrt{1-k_{2\text{TM}}} & \sqrt{k_{2\text{TM}}} \end{bmatrix} \quad (5.14)$$

where  $k_{2\text{TE}}, k_{2\text{TM}}$  are the coupling constants of the MMI coupler for the respective polarizations. The transfer matrix for the phase compensation is:

$$\mathbf{T}_{\text{WG}\Delta L} = \begin{bmatrix} 1 & 0 & 0 & 0 \\ 0 & e^{j\beta_{\text{TE}}\Delta L} & 0 & 0 \\ 0 & 0 & 1 & 0 \\ 0 & 0 & 0 & e^{j\beta_{\text{TM}}\Delta L} \end{bmatrix} \quad (5.15)$$

Here  $\Delta L$  is the additional path length in the lower arm. Ideally this should result in a phase difference of  $\pi/2$  for both polarizations.

From this point on, both the  $1 \times 2$  and  $2 \times 2$  PS are equal. Both polarization splitters have a PC in the upper arm for section  $PC_1$ :

$$\mathbf{T}_{PC_1} = \begin{bmatrix} \sqrt{1-c_{PC}} & 0 & j\sqrt{c_{PC}} & 0 \\ 0 & 1 & 0 & 0 \\ j\sqrt{c_{PC}} & 0 & \sqrt{1-c_{PC}} & 0 \\ 0 & 0 & 0 & 1 \end{bmatrix} \quad (5.16)$$

where  $c_{PC}$  is the conversion of the individual PCs, the transfer of the lower arm is 1.

The next section consists of the birefringent waveguides (WG) of a length  $L$ . The birefringence causes a phase difference of  $(\beta_{TM} - \beta_{TE})L$  between the polarizations. The transfer matrix of this section is:

$$\mathbf{T}_{WG} = \begin{bmatrix} e^{j\beta_{TE}L} & 0 & 0 & 0 \\ 0 & e^{j\beta_{TE}L} & 0 & 0 \\ 0 & 0 & e^{j\beta_{TM}L} & 0 \\ 0 & 0 & 0 & e^{j\beta_{TM}L} \end{bmatrix} \quad (5.17)$$

In section  $PC_2$ , a polarization converter is present in the lower branch. The transfer of this section is described by:

$$\mathbf{T}_{PC_2} = \begin{bmatrix} 1 & 0 & 0 & 0 \\ 0 & \sqrt{1-c_{PC}} & 0 & j\sqrt{c_{PC}} \\ 0 & 0 & 1 & 0 \\ 0 & j\sqrt{c_{PC}} & 0 & \sqrt{1-c_{PC}} \end{bmatrix} \quad (5.18)$$

In the final section (MMI2), a  $2 \times 2$  MMI is used to combine the signals from both branches. The transfer matrix of this output MMI is the same as in eq. (5.14).

Using these matrices, the outputvector can be calculated. For the  $1 \times 2$  splitter the complete transfer is:

$$\mathbf{S}_{1 \times 2out} = \mathbf{T}_{MMI_2} \cdot \mathbf{T}_{PC_2} \cdot \mathbf{T}_{WG} \cdot \mathbf{T}_{PC_1} \cdot \mathbf{T}_{MMI_1} \cdot \mathbf{S}_{in} \quad (5.19)$$

For the  $2 \times 2$  splitter, it is:

$$\mathbf{S}_{2 \times 2out} = \mathbf{T}_{MMI_2} \cdot \mathbf{T}_{PC_2} \cdot \mathbf{T}_{WG} \cdot \mathbf{T}_{PC_1} \cdot \mathbf{T}_{WG_{\Delta L}} \cdot \mathbf{T}_{MMI_2} \cdot \mathbf{S}_{in} \quad (5.20)$$

The  $1 \times 2$  splitter is described in detail, the  $2 \times 2$  splitter is investigated in the same way. For the  $1 \times 2$  splitter with TE polarized light at the input, the output vector is:

$$\mathbf{S}_{1 \times 2out} (TE_{in}) = \begin{bmatrix} \sqrt{k_{1TE}(1-c_{PC})} (\sqrt{k_{2TE}} + j\sqrt{1-k_{2TE}}) e^{jL\beta_{TE}} \\ \sqrt{k_{1TE}(1-c_{PC})} (\sqrt{k_{2TE}} + j\sqrt{1-k_{2TE}}) e^{jL\beta_{TE}} \\ \sqrt{k_{1TE}c_{PC}} (-\sqrt{1-k_{2TM}} e^{jL\beta_{TE}} + j\sqrt{k_{2TM}} e^{jL\beta_{TM}}) \\ \sqrt{k_{1TE}c_{PC}} (-\sqrt{1-k_{2TM}} e^{jL\beta_{TM}} + j\sqrt{k_{2TM}} e^{jL\beta_{TE}}) \end{bmatrix} \quad (5.21)$$

The converted part of the output power (TM polarized in this case) at the upper output (output 1) can be calculated as:

$$P_{TMout1} = k_{1TE} c_{PC} \left( \sqrt{k_{2TM}} e^{j(L\beta_{TM} + \frac{\pi}{2})} - \sqrt{1-k_{2TM}} e^{jL\beta_{TE}} \right) \cdot \left( \sqrt{k_{2TM}} e^{-j(L\beta_{TM} + \frac{\pi}{2})} - \sqrt{1-k_{2TM}} e^{-jL\beta_{TE}} \right) \quad (5.22)$$

This yields:

$$P_{\text{TM}_{\text{out}1}} = k_{1\text{TE}} c_{\text{PC}} \left\{ 1 - \sqrt{k_{2\text{TM}}(1 - k_{2\text{TM}})} 2 \cos \left( L(\beta_{\text{TM}} - \beta_{\text{TE}}) + \frac{\pi}{2} \right) \right\} \quad (5.23)$$

and similarly for the lower output (output 2):

$$P_{\text{TM}_{\text{out}2}} = k_{1\text{TE}} c_{\text{PC}} \left\{ 1 - \sqrt{k_{2\text{TM}}(1 - k_{2\text{TM}})} 2 \cos \left( -L(\beta_{\text{TM}} - \beta_{\text{TE}}) + \frac{\pi}{2} \right) \right\} \quad (5.24)$$

The unconverted part (TE) in both outputs is the same and is in this case:

$$P_{\text{TE}_{\text{out}1,2}} = k_{1\text{TE}} (1 - c_{\text{PC}}) \quad (5.25)$$

The power of TE polarized light from the outputs is only zero if the conversion in the arms  $c_{\text{PC}} = 1$ . For a lower conversion, the non-converted part is split equally over the two branches. With this model the performance of the MZI-PS can be investigated as a function of the parameters of the various components.

The simulation results as a function of the conversion ( $c_{\text{PC}} = \frac{P_{\text{TM}}}{P_{\text{TE}} + P_{\text{TM}}}$ ) of the polarization converters in the arms, with TE polarized light at the input, are shown in Fig. 5.17(a). In the simulations all other sections are assumed to have ideal performance.

Fig. 5.17(b) shows the splitting ratio and the net circuit conversion as a function of the conversion of the PCs in the arms.

The Splitting Ratio of the splitter defined as the total power in the desired port (output1 for TE input) divided by the total power in the undesired port:

$$\text{SR}(\text{TE}_{\text{in}}) = 10 \log \left( \frac{P_{\text{TM}_{\text{out}1}} + P_{\text{TE}_{\text{out}1}}}{P_{\text{TM}_{\text{out}2}} + P_{\text{TE}_{\text{out}2}}} \right) \quad (5.26)$$

For a splitting ratio larger than 13 dB, a conversion  $c_{\text{PC}}$  above 90% is needed.

The net circuit conversion  $c_{\text{PS}}$  is the conversion of the whole polarization splitter circuit, this is the conversion obtained at the desired output port (port 1 for TE input):

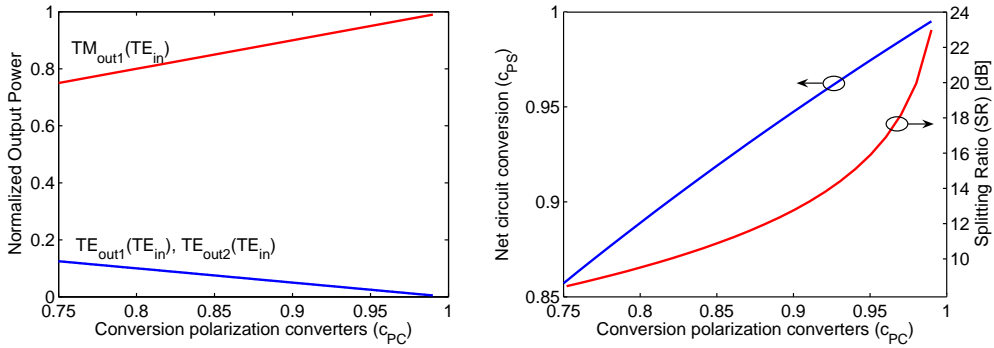
$$c_{\text{PS}}(\text{TE}_{\text{in}}) = \frac{P_{\text{TM}_{\text{out}1}}}{P_{\text{TE}_{\text{out}1}} + P_{\text{TM}_{\text{out}1}}} \quad (5.27)$$

This  $c_{\text{PS}}$  is larger than 95%, for  $c_{\text{PC}}$  above 90%, because the unconverted part is split equally over the outputs.

The conversion of the polarization converters depends critically on the width as is shown in chapter 4 an accuracy of  $\pm 60$  nm is needed for  $c_{\text{PC}} > 90\%$ , so these devices are considered to be the limiting factor in the fabrication.

The dependence on the other parameters is investigated as well. In these simulations, the conversion  $c_{\text{PC}}$  is 95%. The influence of the coupling coefficient of the couplers is considered to be less important as MMIs can be made tolerant to width deviations [27].

In the  $1 \times 2$  case, the input coupler will always be balanced as this is a symmetric device, this cannot cause a problem. The  $2 \times 2$  splitter however, can be unbalanced, and apart from this,



(a) Output power from output ports 1 and 2 ( $TM_{out2}(TE_{in})$  is always zero in this ( $L = \frac{\pi}{2(\beta_{TE} - \beta_{TM})}$ ) case)

(b) Conversion and splitting ratio.

**Figure 5.17:** Simulated performance of the integrated polarization splitter/converter as a function of the polarization conversion of the converters in the branches for TE input.

have a polarization dependent coupling constant. A polarization dependent output coupler will result in a difference in splitting for TE and TM.

In the  $2 \times 2$  PS, the problem is larger. Here a  $2 \times 2$  MMI is used both in the input and in the output. The MMI at the input couples the orthogonal polarization with respect to the output MMI. In Fig. 5.18(a) the influence on the coupling constant of both couplers on the output SR is plotted for the  $2 \times 2$  case. The SR is above 13 dB if the coupling constant is better than 0.42. The length of the waveguides between the PCs determines the phaseshift between the polarizations and hence the splitting. The SR as a function of length is plotted in Fig. 5.18(b). The length has to be accurate within  $\pm 0.1\pi$  rad (corresponding to approximately  $\pm 10 \mu\text{m}$  up to  $\pm 15 \mu\text{m}$ , depending on the choice of the waveguides).

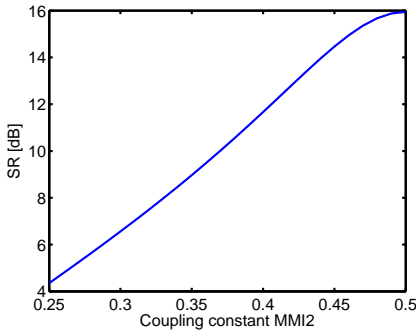
For the  $2 \times 2$  case, the splitting ratio as a function of the length of the phase compensation section ( $\Delta L$ ) is shown in Fig. 5.18(c). The path length difference has to be correct within  $\pm 25$  nm to achieve a splitting ratio larger than 13 dB. The obtained phase difference is somewhat different for TE and TM, but as the pathlength difference is only 120 nm, the error in the phase is smaller than  $5 \cdot 10^{-3}$  rad.

The used components in the splitter operate over a broad wavelength range, thus the wavelength dependence is expected to be small. This is confirmed by the simulated wavelength dependence, plotted in Fig. 5.18(d). The device has an SR above 15 dB for the whole wavelength range from 1500–1600 nm.

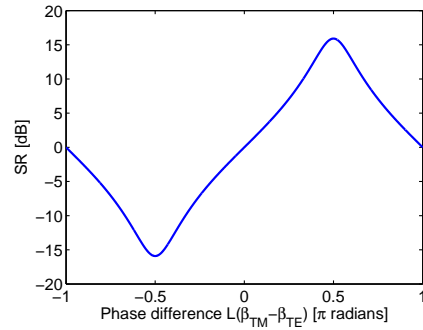
### 5.3.3 Design

A first design is made, compatible with the first generation PC, using waveguides in the splitter that are  $2 \mu\text{m}$  wide, and deeply etched into a layerstack having a 300 nm InP topcladding, and a 500 nm Q(1.25) waveguide layer on an InP substrate. This yields a  $\Delta\beta = \beta_{TM} - \beta_{TE}$  of

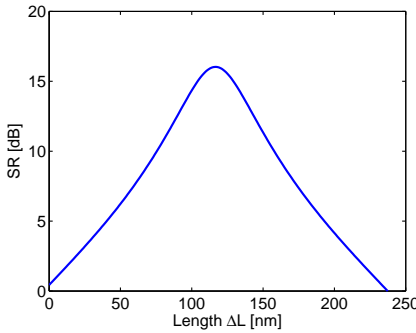




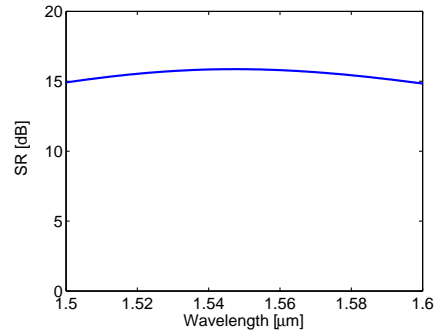
(a) Splitting ratio as a function of the coupling constant of the output MMI.



(b) Splitting ratio as a function of length of the waveguides.



(c) Splitting ratio as a function of the phase compensation path length  $\Delta L$ .



(d) Splitting ratio as a function of wavelength.

**Figure 5.18:** Splitting ratio for the splitter in case of deviations of the parameters. All simulations are done for  $c_{PC} = 0.95$ .

$-0.030 \mu\text{m}^{-1}$ , so for this device an offset  $L$  between the converters of  $52 \mu\text{m}$  is needed. The total length of the device, including in- and output MMIs, is about  $600 \mu\text{m}$ .

This splitter can be made shorter by using smaller MMIs. By using the new PCs, the device can be made compatible with active-passive processing. This is demonstrated in the second design.

### 5.3.4 Fabrication I

The processing of the first design is equal to that of the first generation PC (section 4.3). The MZI-PS and the separate polarization converters are processed on the same chip. A photograph of the finished device is shown in Fig. 5.19. Some roughness is visible on the sidewalls of the waveguides, this is mainly caused by a non-optimal lift-off process for the waveguide

definition.

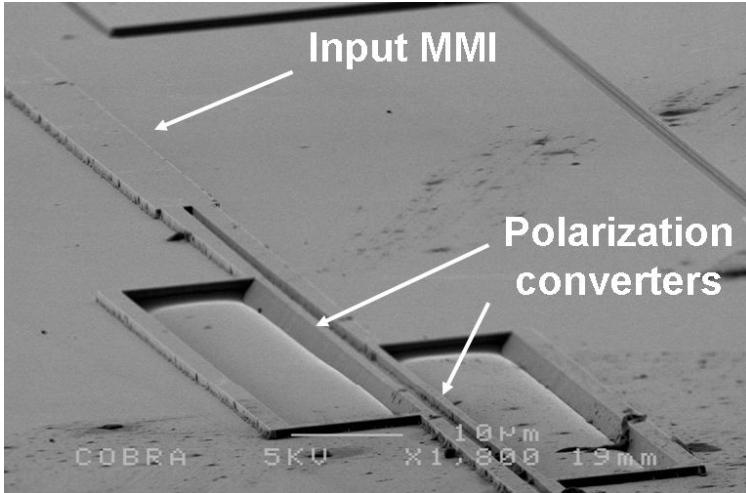


Figure 5.19: SEM photograph of the input MMI and 2 Polarization converters in the arms of the MZI

### 5.3.5 Characterization I

The splitter is examined with the setup shown in Fig. 5.20. The devices are excited using an

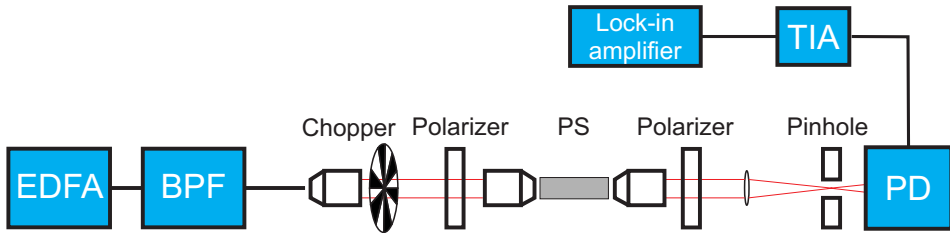


Figure 5.20: Setup used for characterization of the polarization splitter and converter. BPF: Bandpass filter, PD: Photodiode, TIA: Trans impedance amplifier

EDFA as a source and a 2.5 nm wide bandpass filter, set to a central wavelength of 1555 nm. This signal is chopped and the polarization is fixed using a polarizer. The light is coupled into the chip and the output is coupled through a polarizer to determine the output polarization. It is detected with a photodiode connected to a transimpedance amplifier and a lock-in amplifier.

From chapter 4, section 4.3 it can be seen that a conversion of 95% can be achieved for a width of 0.75  $\mu\text{m}$ . The polarization converters used in the splitter are 0.8  $\mu\text{m}$  wide. According to the

measurements in the previous chapter, this converter will have a conversion of 88%. The full splitter/converter is measured and the results are listed in table 5.3.

**Table 5.3:** Measured output powers and resulting Splitting Ratio and Conversion

	$P_{\text{out}}(\text{TE}_{\text{in}})$ [a.u.]	$P_{\text{out}}(\text{TM}_{\text{in}})$ [a.u.]
TE <sub>out1</sub>	4.5	1.3
TE <sub>out2</sub>	2.6	47.3
TM <sub>out1</sub>	43.7	2.5
TM <sub>out2</sub>	3.4	4.9
conversion $c_{PS}$	91%	91%
SR	9.1 dB	11.4 dB

The conversion  $c_{PC}$  of the converters in the branches for TE (or TM) can be calculated by dividing the output power in TM (TE) in both outputs by the total power from both outputs, under the assumption that both PCs are equal:

$$c_{PC}(\text{TE}_{\text{in}}) = \frac{P_{\text{TM}_{\text{out1}}} + P_{\text{TM}_{\text{out2}}}}{P_{\text{TE}_{\text{out1}}} + P_{\text{TE}_{\text{out2}}} + P_{\text{TM}_{\text{out1}}} + P_{\text{TM}_{\text{out2}}}} \times 100\% \quad (5.28)$$

This conversion equals 87%. The net conversion of the device  $c_{PS}$  is 91% for both polarizations. This is less than the expected net conversion from Fig. 5.17(b). This is probably caused by an imperfect output coupler.

The resulting splitting ratio, defined in eq. (5.26), is 9.1 dB for TE<sub>in</sub> and 11.4 dB for TM<sub>in</sub>. The low splitting ratio is caused by a deviation from the actual  $L$  to the optimal  $L = \frac{\pi}{2(\beta_{\text{TE}} - \beta_{\text{TM}})}$ . Probably caused by deviations from the calculated propagation constants of the modes.

The difference in splitting ratio for TE and TM is caused by the polarization dependence of the output coupler. The coupler is not a perfect 50-50 coupler for TM.

The excess losses are  $5.0 \pm 0.1$  dB compared to a straight waveguide. This is mainly caused by the waveguide roughness which is visible in Fig. 5.19.

These problems can be corrected for in a next realization.

### 5.3.6 Design and fabrication II

A next generation of the PS is designed in which the problems from the previous realization are corrected. The PCs are replaced by the second generation devices, discussed in section 4.4. All waveguides in this realization have a topcladding to be fully compatible to the active-passive scheme.

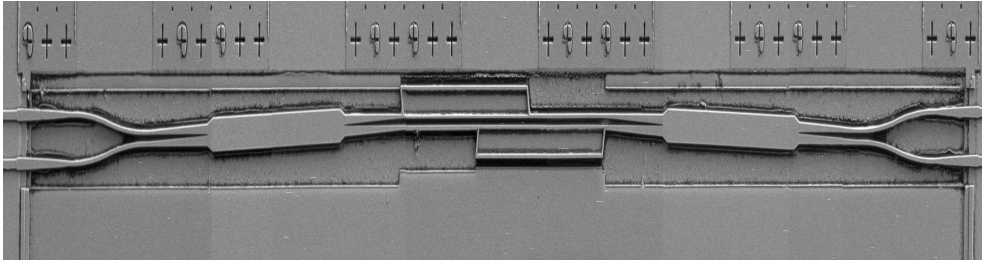
In addition to a  $1 \times 2$  device, a  $2 \times 2$  polarization splitter is demonstrated, based on the same concept.

The waveguides used in the splitter are  $1.21 \mu\text{m}$  wide to couple to the PCs without tapers, and have single-mode waveguides. They are deeply etched into a layerstack having a 1500 nm InP topcladding, and a 500 nm Q(1.25) waveguide layer on an InP substrate. Because of the thicker topcladding, the birefringence is reduced with respect to the first realization. In this

case  $\Delta\beta = \beta_{\text{TM}} - \beta_{\text{TE}} = -0.020 \mu\text{m}^{-1}$ , so for this device an offset  $L$  between the converters of  $78 \mu\text{m}$  is needed. The total length of the device, including in- and output MMIs is about  $800 \mu\text{m}$  for the  $2 \times 2$  case, a similar  $1 \times 2$  device is  $630 \mu\text{m}$  long.

The device is coupled with tapers to  $2.5 \text{ mm}$  long  $3 \mu\text{m}$  wide, shallow waveguides (etched  $100 \text{ nm}$  into the waveguide layer) at both the in- and outputs.

The pathlength difference of  $120 \text{ nm}$  ( $\triangleq \pi/2$ ), in the arms of the MZI is achieved by tilting the in- and output MMI coupler at an angle of  $1^\circ$ , see Fig. 5.21. In this way sharp deeply etched bends, in which unwanted polarization conversion can occur [24], are avoided.



**Figure 5.21:** SEM photograph of the  $2 \times 2$  MZI-PS. The vertical dimensions are  $3 \times$  enlarged for clarity.

The fabrication is based on the processing for the second generation polarization converters using Electron Beam Lithography (EBL) for the lithographical definition. In this case, the complete PS, including the MMI couplers, is defined using EBL. The access waveguides are defined by optical lithography to which the EBL pattern is aligned as shown in chapter 3.

The device spans multiple EBL writefields and critical alignment is needed per field.

### 5.3.7 Characterization II

The integrated splitter is examined on a setup similar to Fig. 5.10, only an extra polarizer is used to determine the output polarization. As before, the output is detected with an InGaAs CCD camera to observe the 2 outputs at the same time. The obtained image is analyzed to obtain the power in both outputs simultaneously by integrating the intensity in both ports over a fixed width. From this, the splitting ratio (SR) is determined.

Devices with increasing  $L$  are fabricated, but show random behavior. A  $2 \times 2$  splitter with a designed  $L$  of  $78 \mu\text{m}$  shows polarization splitting with a splitting ratio of  $7 \text{ dB}$  for TM and  $4 \text{ dB}$  for TE. The polarization converters in the arms have a conversion of  $88\%$ .

According to Fig. 5.17(b) this conversion should yield a splitting ratio of approximately  $13 \text{ dB}$ . The low splitting ratio can be explained by a deviation from  $\pi$  in the phase difference between TE and TM. A phase error in the branches can have multiple causes. First of all, due to the proximity of the waveguides inside the splitter, in the EBL exposure their width can be influenced.

Furthermore, the device spans multiple EBL writefields and critical alignment is needed per field. Misalignment can cause small gaps or offsets in the connection between the fields, these

can yield to phase-errors in the arms.

The difference between the splitting for TE and TM can only result from polarization dependent MMIs, although the MMIs are designed for polarization independent splitting.

## 5.4 Conclusions

Polarization splitters are crucial components for on-chip polarization manipulation. Polarization splitting based on interference is the method of choice for short, low loss, and high splitting ratio devices. Because of the lack of material birefringence, modal birefringence needs to be employed to achieve splitting.

Two different classes of devices are presented. One is a 3 mm long directional coupler. Tapered waveguides together with a tapered coupling region are shown to enhance the tolerance. From simulations it follows that a width deviation of 145 nm yields a splitting ratio of at least 13 dB. This is an increase in the width tolerance of more than a factor of 4 as compared to a straight device.

The best realized splitter has a splitting ratio of 18 dB for TE and 20 dB for TM. The devices show a splitting ratio of 13 dB over a width range of approximately 100 nm and for a wavelength window larger than 45 nm. The measurements agree well with the simulations. Reduction of the sidewall roughness will lower the losses, improve the polarization splitting of the device, and increase the width tolerance.

This splitter has the disadvantage that it is hard to integrate with other components.

Another type of splitter is presented, based on an MZI with polarization converters. This device is shorter (below 1 mm) and has the ability to be integrated with active and passive components.

The device is simulated using the transfer matrix method. Splitting ratios larger than 13 dB are expected for conversion ratios of the converters of more than 90%. The first generation MZI-PS shows a splitting of 9.1 dB for TE, 11.4 dB for TM and a conversion of 91%. This device uses a thin topcladding of the waveguides and is therefore not suited for easy integration. A next generation device is fabricated, suited for integration. The  $2 \times 2$  splitter made in this case shows a maximum splitting of 7 dB and a conversion close to 90%.

This device shows that the generic platform for polarization manipulation can be obtained by only adding the polarization converter to the standard technology.

---

# Chapter 6

## Wavelength converters

---

### 6.1 Introduction

The POLARIS wavelength converter, introduced in chapter 1, is used as a vehicle for the demonstration of the generic technology with polarization handling capability. In this chapter the (polarization dependent) wavelength converter is described, that forms the building block for the POLARIS polarization diversity wavelength converter.

A large variety of wavelength converters is described in literature [10]. In this thesis, integrated SOA - Mach Zehnder Interferometer (SOA-MZI) based wavelength converters (WLC) will be regarded as they are compact, stable, give low chirp and high extinction ratio [95, 96].

Apart from wavelength conversion, SOA-MZIs offer interesting properties for all-optical switching. Their multi-functional nature can be applied to achieve more all-optical functions such as 2R regeneration, and logical functions such as a full-adder. Here the focus will be on the design and characterization of the MZIs used as wavelength converters. These WLCs can be used as building blocks for the POLARIS concept as demonstrated in the next chapter.

The present chapter will discuss two generations of designs of the SOA-MZI. The first design is used to test the feasibility of the active-passive technology for wavelength conversion and will be used to demonstrate the POLARIS principle in the chapter 7. The second generation is an array of SOA-MZI switches suited for packaging. In this array the integration of spot size converters in the generic technology is demonstrated.

In this chapter, first the principle of an SOA-MZI wavelength converter is discussed. Next the design and fabrication and the static and dynamic characterization of the first generation device is treated. Problems are identified and solved in a next generation. The second generation

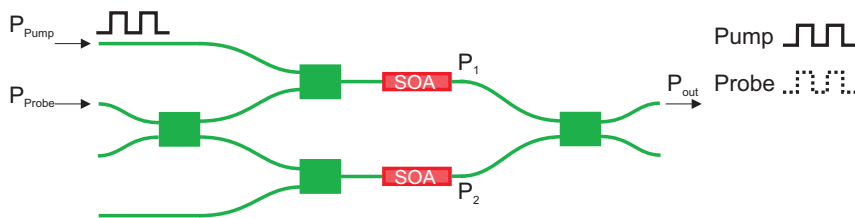
device demonstrated is the SOA-MZI array suited for packaging. On the packaged device both static and dynamic measurements are performed.

## 6.2 Principle

The principle of operation for a wavelength converter using cross-phase modulation (XPM) is based on refractive index changes caused by the optical input signal. The change in refractive index results in a change in phase, this is exploited in a Mach Zehnder interferometer with SOAs in each branch, as shown in Fig. 6.1.

Light from a continuous wave (CW) laser is split in the multimode interference coupler (MMI) and distributed over the two branches. It is combined again in the output MMI after passing through the SOAs. The phase difference from both arms determines whether the signals combine destructively or constructively. The currents in the SOAs are chosen to balance the interferometer. This results in destructive interference in the bar-port when no input signal is present.

If a signal is injected in one of the interferometer arms, the injected power changes the refractive index of the SOA in this arm, and thus the phase. A phase change of  $\pi$  results in constructive interference, and the light from the CW laser can now reach the output port. If the input signal is modulated, the modulation will be transferred to the CW-light.



**Figure 6.1:** Wavelength converter based on XPM

Co-directional conversion (the pump and probe signals propagate in the same direction, as depicted in Fig. 6.1) has a better performance (higher extinction ratio (ER)), larger input dynamic range) at high speed than counter-directional operation, because the interaction time between the two signals in the SOA is longer with co-directional propagation [11].

However, in the co-propagation case both the pump and the probe are present in the output and tuneable filters are needed to separate them. These filters are expensive and difficult to integrate. Conversion to the same wavelength is impossible in this way, but is desirable to keep full flexibility to provide the implicit regeneration of the wavelength converter and to strip the frequency and phase noise from the data signal.

A simple model of the MZI is used to give insight into the functioning of the MZI and to draw conclusions on the effect of the SOA parameters on the conversion. In the model, all MMIs are exact 50–50 splitters, and both SOAs are assumed to be equal: they have the same length

$L$ , unsaturated gain  $g_0$ , and saturation power  $P_{sat}$ .

The modal gain  $g_{net}$  in the SOA for an input power  $P$  can be expressed as:

$$g_{net} = \frac{g_0}{1 + P/P_{sat}}, \quad (6.1)$$

At a power  $P_{sat}$ , the gain of the SOA has decreased 3 dB, caused by depletion of carriers in the device at high power levels. This depletion results in a change of the refractive index so that the phase of the optical signals changes. This is expressed in the alpha-factor, which couples the refractive index change to a change in gain:

$$\alpha = -\frac{4\pi}{\lambda} \frac{dn}{dN} \bigg/ \frac{dg_{net}}{dN}, \quad (6.2)$$

where  $n$  is the refractive index,  $N$  is the carrier density in the SOA and  $g_{net}$  the modal gain.

The outputpower  $P_{out}$  can be calculated:

$$P_{out} = \frac{1}{2} \{P_1 + P_2 + 2\sqrt{P_1 P_2} \cos(\Delta\phi)\} \quad (6.3)$$

where  $P_1$  is the power at the output of the upper SOA:

$$P_1 = 1/4 P_{probe} e^{\frac{g_0 P_{sat} L}{P_{sat} + 1/2 P_{pump} + 1/4 P_{probe}}} \quad (6.4)$$

$P_2$  is the total power at the output of the lower SOA:

$$P_2 = 1/4 P_{probe} e^{\frac{g_0 P_{sat} L}{P_{sat} + 1/4 P_{probe}}} \quad (6.5)$$

and  $\Delta\phi$  is the phase difference between the arms of the MZI:

$$\Delta\phi = 1/2 \alpha L g_0 P_{sat} \left( \frac{1}{P_{sat} + 1/2 P_{pump} + 1/4 P_{probe}} - \frac{1}{P_{sat} + 1/4 P_{probe}} \right) \quad (6.6)$$

Some conclusions that can be drawn from the model are: a large  $g_0$  will yield a large  $P_{out}$ . For a large  $g_0$ , a high current is required, it is a trade-off as the maximum current will be limited by heating effects.

Long SOAs will lead to large phase shifts. The length of the SOAs will be limited by the amount of Amplified Spontaneous Emission (ASE). In a too long SOA, the ASE itself will saturate the device and furthermore contribute to the noise.

A low  $P_{sat}$  will require low pump powers to saturate the SOA.

A high  $\alpha$  will result in a large phase change, the  $\alpha$ -factor is highest for wavelengths longer than the gain-peak [46, 97].

High extinction ( $P_{out}=0$  when  $P_{pump}=0$ ), can only be obtained when both arms are identical:  $P_1$  is exactly equal to  $P_2$  in case  $P_{pump}=0$ , and no additional phasedifferences are present between the arms.

It has to be noted that  $g_0$ ,  $P_{sat}$  and  $\alpha$  usually are polarization dependent and that the conversion will therefore be sensitive to the polarization.



## 6.3 First generation

The first generation SOA-MZI is shown in this section. This device is developed for the STOLAS (Switching Technologies for Optically Labeled Signals) project. In that project, a packet-switched data network is used. The data and the label for the packets are orthogonally modulated: On-Off Keying (OOK) is used for the data, the label is an Frequency Shift Keying (FSK) modulated signal on top of this. In order to preserve the label while traveling through the network, a limited Extinction Ratio (ER) is needed to have sufficient power in the zero-level of the data. Therefore an ER of 6 dB is expected at the input of the WLC [98]. At the output of the WLC, the ER cannot be large either. The output ER can always be reduced by slightly unbalancing the MZI arms by changing the SOA currents.

An important feature of the WLC is the ability to strip the label from the converted signal, for this purpose also conversion to the same wavelength is required.

### 6.3.1 Design and fabrication

The integration of MZIs is a first step towards the realization of a POLARIS wavelength converter. The design of the MZI is based on the device in [16]. The  $1 \times 2$  MMIs are replaced by  $2 \times 2$  MMIs. In the case of a  $2 \times 2$  MZI, destructive interference is obtained in the bar-port (required for non-inverting operation) when the interferometer is balanced. This will enhance the bandwidth with respect to a  $1 \times 1$  MZI [16, 99]. In the  $1 \times 1$  case, a balanced MZI will yield constructive interference in the output port, and a  $\pi$  phaseshift is needed in one of the arms to obtain destructive interference. To obtain this phase difference, the SOAs have to be set to different currents, this condition is expected to be wavelength dependent.

The design of the device is presented in Fig. 6.2(a). The in- and outputs are situated on one facet, all ports are looped back using shallowly etched bends. The waveguides are placed at a pitch of 250  $\mu\text{m}$ , this allows the usage of a fiber-array in which the fibers are placed at this pitch.

The device is fabricated on bulk Q(1.55) active-passive material. The standard processing described in chapter 3, is used except for the passivation and metallization. For the passivation 300 nm  $\text{SiN}_x$  is used, no planarization is done. Sidewall coverage is obtained by sputtering of the contacts in stead of evaporating. Fig. 6.2(b) shows a photograph of the finished chip.

### 6.3.2 Static characterization

A suitable operation point of the SOA-MZI based wavelength converter is first determined with static measurements. All measurements reported here are performed on an MZI with 1000  $\mu\text{m}$  long SOAs in the branches. The 1000  $\mu\text{m}$  is a trade-off between long SOAs for a large phase-shift and short devices to limit the ASE.

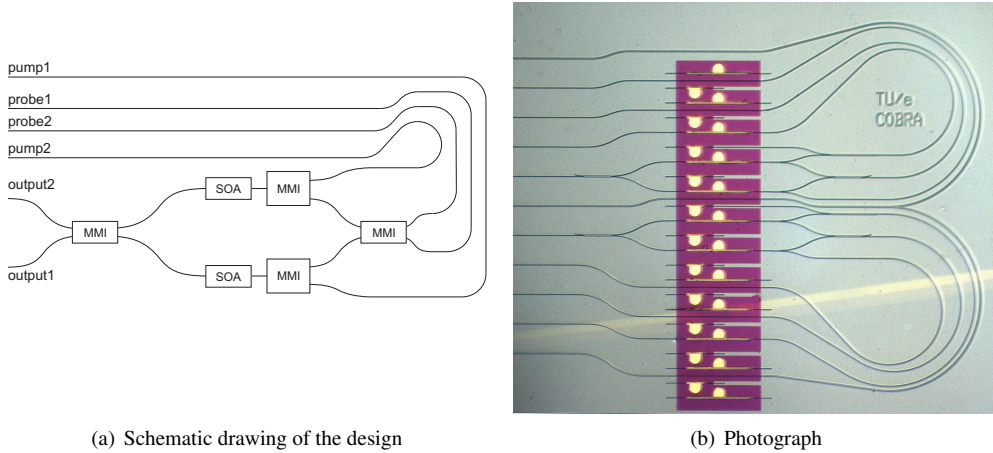


Figure 6.2: Mask design and fabricated MZI wavelength converter.

**Experimental setup**

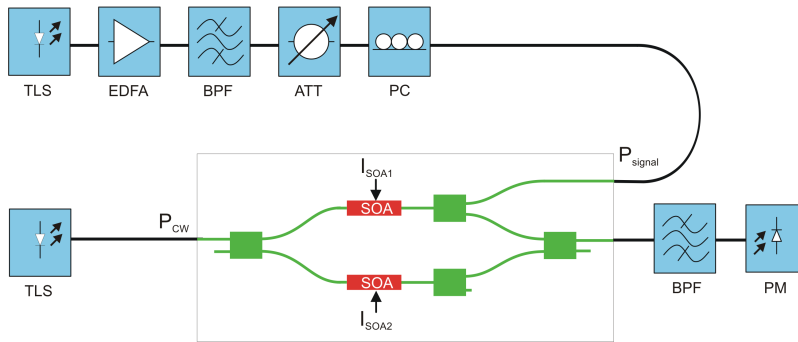
The experimental setup used to perform the static measurements is shown in Fig. 6.3. The CW probe with wavelength  $\lambda_{CW}$  is generated by a Tunable Laser Source (TLS). The light coming from this TLS has a well defined polarization. Since the operation of the SOA-MZI WLC is sensitive to the state of polarization of the probe, a polarization maintaining fiber-array is used to feed the light to the input of the device. The used array consists of cleaved fibers, having a large spotsize, which leads to an overlap loss of approximately 10 dB.

Another TLS is used for the pump signal with wavelength  $\lambda_s$ . The pump is amplified by means of an Erbium Doped Fiber Amplifier (EDFA) followed by a Band Pass Filter (BPF) for suppressing the ASE noise before launching it in the MZI-WLC. At the output, a second BPF (centered on  $\lambda_{CW}$ ) is used to filter the ASE noise from the SOAs in the WLC, and the reflected pump signal. The output is detected using a photodiode.

The measurements are performed in contra-propagation (pump and probe propagate in opposite direction), this configuration has the advantage over co-propagation that it allows conversion to the same wavelength.

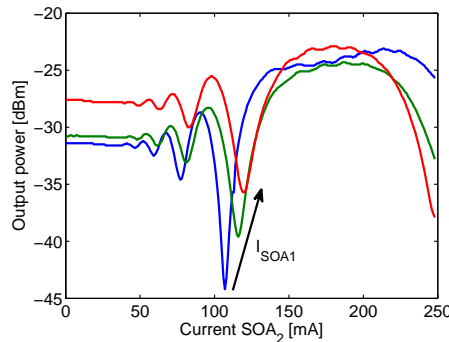
**Electrical switching**

An optimal working point has to be determined. This point is obtained by fixing the current of one SOA (SOA<sub>1</sub> in this case), while sweeping the current of the second SOA. By sweeping this current, the carrier density and thus the phase and the amplitude of the light traveling through this SOA are affected. No pump signal is present, hence by combining the light with that coming from the SOA<sub>1</sub> in the output MMI, an interference curve can be obtained as shown in Fig. 6.4.



**Figure 6.3:** Measurement setup for static measurements

In this graph, the interference curves for different currents of  $SOA_1$  are present: 130 mA, 150 mA and 180 mA. The probe has a power  $P_{CW}$  is 2 dBm, measured at the input of the fiber-array, and a wavelength of 1560.62 nm. The chip is placed on a heatsink that is kept at a constant temperature of 10°C.



**Figure 6.4:** Switching curve for the wavelength converter,  $\lambda_{CW} = 1560.61$  nm,  $P_{CW} = 2$  dBm and  $T=10^\circ\text{C}$ .  $I_{SOA1} = 130$  mA, 150 mA and 180 mA.

A current of 130 mA for  $SOA_1$  yields the largest interference. By setting the current in  $SOA_2$  to 107 mA, non-inverting operation is achieved.

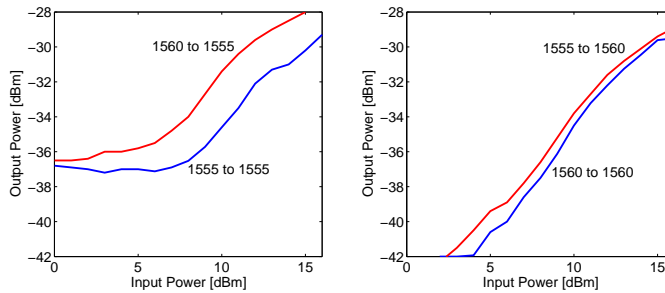
The difference between the currents in the SOAs in this working point indicates that the SOAs are not equal and the interferometer is not balanced. Full destructive interference is not obtained in this case, and a limited ER is expected.

### Optical switching

For the optical switching curves, the currents of both SOAs and the probe power are set, the pump power is changed. The current of SOA<sub>1</sub> is  $I_{SOA1} = 130$  mA, for SOA<sub>2</sub>  $I_{SOA2} = 107$  mA as determined before. The probe power  $P_{CW}$  is increased to 5 dBm into the fiber array to achieve a higher output ER. The optical switching curves are obtained for the conversion between 4 combinations of the wavelengths of 1555.75 nm and 1560.61 nm (Fig. 6.5).

For an input pump power range changing between 9 and 15 dBm, an output ER of at least 6 dB is obtained for all wavelengths.

The need for high pump power is mainly caused by the usage of cleaved fibers, which results in high overlap losses (about 10 dB per fiber-chip coupling).



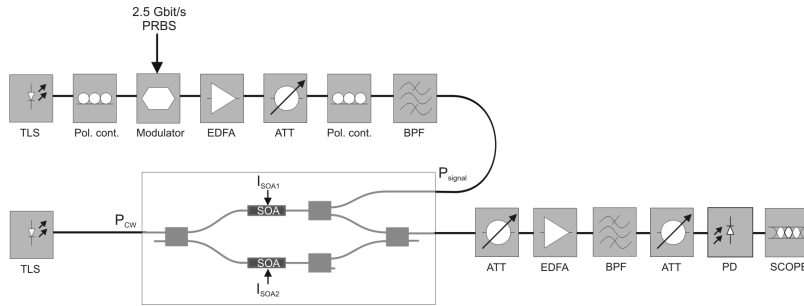
**Figure 6.5:** Optical switching curves for the Mach-Zehnder Interferometer, the label indicate the conversion of  $\lambda_{pump}$  to  $\lambda_{probe}$

The largest modulation depth is obtained for a probe wavelength of 1560 nm, because the current setting for the MZI is optimized for this wavelength and complete interference is only obtained at this wavelength. This confirms that the device is unbalanced, therefore the setting cannot be optimal for 1555 nm. Furthermore a higher  $\alpha$  is expected for higher wavelengths.

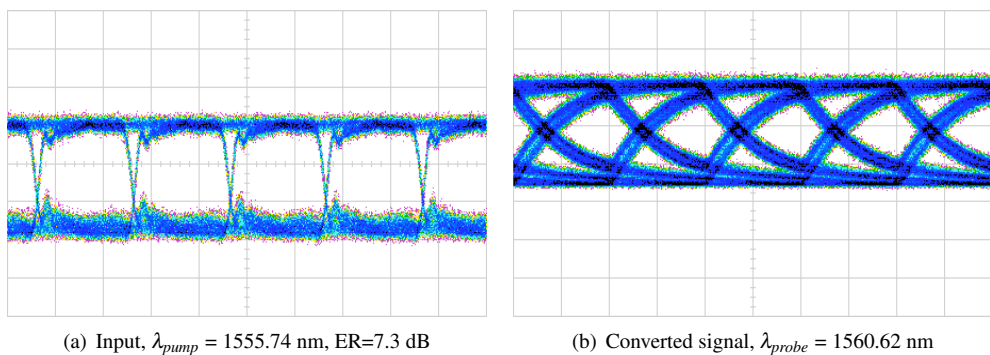
#### 6.3.3 Dynamic characterization

Dynamic all-optical wavelength conversion is performed in non-inverting operation for counter-propagation. A schematic of the setup is shown in Fig. 6.6. The setup is similar to the setup used for the static experiments. The difference is that the pump signal is modulated with a 2.5 Gb/s PRBS signal. The output power is controlled with an attenuator and the signal is amplified and detected using a photodiode and an oscilloscope.

A new working point is determined for which non-inverting operation is obtained at higher output powers. The currents in the SOAs are 187 mA for SOA<sub>1</sub> and 241 mA for SOA<sub>2</sub>. For all measurements the input ER is approximately 7 dB (6.5 dB for 1560.62 nm to 7.3 dB for 1555.74 nm). The input eye is shown in Fig. 6.7.



**Figure 6.6:** Measurement setup for testing the WLC in counter-propagation



(a) Input,  $\lambda_{pump} = 1555.74$  nm, ER=7.3 dB

(b) Converted signal,  $\lambda_{probe} = 1560.62$  nm

**Figure 6.7:** Eye diagrams (200 ps/div)

The device performance depends on the polarization of the input signals. The polarization is optimized to obtain maximum eye opening. The eye diagram of the converted signal at 1560 nm is plotted in Fig. 6.7(b). From the eye diagrams the extinction ratio is measured to be 10.5 dB. From the output eye it can be seen that the rise and fall times are large. They are approximately 400 ps, which is equal to the bittime for 2.5 Gb/s. Furthermore the pattern effect is visible as a double line. This is also a result of the slow behavior of the device.

### Rise and fall times

For operation at higher bitrates, shorter rise times are required. To investigate the behavior, the converted bitpattern (Fig. 6.8(a)), and the amplified pump signal (Fig. 6.8(b)) is recorded. Furthermore the Cross Gain Modulated (XGM) signal is obtained by biasing only one SOA in the MZI. As expected, also this signal (Fig. 6.8(c)) recovers at the same speed.

To understand the origin of this behavior, the SOA is simulated using a rate-equation model [100]. First a XGM simulation with one SOA is done for two values of the injection current.

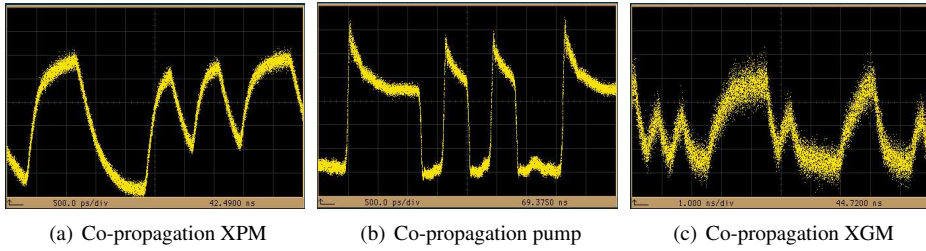
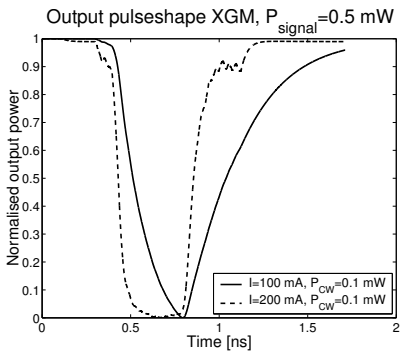


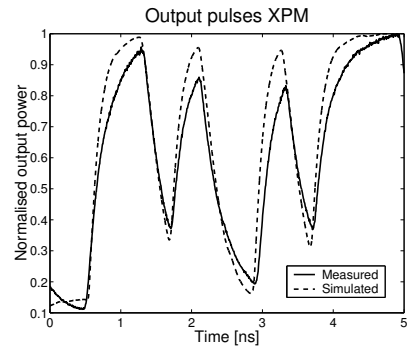
Figure 6.8: Output bitpatterns

The measured input signal is used for the simulation. The results are plotted in Fig. 6.9(a). The simulation shows that for low currents, no fast response can be obtained.

With the settings for the low current, the XPM performance is investigated. The simulated output pulse is compared to the measurement and plotted in Fig. 6.9(b). A similar behavior is visible.



(a) Simulated output pulse shape as a function of current in the SOA for XGM



(b) Simulated output pulse shape compared to measured pulse

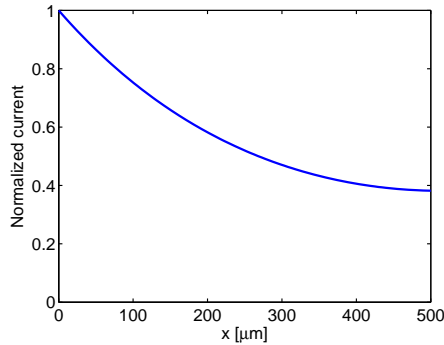
Figure 6.9: Simulated output pulse shapes

The speed of the device is clearly influenced by the current density, and the measured slow response is most probably caused by limited current injection into the SOA. The reason for the bad injection is a problem in the design of the metal contact of the SOA. This contact consists of a 20  $\mu\text{m}$  wide metal stripe with thickness of 250 nm. The gold is the significant conductor, so the resistance of this 500  $\mu\text{m}$  long line (a 1000  $\mu\text{m}$  long SOA contacted in the middle) is:

$$R = \rho_{Au} \frac{L_{SOA}}{wt} = 5\Omega \tag{6.7}$$

This is a high value compared to the resistance of the SOA, which is approximately 7  $\Omega$  at

150 mA. The current distribution in the SOA is approximated by a resistor network, this yields an approximate current distribution as shown in Fig. 6.10. This distribution is the cause that outer regions of the SOA are only slightly pumped. Thus the current density is too low in a part of the device to restore the carrier concentrations fast enough.



**Figure 6.10:** Current distribution inside SOA

To overcome this problem in the next realization, the contacts have to be enlarged to a width of 100  $\mu\text{m}$  and a thickness of more than 1  $\mu\text{m}$ . This will lower the resistance to below 0.5  $\Omega$ . For this case the current distribution will be equally spread along the device.

## Conclusions

An MZI-WLC is realized in an active-passive integration technology. The device is characterized both statically and dynamically. Conversion up to 2.5 Gb/s is found. In counter-propagation the device is working well as ER and output power are concerned. The speed limit of the counter-propagation with respect to co-propagation is not an issue at the low bitrates used in these measurements. The speed in this case is limited by other, more severe, parameters and is not influenced by the propagation direction.

A large rise and fall time is encountered, most probably due to low current injection as can be seen from simulations.

The device performance depends on the polarization of the input signal. The switching speed of the MZI can be improved by decreasing the resistance of the contacts yielding a better current distribution in the device.

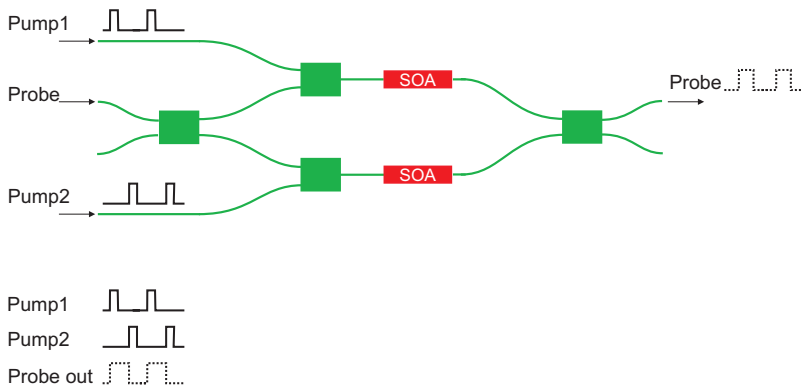
Furthermore by operating in a push-pull configuration [101], the switching speed can be increased. This is not possible with the current device, so a different design is needed in which a pump signal can be input in both arms.

## 6.4 Second generation

The second generation SOA-MZIs are developed for the MUFINS (MUlti - Functional INtegrated arrays of interferometric Switches) project. In this project the multi-functional nature of the SOA-MZI is employed to obtain several optical functions [102, 103, 104]. For these functions multiple MZI switches are needed and hence an array of 4 switches is integrated with spot size converters. In order to use the device in system experiments, the device has to be packaged. For this a number of additional features are integrated as discussed in chapter 3. The device is operated as a wavelength converter in this section.

### 6.4.1 Design and fabrication

A single switch consists of an MZI with SOAs in the arms as shown in Fig. 6.11.  $2 \times 2$  MMIs with angled sides are used to reduce reflections. In both arms an additional coupler is placed to inject a pump signal into the arms to use the device in a push-pull operation [101] as indicated in the figure. For push-pull operation, the delay between the two pump signals determines the output pulse. First a pulse is sent into input Pump1, the carriers are depleted almost instantaneously, and a phase shift occurs. The carriers start to recover slowly, but after a time  $\Delta t$ , shorter than the bit-time, a pulse is sent to port Pump2, and the phases are equalized. This results a fast pulse at the output.

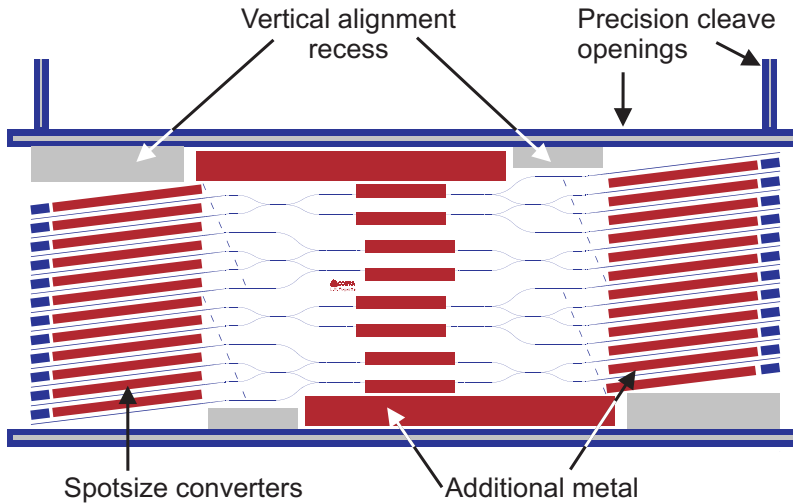


**Figure 6.11:** Schematic overview of the SOA-MZI switch

The chips are designed for flip-chip mounting on a submount that will be placed on a motherboard in which fiber-assemblies are coupled to the in- and outputs of the switches. This is similar to hybrid integration [55]. The mask layout of the chip is shown in Fig. 6.12. In the figure the additional features are indicated.

At all in- and outputs Spot Size converters (SSC) are present. The SSC consists of a vertical and a horizontal taper and is designed to have a spotsize that matches that of a cleaved single mode fiber as is shown in chapter 2.





**Figure 6.12:** Mask layout of the SOA-MZI switch

For the vertical alignment, oxide pillars are placed on the submount. On the InP chip a well-defined level is needed. The bottom of the waveguide layer is used for this. Recesses are etched into the chip using a selective wet etch.

To horizontally align the chip, the chip is pushed to stops on the submount. To ensure exact dimensions of the chip, as well as exact distance from the edge to the in- and outputs, precision cleave openings are defined lithographically at the same mask as the waveguides. After the chip is finished, the cleaving can be initiated at these precision openings.

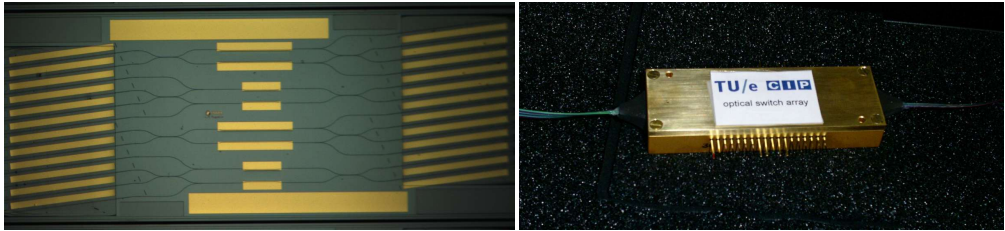
The SOAs in the arms consist of a 2  $\mu\text{m}$  wide shallow waveguide with an active region of 9 strained InGaAs barriers and 8 unstrained InGaAs Quantum Wells (QW) inside a Q(1.25) waveguide layer, with a confinement factor of 0.19 for TE. Bandfilling of the QWs is required to shift the operation wavelength to the desired 1550 nm.

As shown in chapter 2, the waveguide enters the SOA at an angle of  $10^\circ$  to avoid reflections from the active-passive butt-joint [44].

The chip is kept in place by soldering the metal contacts onto thick gold solderbumps on the submount. Because of this, the contacts on the chip are just thin evaporated metal pads, as a good thermal and electrical contact is ensured by the solder. For a good adhesion of the metal contacts to the solder, the metal has to be planarized. Polyimide is used to passivate and planarize the contacts of the SOAs. Apart from these contacts, additional metal is present to enlarge the metal surface and thus enhance the adhesion of the chip.

The full fabrication process is described in section 3.4. A photograph of the finished chip is shown in the left of Fig. 6.13.

### 6.4.2 Packaging

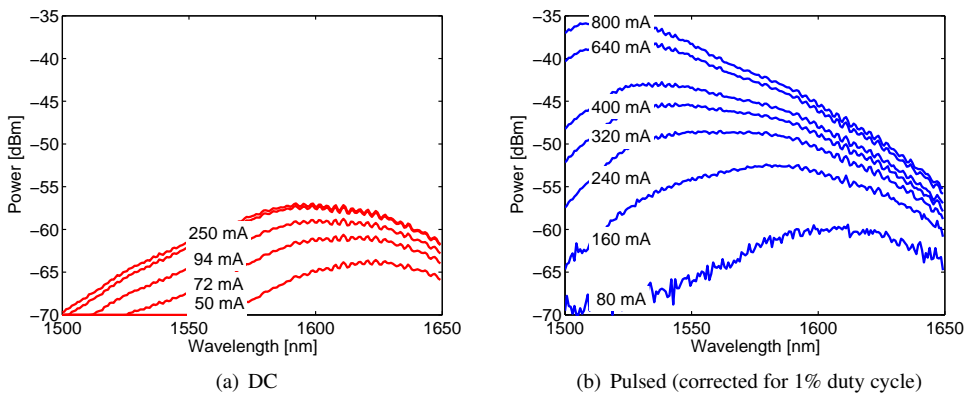


**Figure 6.13:** Photograph of the integrated array of 4 MZI switches (left) and the packaged array (right)

The finished chip is mounted P-side up on a different submount. In this way the chip can be quickly packaged to assess the functioning, but an optimal performance is not possible in this case. In a flip-chip mount it is easy to get rid of the heat at the P-contact. By placing the chip P-side-up, the heat transfer is severely compromised. Furthermore the electrical contact is not good enough to obtain a good uniform injection into the SOAs. Nevertheless for the experiments shown here, the chip packaged in this way (Fig. 6.13 right) can be used.

### 6.4.3 Static characterization

The array consists of 1250  $\mu\text{m}$  long SOAs in the MZI. The InGaAs Quantum Wells used are designed to employ bandfilling to shift the peak wavelength to the right operation wavelength around 1550 nm [46]. The shift is investigated by recording ASE spectra different currents (Fig. 6.14(a)).



**Figure 6.14:** ASE spectra of the packaged MZI switch for different bias conditions.

The peak wavelength shifts over approximately 40 nm because of bandfilling, but due to heating the shift is not large enough to obtain the peak around 1550 nm. The desired current density to completely employ the bandfilling effect cannot be obtained as around 200 mA thermal roll-off starts to occur. It is anticipated that the device will have low gain and will not show proper cross-phase modulation around 1550 nm as the  $\alpha$ -factor is low at the blue side of the gain peak. This poor thermal behavior is most probably caused by the non-optimal mounting of the chip.

Pulsed current injection is used to investigate the thermal characteristics further. 100 ns long pulses with a repetition rate of 100 kHz (i.e. 1% duty cycle) are used to reduce heating of the SOA. The recorded ASE spectra are shown in Fig. 6.14(b). Now a significantly larger shift of more than 100 nm is obtained. The gain-peak can be shifted to approximately 1520 nm. Furthermore the maximum power is increased for more than 20 dB. This demonstrates the feasibility of this device to operate with high gain for wavelengths around 1550 nm.

### Thermal Crosstalk

The MZIs are integrated in an array and the thermal crosstalk between them is an issue, when adjacent MZIs are operated. For the investigation of the thermal crosstalk, a TLS is set to a wavelength of 1580 nm and a power level of 0 dBm. The laser is modulated to be able to detect the outputsignal with a lock-in amplifier. Two SOAs in MZI<sub>3</sub> (Fig. 6.15) are biased to have complete destructive interference in one of the outputs. In this case  $I_{\text{SOA}5} = 200$  mA,  $I_{\text{SOA}6} = 206$  mA. The current in the adjacent SOA (SOA<sub>4</sub>) is swept and the resulting interference is observed, by recording the output power in both outputs.

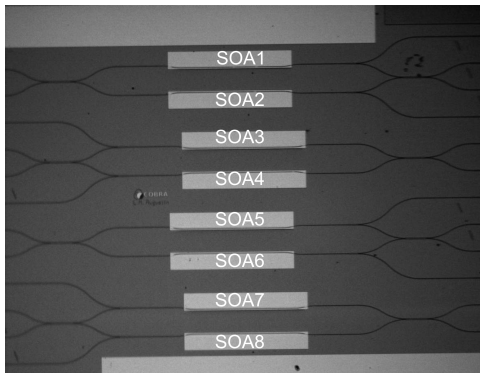


Figure 6.15: Photograph of the integrated array

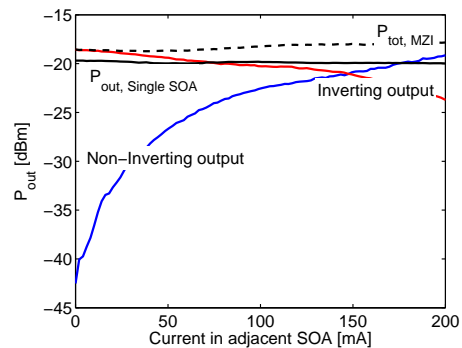


Figure 6.16: Thermal crosstalk in MZI switches

The heating of the branches of the MZI leads to a destroyed interference condition. Biasing the adjacent SOA causes a significant phaseshift between  $\pi/2$  and  $\pi$ .

The gain in the SOA is not much influenced. The black solid line in Fig. 6.16 shows the transmission through SOA<sub>5</sub> when SOA<sub>6</sub> is not biased. The gain is reduced by approximately 0.2 dB.

Thermal crosstalk causes an additional phaseshift in the arms of the MZI, but the effect on the gain is small ( $\approx 0.2$  dB decrease). In an array in which all SOAs are switched on, a steady state can be reached and the additional phase error can be corrected for. In that case the outermost arms of the outer MZIs will have a different temperature than the rest of the array and these MZIs will be unbalanced. In a flip-chip package the heat will be removed through the P-contact and the heating of the adjacent MZI will be reduced.

#### 6.4.4 Electrical switching

For using the MZI in a system, the device has to be operated under DC bias. For determining a working point, one SOA is biased as high as possible without entering the thermal roll-off: at 200 mA, the current into the other SOA is swept. At the input, a Tunable Laser Source (TLS) is used, modulated at 1 kHz to detect the light using a lock-in amplifier. A polarization controller is used to set the polarization for maximum output power. The input power  $P_{\text{probe}}$  is set to 0 dBm.

The interference curve is recorded for input wavelengths of 1550 nm and 1580 nm (which is the maximum wavelength possible with the used equipment, and is closest to the gain-peak). The resulting switching is plotted in Fig. 6.17.

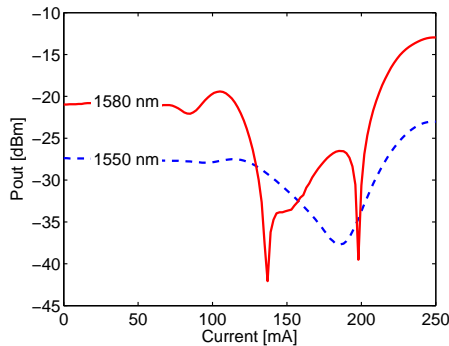


Figure 6.17: Electrical switching

From this plot it is seen that a large extinction ratio ( $\approx 25$ dB) is found for 1580 nm. As expected for 1550 nm both the output power and the ER are lower (the ER is limited to 14 dB). The shape of the curve for 1580 nm around 150 mA is possibly caused by a thermally induced phase shift.

For 1580 nm a sharp destructive interference is present at 206 mA. The currents in both SOAs are almost equal, this indicates that the MZI is very well balanced. This is a large improvement in comparison to the first generation. Furthermore output power is larger and the ER higher. This is a result of the reduced coupling losses by using the integrated spot size converters.

### 6.4.5 Dynamic characterization

The static results are promising and the dynamic performance of the MZI is investigated. The switch is used as an all-optical wavelength converter. For this experiment a setup is used as shown in Fig. 6.18. The pump signal is obtained by modulating the short pulses ( $\approx 7$  ps) from a Mode Locked Laser (MLL) with a 10 Gb/s PRBS signal. A 40 Gb/s signal is obtained by multiplexing the 10 Gb/s signal. This signal has a wavelength of 1560 nm. The switch is operated in a push-pull configuration as stated before.

A TLS set to a wavelength of 1570 nm is used for the probe signal. This is the highest wavelength possible in this setup. It is still far from the gain peak.

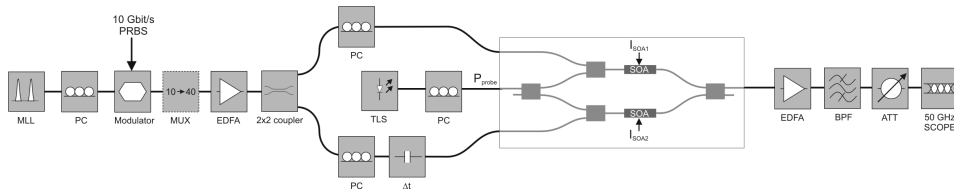


Figure 6.18: Setup for testing dynamic switching of the MZI

The resulting output signals for 10 Gb/s and 40 Gb/s switching are shown in Fig. 6.19. In the 10 Gb/s case a sequence of ones is shown. A pattern-effect is visible, but it is not very strong. An average output ER of more than 10 dB is obtained in this case.

In the 40 Gb/s case more noise is present, but an ER of approximately 9 dB can be obtained.

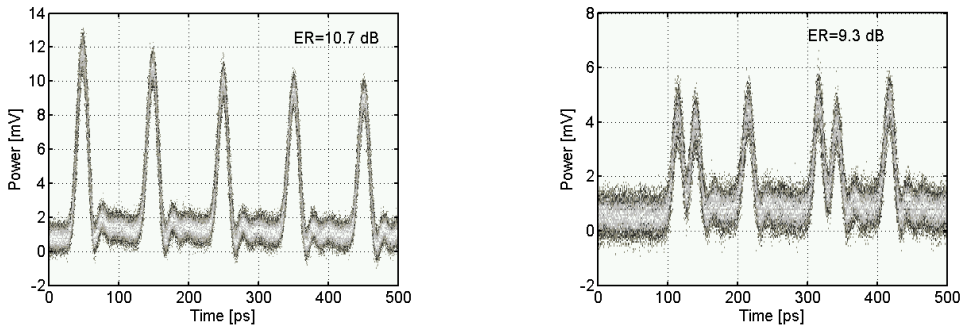


Figure 6.19: output bitpattern at 10 Gb/s (left) and 40 Gb/s (right)

## 6.5 Conclusions

In this chapter two generations of SOA-MZI wavelength converters are discussed. The first generation shows conversion up to 2.5 Gb/s for counter-propagation operation offering the

possibility for conversion to the same wavelength. Large recovery times are encountered, most probably due to low and non-uniform current injection as is inferred from simulations.

In the second generation improvements are made to the design, reflection free MMIs and SOAs are used and the device is designed for flip-chip packaging. The device is mounted P-side-up and the resulting thermal behavior causes heating which prevents a blue-shift of the peak wavelength. Pulsed measurements confirm that a blue-shift and high gain is possible at higher injection currents. This indicates the feasibility of this device to operate with high gain for wavelengths around 1550 nm. Flip-chip packaging will most probably reduce the heating of the device and it is very likely that the MZI will operate at 1550 nm under DC bias in the latter case.

Integration of active structures with SSCs, vertical and horizontal alignment features is successfully demonstrated.

The fiber-to-fiber gain of the second generation device is higher than for the first one, this is a result of the SSC. The device is balanced, which will yield a large operation bandwidth.

Dynamic measurements show switching up to 40 Gb/s.



---

# Chapter 7

## POLARIS

---

### 7.1 Introduction

The generic platform for polarization handling developed in this thesis consists of active and passive components and polarization converters. In this chapter the capability of polarization handling is demonstrated by the application of polarization diversity in a wavelength converter. The polarization is used to add functionality. The polarization is very stable inside a PIC and is not easily transferred from one into the other. The polarization can thus be used to label signals, and by making use of this, select and filter them. This is the principle of POLARIS (Polarization Labeling for Rejection and Isolation of Signals). It is a polarization diversity scheme in which the polarization is used to identify signals. It allows filter-free, co-propagation wavelength conversion and conversion to the same wavelength.

As an additional advantage POLARIS allows polarization independent operation. The polarization dependence of most Photonic Integrated Circuits (PICs) is problematic. By the creation of subcircuits for each of the two polarization states, components optimized for one certain state of polarization can be used and the polarization can be matched to the optimal performance.

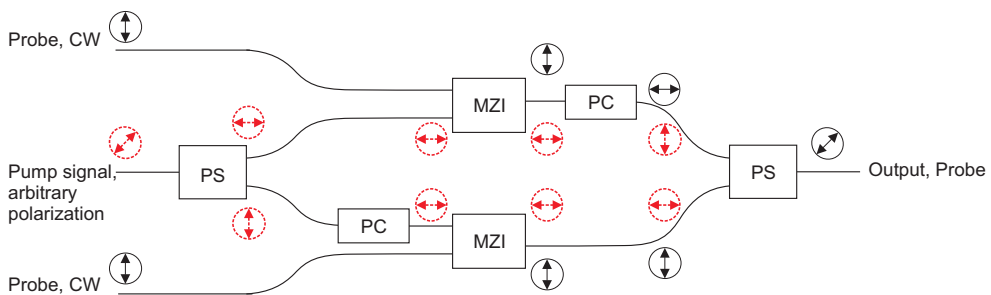
This chapter will first explain the concept of POLARIS as applied to a wavelength converter (WLC) and an all optical switch. With a simulation study of the POLARIS WLC the concept is investigated. Next the concept is experimentally demonstrated by using the WLC from chapter 6 and external fiber-based polarization components. Finally the design and fabrication of the integrated version of POLARIS is discussed. With this the full processing of the generic integration platform with polarization handling capability is introduced.



## 7.2 Principle of the POLARIS wavelength converter

The POLARIS concept can be applied for devices in which two optical signals interact and have to be separated at the output. The basic idea is to give both signals, the pump and the probe signal, well defined, but orthogonal polarizations. The polarization thus is a label for the signals and can be used for filtering. A number of different configurations are possible as will be explained in this chapter. POLARIS has the additional advantage that it can be made polarization insensitive (even when using polarization sensitive SOAs) for one of the signals. The basic principle, applied to a wavelength converter, will be explained first.

Fig. 7.1 shows the schematic configuration of the POLARIS wavelength converter. In the WLC case, the assumption is made that the probe signal, which is locally generated, has a fixed and stable polarization, whereas the pump signal, coming from the fiber-network, has an arbitrary (and varying) polarization.



**Figure 7.1:** POLARIS wavelength converter

In the figure the arrows give an indication of the state of polarization of the signals in the device. TE polarized light is indicated as horizontal, TM as vertical. The pump signal is indicated by the dashed circles, the probe by the solid circles.

The signal from the network (pump signal) arrives in an unknown polarization state. This signal is split into two orthogonal polarizations in the input polarization splitter (PS). In the lower branch, the polarization is rotated in the polarization converter (PC) to have the pump signal in both branches in the same polarization (TE). These signals are injected into the MZIs together with the locally generated CW light (probe signal) in the orthogonal polarization (TM). After interacting in the MZI the signal information is transferred to the probe wavelength and both signals have to be separated. This is done by rotating the polarization of the upper branch and then using a polarization splitter/combiner to combine the (probe) signals from both branches. As only TE in the upper and TM in the lower input of the combiner will couple to the output, filtering of the unwanted remains of the pump signal occurs. Note that this is not an interferometric coupling; hence the phase difference between the signals will not be important. It will influence the state of polarization of the output light, but not the amplitude.

If the polarization converters are not perfect, the small unconverted part of the probe in the upper branch can interfere in the output polarization splitter if this splitter is also imperfect. The same will happen for the pump signal, here the influence is even smaller as this signal is filtered twice, first at the input, and at the output. In both cases it is a very small fraction and will not cause any problems.

## 7.3 Simulation study and POLARIS concepts

The POLARIS concept is studied by simulations using a commercial circuit simulator [105]. The performance of the device is investigated to obtain the window of operation for different parameters of the components.

The polarization components used in the simulations are assumed to have efficiencies (conversion and splitting) of 95% or 99%, and excess losses of 2 dB. The SOA is modeled using a length-averaged rate-equations model. The effective alpha-factor of the SOA is a parameter in the simulation. In the simulations values of 5 and 8 are used. ASE is added as white noise to the output of the SOA. The SOA is wavelength and polarization independent.

The SOA-model can be extended by placing a polarization dependent attenuator in front of the SOA, this will mimic polarization-dependent gain. In the POLARIS concept the polarization definition at the input of the SOA is fixed and therefore no significant influence is expected from polarization dependence of the SOA.

The probe has a power of -8 dBm in each branch, and is TM polarized. For the pump signal, the power and polarization are varied. The pump signal is modulated with a 10 Gb/s PRBS data signal with an Extinction Ratio of 7 dB.

The basic POLARIS design (as shown in Fig. 7.1) is investigated when it consists of well-performing components: SOAs with an  $\alpha$ -factor of 8, and polarization components with 99% efficiency.

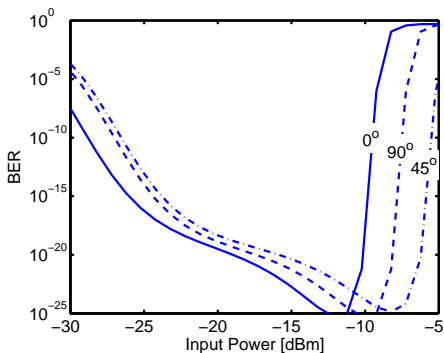
The Bit Error Rate (BER) as function of the input power for different polarizations is plotted in Fig. 7.2.

There is a large input power range of 15 dB for which the BER is well below  $10^{-12}$  for all polarizations. The small difference between the polarizations is explained by the different losses for the different paths. For TE polarized pump light ( $0^\circ$ ), 99% of the light is coupled to the upper POLARIS branch. No additional losses are present in this path, so almost all the power reaches the SOA. Thus for TE the lowest input power is required.

For TM polarized pump light ( $90^\circ$ ), 99% of the light is coupled to the lower branch, here a PC is present with 2 dB loss, hence the BER curve is shifted to 2 dB higher input powers. For  $45^\circ$ , the worst case, the pump light is split equally into the 2 branches, so 3 dB more power is needed to compensate for this. Furthermore, the TM part has an additional 2 dB loss. This explains the shift with respect to TE.

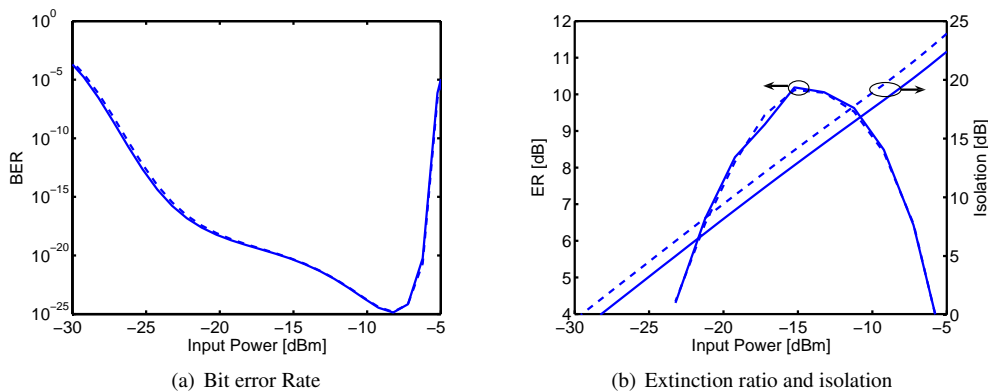
Apart from the BER, the Extinction Ratio (ER) and the filtering of the pump is investigated. The filtering of the pump is expressed as the isolation, defined as the ratio between the probe and pump signal at the output of the device.

In Fig. 7.3 the results are given for all three quantities. A comparison is made between the use



**Figure 7.2:** BER simulation for POLARIS, 99% efficient polarization components, polarization independent SOA with  $\alpha=8$ , changing polarization.

of a polarization-independent SOA and a polarization-dependent SOA. In the latter, the TM-gain is 3 dB lower, and the probe signal is increased by 3 dB to compensate for this. These simulations were performed for the worst case: a polarization of 45° for the pump signal.



**Figure 7.3:** Simulation results for POLARIS, 99% efficient polarization components, solid lines for a polarization independent SOA, dashed lines for a polarization dependent (TM gain 3 dB lower) SOA.

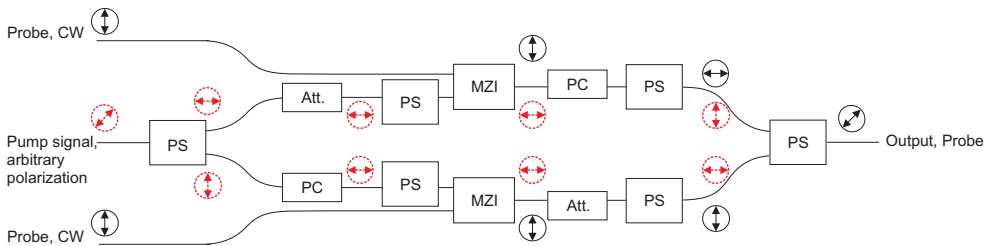
The results indicate that the use of a polarization-dependent SOA does not have a large influence on the performance. The largest difference is in the isolation. This is 1.5 dB higher for the polarization dependent SOA, because the unwanted TM fraction of the pump is less amplified. In the power range from -20.5 dBm – -7.5 dBm the BER is lower than  $10^{-12}$ , and the ER is above 7 dB, so there is regeneration. If an isolation of more than 20 dB is desired, this can only be achieved for powers of -7.5 dBm (or higher).

### Improvements

From the previous section, it is clear that only a limited operation range is possible. Some modifications to the concept are necessary to improve the performance of the wavelength converter.

The PCs in the branches can introduce additional losses. To equalize the loss in both arms, an additional attenuator can be used in the opposite branch of the PCs in both the in- and the outputs. This attenuator is a PC with twice the length. In chapter 4, in Fig. 4.20 it is shown that conversion completely back to the original signal occurs at the full beat length of the converter. As the junction losses dominate the loss of the converter, this attenuator will have similar losses as the normal PC.

The input pump signal into the MZI can be extra filtered to achieve a better polarization definition. The same filtering can be done before reaching the output PS. A polarization filter can be achieved by using the respective output of a polarization splitter. This improved scheme is depicted in Fig. 7.4.



**Figure 7.4:** POLARIS wavelength converter with additional attenuators and filters.

This concept is tested with the worst-case components, in which the  $\alpha$ -factor is 5 and the polarization efficiency is 95%.

The BER, ER and isolation are plotted in Fig. 7.5 for a varying input power. In Fig. 7.5(a) the BER is plotted for different input polarizations. The addition of the attenuators in the arms removes the polarization dependence for full TE and TM, for 45° polarized light, the required power is 3 dB higher because the signal is split into two branches. The ER and isolation are shown for an input polarization of 45°. The device performs much better than the previous case, even with worse components. The additional filtering and equalized losses yield a larger operation range.

The ER and the isolation will increase further for a higher  $\alpha$ -factor. For this purpose an optimization of the SOA is required. This is entirely possible;  $\alpha$  values up to 32 are reported in literature [46].

Another improvement can be achieved by replacing the coupler for the pump signal in the arms of the MZI by polarization splitters. The improvement achieved now is twofold: additional polarization filtering of the signals is obtained, and 3 dB coupling loss is avoided for both the pump and the probe in the coupler. Fig. 7.6 shows an MZI in which the couplers are replaced by polarization splitters. They can be used in the POLARIS concept to replace the normal

SOA-MZI.

This has the same effect as using the filters as is done in the previous case. The improvements with respect to the previous case are the lower required input power and a reduced number of components.

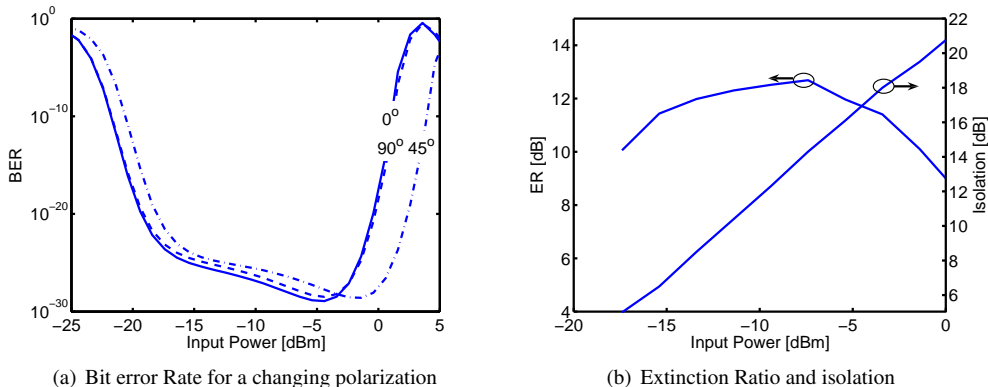


Figure 7.5: Simulation results for POLARIS, 95% efficient polarization components,  $\alpha=5$ . Including loss compensation and additional polarization filters.

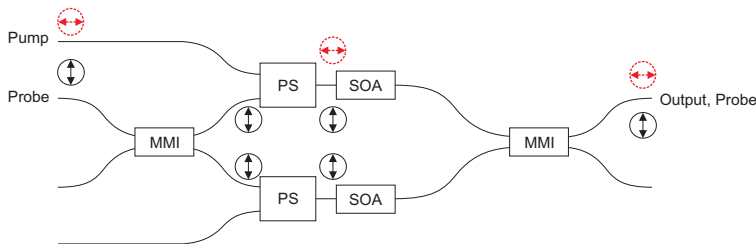


Figure 7.6: MZI with polarization splitters in the arms.

Polarization MZI

A consequence of the polarization diversity approach is the condition that 2 MZIs have to be used. Each MZI contains 2 SOAs, so a total of 4 SOA is required. This results in a large footprint of the POLARIS WLC. By replacing the MZIs with polarization MZIs (PolMZI) [14] introduced in chapter 1, the number of SOAs can be reduced. In Fig. 7.7 the POLARIS WLC scheme in this case is depicted.

The polMZI used in the branches is an MZI in which the two arms are separated by using different polarizations instead of different physical paths. At the input of the polMZI, the

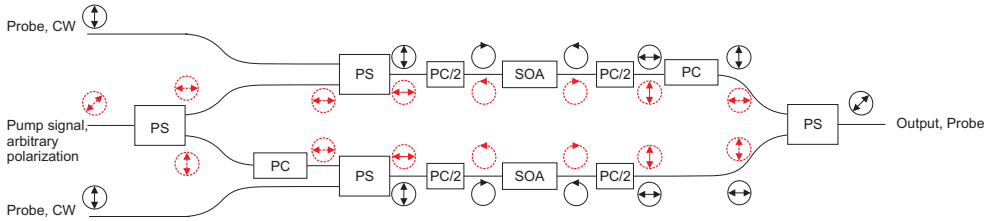


Figure 7.7: POLARIS with polarization MZIs.

pump and the probe are converted to orthogonally circularly polarized signals in the input half PC. Both signals are input into the SOA, which functions as a nonlinear phase shifter. At the output of the SOA the TE and TM polarized parts of the signals have experienced a power dependent phase shift. The signals are recombined into the output half PC. Depending on the relative phase difference between the two polarizations, the probe couples to TE or TM. TE polarized light in the upper output is converted to TM and in the output PS, only TM from the upper arms and TE from the lower arm will couple to the output.

The polMZI should be designed such that the probe is not rotated in case there is no pump signal present. In that case the probe will not couple to the output. An other important issue for the POLARIS filtering to work is that the self-phase modulation (SPM) of the pump signal in the SOA causes a phase shift of exactly  $\pi$  radians. In that case the pump at the output of the SOA is completely orthogonal to the pump at the input and will be filtered by the output PS. Ideally the SPM is equal to the cross-phase modulation of the probe and the probe will be coupled to the output of the PS. A deviation from this will result in a small loss on the probe signal, but the suppression of the pump is not influenced.

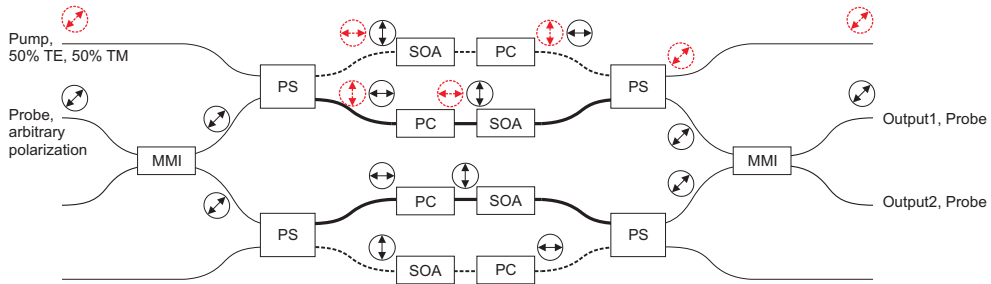
The PS used for coupling the probe into the arms is used as an additional filter as explained in the previous design. A good PS will yield low-loss coupling of the pump and probe into the branches. By using an MMIs at these points, 3 dB inherent loss is introduced.

**POLARIS all-optical switch**

As stated before, in a wavelength converter, the signal coming from the network can have an arbitrary polarization. In that case this signal is used as pump. In an all-optical switch, a different optimization might be preferred as here the signal from the network is the probe which is switched by a local signal. In this case, the POLARIS scheme looks as depicted in Fig. 7.8.

As the POLARIS solution is a polarization diversity solution, the switch consists of two MZIs. In the scheme presented here, both MZIs share the same in- and output MMI. One MZI, used for a TE-polarized probe signal (referred to as "TE-MZI"), uses the inner arms of the device (indicated in the figure by thick lines), the other, the "TM-MZI" consists of the outer arms, indicated by the dashed lines.

The probe signal, in an arbitrary polarization, is split in the input MMI into the two arms. In the polarization splitters, the signal in both arms is split into two orthogonal polarizations. The



**Figure 7.8:** POLARIS all optical switch.

TE part into the inner outputs, the TM part into the outer branches.

The pump signal (the control signal), has to have a polarization with equal power in both TE and TM (the phase between the polarizations is not important), so that it is split in the upper input polarization splitter into equal power parts. This signal is now orthogonal to the probe in both upper arms.

The polarization of the signals in the inner arms is rotated by  $90^\circ$  by the polarization converters. Now in all branches the signals entering the SOAs have equal polarization (pump in TE, probe in TM). The signals interact in the upper SOAs and the phase is modulated. The signals in the outer arms are rotated in the PCs to have the corresponding signals orthogonal at the input of the output PS. In those output PSs, TE polarized light is coupled to the cross-port, while TM polarized light is coupled to the bar-port. In this way, only the probe signal is coupled to the inner outputs of the PSs. The signal is combined in the output MMI and depending on the presence of the pump signal is output at output 1 or 2.

Note that for this concept  $2 \times 2$  polarization splitters are required. The coupling in the input polarization splitters is different than in the output PSs. At the input TE polarized light is coupled to the bar-ports, while at the output it is coupled to the cross-port. This can be easily achieved with the  $2 \times 2$  splitter demonstrated in chapter 5 by exchanging the position of the PCs in this PS. If another PS is to be used with a fixed coupling mechanism, crossings are needed to couple the respective outputs to the output MMI, which complicates the design.

For the all-optical switch similar modifications as shown for the wavelength converter can be made to improve the performance.

In this section the POLARIS concept is explained and explored. Simulations show that even with moderately performing components, good performance of the whole circuit can be expected if loss balancing and sufficient filtering are used. The concept can be applied to WLC and all-optical switches, and can be simplified with polMZIs.

## 7.4 Fiber based POLARIS

The POLARIS concept is experimentally tested by realizing the proposed circuit using the first generation integrated wavelength converter of chapter 6. The polarization handling is realized

with fiber-based polarization splitters and rotators.

### 7.4.1 Experiments

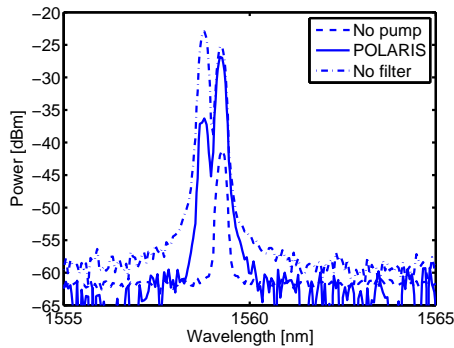
The measurements are performed on a standard transmission setup, similar to the setup shown in Fig. 7.10. Light is coupled into the chip using an array of cleaved Polarization Maintaining Fibers (PMF).

A single branch of POLARIS is tested. This is done by injecting the CW probe and pump signal with orthogonal polarizations. For the probe signal we make use of a TLS with well defined output polarization and a PMF output.

The polarization of the pump signal is defined by using a polarization controller and polarization splitter. The power in the unwanted polarization is monitored and corrected manually. The polarization splitter has a polarization ER of 15 dB. This results in 3% of power in the wrong polarization being also injected in the device. At the output a polarization splitter, also with an ER of 15 dB, is used as a filter.

#### Static characterization

The probe and pump signal wavelengths are spaced 0.5 nm to be able to measure the isolation using an Optical Spectrum Analyzer. The recorded spectra are shown in Fig. 7.9. An isolation

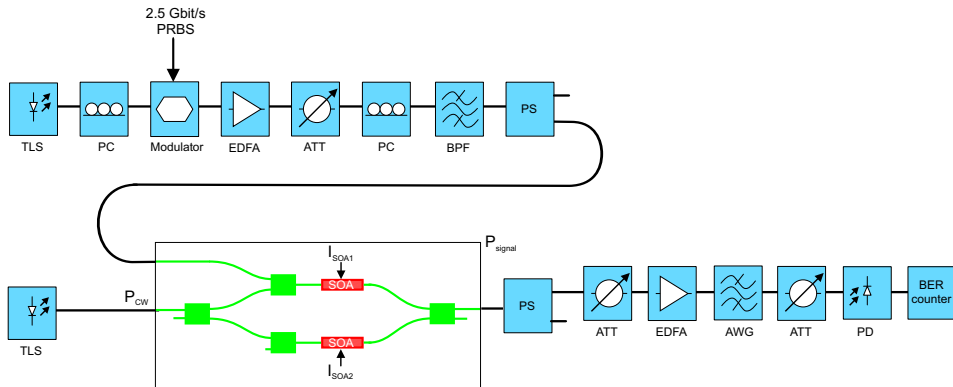


**Figure 7.9:** Output spectrum at the output of POLARIS.

of 10 dB is achieved in this way. For signals with a wider wavelength separation, isolation up to 13 dB is obtained. This demonstrates one of the strengths of POLARIS: signals spaced this closely are very difficult to separate using conventional wavelength filtering as it requires extremely narrow filters.

The level of isolation achieved here reflects the quality of the fiber based polarization components. With integrated devices, with their inherently better definition of the polarization state, higher isolation can be expected.



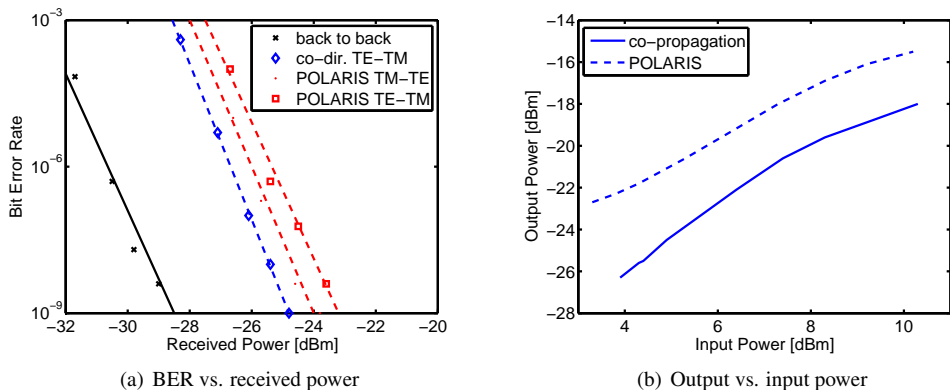


**Figure 7.10:** Measurement setup for testing the POLARIS principle. TLS: Tuneable Laser Source, PC: Polarization Controller, MOD: Intensity Modulator, ATT: Attenuator, BPF: Band Pass Filter, PS: Polarization Splitter, AWG: 8-channel WDM demultiplexer, PD: Photo Diode

### Dynamic characterization

The POLARIS WLC is measured dynamically at 2.5 Gb/s. The setup for testing a single branch of POLARIS is shown in Fig. 7.10.

Standard co-propagation is compared to POLARIS. For co-propagation operation we replace the polarization splitter at the output of the device with a tuneable filter.

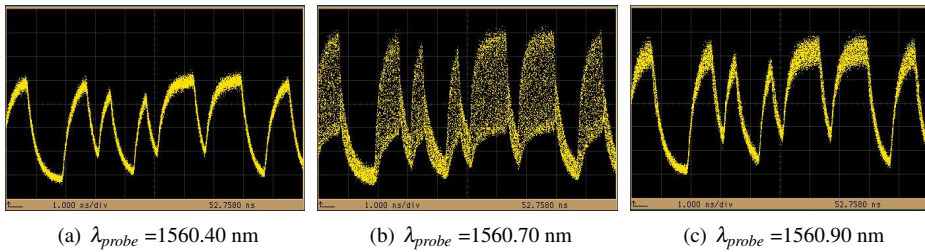


**Figure 7.11:** Co-propagation operation compared to POLARIS  $\lambda_{pump}=1555$  nm,  $\lambda_{probe}=1560$  nm.

The results are presented in Fig. 7.11. From Fig. 7.11(a) it is seen that for POLARIS a power penalty of 5 dB is encountered, in contrast with 4 dB for wavelength filtering. This is probably caused by ASE, which is filtered almost completely by the wavelength filter in the co-propagating case, but only half in the POLARIS case.

In Fig. 7.11(b) the output power as a function of the input power is plotted. The output power is 2 dB higher in case of POLARIS. This is caused by the higher insertion loss of the wavelength filter in the co-propagation case as compared to the polarization filter.

Conversion to the same wavelength is possible in co-propagation with POLARIS. This is another advantage of POLARIS: co-propagation is preferred over contra-propagation for high speeds as explained previously. When converting to the same wavelength a lot of noise is present in the output signal, as can be seen in Fig. 7.12.



**Figure 7.12:** Output bitpattern when converting to almost the same wavelength  $\lambda_{pump} = 1560.66$  nm

Because of the imperfect isolation, resulting from the limited performance of the fiber based polarization components, the received signal will contain not only the probe signal, but also remains of the pump. The wavelengths of both signals are almost the same. The difference frequency will be within the electrical bandwidth of the detector, and is present as noise in the output. A small de-tuning of the wavelength, larger than 25 GHz, is enough to place the difference frequency outside the bandwidth of the detector, then this beating noise disappears. The beating noise results from heterodyne mixing between the signals, and has a power of:

$$P_{mix} = 2\sqrt{P_{pump}P_{probe}} = \frac{2P_{probe}}{\sqrt{A}} \tag{7.1}$$

where  $A$  is the isolation ratio between probe and pump.

This mixed signal is considered as the main contribution to the noise. The Signal-to-Noise-Ratio (SNR) is calculated as the ratio of  $P_{probe}$  and  $P_{mix}$ :

$$SNR = \frac{P_{probe}}{P_{mix}} = \frac{\sqrt{A}}{2} \tag{7.2}$$

With an isolation of 20 dB, this will yield an SNR of 7 dB, which should be sufficient to allow error-free operation.

The measurements demonstrate the feasibility of the POLARIS concept. The limited isolation obtained translates to noise in the signal, particularly if conversion to the same wavelength is regarded. The main cause of the unwanted signal being present in the output is an imperfect

definition of the polarization. This is the result of the fiber-connectors having a limited polarization ER of 15 dB, an accumulation of polarization errors in the connectors, and the 15 dB ER of polarization splitter.

According to the simulations, higher values of the isolation can be obtained by using higher ER polarization filters or by cascading them, and by improving the performance of the MZI. By using SOAs with higher  $\alpha$ -factors, a lower pump power can be used, which yields lower remains of the pump power at the output. These improvements will lead to an isolation of more than 20 dB with good BER performance, as shown in the simulations.

Filtering of signals through an active-passive integrated MZI based on polarization is demonstrated. This avoids the need for (tuneable) filters. Because of the possibility of conversion to the same wavelength the POLARIS WLC simplifies wavelength management in a WDM network.

## 7.5 Integrated POLARIS

The feasibility of the POLARIS concept is demonstrated in the previous section. One of the problems in that experiment is the imperfect definition of the polarization and the accumulation of polarization errors in connecting polarization maintaining fibers and polarization splitters. By integrating the whole concept, these polarization errors can be avoided.

In chapter 4 a polarization converter with a conversion of more than 95% is demonstrated, which should be sufficient to demonstrate POLARIS according to the simulations. By using the MZI polarization splitter from chapter 5, a fully integrated POLARIS circuit can be realized. This is a demonstration of the generic integrated polarization handling technology by integrating a polarization converter in the standard active-passive technology.

### 7.5.1 Design

An integrated version of POLARIS is designed using the building blocks discussed previously in this thesis. The active material is the same as is used for the second generation MZI switch, containing 8 Quantum Wells (see section 6.4).

Three types of the POLARIS concept are present on the mask. First of all the POLARIS wavelength converter according to the schematic of Fig. 7.1. The corresponding mask design is depicted in Fig. 7.13.

As can be seen in the figure, all in- and outputs are positioned at an angle of  $7^\circ$  to avoid reflections, they are all horizontally tapered to a width of  $5\ \mu\text{m}$ , to maximize coupling tolerances. Higher-order modes can be excited in these waveguides, therefore modefilters are placed after the bends in every in- and output. These modefilters, as well as all other MMIs, have their corners cut to reduce reflections as explained in section 2.3. Reflections from the active-passive butt-joint are prevented by entering the active region at an angle of  $10^\circ$ .

Multiple inputs have to be used. This requires the usage of an angled fiber array with a pitch of  $250\ \mu\text{m}$ . Because the waveguides are put at an angle of  $7^\circ$ , the refraction angle is  $23^\circ$  in air. The waveguides are thus placed at a pitch of  $250/\cos(23^\circ)=271.6\ \mu\text{m}$ .

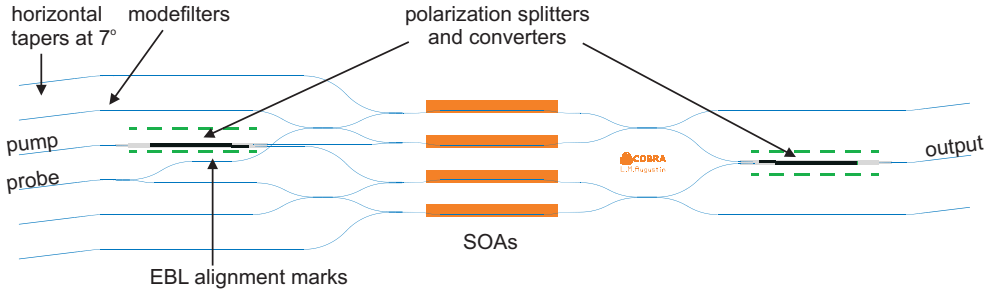


Figure 7.13: Mask design of the POLARIS wavelength converter.

The MZIs use  $2 \times 2$  input and output MMI couplers to improve the balance of the MZIs (see chapter 6). The non-POLARIS in- and outputs are also led to the facets. This gives the possibility to test the MZI separately by circumventing the polarization components. All waveguides are  $3 \mu\text{m}$  shallow waveguides that are designed to have low loss. Only the waveguides inside the polarization splitters and converters are deeply etched. EBL write fields with alignment marks are included in the waveguide design. In these write fields the polarization splitters and converters can be defined. No additional polarization filters are used in this case due to a lack of space.

Apart from the wavelength converter design, also the all-optical switch (schematic in Fig. 7.8) is designed. The mask layout for this is shown in Fig. 7.15. Here  $2 \times 2$  polarization splitters (chapter 5) are used.

Moreover a POLARIS wavelength converter with polarization MZIs is designed according to the schematic of Fig. 7.7. The mask design is shown in Fig. 7.14. The much simpler and smaller mask layout is evident here. For all circuits the same designs are used for the individual components.



Figure 7.14: Mask design of the POLARIS wavelength converter with polarization MZIs.



Figure 7.15: Mask design of the POLARIS all-optical switch.

## 7.5.2 Generic integration technology with polarization handling capability

In this section the active-passive integration technology from chapter 3 is extended by adding the processing of the polarization converter.

The proposed processing scheme, in which active and passive components and polarization converters are combined, is shown in Fig. 7.16. It is based on the second generation designs of the polarization converter (section 4.4), polarization splitter (section 5.3) and the MZI (section 6.4).

The process consists of the following steps:

- a. First the contactlayer is removed from all passives components. To this end a lithography step is done in which the active regions are covered. The InGaAs contact layer is wet chemically removed by  $\text{H}_2\text{SO}_4:\text{H}_2\text{O}_2:\text{H}_2\text{O}$ . This is a selective etch and will stop on the InP topcladding. The contact layer thickness is only 100 nm in our case, therefore the coverage of the etched step with resist or masking material later on in the process is not a problem.
- b. Silicon Nitride ( $\text{SiN}_x$ ) is deposited on the sample. On this, the waveguides, and write-fields for the EBL, including the alignment marks, are optically defined. The  $\text{SiN}_x$  mask layer is etched using  $\text{CHF}_3/\text{O}_2$  RIE.
- c. The sample is covered with EBL resist in which the polarization converters are defined.
- d. Ti is evaporated and the polarization converters are defined in Ti on top of the  $\text{SiN}_x$  using a lift-off process.
- e. A second EBL step is done to open the straight side of the PC. The nitride at the straight side of PC is opened using the resist and the titanium as a mask.
- f. All shallow waveguides are covered with resist. The deep waveguides and the straight side of the PC are opened by optical lithography.
- g. The deep waveguides and the straight side of the PC are etched with  $\text{CH}_4/\text{H}_2$  RIE. Here the same considerations are taken into account as for the double etch process in the standard technology.
- h. The resist is removed from the chip and all waveguides are etched using  $\text{CH}_4/\text{H}_2$  RIE. The shallow waveguide depth is critical in this step.
- i. All waveguides are covered with resist, the PC area is opened with a non-critical optical lithography step. The  $\text{SiN}_x$  at the sloped side of the PC is opened.
- j. The InP topcladding is RIE etched until 300 nm above the waveguide layer. In this step the critical dimensions are kept, because the Ti mask does not erode during the etch and thus the sidewalls are vertical. While etching this side, the straight side of the PC (which is already etched in step h.) is etched even deeper, well below the waveguide layer.

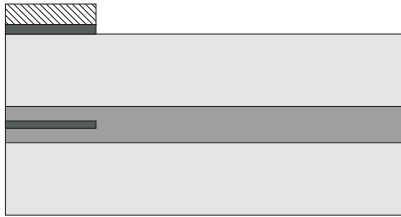
- k. Silicon Nitride is deposited on the whole sample. The PECVD deposition also covers the sidewalls.
- l. All waveguides are again covered with resist. The PC area is opened using a non-critical lithography. The  $\text{SiN}_x$  on the PC area is etched back using  $\text{CHF}_3/\text{O}_2$  RIE. Because of the directional etching, the etched sidewalls stay covered with  $\text{SiN}_x$ , which serves as a mask for the wet etching in the next step.
- m.  $\text{Br}_2$ -Methanol is used to etch the slope. This etchant etches a slope in both InP and InGaAsP, with an angle of  $54.7^\circ$  with respect to the surface. In this step, the straight side of the PC is etched as well. As this side is already etched well below the waveguide layer, the etching will not influence the performance of the converter.
- n. The nitride and the Ti are removed using an HF solution. The SOAs are passivated and planarized by spinning polyimide on the sample. The polyimide is etched back till the contacts are opened.
- o. The sample is covered by negative resist and the contacts are opened. Titanium, platinum, and gold (Ti, Pt, Au) are evaporated twice on the sample, once on the P-contact on top, and once on the backside of the sample for the N-contact. After lift-off in acetone, the P-contacts remain on top. The backside is completely covered for the N-contact. For a low resistance contact, the metal has to be made thicker. This is achieved by electroplating as explained in chapter 3. After this thick gold P-contacts remain.
- p. The final step is to remove the polyimide everywhere from the sample, except below the P-contacts. This is done in an  $\text{CHF}_3/\text{O}_2$  RIE. The metal contacts serve as a mask. They are not attacked if the power is sufficiently low (50 W). The polyimide needs to be removed in order to cleave the sample. Furthermore the PC is designed to have air surrounding the device. The correct index contrast is not obtained if the polyimide is left on the sample.

In the standard COBRA technology, electro-optic phase modulators can be integrated as well. This possibility is taken into account in this scheme. The phase modulators themselves are processed in exactly the same way as the SOAs. Phase modulators are reversely biased, so isolation sections are required in between them. These sections are waveguides from which the highly doped top cladding is removed to increase their resistance. Their top cladding can be etched in step (j) to reach the same level as the start of the sloped side of the PC.

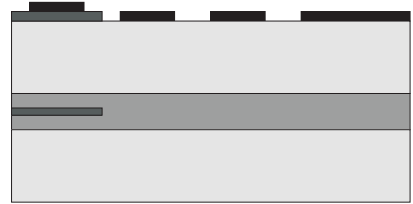
### 7.5.3 Finished chip

The POLARIS chip is fabricated. A photograph of part of the chip is shown in Fig. 7.17. Here 2 POLARIS all-optical switches and 2 POLARIS WLCs with polMZIs are visible.

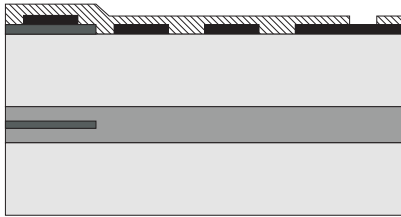
The fabricated chip shows the integration of polarization converters and splitters with other passive and active components. Inspection with an optical microscope and a SEM shows that the realization of a large number of the SOAs, the passive waveguide devices and the



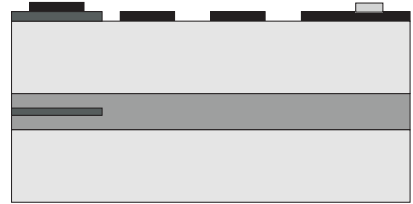
(a) Covering actives and wet-selective removal of the contact layer on passives.



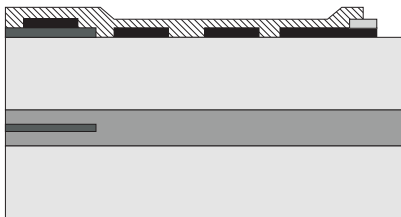
(b)  $\text{SiN}_x$  deposition, waveguide lithography and  $\text{SiN}_x$  etching.



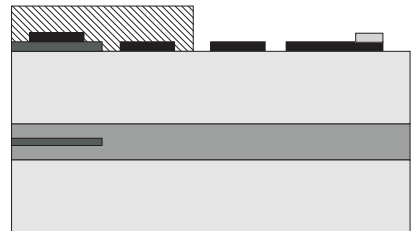
(c) EBL to define PC waveguides.



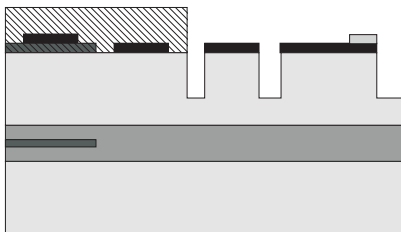
(d) Ti evaporation and lift-off for PC definition.



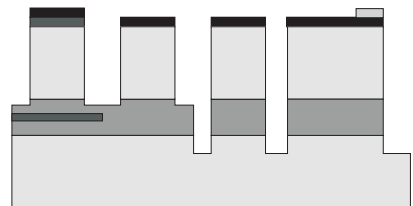
(e) EBL to cover the sloped side of the PC. Etching  $\text{SiN}_x$  at the straight side.



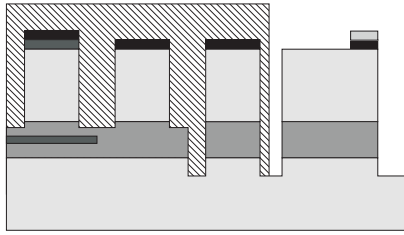
(f) Covering all shallow waveguides with resist.



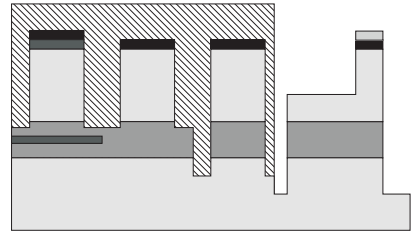
(g) Preliminary etching of deep waveguides.



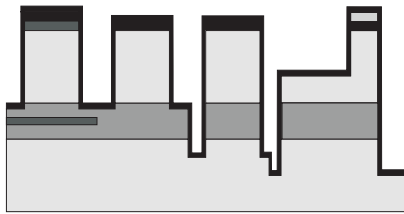
(h) Resist removal and etching of all waveguides.



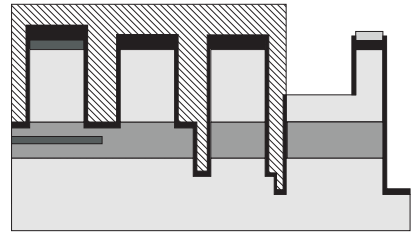
(i) Covering all waveguides, opening of the PC area. Etching SiN<sub>x</sub> to reveal the sloped side of the PC.



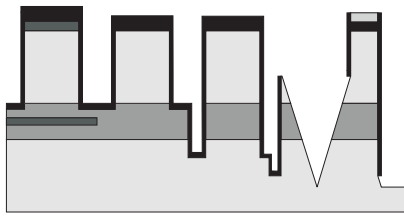
(j) Etching the sloped side of PC to the right depth.



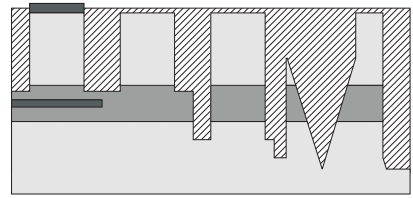
(k) Covering the whole chip with SiN<sub>x</sub>.



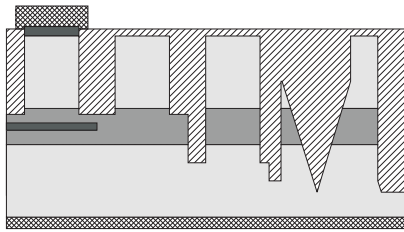
(l) Covering the whole chip with resist and opening the PC area. Etch SiN<sub>x</sub> in the PC area.



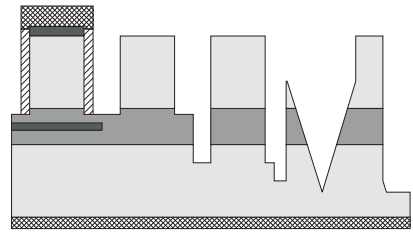
(m) Etching the slope with Br<sub>2</sub>:CH<sub>3</sub>OH.



(n) Removing all SiN<sub>x</sub>. Polyimide planarization and etching back.



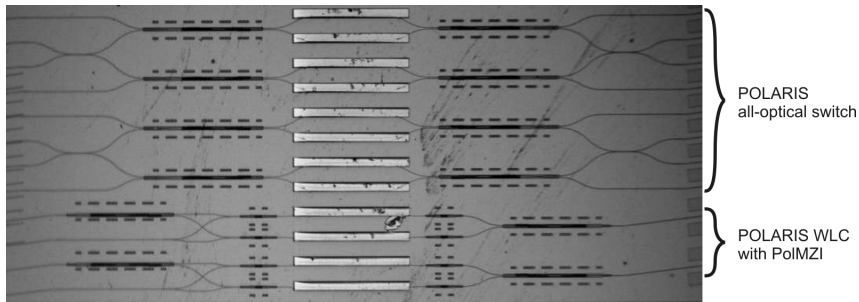
(o) P- and N-contact metallization.



(p) Etching all the polyimide with the metal as a mask.

**Figure 7.16:** integration technology with polarization handling capability





**Figure 7.17:** Photograph of the POLARIS all-optical switch and POLARIS WLC with polMZIs.

polarization converters has succeeded.

The fabrication of the polarization splitters and converters within the full integration scheme was successful. The  $2 \times 2$  polarization splitters from chapter 5 are fabricated in this realization. As stated before, they show a conversion of 88% and a splitting ratio of 7 dB. This limited performance is most probably caused by a non-optimal dose in the EBL. A better proximity effect correction is required for structures close to each other as in the polarization splitter.

Due to bad adhesion of the EBL resist on part of the SOAs in step (e), these devices are etched away. Furthermore, an error during the metallization damaged the contacts on a number of the SOAs. The undamaged SOAs show proper operation.

A number of all the relevant components (SOAs, PCs, PSs) on the chip showed reasonable functioning. The overall yield however was too low to demonstrate the integrated POLARIS circuits. An optimization of the process is required, but due to time constraints this has not been done.

The integration, and the operation of the various components, demonstrate the feasibility of the generic integration scheme with polarization handling capability.

## 7.6 Conclusions

A new configuration is studied for a wavelength converter based on an SOA-MZI, which uses polarization components to isolate the pump and probe signals. The concept is useable for different circuits in which optical-optical interactions are used for all-optical switching. The concept is investigated for a wavelength converter. The configuration is promising since it works in co-propagation and allows conversion to the same wavelength. An input power range of 15 dB is found in simulations in which the BER is lower than  $10^{-12}$ . High ER and high isolation can be obtained at the same time. This is achieved by using components with a performance that is already realized.

The concept is experimentally demonstrated by using an integrated SOA-MZI and external fiber-based polarization handling. An isolation of 10 dB is achieved in this way. This demon-

stration shows one of the strengths of POLARIS: signal wavelengths spaced as close as 0.5 nm are very difficult to separate using conventional wavelength filtering as it requires extremely narrow filters.

By using SOAs with higher  $\alpha$ -factors a lower pump power can be used, which yields lower powers at the output in both the unwanted and wanted polarization. These improvements can lead to an isolation of more than 20 dB.

An integrated version of POLARIS has been designed. A generic integrated polarization handling technology is demonstrated by realizing this circuit. This technology is an extension of the standard technology where the only addition is a polarization converter. The realization clearly showed that the integration scheme is feasible. Unfortunately due to not sufficiently optimized processing steps no POLARIS operation could be shown yet with the integrated device.



---

# Chapter 8

## Conclusions and Outlook

---

### 8.1 Conclusions

In this thesis a technology for polarization manipulation in Photonic Integrated Circuits (PIC) is studied. Applying polarization offers a broad variety of functions. On-chip polarization handling, such as polarization diversity, can solve polarization problems without changing waveguide or material properties and thus without compromising the performance.

A generic technology platform with polarization handling capability is proposed. For full control of the polarization on a PIC, polarization converters and polarization splitters are required that fit in the standard technology for realizing of active and passive components.

A new polarization converter is designed that can be fully integrated in the standard process. The polarization converter shows a maximum conversion of 97%. A conversion larger than 95% is obtained over a wavelength range larger than 35 nm and a temperature range larger than 40°C. As these measured ranges were limited by the equipment used, actually much larger ranges are inferred.

Two novel types of polarization splitters are designed. One tolerant device with a large splitting ratio (larger than 13 dB) and a large window of operation (width range of approximately 100 nm, wavelength range of more than 45 nm). It has however the disadvantages that it is long (2.7 mm), and that it is hard to integrate with other components.

Another type of polarization splitter is presented as well, based on a passive MZI with polarization converters in the arms. This device is shorter (600 – 800  $\mu\text{m}$ ) and, because it consists only

of passive components and PCs, it has the ability to be integrated in the standard active-passive scheme. Simulations show the possibility of high conversion, 9 dB splitting is experimentally achieved. A  $1 \times 2$  and a  $2 \times 2$  polarization splitter are realized.

The demonstration of the PC and PS show that the generic platform for polarization manipulation can thus be obtained by extending the standard technology with the addition of a polarization converter only.

Apart from the polarization handling capability, technology for packaging PICs is required. For this purpose an spot size converter is developed that can be integrated with active and passive components. Experimentally determined overlap with a standard fiber indicates coupling losses around 1.5 dB and a coupling tolerance of  $\pm 1.5 \mu\text{m}$  for 1 dB excess loss.

The feasibility of the packaging technology is demonstrated by the fabrication of integrated MZI switches with spot size converters. An array of these switches is packaged and wavelength conversion at 40 Gb/s is achieved.

The feasibility of polarization handling is demonstrated by a new type of integrated wavelength converter: POLARIS (Polarization LABELling for Rejection and Isolation of Signals). This wavelength converter uses the polarization of the light to label the original and the converted signals. By using a polarization splitter, the two signals can be separated and filtered. This approach can also be used in all-optical switches.

The POLARIS concept is demonstrated by simulations and experimentally verified with external fiber based polarization manipulating components.

An integrated version of POLARIS is designed. The generic integrated polarization handling technology is demonstrated by realizing this circuit. The realization clearly showed that the integration scheme is feasible, because working examples of all relevant components were present on the chip. Unfortunately due to time constraints not all processing steps were sufficiently optimized leading to a too low yield of working components, therefore no POLARIS operation could be shown with the integrated device.

## 8.2 Recommendations

The POLARIS principle and a number of the polarization handling circuits introduced in chapter 1 can be realized with the standard technology extended with polarization converters. Some improvements are required in the components and in the process. They are discussed here.

The losses of the integrateable polarization converter are high (around 2.5 dB) compared to simulations. Excess loss of the device should be below 1 dB, similar to earlier reported devices [72]. Most probably extra losses are caused by the non-optimal coupling of the waveguide and the converter, because of an underetch of the access waveguides. This can be avoided by using a different masking material, with less strain.

The splitting ratio of the integrateable polarization splitter has to be increased. For an integrated POLARIS, values above 13 dB are required. An optimized proximity effect correction

on the mask for the EBL exposure is required, because the width definition of the waveguides, the MMIs and the PCs is critical. Furthermore the EBL exposure spans multiple write fields. An imperfect connection between them can cause gaps or overlaps that lead to overexposure. Small rotations of the write fields can cause phase errors between the arms of the MZI. The alignment of the EBL write fields has to be improved to be able to use the EBL for these devices. By using high-resolution optical lithography, with a reduction stepper, these problems are avoided.

The roughness of the waveguides that is present in the polarization splitters has to be decreased. To this end the lithographical process for lift-off has to be optimized. The resist profile has to be suited for this purpose to reduce the edge roughness. For the EBL defined structures the resist profile is straight and lift-off of Ti did not lead to mayor roughness.

In the standard COBRA technology, electro-optic phase modulators can be integrated as well. This is taken into account in the development of the generic platform developed in this thesis. By using the polarization dependence of the electro-optic Pockels effect, the phase between the two polarizations can be controlled. This opens a new variety of possibilities. In the next section some of these are introduced.

## 8.3 Outlook

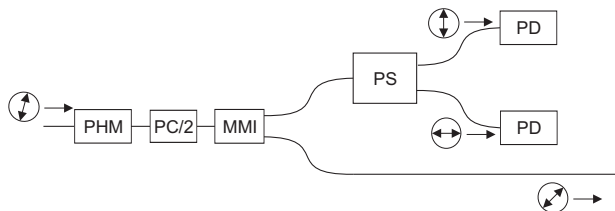
With the integrated polarization handling technology presented in this thesis and by also using electro-optic phase modulators, a number of other polarization based functionalities can be obtained. This section will briefly show some new concepts that can be monolithically integrated with the new standard.

### 8.3.1 Polarization control

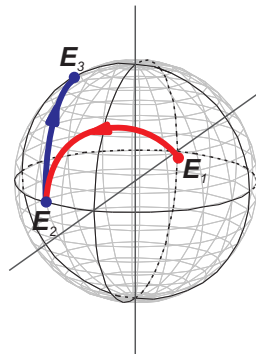
Several solutions for polarization dependence of PICs are proposed in this thesis. One of the solutions is a POLARIS scheme for the all-optical switch as depicted in Fig. 7.8. In this schematic the pump polarization should have equal power in TE and TM. A circuit shown in Fig. 8.1 can change an arbitrary state of the polarization (SOP) of the incoming light to achieve this. On the Poincaré sphere in Fig. 8.2 the relevant manipulations of the SOP are illustrated.

A signal with an arbitrary polarization ( $\mathbf{E}_1$  in Fig. 8.2) is fed into the circuit. The phase modulator equalizes the phase to obtain a linear polarization  $\mathbf{E}_2$  (SOP at the equator of the Poincaré sphere). The half polarization converter equalizes the amplitudes of both polarizations ( $\mathbf{E}_3$  at the meridian in the  $S_2S_3$ -plane). The resulting polarization has equal power in both polarizations but an arbitrary phase between them. The MMI at the output of the PC is a 90/10 MMI, by which 90% of the light is led to the output. The other part of the light is led to the PS. At the outputs of the PS photodiodes (PDs) measure the intensity of the light in each polarization. This information can be fed back to control the phase modulator at the input.

This circuit allows conversion from an arbitrary SOP to a SOP with equal power in both polarizations.

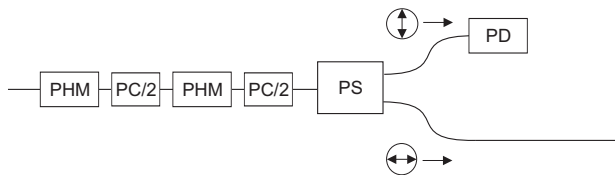


**Figure 8.1:** Schematic of the 50–50 polarization controller.

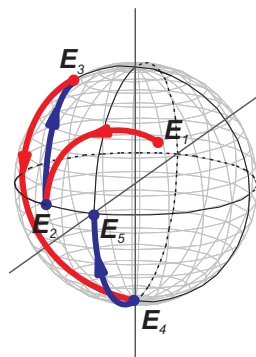


**Figure 8.2:** Poincaré sphere indicating the SOP in the polarization controller.

This concept can be extended to convert an arbitrary polarization at the input to the desired polarization at the PIC. As usually TE polarization is preferred, because of its higher gain, a circuit is presented in which any SOP is converted to TE. The schematic is shown in Fig. 8.3. The SOPs are visualized on the sphere in Fig. 8.4.



**Figure 8.3:** Schematic of the polarization controller.



**Figure 8.4:** Poincaré sphere indicating the SOP in the polarization controller.

The first part (the phase modulator and half PC) of this polarization controller is the same as the previous one. The signal with SOP  $E_3$  enters the second phase modulator. The phase is changed to achieve a left-handed circular polarization ( $E_4$ ). With the last half polarization converter this circular polarization is transformed to the TE output polarization ( $E_5$ ). The detection of the SOP at the output of this controller is much simpler. A PS is used to split the signal in the two polarizations, the TM output is connected to a photodiode. As the desired

output polarization is fully TE, the phase modulators need to be adjusted to have minimum power in TM.

### 8.3.2 Polarization switchable laser

The devices in the previous paragraphs are used as controllers at the input of a PIC. Similar circuits can also be used to achieve polarization control at the output of a PIC. The integration of a laser with a polarization controller is depicted in Fig. 8.5. The integration of the laser depends on the application; it can be a simple Fabry-Pérot laser, a short integrated DBR laser [106] or a multi-wavelength laser [17].

The functioning of the device is the same as in the previous controllers as can be seen in 8.6. The laser has a fixed and stable output polarization, normally TE ( $\mathbf{E}_1$  in 8.6). The first half PC converts the polarization to a circular polarization ( $\mathbf{E}_2$ ). The phase modulator determines the eventual output polarization. The output PC converts the signal back to a linear polarization. If both PCs are the same, a phase shift of  $\pi$  will result in TE output polarization ( $\mathbf{E}_4$ ), zero phase shift will result in TM. Any other phase shift results in a linear SOP with a controllable angle of polarization.



Figure 8.5: Schematic of the laser with switchable polarization.

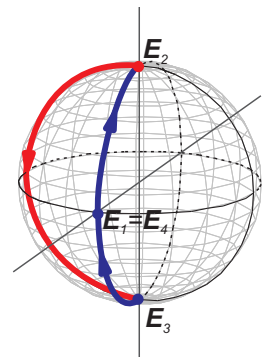


Figure 8.6: Poincaré sphere indicating the SOP in the polarization switchable laser.

The examples treated here, and in the introduction in chapter 1, illustrate the many possibilities that can be achieved if polarization manipulating components are integrated in standard active-passive PICs. On-chip polarization control is very useful in the coherent detection of Differential Phase Shift Keying (DPSK) modulated signals [107, 108], and is required for polarization multiplexing [109, 110].

The generic integration platform for on-chip polarization handling developed in this thesis makes this feasible.





---

# Appendix A

## Polarization description and visualization tools

---

In this appendix the polarization of light in a PIC is described. Jones vectors and matrices are introduced to model the polarization transformation inside optical components. Stokes parameters and the Poincaré sphere are used to visualize the state of polarization.

### A.1 Polarization

A plane wave incident on an interface of two media, as shown in Fig. A.1(a) is reflected at that interface. Two polarizations are observed: TE (Transverse Electric), when the electrical field is parallel to the interface and TM (Transverse Magnetic), when the magnetic field is parallel to the interface. These polarizations differ in the electromagnetic boundary conditions, as the tangential field components of both the Electrical Field  $\mathbf{E}$  and the magnetic field  $\mathbf{H}$  have to be continuous at the boundary. So for TE, the tangential components  $E_x$  and  $H_z$  are continuous over the interface while for TM this holds for  $H_x$  and  $E_z$ .

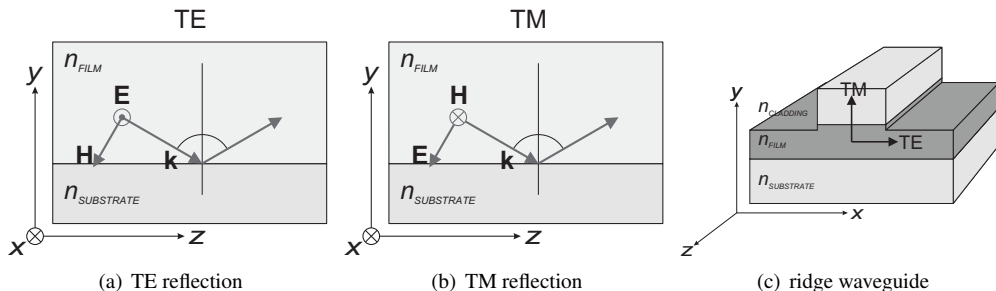
A planar waveguide can be obtained by creating a second reflecting interface, parallel to the first one. The planar waveguide consists of three layers with refractive indices  $n_{\text{FILM}} > n_{\text{SUBSTRATE}}, n_{\text{CLADDING}}$ .

The light will be confined in the layer having the highest index ( $n_{\text{FILM}}$ ), because of total internal reflections.

Two polarization modes for a wave propagating in the  $z$  direction can be found. The definitions

given before, hold for the polarizations: TE polarized light has its electrical field vector  $\mathbf{E}$  parallel to the interfaces, i.e in the  $x$  direction, so  $E_y, E_z = 0$ . . TM polarized light has its magnetic field vector in the  $x$  direction, so  $H_y, H_z = 0$ .

Fig. A.1(c) shows a ridge waveguide used in a PIC. In these waveguides, an additional set of



**Figure A.1:** Waveguides showing the definition of the polarization modes

boundary conditions applies. Because of the presence of the ridge, also two vertical interfaces are present. This ensures that the field is also confined in the  $x$ -direction. In this case pure TE and TM do not exist. A TE polarized mode also has an electric field component perpendicular to an interface: the vertical boundary of the ridge. But, as  $E_y$  (and  $E_z$ ) is close to zero for quasi-TE and  $E_x \approx 0$  (and  $E_z$ ) for quasi-TM, the modes can be approximated by pure TE and TM modes.

The  $\mathbf{H}$  and  $\mathbf{E}$  are related and a wave can be described by regarding the electrical field vector only. Thus, in this thesis, the polarization will be described using the electric field components. Furthermore, the stable polarized modes in waveguide devices will be approximated with TE-modes (only  $E_x$ ) and TM-modes (only  $E_y$ ).

## A.2 Jones vector

The polarization of a mode is defined by the direction of the electrical field vector at a position  $z$ . The polarization can be described as a 2D vector, the Jones vector, containing the two complex amplitudes ( $E_x, E_y$ ) of the electrical field. The transfer function of an optical component can be described by a  $2 \times 2$  Jones matrix. By multiplying the vector with the matrix, the transformation of the polarization state can be described and the output Jones vector can be obtained. In this way a transfer matrix method can be used to model the effect of a set of components on the polarization state.

The electrical field of a mode, propagating in the  $z$ -direction and expressed as a Jones vector, is [111, 112]:

$$\mathbf{E} = \begin{bmatrix} E_x \\ E_y \end{bmatrix} = \begin{bmatrix} |E_x| e^{j\phi_x} \\ |E_y| e^{j\phi_y} \end{bmatrix} \quad (\text{A.1})$$

Here  $|E_{x,y}|$  is the amplitude of the electrical field in the respective direction,  $\phi_{x,y}$  is the phase. For TE polarized light, the electrical field vector is directed in  $x$  direction, hence  $|E_y| = 0$ . For TM  $|E_x| = 0$ , the Jones vectors for the two polarizations are thus:

$$\text{TE} : \begin{bmatrix} |E_x| e^{j\phi_x} \\ 0 \end{bmatrix} \quad \text{TM} : \begin{bmatrix} 0 \\ |E_y| e^{j\phi_y} \end{bmatrix} \tag{A.2}$$

Any state of polarization can be decomposed into the two orthogonal polarizations present inside a waveguide. Some common cases are plotted in Fig. A.2. The magnitude of the electrical field vectors and the phase between them,  $\Delta\phi = \phi_y - \phi_x$ , is indicated.

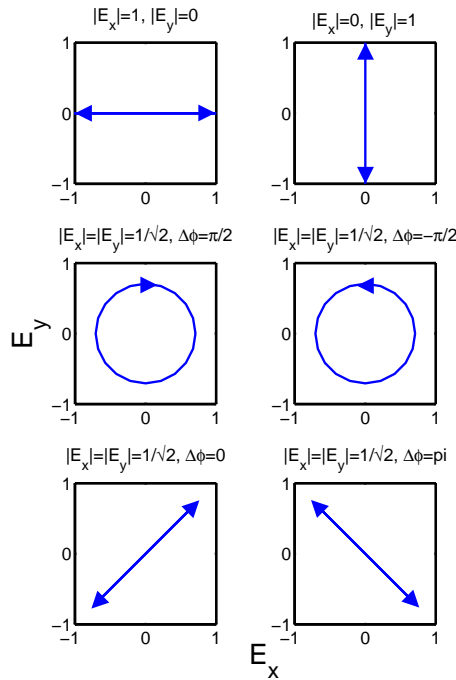


Figure A.2: Different states of polarization constructed from TE and TM polarized modes.

The Jones matrix of an optical component has the form:

$$\mathbf{T} = \begin{bmatrix} J_{11} & J_{12} \\ J_{21} & J_{22} \end{bmatrix} \tag{A.3}$$

Here  $J_{11}$  ( $J_{22}$ ) is the transfer from the TE (TM) at the input to TE (TM) at the output.  $J_{12}$  and  $J_{21}$  are the cross-polarization terms.

### A.3 Stokes parameters

A convenient way to visualize the change in the state of polarization (SOP) will help to understand the polarization behavior of devices. For this, the SOP can be expressed in terms of Stokes parameters [113]. Using the definitions from (A.1), these parameters are written as:

$$s_0 = |E_x|^2 + |E_y|^2 \quad (\text{A.4})$$

$$s_1 = |E_x|^2 - |E_y|^2 \quad (\text{A.5})$$

$$s_2 = 2|E_x||E_y|\cos(\phi_y - \phi_x) \quad (\text{A.6})$$

$$s_3 = 2|E_x||E_y|\sin(\phi_y - \phi_x) \quad (\text{A.7})$$

Here  $s_0$  is the total intensity of the light, equal to  $\sqrt{s_1^2 + s_2^2 + s_3^2}$ . The SOP is expressed by  $s_1$ ,  $s_2$ ,  $s_3$ .  $s_1$  and  $s_2$  describe the portion of the linearly polarized light,  $s_3$  describes the circularly polarized fraction.

A visual interpretation of these Stokes parameters can be obtained by plotting them as coordinates on a sphere having a radius  $s_0$ . From this representation the SOP can be easily observed. Points on the poles of this Poincaré sphere (Fig. A.3) correspond to circularly polarized light: left-handed circular at the south pole, right-handed at the north pole. At the equator the light is linearly polarized, the intersection with the  $s_1$  axis is fully TE or fully TM. At the nearer point,  $s_1 = s_0$ , TE polarized ( $0^\circ$ ). The further point,  $s_1 = -s_0$  indicates TM ( $90^\circ$ ) polarized light. The left and right intersections with the  $s_2$ -axis are the points in which the light has equal amount of TE and TM polarized light ( $\pm 45^\circ$ ). The areas between the poles and the equator describe various elliptical polarization states.

The sphere is very well suited for showing the change in polarization, if the light travels through a photonic device.

This is explained by the example of a polarization-dependent phase shift in a waveguide into which  $45^\circ$  linearly polarized light is fed. The light incident into the waveguide ( $\mathbf{E}_1$ ) can be decomposed into the two orthogonal stable polarization modes present inside the waveguide:  $\mathbf{P}_1$  and  $\mathbf{P}_2$ , in this case TE and TM, respectively, as indicated in Fig. A.4(b).

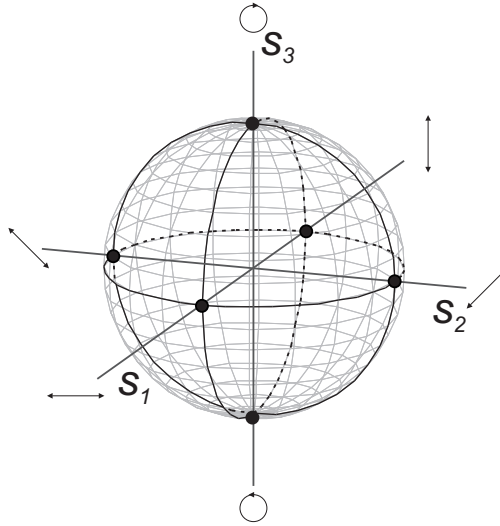
The change in polarization is calculated using the Jones matrix of the phase shifter and is plotted on a Poincaré sphere.

A Jones matrix can be employed to calculate the phase change. The normalized input polarization is:

$$\mathbf{E}_1 = \frac{1}{\sqrt{2}} \begin{bmatrix} 1 \\ 1 \end{bmatrix} \quad (\text{A.8})$$

The transfer matrix of the waveguide employing  $\Delta\phi$  phase shift is given by:

$$\mathbf{T} = \begin{bmatrix} e^{j\Delta\phi} & 0 \\ 0 & 1 \end{bmatrix} \quad (\text{A.9})$$



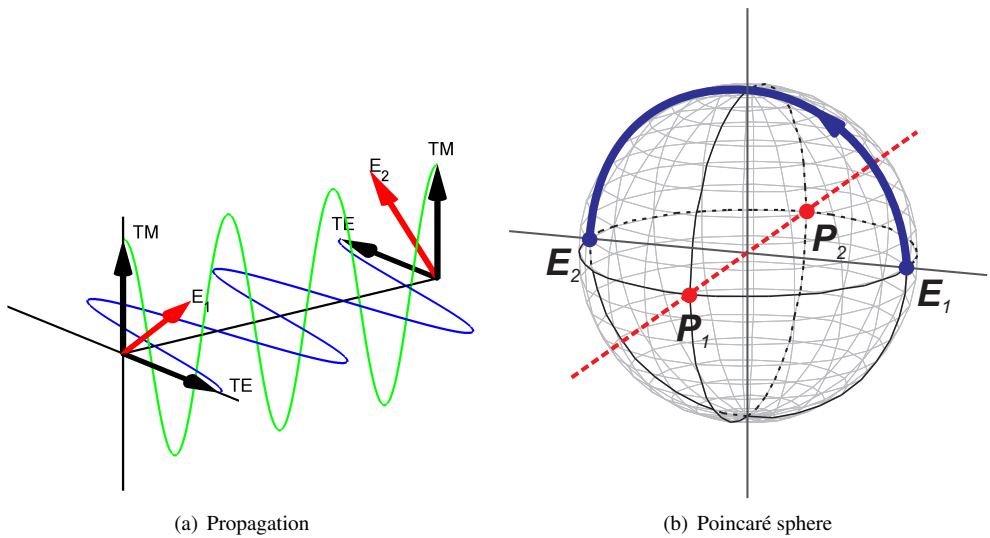
**Figure A.3:** Poincaré sphere for visualizing the state of polarization.

The output polarization  $\mathbf{E}_2$  is obtained from the matrix multiplication:

$$\mathbf{E}_2 = \mathbf{T} \mathbf{E}_1 = \frac{1}{\sqrt{2}} \begin{bmatrix} e^{j\Delta\phi} \\ 1 \end{bmatrix} \tag{A.10}$$

Fig. A.4(a) shows the propagation of the modes through the device. The corresponding Poincaré sphere is plotted in Fig. A.4(b). Those two modes correspond to two points on the sphere, opposite to each other. While propagating through the structure, phase differences between these two stable modes ( $\mathbf{P}_1$  and  $\mathbf{P}_2$ ) occur, which is equivalent to rotating around the axis through these modes. So a phase shift of  $\pi$  translates to a rotation of  $\pi$  radians around the  $s_1$ -axis.

The calculation and visualization methods discussed here will be used to describe the polarization behavior of optical components in PICs. More details can be found in [111, 112, 113].



**Figure A.4:** The change of the polarization when  $\pi$  phaseshift is applied.

---

# References

---

- [1] T. Maiman, "Stimulated optical radiation in ruby," *Nature*, vol. 187, pp. 493–494, Aug. 1960.
- [2] I. Hayashi, M. Panish, P. Foy, and S. Sumski, "Junction lasers which operate continuously at room temperature," *Appl. Phys. Lett.*, vol. 17, no. 3, pp. 109–111, 1970.
- [3] F. Kapron, D. Keck, and R. Maurer, "Radiation losses in glass optical waveguides," *Appl. Phys. Lett.*, vol. 17, no. 10, pp. 423–425, 1970.
- [4] M. Itoh, Y. Shibata, T. Kakitsuka, Y. Kadota, and Y. Tohmori, "Polarization-insensitive SOA with a strained bulk active layer for network device application," *IEEE Photon. Technol. Lett.*, vol. 14, pp. 765–767, June 2002.
- [5] J.-Y. Emery, T. Ducelie, M. Bachmann, P. Doussière, F. Pommereau, R. Ngo, F. Gaborit, L. Goldstein, G. Laube, and J. Barrau, "High performance 1.55  $\mu\text{m}$  polarization-insensitive semiconductor optical amplifier based on low-tensile-strained bulk GaInAsP," *Electron. Lett.*, vol. 33, pp. 1083–1084, June 1997.
- [6] S. Kitamura, K. Komatsu, and M. Kitamura, "Very low power consumption semiconductor optical amplifier array," *IEEE Photon. Technol. Lett.*, vol. 7, pp. 147–148, Feb. 1995.
- [7] P. Doussiere, P. Garabedian, C. Graver, D. Bonnevie, T. Fillion, E. Derouin, M. Monnot, J. Provost, D. Leclerc, and M. Klenk, "1.55  $\mu\text{m}$  polarization independent semiconductor optical amplifier with 25 dB fiber to fiber gain," *IEEE Photon. Technol. Lett.*, vol. 6, pp. 170–172, Feb. 1994.
- [8] R. Hanfoug, J. van der Tol, L. Augustin, and M. Smit, "Wavelength conversion with polarisation labelling for rejection and isolation of signals (POLARIS)," in *Proc. 11th Eur. Conf. on Int. Opt. (ECIO '03)*, pp. 105–108, Prague, Czech Republic, April 2–4 2003.
- [9] J. van der Tol, L. Augustin, U. Khalique, and M. Smit, "Polarization control and its application to waveguide devices," in *Proc. 13th Micro optic Conf. (MOC '07)*, p. C1, Takamatsu, Japan, Oct. 28–31 2007. Invited paper.
- [10] K. Stubkjær, A. Kloch, P. Hansen, H. Poulsen, D. Wolfson, K. Jepsen, A. Clausen, E. Limal, and A. Buxens, "Wavelength converter technology," *IEICE Trans. on Comm.*, vol. E82-B, pp. 390–400, Feb. 1999.



- [11] C. Joergensen, S. Danielsen, K. Stubkjaer, M. Schilling, K. Daub, P. Doussiere, F. Pommerau, P. Hansen, H. Poulsen, A. Kloch, M. Vaa, B. Mikkelsen, E. Lach, G. Laube, W. Idler, and K. Wünstel, "All-optical wavelength conversion at bit rates above 10 Gb/s using semiconductor optical amplifiers," *J. of Sel. Topics in Quantum Electron.*, vol. 3, pp. 1168–1180, Oct. 1997.
- [12] J. Leuthold, J. Eckner, P. Besse, G. Guekos, and H. Melchior, "Dual-order mode (DOMO) all-optical space switch for bidirectional operation," in *Techn. Digest Opt. Fiber Comm. (OFC '96)*, pp. 271–272, San Jose, California, USA, Feb. 20–25 1996.
- [13] D. Wolfson, T. Fjelde, A. Kloch, C. Janz, F. Poingt, I. Guillemot, F. Gaborit, and M. Renaud, "Detailed experimental investigation of an all-active dual-order mode Mach-Zehnder wavelength converter," in *Techn. Digest Opt. Fiber Comm. (OFC '00)*, pp. 72–74, Baltimore, Maryland, USA, March 7–10 2000.
- [14] H. Dorren, D. Lenstra, Y. Liu, M. Hill, and G. Khoe, "Nonlinear polarization rotation in semiconductor optical amplifiers: Theory and application to all-optical flip-flop memories," *IEEE J. Quantum Electron.*, vol. 39, pp. 141–147, Jan. 2003.
- [15] Y. Liu, M. Hill, E. Tangdionga, H. de Waardt, N. Calabretta, G. Khoe, and H. Dorren, "Wavelength conversion using nonlinear polarization rotation in a single semiconductor optical amplifier," *IEEE Photon. Technol. Lett.*, vol. 15, pp. 90–92, Jan. 2003.
- [16] R. Broeke, *A Wavelength Converter Integrated with a Discretely Tunable Laser for Wavelength Division Multiplexing Networks*. PhD thesis, Delft University of Technology, Delft, The Netherlands, 2003.
- [17] J. den Besten, *Integration of Multiwavelength Lasers with Fast Electro-Optical Modulators*. PhD thesis, Technische Universiteit Eindhoven, Eindhoven, The Netherlands, 2004. ISBN 90-386-1643-0.
- [18] Photon Design. FimmWave/FimmProp. <http://www.photond.com>.
- [19] S. Adachi, *Physical properties of III-V semiconductor compounds*. New York: John Wiley and Sons, 1992.
- [20] J. Soole, C. Caneau, H. LeBlanc, N. Andreadakis, A. Rajhel, C. Youtsey, and I. Adesida, "Suppression of modal birefringence in InP-InGaAsP waveguides through use of compensated tensile strain," *IEEE Photon. Technol. Lett.*, vol. 9, pp. 61–63, Jan. 1997.
- [21] EMIS Datareviews Series No. 6, *Properties of Indium Phosphide*. London and New York: INSPEC, 1991. ISBN 0-85296-491-9.
- [22] S. Adachi, *Properties of group-IV, III-V and II-VI semiconductors*. Chichester, England: John Wiley and Sons, 2005. ISBN 0-470-09032-4.
- [23] S. Adachi and K. Oe, "Internal strain and photoelastic effects in  $\text{Ga}_{1-x}\text{Al}_x\text{As}/\text{GaAs}$  and  $\text{In}_{1-x}\text{Ga}_x\text{As}_y\text{P}_{1-y}/\text{InP}$  crystals," *J. Appl. Phys.*, vol. 54, pp. 6620–6627, Nov. 1983.
- [24] C. van Dam, L. Spiekman, F. van Ham, F. Groen, J. van der Tol, I. Moerman, W. Pascher, M. Hamacher, H. Heidrich, C. Weinert, and M. Smit, "Novel compact polarization converters based on ultra short bends," *IEEE Photon. Technol. Lett.*, vol. 8, pp. 1346–1348, Oct. 1996.
- [25] D. Maat, *InP-based integrated MZI switches for optical communications*. PhD thesis, Delft University of Technology, Delft, The Netherlands, 2001. ISBN 90-9014700-4.
- [26] L. Soldano and E. Pennings, "Optical multi-mode interference devices based on self-imaging: Principles and applications," *J. Lightwave Technol.*, vol. 13, pp. 615–627, Apr. 1995.

- [27] M. Hill, X. Leijtens, G. Khoe, and M. Smit, "Optimizing imbalance and loss in  $2 \times 2$  3-dB multimode interference couplers via access waveguide width," *J. Lightwave Technol.*, vol. 21, pp. 2305–2313, Oct. 2003.
- [28] X. Leijtens, P. Le Lourec, and M. Smit, "S-matrix oriented CAD-tool for simulating complex integrated optical circuits," *J. of Sel. Topics in Quantum Electron.*, vol. 2, pp. 257–262, June 1996.
- [29] E. Pennings, R. van Roijen, M. van Stralen, P. de Waard, R. Koumans, and B. Verbeek, "Reflection properties of multimode interference devices," *IEEE Photon. Technol. Lett.*, vol. 6, pp. 715–718, June 1994.
- [30] D. Erasme, L. Spiekman, C. Herben, M. Smit, and F. Groen, "Experimental assessment of the reflection of passive multimode interference couplers," *IEEE Photon. Technol. Lett.*, vol. 9, pp. 1604–1606, Dec. 1997.
- [31] Y. Gottesman, E. Rao, and B. Dagens, "A novel design proposal to minimize reflections in deep-ridge multimode interference couplers," *Electron. Lett.*, vol. 12, pp. 1662–1664, Dec. 2000.
- [32] Y. Barbarin, E. Bente, C. Marquet, E. Leclère, J. Binsma, and M. Smit, "Measurement of reflectivity of butt-joint active-passive interfaces in integrated extended cavity lasers," *IEEE Photon. Technol. Lett.*, vol. 17, pp. 2265–2267, Nov. 2005.
- [33] F. Soares, F. Karouta, B. Smalbrugge, S. Oei, R. Baets, and M. Smit, "InP-based photonic integrated circuit with WDM switched optical delay lines for true-time-delay beamsteering of a 40 GHz phased-array antenna," in *Proc. 12th Eur. Conf. on Int. Opt. (ECIO '05)*, pp. 129–132, Grenoble, France, April 6–8 2005.
- [34] F. Soares, F. Karouta, E. Geluk, J. van Zantvoort, and M. Smit, "A compact and fast photonic True-Time-Delay beamformer with integrated Spot-Size Converters," in *Technical Digest Integr. Photon. Res. and Apps. (IPRA '06)*, p. IMF5, Uncasville, USA, Apr. 24–Apr. 28 2006.
- [35] L. Chusseau, P. Martin, C. Brasseur, C. Alibert, P. Hervé, P. Arguel, F. Lozes-Dupuy, and E. Rao, "Carrier-induced change due to doping in refractive index of InP: Measurements at 1.3 and 1.5  $\mu\text{m}$ ," *Appl. Phys. Lett.*, vol. 69, pp. 3054–3056, Nov. 1996.
- [36] P. Martin, E. M. Skouri, L. Chusseau, C. Alibert, and H. Bissessur, "Accurate refractive index measurements of doped and undoped InP by grating coupling technique," *Appl. Phys. Lett.*, vol. 67, pp. 881–883, Aug. 1995.
- [37] F. Fiedler and A. Schlachetzki, "Optical parameters of InP-based waveguides," *Solid State Electron.*, vol. 30, no. 1, pp. 73–83, 1987.
- [38] C2V. OlympIOs. <http://www.c2v.nl>.
- [39] T. Visser, B. Demeulenaere, J. Haes, D. Lenstra, R. Baets, and H. Blok, "Confinement and modal gain in dielectric waveguides," *J. Lightwave Technol.*, vol. 14, pp. 885–887, May 1996.
- [40] T. Visser, H. Blok, B. Demeulenaere, and D. Lenstra, "Confinement factors and gain in optical amplifiers," *IEEE J. Quantum Electron.*, vol. 33, pp. 1763–1766, Oct. 1997.
- [41] Y. Liu, *All-optical buffering based on nonlinear optical processing with semiconductor optical amplifiers*. PhD thesis, Technische Universiteit Eindhoven, Eindhoven, The Netherlands, 2004. ISBN 90-386-0922-1.

- [42] P. Thijs, *Strained layer InGaAs(P)/InP Quantum Well semiconductor laser grown by organometallic vapour phase epitaxy*. PhD thesis, Technische Universiteit Delft, Delft, The Netherlands, 1994.
- [43] G. Agrawal and N. Olsson, "Self-phase modulation and spectral broadening of optical pulses in semiconductor laser amplifiers," *IEEE J. Quantum Electron.*, vol. 25, pp. 2297–2306, Feb. 1989.
- [44] Y. Barbarin, *1.55  $\mu\text{m}$  integrated modelocked semiconductor lasers*. PhD thesis, Technische Universiteit Eindhoven, Eindhoven, The Netherlands, 2007. ISBN 978-90-386-2013-8.
- [45] N. Storkfelt, M. Yamaguchi, B. Mikkelsen, and K. Stubkjaer, "Recombination constants and  $\alpha$ -factor in 1.5  $\mu\text{m}$  MQW optical amplifiers taking carrier overflow into account," *Electron. Lett.*, vol. 28, pp. 1774–1776, Sept. 1992.
- [46] R. Manning, A. Kelly, A. Poustie, and K. Blow, "Wavelength dependence of switching contrast ratio of semiconductor optical amplifier-based nonlinear loop mirror," *Electron. Lett.*, vol. 34, pp. 916–918, Apr. 1998.
- [47] D. Rogers. CIP. Private communication.
- [48] E. Skogen, J. Barton, S. Denbaars, and L. Coldren, "A quantum-well-intermixing process for wavelength-agile photonic integrated circuits," *IEEE J. Sel. Topics in Quantum Electron.*, vol. 8, pp. 863–869, Jul./Aug. 2002.
- [49] N. Futakuchi, X. Song, D. Miyashita, M. Kato, and Y. Nakano, "Fabrication of InGaAsP/InP Mach-Zehnder interferometer optical amplifier switches by metalorganic vapor phase selective area epitaxy," in *Proc. IPRM01 conference*, pp. 583–586, Nara, Japan, May 14–18 2001.
- [50] L. Xu, M. Gokhale, P. Studenkov, J. Dries, C.-P. Chao, D. Garbuzov, and S. Forrest, "Monolithic integration of an InGaAsP-InP MQW Laser/Waveguide using a Twin-Guide structure with a mode selection layer," *IEEE Photon. Technol. Lett.*, vol. 9, pp. 569–571, May 1997.
- [51] R. Varrazza, I. Djordjevic, and S. Yu, "Active vertical-coupler-based optical crosspoint switch matrix for optical packet-switching applications," *J. Lightwave Technol.*, vol. 22, pp. 2034–2042, Sept. 2004.
- [52] U. Khalique, J. van der Tol, F. Groen, F. Karouta, E. Geluk, and M. Smit, "Polarization based integration scheme (POLIS) for active and passive components," in *Proc. 11th Eur. Conf. on Int. Opt. (ECIO '03)*, pp. 137–140, Prague, Czech Republic, April 2–4 2003.
- [53] J. Binsma, M. van Geemert, F. Heinrichsdorff, T. van Dongen, R. Broeke, and M. Smit, "MOVPE waveguide regrowth in InGaAsP/InP with extremely low butt joint loss," in *Proc. IEEE/LEOS Symposium (Benelux Chapter)*, pp. 245–248, Brussels, Belgium, Dec. 2001.
- [54] 3M. Scotch Magic Tape 810. <http://www.3M.com>.
- [55] G. Maxwell, A. Poustie, C. Ford, M. Harlow, P. Townley, M. Nield, T. Lealman, S. Oliver, L. Rivers, and R. Waller, "Hybrid integration of monolithic semiconductor optical amplifier arrays using passive assembly," in *Electronic Components and Technology Conference (ECTC '05)*, vol. 2, pp. 1349–1352, 31 May–3 June 2005.

- [56] S. Adachi and H. Kawaguchi, "Chemical etching characteristics of (001) InP," *J. Electrochem. Soc.*, vol. 128, pp. 1342–1349, June 1981.
- [57] F. Soares, *Photonic integrated True-Time-Delay Beamformers in InP technology*. PhD thesis, Technische Universiteit Eindhoven, Eindhoven, The Netherlands, 2006. ISBN 90-386-1833-6.
- [58] D. Trommer, R. Steingrüber, R. Löffler, and A. Umbach, "A novel flexible, reliable and easy to use technique for the fabrication of optical spot size converters for InP based PICs," in *Proc. IPRM99 conference*, pp. 12–13, Davos, Switzerland, May 1999.
- [59] J. van der Tol, J. Pedersen, E. Metaal, F. Hakimzadeh, Y. Oei, F. Groen, and I. Moerman, "Realization of a short integrated optic passive polarization converter," *IEEE Photon. Technol. Lett.*, vol. 7, pp. 893–895, Aug. 1995.
- [60] A. Stano, "Chemical etching of InGaAs/InP and InAlAs/InP heterostructures," *J. Electrochem. Soc.*, vol. 134, pp. 448–452, Feb. 1987.
- [61] P. Bowman, E. Ko, and P. Sides, "Potential hazard in preparing bromine-methanol solutions," *J. Electrochem. Soc.*, vol. 137, pp. 1309–1311, Apr. 1990.
- [62] M. Schlak, C. Weinert, P. Albrecht, and H.-P. Nolting, "Tunable TE/TM-mode converter on (001)-InP-substrate," *IEEE Photon. Technol. Lett.*, vol. 3, pp. 15–16, Jan. 1991.
- [63] Y. Shani, R. Alferness, T. Koch, U. Koren, M. Oron, B. Miller, and M. Young, "Polarization rotation in asymmetric periodic loaded rib waveguides," *Appl. Phys. Lett.*, vol. 59, pp. 1278–1280, Sept. 1991.
- [64] H. Heidrich, P. Albrecht, M. Hamacher, H. Nolting, H. Schroeter-Janssen, and C. Weinert, "Passive mode converter with a periodically tilted InP/GaInAsP rib waveguide," *IEEE Photon. Technol. Lett.*, vol. 4, pp. 34–36, Jan. 1992.
- [65] M. Watts and H. Haus, "Integrated mode-evolution-based polarization rotators," *Opt. Lett.*, vol. 30, pp. 138–140, Jan. 2005.
- [66] T. Barwicz, M. Watts, M. Popović, P. Rakich, L. Socci, F. Kärtner, E. Ippen, and H. Smith, "Polarization-transparent microphotonic devices in the strong confinement limit," *Nature Photonics*, vol. 1, pp. 57–60, Jan. 2007.
- [67] D. Beggs, M. Midrio, and T. F. Krauss, "Compact polarization rotators for integrated polarization diversity in InP-based waveguides," *Opt. Lett.*, vol. 32, pp. 2176–2178, Aug. 2007.
- [68] M. Kotlyar, L. Bolla, M. Midrio, L. O'Faolain, and T. F. Krauss, "Compact polarization converter in InP-based material," *Optics Express*, vol. 13, pp. 5040–5045, June 2005.
- [69] B. Holmes and D. Hutchings, "Realization of novel low-loss monolithically integrated passive waveguide mode converters," *IEEE Photon. Technol. Lett.*, vol. 18, pp. 43–45, Jan. 2006.
- [70] F. Groen, Y. Zhu, and J. van der Tol, "Compact polarisation converter on InP/InGaAsP using an asymmetrical waveguide," in *Proc. 11th Eur. Conf. on Int. Opt. (ECIO '03)*, pp. 141–144, Prague, Czech Republic, April 2–4 2003.
- [71] H. El-Refaei, D. Yevick, and T. Jones, "Slanted-rib waveguide InGaAsP-InP polarization converters," *J. Lightwave Technol.*, vol. 22, pp. 1352–1357, May 2004.
- [72] U. Khalique, Y. Zhu, J. van der Tol, L. Augustin, R. Hanfoug, F. Groen, P. van Veldhoven, M. Smit, M. van de Moosdijk, W. de Laat, and K. Simon, "Ultrashort polarization converter on InP/InGaAsP fabricated by optical lithography," in *Technical Digest Integr. Photon. Res. and Apps. (IPRA '05)*, p. IWA3, San Diego, USA, Apr. 11–Apr. 13 2005.

- [73] J. Binsma, R. Broeke, and J. den Besten, "InP-based photonic integration technology," in *Technical Digest Integr. Photon. Res. (IPR '04)*, p. IFB1, San Francisco, USA, Jun. 30–Jul. 2 2004. Invited paper.
- [74] L. Augustin, J. van der Tol, and M. Smit, "A compact passive polarization converter for active-passive integration on InP/InGaAsP," in *Proc. 13th Eur. Conf. on Int. Opt. (ECIO '07)*, p. WA3, Copenhagen, Denmark, April 25–27 2007.
- [75] J. den Besten, M. Dessens, C. Herben, X. Leijtens, F. Groen, M. Leys, and M. Smit, "Low-loss, compact, and polarization independent PHASAR demultiplexer fabricated by using a double-etch process," *IEEE Photon. Technol. Lett.*, vol. 14, pp. 62–64, Jan. 2002.
- [76] Y. Zhu, U. Khalique, J. van der Tol, E. Geluk, F. Groen, F. Karouta, and M. Smit, "Ultrashort, highly efficient integrated optical polarization converter," in *Proc. 12th Eur. Conf. on Int. Opt. (ECIO '05)*, pp. 96–99, Grenoble, France, April 6–8 2005.
- [77] P. Albrecht, M. Hamacher, H. Heidrich, D. Hoffmann, H. Nolting, and C. Weinert, "TE/TM mode splitters on InGaAsP/InP," *IEEE Photon. Technol. Lett.*, vol. 2, pp. 114–115, Feb. 1990.
- [78] L. Soldano, A. de Vreede, M. Smit, B. Verbeek, E. Metaal, and F. Groen, "Mach-Zehnder interferometer polarization splitter in InGaAs/InP," *IEEE Photon. Technol. Lett.*, vol. 6, pp. 402–405, Mar. 1994.
- [79] A. Vellekoop and M. Smit, "A small-size polarization splitter based on a planar optical phased array," *J. Lightwave Technol.*, vol. 8, pp. 118–124, Jan. 1990.
- [80] F. Ghirardi, J. Brandon, M. Carré, A. Bruno, L. Maignaux, and A. Carenco, "Polarization splitter based on modal birefringence in InP/InGaAsP optical waveguides," *IEEE Photon. Technol. Lett.*, vol. 5, pp. 1047–1049, Sept. 1993.
- [81] I. Kiyat, A. Aydinli, and N. Dagli, "A compact silicon-on-insulator polarization splitter," *IEEE Photon. Technol. Lett.*, vol. 17, pp. 100–102, Jan. 2005.
- [82] H. Fukuda, K. Yamada, T. Tsuchizawa, T. Watanabe, H. Shinjima, and S. i. Itabashi, "Ultrasmall polarization splitter based on silicon wire waveguides," *Optics Express*, vol. 14, pp. 12401–12408, Dec. 2006.
- [83] J. van der Tol, J. Pedersen, E. Metaal, Y. Oei, H. van Brug, and I. Moerman, "Mode evolution type polarization splitter on InGaAsP/InP," *IEEE Photon. Technol. Lett.*, vol. 5, pp. 1412–1414, Dec. 1993.
- [84] J. van der Tol, J. Pedersen, E. Metaal, J.-W. van Gaalen, Y. Oei, and F. Groen, "A short polarization splitter without metal overlays on InGaAsP-InP," *IEEE Photon. Technol. Lett.*, vol. 9, pp. 209–211, Feb. 1997.
- [85] R. M. de Ridder, A. Sander, A. Driessen, and J. Fluitman, "An integrated optic adiabatic TE/TM mode splitter on silicon," *J. Lightwave Technol.*, vol. 11, pp. 1806–1811, Nov. 1993.
- [86] M. Watts, H. Haus, and E. Ippen, "Integrated mode-evolution-based polarization splitter," *Opt. Lett.*, vol. 30, pp. 967–969, May 2005.
- [87] V. Zabelin, L. Dunbar, N. L. Thomas, R. Houdré, M. Kotlyar, L. O'Faolain, and T. Krauss, "Self-collimating photonic crystal polarization beam splitter," *Opt. Lett.*, vol. 32, pp. 530–532, Mar. 2007.
- [88] M. G. Wilson and G. Teh, "Tapered optical directional coupler," *IEEE Transactions on Microwave Theory and Techniques*, vol. 23, pp. 85–92, Jan. 1975.

- [89] H. Zappe, *Introduction to Semiconductor Integrated Optics*. Boston: Artech House Publishers, 1995. ISBN 0-089006-789-9.
- [90] K. Chiang, "Performance of the effective-index method for analysis of dielectric waveguides," *Opt. Lett.*, vol. 16, pp. 714–716, Oct. 1991.
- [91] H. Unger, *Planar optical waveguides and fibres*. Oxford: Clarendon press, 1977.
- [92] E. Patent, *Optical Self-Switching Effects in Mach-Zehnder Interferometers*. PhD thesis, Technische Universiteit Eindhoven, Eindhoven, The Netherlands, 2005. ISBN 90-744-4571-3.
- [93] L. Augustin, J. van der Tol, R. Hanfoug, and M. Smit, "Design of a single etchstep fabrication-tolerant polarisation splitter," in *Proc. 12th Eur. Conf. on Int. Opt. (ECIO '05)*, pp. 125–128, Grenoble, France, April 6–8 2005.
- [94] W.-P. Huang, "Coupled-mode theory for optical waveguides: an overview," *J. Opt. Soc. Am. A*, vol. 11, Mar. 1994.
- [95] C. Janz, B. Lavigne, F. Poingt, I. Guillemot, F. Gaborit, B. Dagens, D. Chiaroni, and M. Renaud, "Low-penalty 10 Gbit/s operation of polarization-insensitive Mach-Zehnder wavelength converters based on bulk-tensile active material," in *Techn. Digest Opt. Fiber Comm. (OFC '98)*, pp. 101–102, San Jose, California, USA, February 22–27 1998.
- [96] C. Joergensen, S. Danielsen, T. Durhuus, B. Mikkelsen, K. Stubkjaer, N. Vodjdani, F. Ratovelomanana, A. Enard, G. Glastre, and D. R. R. Blondeau, "Wavelength conversion by optimized monolithic integrated Mach-Zehnder interferometer," *IEEE Photon. Technol. Lett.*, vol. 8, pp. 521–523, Apr. 1996.
- [97] T. Keating, J. Minch, C. Chang, P. Enders, W. Fang, S. Chuang, T. Tanbun-Ek, Y. Chen, and M. Sergent, "Optical gain and refractive index of a laser amplifier in the presence of pump light for cross-gain and cross-phase modulation," *IEEE Photon. Technol. Lett.*, vol. 9, pp. 1358–1360, Oct. 1997.
- [98] J. Vegas Olmos, *Label-controlled optical switching nodes*. PhD thesis, Technische Universiteit Eindhoven, Eindhoven, The Netherlands, 2006. ISBN 978-90-386-1843-2.
- [99] R. Hanfoug, L. Augustin, J. van der Tol, R. Broeke, and M. Smit, "Optical bandwidth of Mach-Zehnder interferometer wavelength converters," in *Technical Digest Integr. Photon. Res. (IPR '04)*, p. JWB19, San Fransisco, USA, Jun. 30–Jul. 4 2004.
- [100] M. Heck, E. Bente, Y. Barbarin, D. Lenstra, and M. Smit, "Simulation of mode-locked ring lasers including integrated passive components for dispersion compensation," in *Proc. IEEE/LEOS Symposium (Benelux Chapter)*, pp. 159–162, Ghent, Belgium, Dec. 2004.
- [101] B. Mikkelsen, M. Vaa, H. Poulsen, S. Danielsen, C. Joergensen, A. Kloch, P. Hansen, K. Stubkjaer, K. Wünnstel, K. Daub, E. Lach, G. Laube, W. Idler, M. Schilling, and S. Bouchoule, "40 Gbit/s all-optical wavelength converter and RZ-to-NRZ format adapter realised by monolithic integrated active Michelson interferometer," *Electron. Lett.*, vol. 33, no. 2, pp. 133–134, 1997.
- [102] D. Tsiokos, P. Bakopoulos, O. Zouraraki, D. Apostolopoulos, D. Petrantonakis, G. Maxwell, A. Poustie, and H. Avramopoulos, "Integrated MZI-based all-optical clock and data recovery for asynchronous variable packet length traffic," in *Proc. 31st Eur. Conf. on Opt. Comm. (ECOC '05)*, p. We4.P.022, Glasgow, Scotland, Sep. 25–29 2005.

- [103] P. Bakopoulos, D. Tsiokos, O. Zouraraki, H. Avramopoulos, G. Maxwell, and A. Poustie, "Compact all-optical packet clock and data recovery circuit using generic integrated MZI switches," *Optics Express*, vol. 13, pp. 6401 – 6406, Aug. 2005.
- [104] H.-D. Jung, I. Monroy, A. Koonen, and E. Tangdiongga, "All-optical data vortex node using an MZI-SOA switch array," *IEEE Photon. Technol. Lett.*, vol. 19, pp. 1777–1779, Nov. 2007.
- [105] Virtual Photonics Incorporated. VPItransmissionMaker. <http://www.vpiphotonics.com>.
- [106] B. Docter, T. Segawa, T. Kakitsuka, S. Matsuo, T. Ishii, Y. Kawaguchi, Y. Kondo, H. Suzuki, F. Karouta, and M. Smit, "Short-cavity DBR laser using vertical groove gratings for large-scale photonic integrated circuits," *IEEE Photon. Technol. Lett.*, vol. 19, pp. 1469–1471, Oct. 2007.
- [107] C. Doerr, Zhang, S. Chandrasekhar, and L. Buhl, "Monolithic DQPSK receiver in InP with low polarization sensitivity," *IEEE Photon. Technol. Lett.*, vol. 19, pp. 1765–1767, Nov. 2007.
- [108] C. R. Doerr, L. Zhang, L. L. Buhl, J. H. Sinsky, A. H. Gnauck, P. J. Winzer, A. L. Adamiecki, and N. J. Sauer, "High-speed InP DQPSK receiver," in *Techn. Digest Opt. Fiber Comm. (OFC '08)*, p. PDP23, San Diego, USA, Feb. 2008.
- [109] D. van den Borne, S. Jansen, E. Gottwald, P. Krummrich, G. Khoe, and H. de Waardt, "1.6-b/s/Hz spectrally efficient transmission over 1700 km of SSMF using  $40 \times 85.6$ -Gb/s POLMUX-RZ-DQPSK," *J. Lightwave Technol.*, vol. 25, pp. 222–232, Jan. 2007.
- [110] C. R. Doerr and L. Zhang, "Monolithic 80-Gb/s dual-polarization On-Off-Keying modulator in InP," in *Techn. Digest Opt. Fiber Comm. (OFC '08)*, p. PDP19, San Diego, USA, Feb. 2008.
- [111] B. Saleh and M. Teich, *Fundamentals of Photonics*. John Wiley & Sons Inc., 2007. ISBN 0-471-35832-9.
- [112] C.-L. Chen, *Elements of optoelectronics and fiber optics*. USA: Irwin, 1996. ISBN 0-256-14182-7.
- [113] M. Born and E. Wolf, *Principles of Optics*. Pergamon Press, sixth ed., 1993.

---

# List of abbreviations

---

ASE	Amplified Spontaneous Emission
BER	Bit Error Rate
BPF	Bandpass filter
BPM	Beam Propagation Method
CW	Continuous Wave
DC	Direct Current
DPSK	Differential Phase Shift Keying
EDFA	Erbium Doped Fiber Amplifier
EIM	Effective Index Method
ER	Extinction Ratio
FSK	Frequency Shift Keying
FFT	Fast Fourier Transformation
FMW	Fiber Matched Waveguide
MFD	Mode Field Diameter
MMI	Multimode Interference
MOVPE	Metal-Organic Vapour-Phase Epitaxy
MUFINS	MUlti - Functional INtegrated arrays of interferometric Switches
MZI	Mach-Zehnder Interferometer
OOK	On-Off Keying
OSA	Optical Spectrum Analyzer
PC	Polarization Converter
PECVD	Plasma Enhanced Chemical Vapour Deposition
PESSOA	Polarization Effect Suppression in Semiconductor Optical Amplifiers
PI	Polyimide
PIC	Photonic Integrated Circuit
PMF	Polarization Maintaining Fiber
PolMZI	Polarization Mach Zehnder Interferometer



---

POLARIS	POLarization LABELing for Rejection and Isolation of Signals
PS	Polarization Splitter
QW	Quantum Well
RIE	Reactive Ion Etching
SMF	Single Mode Fiber
SOA	Semiconductor Optical Amplifier
SOP	State Of Polarization
SPM	Self Phase Modulation
SSC	Spot Size Converter
STOLAS	Switching Technologies for Optically Labeled Signals
TE	Transverse Electric
TM	Transverse Magnetic
TLS	Tuneable laser source
WDM	Wavelength Division Multiplexing
VPI	Virtual Photonics Incorporated
WLC	Wavelength Converter
XPM	Cross Phase Modulation

---

# Summary

---

## Polarization Handling in Photonic Integrated Circuits

Photonic Integrated Circuits (PICs) are usually polarization dependent. A changing polarization of the light coupled into these circuits can severely degrade their performance. On-chip manipulation of the polarization can help to improve this and to add extra functionality based on polarization.

The aim of this thesis is to develop a generic integration technology with polarization handling capability. The main effort of the work focusses on extending the standard technology for PICs with a new type of polarization converter. Furthermore a novel type of polarization splitter has been developed that consists of a passive Mach Zehnder Interferometer and polarization converters. Thus by only adding a polarization converter, the generic platform with polarization handling, including a polarization splitter is obtained. Moreover by the addition of a spot size converter packaging of the PICs becomes feasible.

The polarization can be applied to add functionality. For example the performance of a wavelength converter can be optimized using the polarization. Wavelength converters are key components in optical telecommunications networks, but the available devices have several problems. Firstly they need expensive tunable wavelength filters at the output, and secondly they are highly polarization dependent.

The application of polarization handling is demonstrated by a new type of integrated wavelength converter: POLARIS (Polarization LABelling for Rejection and Isolation of Signals). This wavelength converter uses the polarization of the light to label the original and the converted signals. By using a polarization splitter, the two signals can be separated and filtered. This approach can also be used in all-optical switches. In this way tunable filters and polarization dependence are avoided.

On-chip polarization manipulation can be used in a number of other circuits as well to enable a broad variety of functions and improvements (for example: polarization independent optical amplifiers, on-chip polarization controller, a laser with a switchable output polarization).

To demonstrate the generic integration platform, the development and realization of polarization converters and polarization splitters, together with standard passive (waveguides, couplers) and active (semiconductor optical amplifiers) components is needed.

The standard components are designed and a standard fabrication process is developed in which all these components can be integrated.

Two generations of polarization converters are realized. The first device has an efficient and short design, but it proved to be difficult to integrate it with active components. A second generation converter is designed, fabricated and characterized. This device is well suited for integration and has a high conversion.

Furthermore, two types of polarization splitters are demonstrated. Also these devices need to fit in the standard fabrication. One design is a relatively long device, tolerant to fabrication variations, but leading to complications with integration. A second design is shorter and consists only of a passive Mach Zehnder interferometer with polarization converters in the arms. This splitter fits exactly in the integration scheme, so this is the device of choice for the generic integration technology.

Moreover an array of Mach Zehnder Interferometers with SOAs in the arms is designed and fabricated. This circuit can be used in wavelength converters and all-optical switches. The device is integrated with spotsizer converters to enable packaging. With the packaged device wavelength conversion up to 40 Gb/s is demonstrated.

The POLARIS concept is demonstrated by simulations and experimentally verified. An integrated version of POLARIS is designed. The generic integrated polarization handling technology is demonstrated by realizing this circuit. The realization clearly showed that the integration scheme is useable, because working examples of all relevant components were present on the chip. Unfortunately due to time constraints not all processing steps were sufficiently optimized, leading to a too low yield of working components; therefore no POLARIS operation could be shown with the integrated device.

This thesis describes the theory, design, fabrication and characterization of polarization handling components, as well as passive and active components, integrated in InP/InGaAsP. A generic integration technology for Photonic Integrated Circuits is developed. Circuits constructed with the components of this technology can be made polarization insensitive and can have additional functionality based on polarization.

---

# Samenvatting

---

## Polarisatie beheer in geïntegreerde fotonische schakelingen

Geïntegreerde fotonische schakelingen (PICs = Photonic Integrated Circuits) zijn meestal polarisatie afhankelijk. Een veranderende polarisatie van het licht aan de ingang van deze circuits kan hun functionaliteit aanzienlijk laten afnemen. Flinkere verbeteringen kunnen verkregen worden door de polarisatie te manipuleren op de chip. Bovendien kan de polarisatie gebruikt worden om nieuwe functies te realiseren op de chip.

Het doel van dit proefschrift is het ontwikkelen van een generieke integratie technologie met de mogelijkheid om de polarisatie te manipuleren. Het hoofddeel van het werk is gericht op het uitbreiden van de standaard technologie voor PICs met een nieuw type polarisatie omzetter. Verder is een nieuw soort polarisatie splitser ontwikkeld die bestaat uit een passieve Mach Zehnder interferometer en polarisatie omzeters. Dus door het toevoegen van de technologie voor polarisatie omzeters aan de bestaande standaard ontstaat een generiek technologie platform voor geïntegreerd polarisatie beheer, inclusief polarisatie splitsers. Door de toevoeging van een bundelgrootte-aanpasser aan deze technologie, wordt het mogelijk om glasvezels makkelijker en nauwkeuriger uit te lijnen ten opzichte van de chips en zo de mogelijkheid te hebben om de chips af te monteren.

De polarisatie kan gebruikt worden om extra functies toe te voegen. Zo kunnen de prestaties van bijvoorbeeld een golflengte omzetter geoptimaliseerd worden door gebruik te maken van polarisatie. Golflengte omzeters zijn cruciale componenten in optische telecommunicatie netwerken, maar de huidige beschikbare componenten hebben een aantal problemen. Allereerst is het noodzakelijk om dure verstembare filters toe te passen aan de uitgang om het originele en het omgezette signaal te scheiden. Bovendien zijn ze erg polarisatie afhankelijk.

Het beheer van de polarisatie is aangetoond door de toepassing hiervan in een nieuw soort geïntegreerde golflengte omzetter: POLARIS (POLarization LABelling for Rejection and Isolation of Signals). Deze golflengte omzetter benut de polarisatie van het licht om een label

toe te kennen aan het originele en omgezette signaal. Met een polarisatie splitter kunnen deze twee signalen van elkaar gescheiden worden. Op deze manier hoeven geen verstembare filters gebruikt te worden en wordt polarisatie afhankelijkheid vermeden.

Voor de toepassing van de generieke integratie technologie, is het noodzakelijk om polarisatie omzeters en polarisatie splitters, en standaard passieve (golfgeluiders, koppelaars) en actieve (optische versterkers) componenten te realiseren. De standaard componenten zijn ontworpen en een standaard fabricage technologie is ontwikkeld waarmee deze componenten geïntegreerd kunnen worden.

Twee generaties polarisatie omzeters zijn ontwikkeld. De eerste generatie omzetter heeft een efficiënt en kort ontwerp, maar is moeilijk te integreren met actieve componenten. Een tweede generatie is ontworpen, gerealiseerd en gekarakteriseerd. Deze component is zeer geschikt om te integreren en heeft een hoge efficiënte omzetting.

Verder zijn twee types polarisatie splitters gedemonstreerd. Deze moeten ook passen in de standaard fabricage technologie. Het eerste ontwerp is een relatief lange component, tolerant voor fabricage variaties, maar lastig om te integreren. Een tweede ontwerp is korter, dit bestaat alleen uit een passieve Mach Zehnder interferometer met polarisatie omzeters in de armen. Deze component past precies in het voorgestelde integratie schema, dus dit is de component die zich het beste leent voor een generiek integratie platform.

Bovendien is een geïntegreerde reeks van Mach Zehnder interferometers met optische versterkers in de armen ontworpen en gerealiseerd. Deze schakeling kan toegepast worden als golfengte omzetter en als volledig optische schakelaar. Het circuit is geïntegreerd met bundelgrootte-aanpassers zodat het mogelijk is om de chip af te monteren. De afgemonteerde schakeling is gebruikt als golfengte omzetter en werking op 40 Gb/s is gedemonstreerd.

Het POLARIS concept is aangetoond met behulp van simulaties en experimenteel geverifieerd. Een geïntegreerde versie van POLARIS is ontworpen. De generieke technologie voor polarisatie beheer is aangetoond met de realisatie van deze schakeling. Deze realisatie bewijst dat het voorgestelde integratie schema bruikbaar is, want er zijn werkende voorbeelden van alle op de chip aanwezige componenten. Helaas zijn door tijdgebrek niet alle proces stappen voldoende geoptimaliseerd. Dit heeft geleid tot een onvoldoende hoge opbrengst van werkende componenten; hierdoor kan het POLARIS principe niet aangetoond worden met de geïntegreerde schakeling.

Dit proefschrift beschrijft de theorie, het ontwerp, de fabricage en de karakterisatie van zowel polarisatie componenten, als passieve en actieve componenten, geïntegreerd in InP/InGaAsP. Een generieke integratie technologie voor geïntegreerde fotonische schakelingen is ontwikkeld. Schakelingen, die gebruik maken van componenten gemaakt met deze technologie, kunnen ongevoelig voor polarisatie gemaakt worden en bovendien extra functionaliteit bezitten, gebaseerd op polarisatie.

---

# Dankwoord

---

Dan is het zover, aan het eind van het schrijfwerk ben je eindelijk op het punt beland dat je aan het dankwoord mag beginnen. Al snel loopt het over van de cliché's, die allemaal even waar zijn: "promoveren kun je niet alleen" en zeker niet in een zo multidisciplinaire vakgroep als OED. Daarom wil ik dan ook iedereen bedanken die zijn of haar steentje heeft bijgedragen aan het tot stand komen van dit proefschrift.

Uiteraard wil ik als allereerste Meint bedanken. Het is een fijne tijd geweest bij OED, en dat is het nog steeds! Bedankt voor je kritische blik op mijn artikelen en zeker op mijn proefschrift, dat was voor mij erg nuttig. Ik ben blij dat ik nog een tijdje mag blijven in je groep en zo kan meewerken aan de volgende stap.

Natuurlijk wil ik Jos enorm bedanken, niet enkel als copromotor, maar zeker als begeleider en mentor. Met veel plezier heb ik met jou samengewerkt, en veel van je geleerd. Ik ben blij dat ik de passie voor polarisatie met je mag delen! Bedankt voor het motiveren als een chip mislukt was en voor het bijschaven van zo ongeveer alles wat ik de afgelopen jaren geproduceerd heb: van ontwerpen, tot masker layouts, tot en met dit proefschrift. Bovendien was het altijd weer gezellig om samen te reizen naar conferenties en vergaderingen van Japan tot de VS en van Griekenland tot Noorwegen.

Prof. Roel Baets, mijn tweede promotor, van harte bedankt voor het luisteren en vragen stellen tijdens de twee-maandelijks sessies in Eindhoven. Deze waren steeds een nuttige aanvulling. Verder wil ik de leden van de promotie commissie bedanken: Prof. Alfred Driessen, bedankt voor uw opmerkingen op mijn manuscript. Prof. Anton Tjihuis, hartstikke bedankt voor uw grondige en zeer zinvolle commentaar.

Graeme Maxwell, thanks a lot for your participation in my committee, for your comments and questions and for the fun time we had on the MUFINS meetings. Rabah, thanks for the nice time we had together when you were working here. Thanks for participating in the committee.

Verder wil ik op deze plaats onze cleanroom-technici bedanken. In alfabetische volgorde, dat is

het eerlijkste want jullie hebben me allemaal geweldig geholpen. Barry, de OED-troubadour, je hebt me al fantastisch geholpen met mijn gepruts met kleine stukjes GaAs voor mijn VCSELs tijdens mijn afstuderen. En je hulp is sindsdien alleen maar toegenomen, van broom-methanol etsen tot goud-platen en van stain-etsen tot klieven. Ik hoop dat je 2 juni je gitaar bij je hebt.

Ben, wat hebben we veel aan jou te danken! Zowel technisch, wat betreft de mooie nieuwe machines maar zeker ook sociaal: de OED-borrels, koffiepauzes en groepsuitjes.

Erik Jan, dit proefschrift zou dun zijn zonder jouw hulp. Hartstikke bedankt voor al die uren SEMmen en EBLen. Je hebt me hier veel over geleerd en ze zijn een belangrijk onderdeel van mijn werk geworden. Het is prijzenswaardig hoe je je rust bewaart, zelfs als het platina bijgevoeld moet worden in een opgedroogde FC2000.

Kitty, wat is het jammer dat je weg bent! Jij was een aanwinst voor de groep, je verhelderende kijk op onze processing heeft me echt grote stappen vooruit geholpen. Aan jou heb ik bijna een heel hoofdstuk te danken: de schuivende maskers, lastige ICP etsen en de diepe precisieklief-etsen hebben erg mooie resultaten opgeleverd. Hartstikke bedankt!

Tjibbe, van harte bedankt voor de vele hulp. Er is geen chip te vinden waar jij niet aan hebt meegewerkt. Van polyimide spinnen tot RIE etsen, dat heb ik allemaal van jou geleerd. Buiten het technische deel was het altijd weer gezellig tijdens en na de borrels en kerstvieringen.

Vanzelfsprekend wil ik alle andere collega's bedanken. Fouad en Siang, bedankt voor jullie hulp op technologisch gebied, voor het antwoord op de vele vragen en voor de ontwikkeling van standaard en niet-zo-standaard technologie. Xaveer, bedankt voor alle hulp op software en modelleer gebied. Erwin bedankt voor alle hulp wat betreft metingen en karakteriseren van mijn chips.

Hans, hartstikke bedankt voor je hulp bij zo ongeveer alles: van computers, bureaus, bestellingen, tot en met de koffie. Ik ga geen poging wagen om een opsomming te maken, die zou toch niet toereikend zijn.

Martijn en Els, als generatiegenootjes hebben we veel samen opgetrokken. Martijn, jij hebt het al gezegd, we hebben veel positieve maar ook frustrerende momenten meegemaakt. Bedankt voor het luisteren en voor jullie adviezen, en natuurlijk voor de discussies over en op het werk, maar zeker ook daarnaast.

Boudewijn, mijn kamergenoot. Jij hebt flink wat te verduren gehad het afgelopen jaar, met die twee gestreste collega's. Bedankt voor je begrip en succes met jouw onderzoek. Milan, bedankt voor je gezelligheid en veel succes met je lasertjes.

Uzma and Youcai, thanks for your help and cooperation in making the polarization converters. Fokke bedankt voor je hulp en ideeën voor de polarisatie metingen.

Bauke, Pietro, Ling, Omar, Jose, Stefano, Hugo, Frederic, and Martin, thanks for being nice colleagues.

Susan, José en zeker Els, bedankt voor de ondersteuning op velerlei gebied.

Genia, heel erg bedankt voor de fijne tijd die we samen hebben gehad bij OED. Ik heb veel van je geleerd en ben goed bevriend geraakt met jou. Vooral onze etentjes moeten we blijven voortzetten.

Jan Hendrik, Mirvais, Mark, Roger, Francisco, Ronald, Yohan, Thieu, Aert, de oud-gedienden, ik heb jullie altijd als fijne collega's ervaren.

Buiten onze eigen groep is er nog een aantal mensen dat ik wil bedanken. Iedereen bij voormalig JDS-Uniphase in Eindhoven, en met name Hans Binsma, bedankt voor de wafers.

I want to thank everybody at CIP for the wafers that were the basis of many of my successful experiments. Special thanks to Dave Rogers and Alistair Poustie, for your questions and answers, and of course for the good time on the Greek islands.

Ik wil iedereen bij ASML, en met name Wim de Laat, Michel van de Moosdijk en Paul van Dijk bedanken voor de vele hulp in het maken van de polarisatie componenten op de ASML machines. Het was flink klussen, maar het heeft hele mooie resultaten opgeleverd!

Johan van Zantvoort, bedankt voor de hulp bij het meten met de fiber-arrays, met de technische hulp van allerlei aard, en natuurlijk voor de gezelligheid op de borrels, barbecues en andere gelegenheden.

Hyun-Do thanks for helping me with the dynamic measurements.

Bas, bedankt voor de fijne samenwerking, de chips die we samen hebben gemaakt hebben een mooi lijstje publicaties opgeleverd! Het is erg plezierig om werk en vriendschap te kunnen combineren.

Naast fijne collega's is het cruciaal om mensen om je heen te hebben waar je te allen tijde op kunt rekenen voor steun en zeker voor ontspanning. Nu heb ik de mogelijkheid om jullie te bedanken, de vrienden van Praeclara, mijn familie, en uiteraard mijn vrienden in Maastricht. Ivo en Gerard wil ik hierbij speciaal noemen. Bedankt dat jullie als mijn paranimfen willen optreden.

In het bijzonder wil ik Gwennie bedanken, "hiel erreg bedaank veur alles, veur dien interesse, gedöld en steun". Ik wil afsluiten met het bedanken van mijn ouders, "pap en mam, hartstikke bedaank veur de motivatie, begrip en höllep, zonder uuch waor dit noets gelök!"

Luc





---

# Curriculum Vitae

---

Ludovicus (Luc) M. Augustin was born in Maastricht, The Netherlands, in 1978. He received the M.Sc. degree in electrical engineering from Eindhoven University of Technology, Eindhoven, The Netherlands, in 2002.

His masters thesis work was carried out at the COBRA Research institute, Eindhoven University of Technology, on the manufacturing and characterization of polarization controlled VCSELS.

In 2002 he started his Ph.D. research in the Opto Electronic Devices group. He was involved in research on the integration of polarization components with active and passive structures on InP-based material.

He is currently working as a researcher in the same group working on the optimization of the active-passive integration technology.



---

# List of publications

---

## Journal articles

- L.M. Augustin, J.J.G.M. van der Tol, E.J. Geluk and M.K. Smit, “Short polarization converter optimized for active-passive integration in InGaAsP/InP,” *IEEE Photon. Technol. Lett.*, vol. 19, no. 20, pp. 1673-1675, Oct. 2007.
- L.M. Augustin, R. Hanfoug, J.J.G.M. van der Tol, W.J.M. de Laat, and M.K. Smit, “A Compact Integrated Polarization Splitter/Converter in InGaAsP/InP,” *IEEE Photon. Technol. Lett.*, vol. 19, no. 17, pp. 1286-1288, Sep. 2007.
- B. Huiszoon, L.M. Augustin, E.A.J.M. Bente, H. de Waardt, G.D. Khoe, M.K. Smit, and A.M.J. Koonen, “Integrated Mach-Zehnder based spectral amplitude OCDMA on a passive optical network,” *IEEE J. Sel. Topics in Quantum Electron.*, vol. 13, no. 5, pp. 1487-1496, Sep./Oct. 2007.
- B. Huiszoon, L.M. Augustin, R. Hanfoug, L. Bakker, M. Sander-Jochem, E. Fledderus, G.D. Khoe, J.J.G.M. van der Tol, H. de Waardt, M.K. Smit, and A.M.J. Koonen, “Integrated parallel spectral OCDMA en/decoder,” *IEEE Photon. Technol. Lett.*, vol. 19, no. 7, pp. 528–530, Apr. 2007.
- L.M. Augustin, J.J.G.M. van der Tol, R. Hanfoug, W.J.M. de Laat, M.J.E. van de Moosdijk, P.W.L. van Dijk, Y.S. Oei, and M.K. Smit, “A single etch-step fabrication-tolerant polarization splitter,” *J. Lightwave Technol.*, vol. 25, no. 3, pp. 740–746, Mar. 2007.
- R. Hanfoug, L.M. Augustin, Y. Barbarin, J.J.G.M. van der Tol, E. Bente, F. Karouta, D. Rogers, S. Cole, Y. Oei, X. Leijtens, and M.K. Smit, “Reduced reflections from multimode interference couplers,” *Electron. Lett.*, vol. 42, pp. 465–466, Apr. 2006.

## Conference contributions

### International conferences

- L.M. Augustin, J.J.G.M. van der Tol, E.J. Geluk, Y.S Oei, and M.K. Smit, “Method for polarization effect suppression in semiconductor optical amplifiers,” accepted for *Proc. 14th Eur. Conf. on Int. Opt. (ECIO '08)*, Eindhoven, The Netherlands, Jun. 2008.

- J.J.G.M. van der Tol, L.M. Augustin, A.A.M. Kok, U. Khalique, and M.K. Smit, "Use of polarization in InP-based integrated optics," in *2008 Conference on Lasers and Electro-Optics (CLEO)*, San Jose, USA, May 2008. Invited paper.
- B. Huiszoon, A. Leinse, D.H. Geuzebroek, L.M. Augustin, E.J. Klein, H. de Waardt, G.-D. Khoe, and A.M.J. Koonen, "Multi-stage cascade and tree en/decoders integrated in  $\text{Si}_3\text{N}_4$ - $\text{SiO}_2$  for spectral amplitude OCDMA on PON," in *Techn. Digest Opt. Fiber Comm. (OFC '08)*, p. OMR4, San Diego, USA, Feb. 2008.
- J.J.G.M. van der Tol, L.M. Augustin, U. Khalique, and M.K. Smit, "Polarization control and its application to waveguide devices," in *Proc. 13th Micro Optic Conf. (MOC '07)*, p. C1, Takamatsu, Japan, Oct. 28-31 2007. Invited paper.
- L.M. Augustin, J.J.G.M. van der Tol, and M.K. Smit, "A compact passive polarization converter for active-passive integration on InP/InGaAsP," in *Proc. 13th Eur. Conf. on Int. Opt. (ECIO '07)*, p. WA3, Copenhagen, Denmark, Apr. 25–27 2007.
- L.M. Augustin, J.J.G.M. van der Tol, R. Hanfoug, W.J.M. de Laat, and M.K. Smit, "A short integrated polarization splitter/converter on InP/InGaAsP," in *Proc. Int. Symposium on Contemporary Photonics Technology*, pp. 101–102, Tokyo, Japan, Jan. 2007.
- J.J.G.M. van der Tol, U. Khalique, L.M. Augustin, and M.K. Smit, "Using polarization for optoelectronic integrated devices," in *Proc. Int. Symposium on Contemporary Photonics Technology*, pp. 57–60, Tokyo, Japan, Jan. 2007. Invited paper.
- B. Huiszoon, M.K. Smit, A.M.J. Koonen, L.M. Augustin, R. Hanfoug, L. Bakker, M. Sander - Jochem, E. Fledderus, G.D. Khoe, J.J.G.M. van der Tol, and H. de Waardt, "Novel building block for multiple encoding and decoding in spectral amplitude encoded OCDMA," in *Proc. IEEE/LEOS Annual Meeting (LEOS '06)*, pp. 905–906, Montreal, Canada, Oct. 29 – Nov. 2 2006.
- L.M. Augustin, J.J.G.M. van der Tol, R. Hanfoug, W.J.M. de Laat, and M.K. Smit, "Design and fabrication of a single etch-step polarization splitter on InP/InGaAsP with increased width tolerance," in *Technical Digest Integr. Photon. Res. and Apps. (IPRA '06)*, p. ITuG4, Uncasville, USA, Apr. 24–Apr. 28 2006.
- U. Khalique, Y. Zhu, J.J.G.M. van der Tol, L.M. Augustin, R. Hanfoug, F. Groen, P. van Veldhoven, M.K. Smit, M. van de Moosdijk, W.J.M. de Laat, and K. Simon, "Ultrashort polarization converter on InP/InGaAsP fabricated by optical lithography," in *Technical Digest Integr. Photon. Res. and Apps. (IPRA '05)*, p. IWA3, San Diego, USA, Apr. 11–Apr. 13 2005.
- L.M. Augustin, J.J.G.M. van der Tol, R. Hanfoug, and M.K. Smit, "Design of a single etchstep fabrication-tolerant polarisation splitter," in *Proc. 12th Eur. Conf. on Int. Opt. (ECIO '05)*, pp. 125–128, Grenoble, France, April 6–8 2005.
- L.M. Augustin, R. Hanfoug, J.J.G.M. van der Tol, J. Binsma, Y.S. Oei, and M.K. Smit, "Polarisation based isolation in wavelength converter," in *Proc. 30th Eur. Conf. on Opt. Comm. (ECOC '04)*, p. We4.P.072, Stockholm, Sweden, Sep. 5–9 2004.
- R. Hanfoug, L.M. Augustin, J.J.G.M. van der Tol, R.G. Broeke, and M.K. Smit, "Optical bandwidth of Mach-Zehnder interferometer wavelength converters," in *Technical Digest Integr. Photon. Res. (IPR '04)*, p. JWB19, San Francisco, USA, Jun. 30–Jul. 4 2004.
- R. Hanfoug, J.J.G.M. van der Tol, L.M. Augustin, and M.K. Smit, "Wavelength conversion with polarisation labelling for rejection and isolation of signals (POLARIS)," in *Proc. 11th Eur. Conf. on Int. Opt. (ECIO '03)*, pp. 105–108, Prague, Czech Republic, Apr. 2–4 2003.

## Local conferences

- L.M. Augustin, J.J.G.M. van der Tol, M.J.H. Sander-Jochem, R. Hanfoug, F. Karouta, H.D. Jung, D. Rogers, and M.K. Smit, “Monolithically integrated SOA-MZI array in InP/InGaAsP suited for flip-chip packaging,” in *Proc. IEEE/LEOS Symposium (Benelux Chapter)*, pp. 75–78, Brussels, Belgium, Dec. 2007.
- L.M. Augustin, J.J.G.M. van der Tol, E.J. Geluk, and M.K. Smit, “Short  $2 \times 2$  polarization splitter in InP/InGaAsP using polarization converters,” in *Proc. IEEE/LEOS Symposium (Benelux Chapter)*, pp. 71–74, Brussels, Belgium, Dec. 2007.
- B. Huiszoon, A. Leinse, D.H. Geuzebroek, L.M. Augustin, E.J. Klein, H. de Waardt, G.D. Khoe, and A.M.J. Koonen, “Multi-stage en/decoders integrated in low loss  $\text{Si}_3\text{N}_4$ - $\text{SiO}_2$  for incoherent spectral amplitude OCDMA on PON,” in *Proc. IEEE/LEOS Symposium (Benelux Chapter)*, pp. 159–162, Brussels, Belgium, Dec. 2007.
- L.M. Augustin, J.J.G.M. van der Tol, and M.K. Smit, “Polarization based filtering in a wavelength converter,” in *Proc. IEEE/LEOS Benelux Workshop on Progress in Optical Devices and Materials*, pp. 9–10, Eindhoven, The Netherlands, May 2007.
- L.M. Augustin, J.J.G.M. van der Tol, R. Hanfoug, W.J.M. de Laat, and M.K. Smit, “An integrated polarization splitter and converter,” in *Proc. IEEE/LEOS Symposium (Benelux Chapter)*, pp. 89–92, Eindhoven, The Netherlands, Dec. 2006.
- R. Hanfoug, M.K. Smit, L.M. Augustin, Y. Barbarin, J.J.G.M. van der Tol, E. Bente, F. Karouta, D. Rogers, Y.S. Oei, and X. Leijtens, “A multimode interference coupler with low reflections,” in *Proc. IEEE/LEOS Symposium (Benelux Chapter)*, pp. 97–100, Mons, Belgium, Dec. 2005.
- U. Khalique, Y.C. Zhu, J.J.G.M. van der Tol, L.M. Augustin, R. Hanfoug, F. Groen, M. van de Moosdijk, W.J.M. de Laat, K. Simon, P. van Veldhoven, and M.K. Smit, “Polarization converter on InP/InGaAsP fabricated with optical reduction wafer stepper,” in *Proc. IEEE/LEOS Symposium (Benelux Chapter)*, pp. 131–134, Ghent, Belgium, Dec. 2004.
- L.M. Augustin, J.J.G.M. van der Tol, R. Hanfoug, and M.K. Smit, “Improved tolerance in polarisation splitters,” in *Proc. IEEE/LEOS Symposium (Benelux Chapter)*, pp. 123–126, Gent, Belgium, Dec. 2004.
- R. Hanfoug, L.M. Augustin, J.J.G.M. van der Tol, R. Broeke, and M.K. Smit, “Static extinction ratio bandwidth of Mach-Zehnder interferometer wavelength converters,” in *Proc. IEEE/LEOS Symposium (Benelux Chapter)*, pp. 73–76, Enschede, The Netherlands, Nov. 2003.







